Investigations on Latent Thermal Storage Systems for Concentrating Solar Power

Karthik Nithyanandam

Dissertation submitted to the Faculty of the
Virginia Polytechnic Institute and State University
in partial fulfillment of the requirements for the degree of

Doctor of Philosophy
In
Mechanical Engineering

Ranga Pitchumani, Chair
Kenneth S. Ball
Srinath V. Ekkad
Roop Mahajan
Christopher J. Roy

May 13, 2013
Blacksburg, Virginia

Keywords: concentrating solar power, power tower, molten salt, thermal energy storage, heat pipes, encapsulated phase change material, system analysis, Rankine cycle, supercritical carbon-dioxide cycle, optimization

Investigations on Latent Thermal Storage Systems for Concentrating Solar Power

Karthik Nithyanandam

Abstract

Thermal energy storage (TES) in a concentrating solar power (CSP) plant allows for continuous operation even during times when solar radiation is not available, thus providing a reliable output to the grid. Energy can be stored either as sensible heat or latent heat, of which latent heat storage is advantageous due to its high volumetric energy density and the high Rankine cycle efficiency owing to the isothermal operation of latent thermal energy storage (LTES) system. Storing heat in the form of latent heat of fusion of a phase change material (PCM), in addition to sensible heat, significantly increases the energy density, thus potentially reducing the storage size and cost. However, a major technical barrier to the use LTES is the high thermal resistance to energy transfer due to the intrinsically low thermal conductivity of PCMs, which is a particularly acute constraint during the energy discharge. Secondly, for integration of TES in CSP plants, it is imperative that the cyclic exergetic efficiency be high, among other requirements, to ensure that the energy extracted from the system is at the maximum possible temperature to achieve higher cycle conversion efficiency in the power block.

The first objective is addressed through computational modeling and simulation to quantify the effectiveness of two different approaches to reduce the thermal resistance of PCM in a LTES, viz. (a) developing innovative, inexpensive and passive heat transfer devices that efficiently transfer large amount of energy between the PCM and heat transfer fluid (HTF) and (b) increase the heat transfer area of interaction between the HTF and PCM by incorporating the PCM mixture in small capsules using suitable encapsulation techniques.

The second portion of the research focuses on numerical modeling of large scale latent thermal storage systems integrated to a CSP plant with the aforementioned enhancement techniques and cascaded with more than one PCM to maximize the exergetic efficiency. Based on systematic parametric analysis on the various performance metrics of the two types of LTES, feasible operating regimes and design parameters are identified to meet the U.S. Department of Energy SunShot Initiative requirements including storage cost < \$15/kWh$_t$ and exergetic efficiency > 95%, for a minimum storage capacity of 14 h, in order to reduce subsidy-free levelized cost of electricity (LCE) of CSP plants from 21¢/kWh (2010 baseline) to 6¢/kWh, to be on par with the LCE associated with fossil fuel plants.

Acknowledgements

First and foremost, I would like to express the deepest appreciation to my advisor, Dr. Ranga Pitchumani, for presenting me with an opportunity to pursue research in this exciting field. I am extremely thankful for his patient guidance and constant encouragement throughout my PhD program. His zest for solving a problem fully, with both basic and applied scientific approaches has been a source of inspiration to me. I would also like to thank my advisory committee, Drs. Roop Mahajan, Srinath Ekkad, Kenneth Ball, and Christopher Roy for their assistance and guidance. I am extremely thankful for the lively and interesting discussions with Mr. Anoop Mathur, CTO of Terrafore, Inc., who subcontracted a part of their funded work by the U.S. Department of Energy, which forms a good portion of the work presented in this dissertation.

The opportunity to express gratitude to one's family on writing does not present itself often and I truly appreciate their continuous love. My parents have always believed in me and supported me in times of adversity. I am also indebted to my grandmother, who raised me as a kid and inculcated the virtue of hard work in me. My brother, lab mates, and friends are a source of enjoyment and fulfillment, and I enjoy their companionship.

The research in this dissertation is funded by the U.S. Department of Energy under Award Numbers DE-EE0003589 and DE-FG36-08GO18146. Their support is gratefully acknowledged.

Table of Contents

List of Figures

List of Tables

Chapter 1: Introduction

This dissertation addresses several fundamental challenges pertaining to latent thermal energy storage system for integration with CSP plant, specifically low heat transfer rate out of the phase change material and the low exergetic efficiency. First, a review of research involving the various approaches to address the aforementioned challenges is presented along with a discussion of the current state-of-the-art thermal storage systems deployed in CSP plants.

Fossil fueled power plants pose a potential risk to the environment through an increased carbon footprint, and efforts are underway to supplant fossil energy with renewable sources including solar energy. Concentrating solar power (CSP) plants harness solar energy from the sun and store as heat, which can be used to drive a turbine in a power plant to generate electricity. CSP plants thus provide low-cost energy generation and have the potential to become the leading source of renewable energy for future power generation. Although energy from the sun is clean and abundant, the intermittent nature of solar availability makes it necessary to capture and store energy when available and discharge the energy on demand. Integration of a thermal energy storage unit eliminates the need for any fossil fuel backup to compensate for cloud transients and diurnal insolation variations.

Thermal energy storage systems for potential integration with the operation of a CSP plant fall into one of the following three types (a) sensible heat storage, (b) latent heat storage and (c) thermo-chemical storage [1]. Most of the thermal energy storage systems in operation are based on sensible heat storage. Stekli et al. [1] provide a comprehensive list of studies in the literature that are focused on each of the three storage systems and enumerate the technical challenges concerned with each of the three storage systems. Of primary interest among researchers is the deployment of

latent heat based thermal storage system in a CSP plant operation. Latent thermal energy storage (LTES) is a desired form of storing energy in a CSP plant due to its isothermal operation, high power cycle efficiency, high latent heat of fusion and high volumetric energy density [2–5]. For instance, the energy required to melt one kilogram of KNO_3 (latent heat) is 95 times higher compared to the energy required to raise the temperature of one kilogram of KNO_3 by 1K (sensible heat). Storing thermal energy in the form of latent heat of fusion of phase change material (PCM) in addition to sensible heat significantly increases the energy density of the storage system, resulting in a reduced storage capital cost per unit thermal energy.

The working of a LTES involves the exchange of energy between the heat transfer fluid (HTF) and the PCM through one of two cycles namely, charging and discharging. During the charging cycle, the solar field of a CSP plant focuses the solar energy to heat the HTF, which is flowed along the LTES compartment housing a solid PCM causing it to melt at a constant temperature, thereby resulting in energy storage through latent heat. During the discharging cycle, cold HTF flows through LTES compartment containing PCM in a molten state causing heat transfer from the PCM to the HTF resulting in the solidification of the PCM and a heated HTF, which may then be used to run the turbine of a power plant to generate electricity. The charging cycle takes place during the day when solar energy is available while discharging cycle occurs whenever the sun's energy is unavailable or when there is a peak demand in electricity. Several studies on the performance of LTES have suggested that the melting of a PCM in LTES (charging) is convection dominated due to the presence of free convection currents in the LTES whereas the solidification of PCM (discharging) is conduction dominated [6–9].

A fundamental challenge with LTES, however, is the low thermal conductivity of the PCM, which significantly reduces the heat transfer rate between the PCM and the HTF. Toward

addressing the challenge this dissertation explores two approaches: (1) use of embedded heat pipes and thermosyphons and (2) use of a single tank filled with encapsulated phase change materials (EPCM), both aimed at augmenting the heat transfer between the PCM and the HTF. These two approaches are systematically investigated: Chapter 2 presents a simplified network modeling of a single module of a heat pipe integrated TES; Chapter 3 discusses a detailed computational modeling of a single module of a heat pipe integrated TES; Chapter 4 presents analysis and optimization of a full TES system with embedded gravity assisted heat pipes (HP-TES) with the objective of meeting the cost and performance targets; Chapter 5 details a computational analysis of an EPCM based TES (EPCM-TES) system; and Chapter 6 describes the design and optimization of an EPCM-TES with the objective of meeting the cost and performance targets.

The two TES options are further investigated in Chapter 7 through their integration in a CSP plant with steam Rankine and supercritical carbon dioxide (s-CO_2) Brayton power cycles. Using the integrated system-level description, a technoeconomic analysis is conducted to derive optimum TES design configurations that meet the cost and performance targets of the U.S. Department of Energy SunShot Initiative goal of CSP systems attaining grid parity levelized cost of energy.

1.1 Basic and Applied Contributions

The fundamental contribution of this dissertation involves addressing the poor heat transfer rate of molten salt PCMs due to their low thermal conductivity, through investigating two approaches: (a) embedding heat pipes or thermosyphons between the PCM and the heat transfer fluid (HTF) for efficient energy transfer and (b) encapsulating the PCM mixture in small capsules to increase the surface area for heat transfer. Another fundamental contribution is investigation, for

the first time in the open literature, of the dynamic performance of latent thermal energy storage systems subjected to repeated charging and discharging cycles.

The applied contribution of this research involves detailed computational modeling and designing of large scale LTES integrated into a CSP plant operating with a conventional steam Rankine cycle as well as a next generation supercritical carbon dioxide (s-CO_2) Brayton cycle to meet the techoeconomic targets in order to reduce subsidy-free levelized cost of electricity (LCE) of CSP plants to 6¢/kWh, to be on par with the LCE associated with fossil fuel plants.

Chapter 2: Simplified Network Modeling of a Latent Thermal Energy Storage Unit Module with Embedded Heat Pipes

This chapter considers an approach to reducing the thermal resistance of LTES through embedding heat pipes to augment the energy transfer from the heat transfer fluid (HTF) to the PCM. Using a thermal resistance network model of a shell and tube LTES with embedded heat pipes, detailed parametric studies are carried out to assess the influence of the heat pipe and the LTES geometric and operational parameters on the performance of the system during charging and discharging. The physical model is then coupled with a numerical optimization method to identify the design and operating parameters of the heat pipe embedded LTES system that maximizes energy transferred, energy transfer rate and effectiveness.

2.1 Introduction

Several approaches to reduce the thermal resistance within the PCM are reported in the literature. Jegadheeswaran et al. [10] presented a brief review of the literature over the past decade on enhancing the performance of LTES. Extended surfaces such as fins are commonly used to provide additional heat transfer area for heat transfer in thermal energy storage systems [11], [12]. A technique of layering different PCMs in the order of decreasing melting temperatures along the HTF flow direction has also been analyzed in order to maintain constant heat flux to the PCM [13], [14]. Other techniques include the impregnation of a porous structure formed of materials such as exfoliated graphite nanoplatelets [15], [16] and dispersion of micro/nanoparticles within the PCM [17–19] to improve its thermal conductivity.

The use of embedded heat pipes or thermosyphons between the PCM and the HTF as a means of enhancing the thermal energy transport between them has also been explored. The operation of

a heat pipe involves the evaporation of a working fluid at the high temperature (evaporator) end creating a high vapor pressure in its vapor core. Due to the pressure difference, the vapor migrates along the length of the central vapor core to the low temperature (condenser) end where it condenses back to liquid onto a porous wick, and flows back to the high temperature end by means of capillary action. Since the return mechanism is not gravity assisted, heat pipes are effective in any orientation with respect to gravity, and are capable of transferring large amounts of energy nearly isothermally. Horbaniuc et al. [20] reported on modeling of two-dimensional solidification of a low melting temperature PCM surrounding a longitudinally finned heat pipe, and investigated the duration of freezing as a function of the number of fins. Liu et al. [21] extended the work of Horbaniuc et al. using a circumferentially finned thermosyphon, to analyze the effect of HTF inlet temperature and the flow rate on the freezing rate of paraffin PCM. Lee et al. [22] used a thermosyphon to investigate its sensitivity on a variety of PCMs. Tardy and Sami [23] investigated numerically and experimentally the use of heat pipes to melt a low melting-temperature PCM and presented a thermal resistance model to determine the heat transfer rate with the HTF (air), and the associated melting process.

From the foregoing review, it is found that none of the previous studies reported a quantitative performance enhancement due to embedding heat pipes and were focused only on low temperature applications ($< 100^{o}$C). This chapter investigates an approach to reduce the thermal resistance of PCM through embedded heat pipes and improve the overall energy storage and discharge rates of the LTES. The primary goals are the following: (1) to elucidate the effects of the heat pipe and the LTES system geometry and the LTES operational parameters on the performance of the system during charging and discharging; to this end, a thermal resistance network model of a shell and tube LTES with embedded heat pipes is utilized to describe the system during charging and

discharging processes, and (2) using the physical model combined with a numerical optimization scheme, to determine the optimum design of the system for maximizing energy transferred, effectiveness, and energy transfer rate during charging and discharging processes individually as well as based on combined charging and discharging considerations.

2.2 Mathematical Model

The LTES configuration considered in this chapter consists of a rectangular array of tubes of outer radius r_t and tube wall thickness b_t, arranged with a horizontal center-to-center spacing S_L and a vertical center-to-center spacing S_T and enclosed in a shell. Heat pipes are placed through the tube walls at m (taken to be 4 in this study with two horizontally oriented and two vertically oriented heat pipes) circumferential locations and are spaced by a distance L_m along the tube length. The periodic configuration of the heat-pipe-embedded tube-in-shell geometry allows for identification of a representative rectangular volume element of dimensions $S_T \times S_L \times L_m$ as shown in Figure 1 for the analysis. Figure 1a illustrates two different configurations based on the relative locations of the PCM and the HTF in the LTES. In Module 1, the HTF flows within the tube surrounded by the PCM, while in Module 2, the PCM is contained within the tube over which the HTF flows transverse to the tube axis. In both configurations, the heat pipes are placed in such a way that the interface of the evaporator and adiabatic sections of the heat pipe coincides with the wall of the tube in contact with the HTF to ensure that for a given design configuration, the surface area of the heat pipes exposed to the HTF remains the same in both modules. Figure 1b shows a schematic of the longitudinal cross section of a heat pipe of radius r_{HP} identifying the internal components and the associated dimensions. The working principle of a heat pipe is not described here, but may be found in [24].

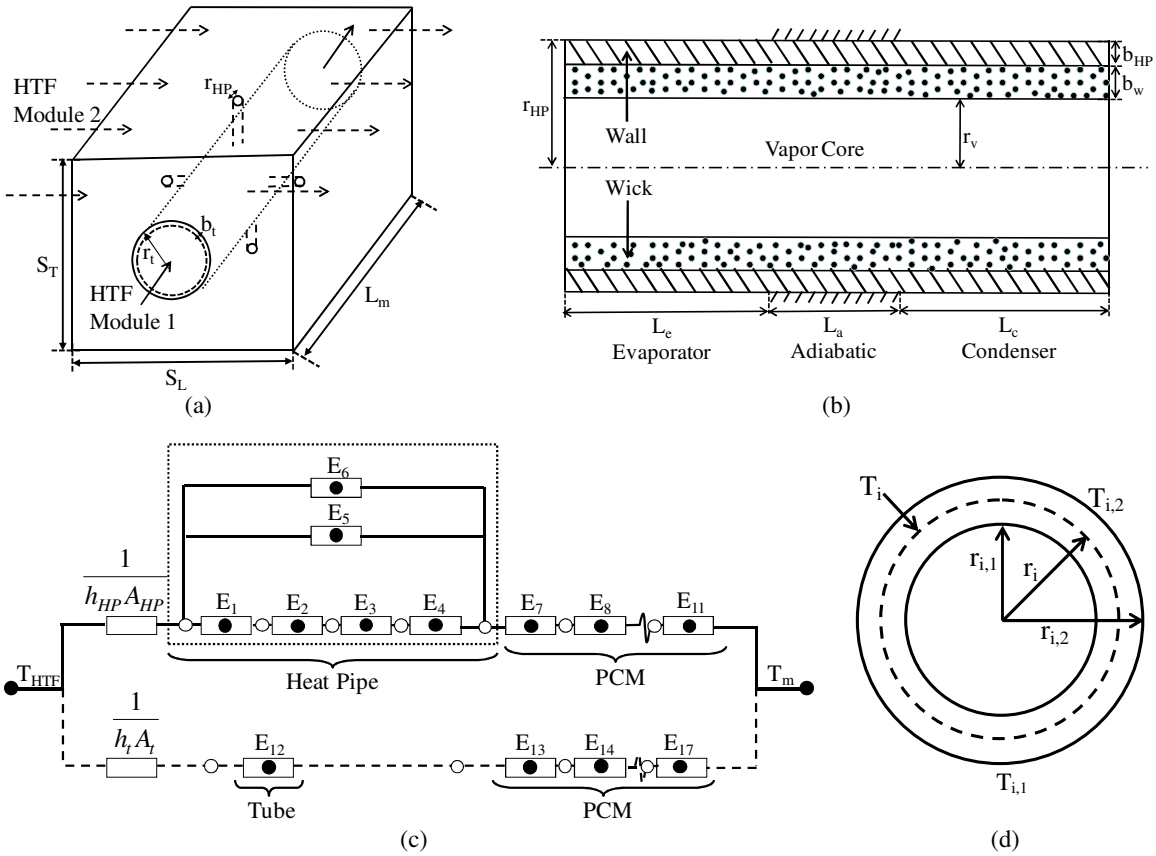

Figure 1: Schematic illustration of LTES (shaded areas denote PCM) with embedded heat pipes: (a) Module 1 configuration, (b) Module 2 configuration, (c) unit cell and (c) heat pipe cross section

The physical phenomena governing the phase change rate of the PCM in the LTES system described in Figure 1 are: forced convection between the HTF and the heat pipes and between the HTF and the tube; conduction within the wick and the walls of the heat pipes; evaporation and condensation heat transfer in the vapor core of the heat pipes; conduction within the tube wall material; free convection within the liquid PCM adjoining the tube and the heat pipes during melting; and conduction within the solid PCM adjoining the tube and heat pipes during solidification. It is expected that the melting (charging) of the PCM is convection dominated whereas the discharging of the PCM in LTES is dominated by conduction.

The transient operation of the LTES is described using a thermal resistance network model with a quasi-steady approximation adopted from ref. [25] with modifications in the determination of certain thermal resistances as noted with the model equations later in this section. Figure 1c shows the thermal resistance network for the LTES system with embedded heat pipes. Thermal energy is transferred between the HTF at temperature T_{HTF} and the liquid (solid) PCM at temperature T_m through the heat pipes (the solid lines of the network in Figure 1c) and the tube (the dashed lines of the network in Figure 1c), which are represented in Figure 1c as two parallel thermal resistance networks from the HTF to the PCM. A transient analysis of the LTES system represented by a network of coupled thermal elements as in Figure 1c is conducted with the following assumptions: the vapor flow thermal resistance in the heat pipes is negligible compared to other processes and is not considered [26]; the evaporation and condensation thermal resistances in the heat pipes are negligible; the change in the HTF temperature from the module inlet to its outlet is negligibly small; and the PCM solidifies as a pure material for which the changes in the thermo-physical properties between the solid and liquid PCM are not considered.

The network model assumes that the radius of the melt front at any instant of time is uniform throughout its circumference but the increase in the rate of progression of the melt front is captured by an enhanced thermal conductivity of the PCM melt. The consequences to the quasi-steady approximation are that (i) the exact temperature distributions within the liquid PCM cannot be predicted and (ii) the possible effect of complex pool geometries on convection heat transfer rates is not accounted for; however, these limitations are relatively minor since the sensible energy of the entire liquid phase is not highly dependent on the temperature distribution within the liquid phase and the spatially-averaged free convection heat transfer coefficients are known to be relatively insensitive to the liquid phase domain [27]. Furthermore, simplified network modeling

has been shown to yield reasonably accurate results for phase change systems that compared favorably with the rigorous, detailed modeling as well as experimental measurements [28].

For any thermal element E_i in the network, Figure 1c, an overall energy balance dictates that the rate of increase of thermal energy stored in the control volume equals the difference in the rate at which thermal energy enters the control volume and the rate at which thermal energy leaves the control volume, which can be represented in mathematical form as:

$$\rho_i c_{p,i} V_i \frac{dT_i}{dt} = \left[\frac{\left(T_{i,1} - T_i\right)}{R_{i,1}} - \frac{\left(T_i - T_{i,2}\right)}{R_{i,2}} \right] \tag{1}$$

where the density, specific heat and volume of the element E_i are represented by ρ_i, $c_{p,i}$ and V_i, respectively, the first and second terms within square brackets on the right hand side of Eq. (1) represent the rates of energy transferred in to and out of the thermal element, respectively, in which, the temperatures $T_{i,1}$ and $T_{i,2}$ represent the surface temperatures at either end of the heat conductor element, denoted by the open circles in Figure 1c, and T_i denotes the temperature at the middle of the thermal element as identified by the solid circles in Figure 1c. For axial heat conduction in the adiabatic sections of the wick and the wall of the heat pipes, the resistances can be expressed as $R_{i,1} = R_{i,2} = \frac{\ell_i}{2k_i A_i}$ [29], where ℓ_i is the element length in the direction of heat transfer and A_i is the cross sectional area of the element normal to heat flow direction. In ref. [25], the radial elements were approximated to be planar and the corresponding thermal resistances were evaluated using an expression for axial conduction as given above. The present modeling differs from [25] in eliminating this approximation and determining the thermal resistances, $R_{i,1}$ and $R_{i,2}$, for the radial heat conduction elements (Figure 1d) based on an analysis of the radial conduction heat transfer through the elements as: $R_{i,1} = \frac{1}{2\pi L_i k_i} \ln\left(\frac{r_i - c}{r_{i,1} - c}\right)$ and $R_{i,2} = \frac{1}{2\pi L_i k_i} \ln\left(\frac{r_{i,2} - c}{r_i - c}\right)$, where

$r_{i,1}$, r_i, and $r_{i,2}$ are the inner, mid, and outer radii, respectively, of the radial element as shown in Figure 1d, L_i denotes the radial element length (in the direction normal to the plane of Figure 1d), k_i denotes the thermal conductivity of the element, and c accounts for the reduction in the area of the tube available for heat transfer, due to the presence of heat pipes. During the charging cycle, the thermal conductivity of the PCM elements, k_i for i = 7–11 and 13–17 (Figure 1c), is replaced by an *enhanced* thermal conductivity to account for the natural convection effects in the augmenting the heat transfer, as discussed later in this Section.

The expressions for the thermal resistances given above are applicable for very small thickness of the thermal element, for which the thermal and thermophysical properties may be considered constant. The small wall thickness of the heat pipes and the tube render the expressions acceptable while as the PCM melt/solid front grows, the linear approximation progressively becomes less valid. For improved accuracy, the PCM melt (solid) front thickness at any instant of time was divided into five discrete thermal elements each with uniform thickness. Note that, in general, the PCM melt or solid region may be discretized into any number of elements, however, in the present study, discretization beyond 5 elements was found to yield no appreciable change in the results, and this number is used in the description presented here. Accordingly, in Figure 1c the thermal elements represented by E_i for i = 1–6 pertains to that of heat pipes; i = 7–11 represents the PCM melt (solid) front adjoining the heat pipes; i = 12 represents the tube wall and i = 13–17 pertains to that of the PCM melt (solid) front adjoining the tube. The thermal elements in the heat pipe network system are composed of radial conduction in the wall of heat pipes represented by E_1 in the evaporator section, E_2 for the wick in the evaporator, E_3 for the wick in the condenser and E_4 in the condenser section; and axial conduction in the adiabatic sections of the wick and wall are

represented by E_5 and E_6, respectively. The reduction of tube surface area incorporating m (= 4 in this study) heat pipes is: $c = \frac{m \cdot r_{HP}^2}{2L_m}$ for elements i = 12–17 and c = 0 for the remaining elements.

For each thermal element, E_i, the unknown surface temperatures $T_{i,1}$ and $T_{i,2}$ can be represented in terms of the middle temperatures of the thermal elements, T_i, by performing an energy balance on all the nodes as described in [24]. Considering the heat transfer through the part of the network via the heat pipes (shown by the solid line in Figure 1c), the surface temperatures for the thermal elements, i = 1,…,11, in the solid line network of Figure 1c can be expressed in terms of T_i as follows:

$$T_{1,1} = T_{5,1} = T_{6,1} = \eta' \cdot T_{HTF} + \eta_1 T_1 + \eta_5 T_5 + \eta_6 T_6 \quad (2)$$

$$T_{(i+1),1} = T_{i,2} = \xi_{i,(i+1)} T_i + \xi_{(i+1),i} T_{i+1}, \text{ for } i = 1,2,3 \quad (3)$$

$$T_{7,1} = T_{4,2} = T_{5,2} = T_{6,2} = \psi_4 T_4 + \psi_5 T_5 + \psi_6 T_6 + \psi_7 T_7 \quad (4)$$

$$T_{i,1} = T_{(i-1),2} = \xi_{(i-1),i} T_{i-1} + \xi_{i,(i-1)} T_i, \text{ for } i = 8–11 \quad (5)$$

where the coefficients η', η_i, ψ_i and $\xi_{i,j}$ are given by: $\eta' = \frac{\pi h_{HP} r_{HP} L_e}{1/R_1 + 1/R_5 + 1/R_6 + \pi h_{HP} r_{HP} L_e}$, $\eta_i = \frac{1/R_i}{1/R_1 + 1/R_5 + 1/R_6 + \pi h_{HP} r_{HP} L_e}$ (i = 1, 5, 6), $\psi_i = \frac{1/R_i}{1/R_4 + 1/R_5 + 1/R_6 + 1/R_7}$ (i = 4, 5, 6, 7), and $\xi_{i,j} = \frac{1}{1 + R_i/R_j}$ in which the thermal resistances, R_i are defined as $R_i = \frac{1}{2\pi L_i k_i} \ln\left(\frac{r_i}{r_i - \ell_i}\right)$, L_e denotes the evaporator length of the heat pipe, h_{HP} is the convective heat transfer coefficient between the HTF and heat pipes and T_{HTF} is the temperature of the HTF. The correlations for determining the convective heat transfer coefficients and incorporating the natural convection effects are discussed later in this section.

The advancement of the solid-liquid PCM interface in the vicinity of the heat pipes is tracked by incorporating a surface energy balance for element, E_{11} (Figure 1c), which leads to

$$\rho \cdot \Delta H_f A_{11} \frac{ds_{HP}}{dt} = \pm \frac{2\pi L_{11} k_{11} (T_{11} - T_m)}{\ln\left(1 - \frac{\ell_{11}}{2s_{HP}}\right)} \tag{6}$$

where, T_m is the melting temperature of PCM, A_{11} is the surface area of the melt (solid) front of the PCM adjacent to the heat pipes, s_{HP} is the position of the melt (solid) front of the PCM adjoining the heat pipes, and ΔH_f represents the latent heat of fusion of the PCM. For charging (discharging) the negative (positive) sign on the right hand side of Eq. (6) applies.

The elements E_{12}–E_{17} in the dotted line network of Figure 1c correspond to the combined convective and conduction heat transfer from the HTF to the PCM via the tube for which the surface nodal temperatures can be expressed as:

$$T_{12,1} = \frac{T_{HTF} h_t A_t + 2T_{12}/R_{12}}{h_t A_t + 2/R_{12}} \tag{7}$$

$$T_{(i+1),1} = T_{i,2} = \xi_{i,(i+1)} T_i + \xi_{(i+1),i} T_{i+1} \text{ ; for } i = 12\text{–}16 \text{ and } T_{17,2} = T_m \tag{8}$$

where T_{HTF} is the temperature of the HTF, A_t represents the surface area of the tube exposed to the HTF, h_t denotes the convective heat transfer coefficient between the HTF and the tube and the thermal resistance, R_{12} is defined as $R_{12} = \frac{1}{2\pi L_m k_t} \ln\left(\frac{r_{12}}{r_{12} - \ell_{12}}\right)$ where k_t is the thermal conductivity of the tube.

Similar to Eq. (6), the transient progression of the melt (solid) front of the PCM adjacent to the tube (s_t) can be tracked by applying a surface energy balance for element E_{17} (Figure 1c) which yields

$$\rho \cdot \Delta H_f A_{17} \frac{ds_t}{dt} = \pm \frac{2\pi L_{17} k_{17} (T_{17} - T_m)}{\ln\left(1 - \frac{\ell_{17}}{2s_t}\right)} \tag{9}$$

The convection heat transfer coefficients (h_t and h_{HP}) and the *enhanced* thermal conductivity of the PCM (k_i for i = 7–11 and 13–17) due to the free convection effects during charging are implemented using appropriate correlations from the literature ensuring their applicability over the range of dimensionless parameters considered in this study. Forced convection heat transfer takes place between the HTF and the tube wall in both Module 1 and Module 2 (Figure 1a). For HTF flow inside a cylindrical tube as in Module 1, the correlation provided by Gnielinski [29], which is valid over a large Reynolds number range including the transition region, is used to determine h_t. Note that the Gnielinski equation improves the estimation of the heat transfer coefficients over the Dittus-Boelter equation [29] that was used in ref. [25] for determining h_t for Module 1. For Module 2, in which the HTF flows transversely over the tube, the correlations developed by Zukauskas [29] for an aligned bank of circular cylinders in cross flow is used to calculate the convective heat transfer coefficient between the HTF and the tube outer wall.

Forced convection heat transfer also occurs between the HTF and the evaporator/condenser sections of the heat pipe. For m = 4 radial heat pipes considered in this study, two different orientations of the heat pipes are presented to the HTF flow namely, horizontal heat pipes (HHP) and vertical heat pipes (VHP). In Module 1, the HTF flows normal to the axis of the circular heat pipe irrespective of the orientation of heat pipes whereas in Module 2 the HTF flows parallel to the axis of a HHP and normal to the axis of the VHP. The Zukauskas correlation [29] developed for an aligned tube bank in cross flow is used to define h_{HP} in Module 1 and for the VHP configuration in Module 2, and the convective heat transfer coefficient between HTF and HHP, h_{HP} in Module 2 is defined as [30]:

$$h_{HP} = \left(0.662\,\mathrm{Re}_{Le}^{1/2}\mathrm{Pr}^{1/3} + \frac{0.7613\,\mathrm{Pr}^{1/3}\,L_e}{r_{HP}} \right) \times \frac{k_{HTF}}{2r_{HP}} \tag{10}$$

where Re_{Le} and Pr are the Reynolds number of the HTF in the vicinity of the HHP and the Prandtl number of the HTF, respectively. L_e represents the length of the evaporator section of the heat pipe, r_{HP} represents the radius of the heat pipe, and k_{HTF} denotes the thermal conductivity of the HTF. Hence the flow over the cylindrical HHP in Module 2 is not approximated to flow over a flat plate as in ref. [25].

The natural convection effects during the melting of PCM are modeled using empirical correlations to determine the *enhanced* thermal conductivity of the PCM melt front (k_i for i = 7–11 and 13–17). Two types of melt domain shapes can be formed in either Module 1 or Module 2. The first domain is nominally horizontal consisting of a hot circular cylinder and a second nominally circular cold surface. The second type is a predominantly vertical melt domain consisting of hot inner cylinder and a surrounding nominally circular cold surface. For the horizontal domain, the effective thermal conductivity is evaluated using the correlation of [31], which covers both the conduction and convection regimes. This correlation is valid for a wide range of Pr, s_{HP}/r_{HP}, and s_t/r_t ratios. For the vertical melt domain, heat transfer through the melt is calculated by evaluating both (i) a conduction heat transfer rate and (ii) a rate associated with use of a correlation for free convection in a vertical annulus [32] and the expression that yields the largest heat transfer rate was used in the computations.

The energy charged (discharged) by the PCM at any instant of time is composed of sensible energy and latent energy components calculated as the summation of energy stored in all the PCM thermal elements which can be determined from the following expressions:

$$Q_t = \sum_{i=13}^{17} \left[\pm \rho_{PCM}\, c_p \left(T_i - T_m\right) + \rho_{PCM}\, \Delta H_f \right] \times \left[\pi \left(r_{i,2}^2 - r_{i,1}^2 \right) L_m - m\pi r_{HP}^2 \left(s_t - r_t \right) \right] \tag{11a}$$

$$Q_{HP} = \sum_{i=7}^{11} \left[\pm \rho_{PCM} c_p (T_i - T_m) + \rho_{PCM} \Delta H_f \right] \times \left[\pi \left(r_{i,2}^2 - r_{i,1}^2 \right) L_c \right] \quad (11b)$$

where the energy stored (discharged) within (from) the melt (solid) front of the PCM in the vicinity of the tube and heat pipes are represented by Q_t and Q_{HP}, respectively and the terms within the second set of square brackets in the above expressions represent the volume of each element V_i. The negative sign in Eq. (11) applies to solidification of the PCM and m represents the number of heat pipes installed in the module, fixed at 4 for this study involving 2 HHP and 2 VHP. In the discussion that follows, the total energy stored during charging and released during discharging for the LTES with heat pipes, computed using $(Q_t + m \times Q_{HP})$, are denoted as Q_C and Q_D respectively. Further, the augmentation in the thermal performance of the LTES due to embedding heat pipes is quantified in terms of the *effectiveness* of the system, defined for charging and discharging as $\varepsilon_C = Q_C / Q_{C,0}$ and $\varepsilon_D = Q_D / Q_{D,0}$, respectively, where the energy stored during charging (discharging) for the case of tube with no heat pipes is $Q_{C,0}$ ($Q_{D,0}$).

Equations (1)–(10) result in a set of coupled first order, linear, ordinary differential equations for the element temperatures, T_i, which are solved in MATLAB using the fourth order *Runge-Kutta* method [33].

The resulting temperature field is used in Eq. (11) to determine the energy charged or discharged and the effectiveness measures. Mercury-Stainless steel heat pipe is used for the present analysis while the PCM material and HTF are potassium nitrate (KNO_3) and Therminol, respectively [23]. Table 1 lists the various geometrical parameters and thermophysical properties used in the simulations and their values, where the LTES dimensions presented are representative of those used for large-scale energy storage [34]. An initial melt (solid) layer thickness of 100 μm is assumed for charging (discharging) to start the simulations, and all the thermal elements are initialized to be at the melting temperature of PCM. Initially, at $t = 0$, the HTF is introduced at

Table 1: Geometrical parameters and thermophysical properties of heat pipes, PCM and HTF considered in Chapter 2

a. Heat Pipe and Tube Parameters			
Heat pipe radius, r_{HP} [m]	0.009	Condenser length, L_c [m]	0.140
Heat pipe wall thickness, b_{HP} [m]	0.001	Evaporator length, L_e [m]	0.100
Heat pipe wick thickness, b_w [m]	0.001	Adiabatic length, L_a [m]	0.060
Wick porosity, φ	0.900	Tube outer radius, r_t [m]	0.250
Wick thermal conductivity, k_w [W/m-K]	15	Tube wall thickness, b_t [m]	0.003
Wick heat capacity, $\rho_w c_{pw}$ [J/m^3-K]	2.89×10^6	Module length, L_m [m]	0.120

b. Other Properties	PCM (KNO_3)	HTF (Therminol)	Stainless Steel
Density, ρ [kg/m^3]	2109	709	7900
Thermal conductivity, k [W/m-K]	0.5	0.078	20.1
Specific heat, c_p [J/kg-K]	953	2588	559.9
Dynamic viscosity, μ [Pa-s]	2.59×10^{-3}	0.152×10^{-3}	
Melting temperature, T_m [K]	608	–	–
Thermal expansion coefficient, β[K^{-1}]	200×10^{-6}	–	–
Latent heat of fusion, h_{sl} [J/kg]	95×10^3	–	–

T_{HTF} = 391°C for charging and at T_{HTF} = 295°C for discharging.

The outputs from the numerical simulation include the melt front progression with time, transient profile of the energy stored, melt (solid) fraction of the PCM, effectiveness of the LTES embedded with heat pipes and transient temperature of the PCM melt front. The network model is valid only until the instant any two melt (solidification) fronts meet—referred to as the *charging (discharging) time*, t_C (t_D), in this article—and the simulation is conducted until such a merger occurs.

The numerical model presented in Section 2.1 forms the basis of the parametric studies discussed in Section 2.2 and is also used in a numerical optimization of the system as formulated in the following Section.

2.3 Numerical Optimization

The goal of the optimization is to determine the optimum values of the operating and design parameters of the LTES system so as to maximize selected performance metrics. For this study, five optimization objectives are considered: (1) maximizing charging effectiveness, ε_C; (2) during charging, it may be desirable to simultaneously maximize the amount of energy stored Q_C and the charging effectiveness ε_c while minimizing the charging time t_c, which may be formulated as maximizing an *effective charge rate* $Q_C \varepsilon_C / t_C$; (3) maximizing discharging effectiveness, ε_D; (4) following similar considerations as in (2) above, maximizing an *effective discharge rate* formulated as $Q_D \varepsilon_D / t_D$; and (5) from a combined consideration of optimizing the system for both charging and discharging, maximizing an overall *LTES energy transfer rate*, $P = (Q_C / t_C + Q_D / t_D)$.

For the optimization objectives (1)–(4) above, the decision variables whose optimum values are sought to be determined are the HTF mass flow rate $\dot{m}$ (operational parameter) and six geometric parameters of the LTES: length of the module L_m, outer radius of the tube r_t, length of the evaporator section of the heat pipe L_e, length of the condenser section of the heat pipe L_c, radius of the vapor core of the heat pipe r_v, thickness of the wick of the heat pipe b_w. Optimization objective (5) above was solved from the consideration of determining the optimum values of the six LTES geometric parameters for specified HTF mass flow rate, $\dot{m}$. To this end, three different mass flow rate values, $\dot{m}$ = 0.589 kg/s, 2.80 kg/s and 5.89 kg/s, were considered. The design intervals of the geometrical parameters considered for the study are $0.2 \le r_t \le 0.4$, $0.08 \le L_m \le 0.2$, $0.05 \le L_e \le 0.3$, $0.05 \le L_c \le 0.243$, $0.007 \le r_v \le 0.038$, $0.007 \le b_w \le 0.032$. The upper and lower bounds of the decision variables are chosen so as to accommodate multiple heat pipe installations in a module width (S_L) and height (S_T) of 1 m each (Figure 1a).

The seven optimization problems may be mathematically expressed as:

$$\underset{\dot{m}, L_m, r_t, L_e, L_c, r_v, b_w}{Maximize} \begin{cases} \varepsilon_C, \; Q_C \varepsilon_C / t_C \;\; (Charging) \\ \varepsilon_D, \; Q_D \varepsilon_D / t_D \; (Discharging) \end{cases} \tag{12a}$$

$$\underset{L_m, r_t, L_e, L_c, r_v, b_w}{Maximize} \left(\frac{Q_C}{t_C} + \frac{Q_D}{t_D} \right), \dot{m} = 0.589, 2.800, 5.890 \, kg/s \tag{12b}$$

Note that Objectives (1)–(4) [Eq. (12a)] and Objective (5) for three mass flow rates [Eq. (12b)] were used to design for each of Modules 1 and 2, resulting in a total of 14 optimization cases considered. The optimization is subject to physical constraints on the geometrical parameters defined as follows:

$$\begin{array}{rr} r_t + L_c - 0.5 + (L_a - b_t) \le 0 & r_t + L_e - 0.5 \le 0 \\ 0.035 - r_t + L_e + r_{HP} + b_t \le 0 & 0.031 - r_t + L_c + r_{HP} + L_a \le 0 \\ \underbrace{0.031 - 0.5 L_m + r_{HP} \le 0}_{Module\ 1} & \underbrace{0.031 - 0.5 L_m + r_{HP} \le 0}_{Module\ 2} \end{array} \tag{13}$$

The constraints on the decision variables presented in Eq. (13) were chosen to allow a minimum distance of $s_t - r_t = 0.057$ m for the melt front adjacent to the tube to travel and assumes $s_{HP} - r_{HP} = 0.031$ m. Since the objective functions involves looking at the rate of charging and discharging, irrespective of whether the melt fronts meet, the optimization runs were carried out until either s_t or s_{HP} reaches the mentioned values. The optimization problem represented by Eqs. (12) and (13) were solved using the nonlinear programming technique of sequential quadratic programming [35] implemented in MATLAB. The numerical model described in Section 2.1 was used to obtain the objective function and constraint values as well as the Jacobian information needed during the optimization, and convergence of the optimization was based on the Karush-Kuhn-Tucker (KKT) criterion. Further details on the optimization method may be found in [35–37].

2.4 Model Validation

The network model presented in Section 2.1 was validated with numerical results found in the literature. Figure 2a compares the transient vapor temperature of the heat pipe, $T_{2,2}$ (Figure 1c) from a network modeling of the heat pipe alone (without the rest of the LTES) with that of the two-dimensional numerical results presented by Cao and Faghri [28]. It is observed that the increasing trend of the vapor temperature with time obtained from the network model closely agrees with the more detailed numerical model results. Figure 2b–d compares the predictions of the network model for the LTES with four heat pipes with the results for the same system reported by Shabgard et al. [25] on various performance metrics. Figure 2b presents the transient progression of the melt front adjacent to the tube and the temperature of the tube wall for Module 1 and shows that the tube wall temperature increases initially and remains constant at later times as it reaches steady state, while the melt front location around the tube increases monotonically with time. The melt front progression adjacent to the tube and the temperature of the tube wall from the present study (dashed lines) are found to be higher than those predicted by Shabgard et al. [25] (solid lines), owing to the fact that the convective heat transfer coefficient between the tube and HTF, h_t, provided by the Gnilenski correlation used in this study [29] is 43 W/m^2-K compared to 35 W/m^2-K predicted by the relatively less-accurate Dittus-Boelter correlation [29] used by Shabgard et al. [25].

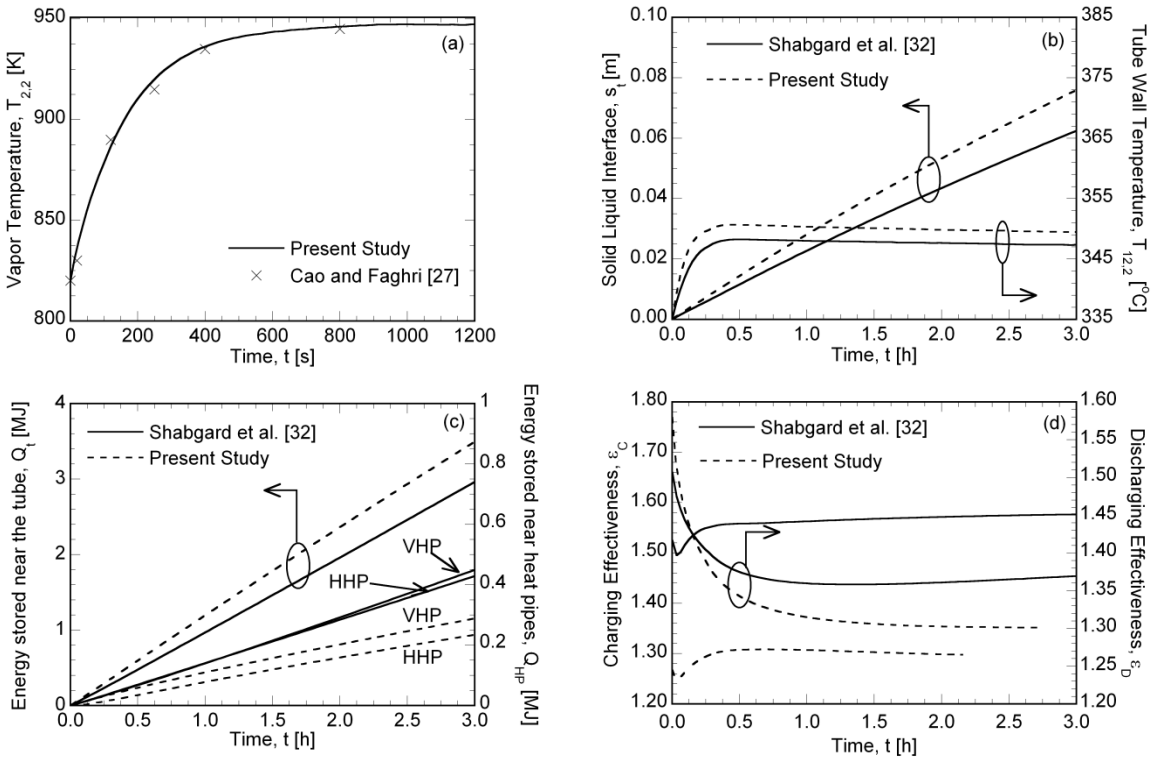

Figure 2: (a) Comparison of the transient variation of the vapor temperature in heat pipe with Cao and Faghri [28] and comparisons of the time evolution of the (b) tube wall temperature and melt front location, (c) energy stored in the PCM near the tube and near the heat pipe and (d) charging and discharging effectiveness, all for Module 1, with the results of Shabgard et al. [25]

Figure 2c compares the time history of energy stored in the vicinity of the tube and heat pipes. The energy stored is higher compared to the results obtained by Shabgard et al. [25] due to the reasons mentioned before, while the energy stored in the vicinity of heat pipes is found to be lesser than that obtained in [25] even though the heat transfer coefficients between the HTF and heat pipe are found to be equal in both the studies. However, the approximation of the radial thermal resistances to planar thermal resistances in ref. [25] underestimates the resistance provided to heat transfer, for the scale of the melt front radii on the order of the heat pipe radius, which leads to a delayed onset of natural convection within the melt fronts in the vicinity of heat pipes (3.4 min) compared to that in ref. [25] (2.0 min). The variation of the effectiveness with time is compared in

Figure 2d for both charging and discharging cycles of Module 1. For charging, the effectiveness of the system is seen to initially decrease while the heat transfer is conduction dominated, but starts increasing once the natural convection currents are triggered in the melt front adjacent to the heat pipes, as seen by the dip in the effectiveness curves in Figure 2d. The effectiveness of the system eventually settles at a steady value once the natural convection current within the melt front adjacent to the tube takes effect. The discharging of the PCM is purely conduction dominated as evidence by a monotonic drop in the effectiveness with time. The differences in the present modeling approach that improves upon the model of [25], as explained in the foregoing discussion, is seen in the difference in the results between the two studies in Figure 2d. Similar trends were obtained for Module 2, which are omitted here for brevity.

The network model is used to study the various parametric effects on the performance of the LTES with embedded heat pipes in the configurations of Module 1 and Module 2 as discussed in this Section. The studies on charging are presented first in Section 2.4 followed by the results on discharging in Section 2.5, and a discussion on the optimum design considerations in Section 2.6.

2.5 LTES Charging

Figure 3 shows the variation of the onset time for natural convection currents, t_{nc}, within the melt front adjacent to the tube and heat pipes as a function of the HTF mass flow rate (Figure 3a and b) and evaporator/condenser length of the heat pipes (Figure 3c and d) during charging of Module 1 and Module 2 as indicated in the figures. Although the onset of natural convection within the melt front adjacent to the tube and heat pipes happens at different times for different parametric combinations, they share a common Rayleigh number, *Ra*, which is a measure of the relative strength of buoyancy force compared to viscous force. It was found that for all the

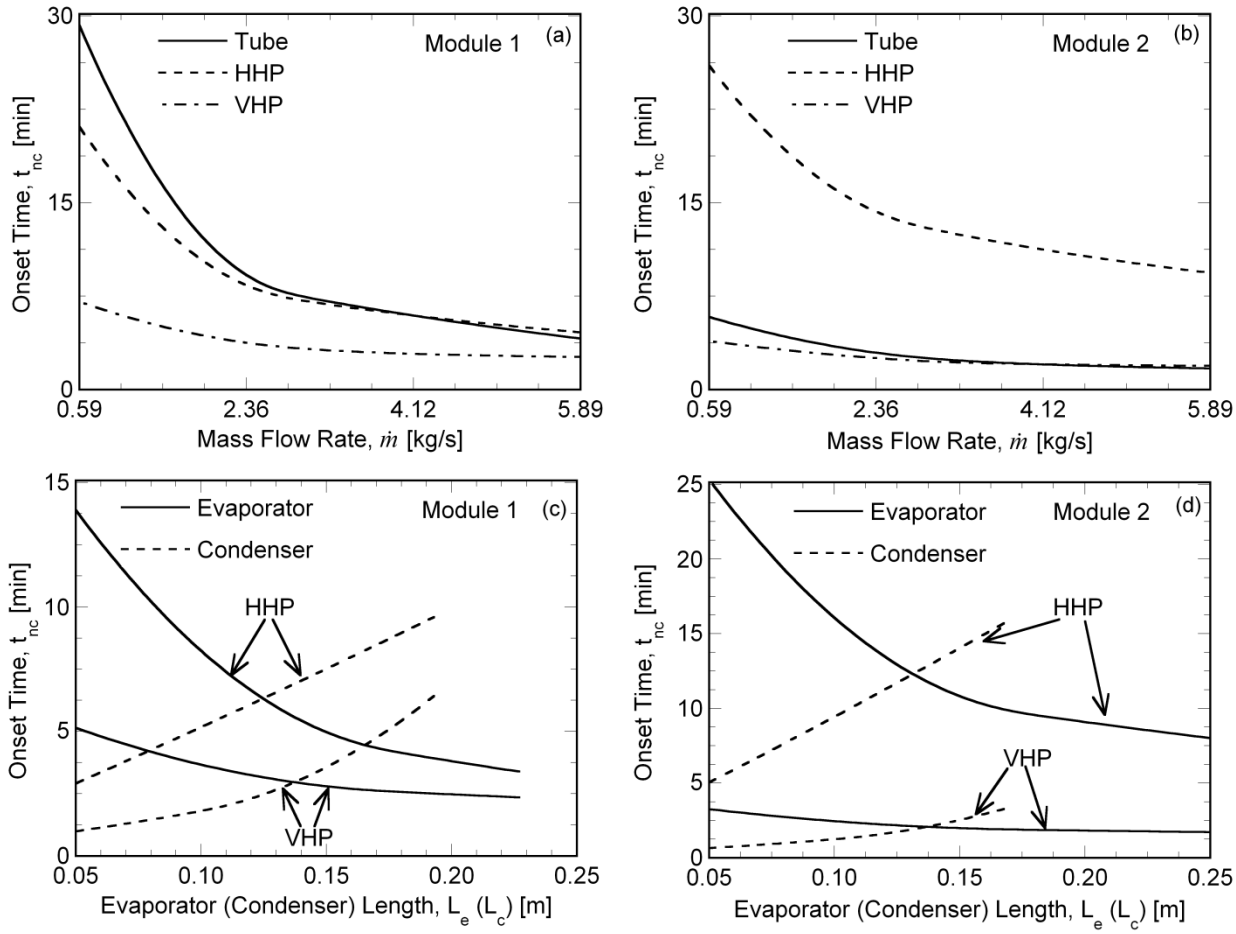

Figure 3: Variation of the onset of natural convection currents within the PCM as a function of (a, b) mass flow rate and (c, d) evaporator (condenser) length for Modules 1 and 2.

parameter combinations considered in this study, the natural convection in the melt front surrounding the tube, a HHP, and a VHP started at $Ra = 5.5\times10^8$, 2.9×10^5 and 8.0×10^3, respectively. In general, the onset time is observed to decrease with increasing mass flow rate (Figure 3a and b) and evaporator length (Figure 3c and d), but increases with the condenser length (Figure 3c and d) of the heat pipe. From a comparison of Figure 3a and b, it is seen that natural convection within the melt front surrounding the VHP and the tube start earlier in Module 2 than those in Module 1 due to the significantly larger convective heat transfer coefficients for the tube and the VHP in Module 2 compared to Module 1, which enhance the progression rate of the melt

front adjacent to the tube and the VHP to quickly form the critical melt volume needed for natural convection. For the melt front surrounding the HHP, however, the onset of natural convection in Module 2 is delayed compared to Module 1 (cf. Figure 3), since by virtue of their alignment with the flow direction, the HHPs in Module 2 are subjected to smaller convective heat transfer from the HTF compared to those in Module 1. The variation of t_{nc} for other parameters are not plotted here and may be summarized as follows: the onset time for natural convection currents is seen to increase with the tube radius and the vapor core radius of the heat pipe for both Module 1 and Module 2. An increase in the length of Module 1 did not alter the onset time for natural convection, while an increase in the length of Module 2 increases the area of the cross flow, thereby decreasing the flow velocity for a fixed $\dot{m}$ and, in turn, reducing the convective heat transfer coefficients, which leads to a delayed onset of natural convection in the melts. The trends of the onset time will be used in discussing the effects of the parameters on the energy stored and the effectiveness in Figure 4 and Figure 5.

Figure 4a–c shows the time variation of the thermal energy stored during charging of an LTES with heat pipes in the configuration of Module 1 and the corresponding effectiveness for different values of the HTF mass flow rate, $\dot{m}$ = 0.589 kg/s (solid), 2.8 kg/s (dashed) and 5.89 kg/s (dotted); module length, L_m = 0.08 m (solid), 0.16 m (dashed) and 0.20 m (dotted); and tube radius, r_t = 0.2 m (solid), 0.275 m (dashed) and 0.3 m (dotted), respectively. The final state of the system corresponds to the merging of the melt front surrounding the tube with that surrounding the heat pipes for all the cases except for L_m = 0.08 m, where the melt fronts between the VHP in the adjacent modules met first. For the parameters considered, the Reynolds number based on the tube radius, Re_t was in the turbulent regime while the Reynolds number based on the heat pipe radius, Re_{HP} fell in the laminar regime.

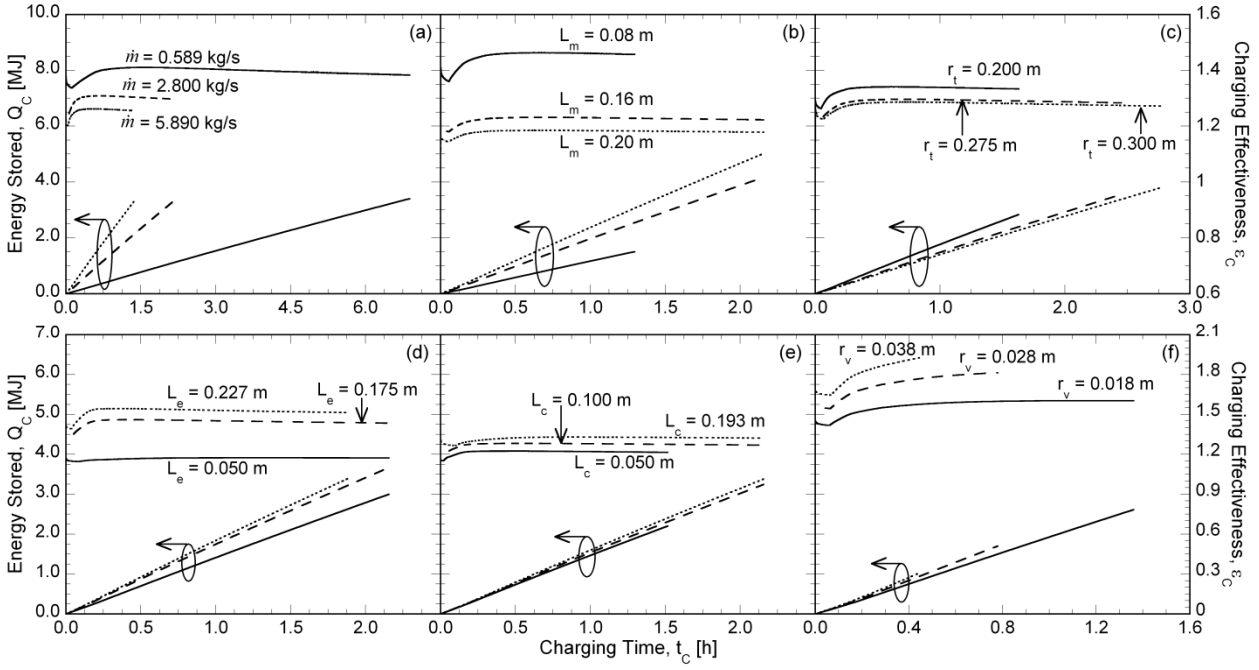

Figure 4: Parametric effects of (a) mass flow rate, (b) module length, (c) tube radius, (d) evaporator length, (e) condenser length and (f) vapor core radius of the heat pipe on the time history of energy stored and charging effectiveness for Module 1.

It is seen from Figure 4a that the charging rate (rate of energy stored) increases with $\dot{m}$ due to the increase in the convective heat transfer coefficients; over the range of $\dot{m}$ = 0.589–5.89 kg/s, Re_t ranged from 9987.5 to 99,875, and the corresponding convective heat transfer coefficients ranged between 11.06 and 81.66 W/m^{2}K. Correspondingly, the melting rate of the PCM also increases with $\dot{m}$ and the critical volume of the melt front to induce natural convection is formed sooner for larger $\dot{m}$. This is reflected in the decrease in the charging time (the end time of the curves in Fig. 4a) with increasing $\dot{m}$. Although not presented in Figure 4a, the percentage of sensible energy stored within the system was also found to increase with $\dot{m}$. It was seen in Figure 3a that for the smaller values of $\dot{m}$ the natural convection in the melt surrounding the VHP started the earliest, whereas at the largest value of $\dot{m}$ = 5.89 kg/s, all the onset times are approximately the same for all the melts—surrounding the tube, the VHP and the HHP. This suggests that the heat pipes are

most effective for smaller HTF flow rates, and the utility of the heat pipes in augmenting the thermal performance of the LTES reduces with increasing $\dot{m}$ as reflected in the effectiveness values in Figure 4a. From Figure 3a, it is noted that for all mass flow rates, natural convection sets in the earliest in the melt pool around the VHP, which primarily governs the dips in the effectiveness curves in Figure 4a. Since the onset time for natural convection around the VHP decreases with increasing $\dot{m}$, the dip in the effectiveness variation in Figure 4a occurs at earlier times as $\dot{m}$ is increased.

The effect of L_m on the energy stored and the charging effectiveness with time is illustrated in Figure 4b. As the module length is increased, the surface area of the tube available for PCM melting increases, leading to an increase in the energy stored as well as the charge rate, as seen in Figure 4b for L_m between 0.08 m and 0.20 m. The charging time (t_C); however, increases with increasing module length owing to the increased PCM volume to be melted, although the increase in the charge rate makes up for the increasing volume, resulting in a less than proportional increase of t_C with L_m. The onset of natural convection was found to be independent of the module length for Module 1, and is reflected in the nearly identical time instants of the dips in the effectiveness variations in Figure 4b. Figure 4b shows that the effectiveness of the heat pipes in augmenting the performance of the LTES is greater if the heat pipes are closely spaced longitudinally (smaller L_m).

Figure 4c depicts the time history of energy stored and effectiveness of the system for different values of the tube radius, r_t. It was observed that earlier in the charging process when the melting is conduction-dominated, the charging rate remained the same with increasing r_t. Also the natural convection current sets in the earliest in the melt surrounding the VHP and t_{nc} increases with increasing tube radius. As a result, Figure 4c shows that both the charge rate and the energy stored decrease with increasing r_t for times beyond the onset of natural convection. Following this trend,

Figure 4c also shows that the effectiveness of the system decreases as the tube radius increases, and furthermore, the minimum of the effectiveness curves is seen to occur at later times with increasing r_t (t_{nc} = 2.9 min, 3.82 min, 3.93 min for r_t = 0.2 m, 0.275 m and 0.3 m respectively).

Figure 4d–f shows the time variation of thermal energy stored in the PCM and the effectiveness of LTES for different values of the heat pipe evaporator and condenser lengths, L_e = 0.05 m (solid), 0.175 m (dashed), 0.227 m (dotted) and L_c = 0.05 m (solid), 0.1 m (dashed) and 0.193 m (dotted), respectively, and the vapor core radius, r_v = 0.018 m (solid), 0.028 m (dashed) and 0.038 m (dotted). It is observed that the charging rate increases with L_e (Figure 4d) and L_c (Figure 4e). Despite the improved charging rate with increasing L_e, it is evident from Figure 4d that the final charging time and the energy stored for L_e = 0.227 m are less than those for L_e = 0.175 m because for the former case, the merging of the melt fronts between the heat pipes of the adjacent modules happens first when s_t = 0.050 m while in the latter case the melt front in the vicinity of the tube merges with the melt front of the heat pipes when s_t = 0.057 m. A similar trend is noted, albeit to a reduced magnitude, with respect to the final charging time for condenser lengths of 0.1 m and 0.193 m in Figure 4e. However, with the increased charging rate, the maximum energy stored is slightly higher for L_C = 0.193 m over L_C = 0.100 m. Figure 4d (Figure 4e) shows that the trend in the effectiveness with evaporator (condenser) length follows that of the charging rate in Figure 4d (Figure 4e). A comparison of Figure 4d with Figure 4e reveals that for a given total length of the heat pipe, a longer evaporator section provides a slightly higher charging rate and a higher effectiveness compared to having a longer condenser section. This implies that though the surface area for melting increases with increase in the length of the condenser section, the surface area for interaction with HTF is more important for enhanced melting rate. With an increase in the condenser length, although the surface area for melting increases, the melt front

progresses slower and leads to delayed onset of convection dominated melting (Figure 3c); as a result, the increase in effectiveness of the system in the convection dominated region (past the dip in Figure 4e) was not as high as that obtained for an increase in L_e (Figure 4d). From Figure 3b, it can also be observed that t_{nc} for the melt front in the vicinity of the VHP reaches approximately a steady value at 2.36 min for L_e = 0.227 m which implies that increasing L_e further will likely result in negligible additional improvement in the system effectiveness and that L_e = 0.227 m could be considered as a practically useful design value for maximizing the charging effectiveness of Module 1.

Figure 4f highlights the dependence of the energy stored and the effectiveness for different values of the heat pipe vapor core radius, r_v. It was found that as r_v increases, the convection dominated melting started at a later time although the increase in t_{nc} was not significant, particularly in the melt region surrounding the VHP. Also, the convection heat transfer coefficient between the HTF and the heat pipes decreases as r_v and, in turn, the heat pipe radius increases. Yet, there is a slight increase in the charging rate (Figure 4f) due to the decrease in the conduction thermal resistance within the heat pipes as r_v increases; correspondingly, it is observed from Figure 4f that the effectiveness of the system increases with an increase in r_v. Figure 4f further indicates that the charge time decreases monotonically with increasing r_v since the corresponding increase in the heat pipe radius causes the melt fronts around the VHPs of adjacent modules to meet earlier. As a consequence of the constant charge rate and the decreasing charge time, the total energy stored at the completion of charging is seen to decrease with increasing radius of the vapor core.

The effect of varying the wick thickness, b_w, within the heat pipes was also investigated. It was found that the time for onset of natural convection was longer as b_w increased because, in addition to the decrease in radial conduction thermal resistance within the heat pipes, the thermal resistance

for axial heat conduction within the adiabatic section of the wick also decreases, thus enhancing the heat transfer rate from the heat pipes to the PCM. The charge rate and the effectiveness values increased, albeit rather unremarkably, with an increase in the wick thickness. The charge time as well as the total energy stored at the completion of charging decreased with increasing b_w following a similar trend and its reasoning as with increasing r_v in Figure 4f. It was observed that for a given heat pipe radius, an increase in the radius of the vapor core produced more enhancement in the effectiveness than increasing the wick thickness. Owing to the similarity of the effects of the wick thickness with those of the vapor core radius, as noted above, the plots for the wick thickness effects are omitted for brevity.

Figure 5 presents the effects of the various parameters on the performance of an LTES with embedded heat pipes in the configuration of Module 2, in which the PCM is housed within the tube while the HTF flows around the tube transverse to its axis. Figure 5a–c shows the time evolution of thermal energy storage and the effectiveness during charging of Module 2 for different values of the HTF mass flow rate, $\dot{m}$ = 0.589 kg/s (solid), 2.8 kg/s (dashed) and 5.89 kg/s (dotted); module length, L_m = 0.08 m (solid), 0.16 m (dashed) and 0.20 m (dotted); and tube radius, r_t = 0.2 m (solid), 0.275 m (dashed) and 0.3 m (dotted), respectively. From Figure 5a, it is observed that the charging rate increases and the effectiveness decreases with increase in $\dot{m}$. As in the case of Module 1 (Figure 4a), the charging time decreases with increased mass flow rate (Figure 5a) owing to the accompanying increase in the convective heat transfer rates; however, combined with the increase in the charging rate with $\dot{m}$, the total energy stored at the end of the charging process is nearly independent of the mass flow rate (Figure 5a). From Figure 3b, it is seen that as $\dot{m}$ increases, t_{nc} for the melt front near the tube decreases faster and approaches the t_{nc} for the melt front surrounding the VHP. This implies that increasing the mass flow rate significantly

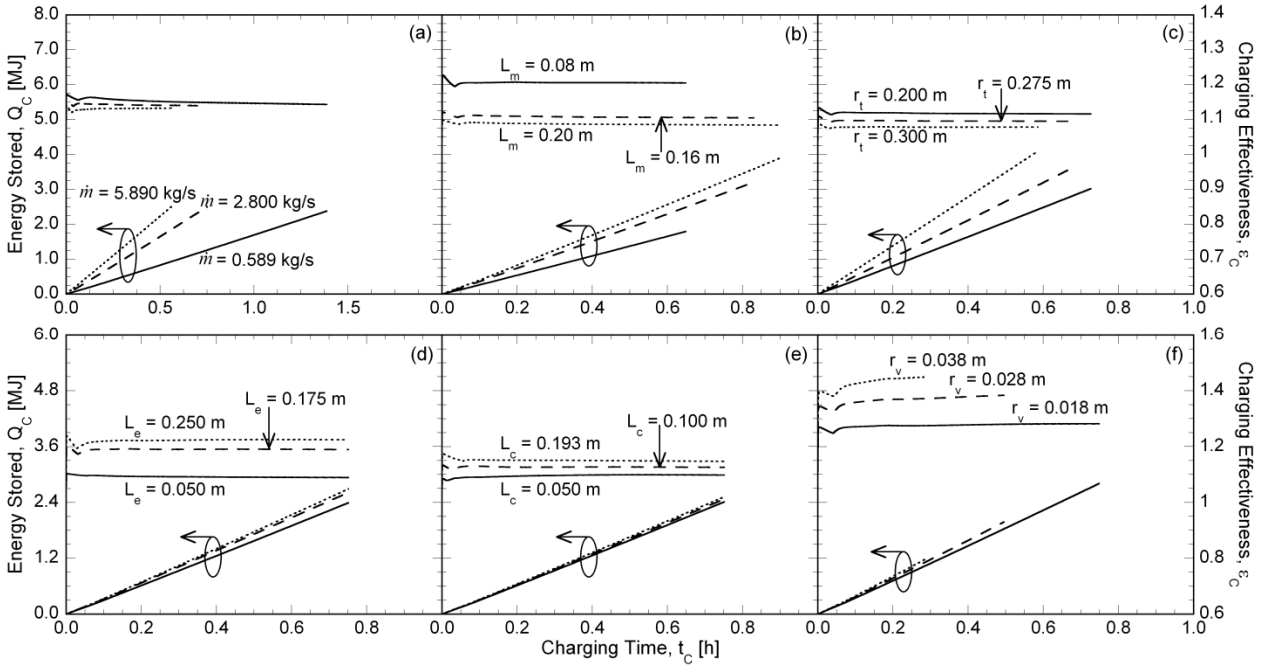

Figure 5: Parametric effects of (a) mass flow rate, (b) module length, (c) tube radius, (d) evaporator length, (e) condenser length and (f) vapor core radius of the heat pipe on the time history of energy stored and charging effectiveness for Module 2.

improves the heat transfer rate between the tube and the PCM to the extent that the utility of heat pipes in augmenting the thermal performance of the LTES at higher $\dot{m}$ is outweighed and correspondingly the effectiveness of the system decreases as noted in Figure 5a. Furthermore, since the natural convection effects set in relatively quickly in the case of Module 2 and the time difference between the onset of natural convection in the melt front near the tube and that around the VHP is relatively less, the dip in the effectiveness corresponding to the initially conduction dominated heat transfer

is confined to a very small early time period, which appears as a sharp initial change in the effectiveness curves in Figure 5a. This sharp dip is generally noted in all the cases in Module 2 presented in Figure 5and is not reiterated in the following discussion.

Figure 5b depicting the effect of L_m on the thermal energy stored and the effectiveness, follow the same general trend as in the corresponding Figure 4b for Module 1. The charging rate and the charging time are both seen in Figure 5b to increase with increasing L_m. As mentioned earlier, the final state of the system for L_m of 0.08 m (solid line in Figure 5b) corresponds to the merging of melt front of the VHP with the vertical edges of the module while for L_m of 0.16 m (dashed line in Figure 5b) and 0.20 m (dotted line in Figure 5b), the final state of the system is dictated by the merging of the melt front near the tube and the melt front near the heat pipes; as a consequence, the charging time for L_m of 0.08 m is much less than the charging time for the other two module lengths in Figure 5b. As the module length increases, the surface area of the tube for heat transfer proportionally increases. However, for a fixed HTF mass flow rate, the increase in the module length corresponds to a decrease in the cross flow velocity, which reduces the convective heat transfer coefficients and consequently the charging time for L_m = 0.16 m is faster than the charging time for L_m = 0.2 m. But, the area increase outweighs the reduction in the heat transfer coefficients leading to an increase in the charge rate with increasing module length, as seen in Figure 5b. The effectiveness, on the other hand, decreases with increasing module length as evident in Figure 5b. For fixed number of heat pipes (four, in this study), as the module length increases, the contribution of the heat pipe to augmenting the heat transfer per unit length of the module decreases, resulting in the diminished effectiveness.

Increasing the tube radius decreases the convective heat transfer coefficients for the tube as well as for the VHP while the heat transfer coefficients for the HHPs are relatively unaffected. However, the increase in the surface area for heat transfer as the square of the tube radius dominates the heat transfer rate and, as a result, the charging rate increases with the tube radius in Figure 5c. Owing to the increased heat transfer rate, the charging time is seen to decrease with

increasing tube radius. Furthermore, it was found that the sensible energy stored also increases with the tube radius, r_t (in general, the percentage of total energy stored as sensible heat was found to be higher for Module 2 in comparison to Module 1). Combined with the increase in latent energy storage due to the enhanced charging rate, Figure 5c shows that the total energy stored increases with the tube radius. With increase in the surface area with increasing tube radius, and the concomitant increase in the heat transfer rate, the relative contribution of the heat pipes to augmenting the heat transfer becomes progressively less. Figure 5c shows this effect in the decrease of the effectiveness with increase in r_t.

Figure 5d–f shows the transient variation of the thermal energy stored in the PCM and the effectiveness of LTES for different parametric values of the evaporator length, L_e = 0.05 m (solid), 0.175 m (dashed), and 0.25 m (dotted); the condenser length, L_c = 0.05 m (solid), 0.1 m (dashed) and 0.193 m (dotted); and the vapor core radius of the heat pipe, r_v = 0.018 m (solid), 0.028 m (dashed) and 0.038 m (dotted), respectively, during the charging of Module 2, for a fixed adiabatic section length L_a = 0.06 m. From Figure 5d and Figure 5e it is observed that the charging rate increases with increase in L_e and L_c, respectively, primarily due to the increased surface area for interaction of the evaporator with the HTF (Figure 5d) and for interaction of the condenser with the PCM (Figure 5e). As L_c increases, the extended surface area of melting decreases the melt front progression rate in the vicinity of VHP due to an increase in the thermal resistance to heat transfer, and delays the start of the natural convection process. Since the onset of convection dominated melting is slower for a longer condenser section (Figure 3d), the increase in the charging rate with increasing L_c (Figure 5e) is not as high as that obtained for an increase in L_e (Figure 5d). The charging time, however, is nearly invariant to change in the evaporator or the condenser lengths, as seen in Figure 5d and Figure 5e because in all the cases the final state of the

system corresponded to merging of the tube melt front with that of the heat pipe melt front. As a result of the increased charging rate but nearly constant charging time, the total energy stored increases with increasing L_e and L_c (Figure 5d and Figure 5e). Figure 5d and Figure 5e also show that the effectiveness increases with increasing L_e and L_c following the trend of the charging rate and the energy stored and the associated reasoning discussed above. Furthermore, as presented in Figure 3d, increasing the evaporator length quickens the natural convection process, whereas increasing the condenser length delays the start of the natural convection process; as a result, the steady state effectiveness values obtained for the various condenser lengths in Figure 5e are less than the steady state effectiveness values obtained for the various evaporator lengths in Figure 5d.

Figure 5f highlights the influence of the vapor core radius, r_v, on the energy stored and the charging effectiveness, respectively. Figure 5f shows that the charging rate increases slightly with increasing r_v, but the effect is seen to be more pronounced on the charging time which decreases as the vapor core radius increases. With an increase in the vapor core size, the overall heat pipe size increases, which causes the melt fronts to meet sooner within the module resulting in reduced charging time. Correspondingly, the total energy stored decreases with increasing vapor core radius in the heat pipe. Figure 5f also shows that the effectiveness increases with increasing vapor core radius owing to the associated decrease in thermal resistance within the heat pipe, which makes the heat pipes more effective in augmenting the heat transfer in the system.

As discussed in Module 1, varying the wick thickness in the heat pipe was seen to yield little variation in the charging rate or the final effectiveness values. However, the increase in the heat pipe radius corresponding to an increased wick thickness led to a decrease in the charging time due to the melt fronts meeting sooner, as with increasing the vapor core radius discussed above. Overall, it was observed that for a given heat pipe radius, an increase in the radius of the vapor

core is more effective in enhancing the heat transfer than increasing the wick thickness of the heat pipes. The corresponding plots are omitted in the interest of brevity.

2.6 LTES Discharging

Unlike the charging process, which was governed by conduction as well as natural convection modes of heat transfer, discharging of the LTES through solidification of the PCM is purely conduction dominated during which the thermal conductivity of the PCM stays constant at 0.425 W/m-K. For the discharging studies, the PCM was considered to be initially fully molten at its melting point, T_m. The parameter ranges chosen to study the discharging process of both Module 1 and Module 2 are identical to those considered for the corresponding cases of charging.

Figure 6a depicts the time history of energy discharged and effectiveness of the system for different values of the tube radius, r_t = 0.2 m (solid), 0.275 m (dashed) and 0.3 m (dotted), during the discharging of Module 1. Due to conduction dominated heat transfer during solidification, the PCM solidifies at a slower rate than it melts during charging and hence the progression of the solid front is slower. The final states of the system in all the cases correspond to the instant when the solid front near the tube merges with the solid front around the heat pipes. Figure 6a shows a decreasing rate of energy discharge with time for all the values of r_t, explained as follows: initially during the process, in addition to discharge of latent energy, a larger amount of sensible energy is discharged, but as the solid front grows, the rate of sensible energy discharge progressively decreases resulting in the reduced overall discharge rate. Although increase in r_t reduces the heat transfer rate between the HTF and the tube and also decreases the convective heat transfer magnitude between the HTF and the heat pipes, the discharging rate of the PCM (Figure 6a) increases due to the fact that a higher surface area of the tube is available for PCM solidification

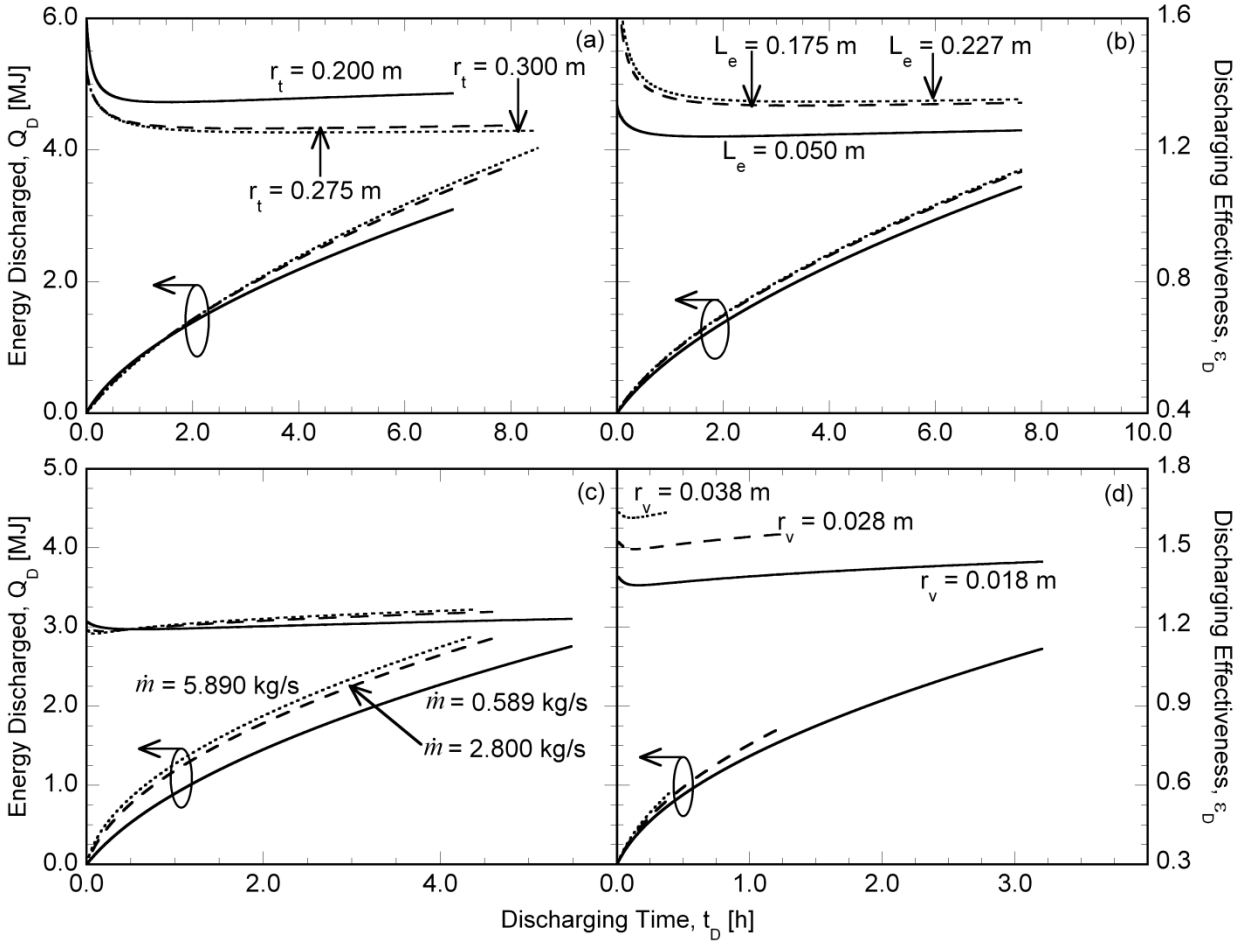

Figure 6: Parametric effects of (a) tube radius and (b) evaporator length of the heat pipes on the time history of energy discharged and discharging effectiveness for Module 1; (c) mass flow rate and (d) vapor core radius of the heat pipe on the time history of energy discharged and discharging effectiveness for Module 2.

leading to an increase in the total energy discharged (Q_D) as well. The discharging time (t_D) is seen to increase with r_t owing to the increased PCM volume to be solidified. Figure 6a also shows that the effectiveness of the system drops as the tube radius increases due to the decrease in the convective heat transfer coefficient between the HTF and the heat pipes with increase in r_t, which reduces the utility of the heat pipes in augmenting the thermal performance of the LTES. Moreover, due to the increase in the tube surface area as the square of r_t, the tube to PCM heat

transfer dominates over the heat pipe to PCM heat transfer, further contributing to the diminished effectiveness of the heat pipes.

The effect of the evaporator length, L_e = 0.05 m (solid), 0.175 m (dashed), and 0.227 m (dotted), on the energy discharged and discharging effectiveness with time for Module 1 are illustrated in Figure 6b. Since the final state of the system for the different values of L_e corresponds to the merging of the solid front around the tube with that surrounding the heat pipes, the discharging time is seen to be invariant with L_e. Note that the variation of L_e (which is outside the tube carrying the HTF) does not have any effect on the convective heat transfer coefficients, h_t and h_{HP}, and the increase in the discharging rate with increase in L_e observed in Figure 6b is essentially due to the increased surface area of interaction between the HTF and the heat pipes. The corresponding increase in the energy discharged and the discharge rate of the PCM between L_e = 0.175 m and L_e = 0.227 m is negligible compared to between L_e = 0.05 m and L_e = 0.175 m due to the linearly decreasing increase in surface area of interaction between two higher L_e values. Following the trend of the increase in the energy discharged with the evaporator length, Figure 6b also shows that the effectiveness of the system increases as L_e increases.

The parametric effects of $\dot{m}$, L_m, L_c, r_v and b_w on the discharging of Module 1 are not illustrated here for conciseness but may be summarized as follows: the thermal energy discharge rate of the PCM increased while the discharge time decreased with increase in $\dot{m}$ due to the accompanying increase in the convection heat transfer rate between the HTF and heat pipes and between the HTF and the tube. However, the effectiveness of the final state of the system decreased as $\dot{m}$ increased because the increase in heat transfer coefficient between the HTF and the tube wall was more compared to the increase in the heat transfer coefficient between the HTF and heat pipes. The effects of L_m on the discharging of the PCM exhibited the same characteristics

as during charging in that the thermal energy discharge rate and the energy discharged increased, while the effectiveness of the LTES decreased, with increase in L_m reiterating that the heat pipes should be spaced close together to realize high effectiveness. The effect of increase in L_c on the discharging of the PCM showed that the effectiveness, discharge rate and energy discharged increased while the discharging time, t_D, is invariant to change in L_c. As opposed to the trend observed for L_e in Figure 6b, where the magnitude of the increase in Q_D and the discharge rate reduced with increase in L_e, for an increase in L_c, it was found that the increase in Q_D and the discharge rate from L_c = 0.1 m to 0.193 m was larger than that from L_c = 0.05 m to 0.1 m, owing to the increased length for interaction of the heat pipes with the PCM and the reduced thermal resistance for radial heat transfer in the condenser section of the heat pipes. The effects of increase in r_v and b_w on LTES discharging followed the same trend as during charging, in that the discharge rate and the effectiveness increased with increase in the corresponding parametric values due to the decrease in conduction thermal resistance within the heat pipes, while the discharge time (t_D) decreased as the melt fronts around the VHPs of adjacent modules met sooner due to increasing r_{HP}.

Figure 6c and d presents the effects on the discharging performance of Module 2 for different values of $\dot{m}$ = 0.589 kg/s (solid), 2.8 kg/s (dashed) and 5.89 kg/s (dotted); and r_v = 0.018 m (solid), 0.028 m (dashed) and 0.038 m (dotted), respectively. As the HTF mass flow rate, $\dot{m}$, increases from 0.589 kg/s to 5.89 kg/s, the convective heat transfer coefficient correspondingly increases from 51.91 W/m^2-K to 247.4 W/m^2-K. This is reflected in Figure 6c as an increase in the thermal energy discharge rate of the PCM and a corresponding decrease in the discharge time with increasing $\dot{m}$. For any value of $\dot{m}$, the total energy discharge rate is noted to decrease with time due to the gradual decrease in the sensible energy extracted as the solidified PCM volume

increases, and the magnitude of total energy discharge rate approaches the latent energy discharge rate. In contrast to Module 1, the effectiveness of the final state of the system, depicted in Figure 6c, increases slightly with $\dot{m}$ because the increase in the heat transfer coefficient between the HTF and the VHP is much higher compared to the increase in heat transfer coefficient between the HTF and tube, rendering the heat pipes to be effective in augmenting the energy transfer rate.

The effect of changing the radius of the vapor core and, in turn, the radius of the heat pipe, is depicted in Figure 6d. Although an increase in the heat pipe radius reduces h_{HP}, the discharging rate of the PCM as illustrated in Figure 6d is found to increase owing to the increased surface area of the heat pipe available for solidifying the PCM. However, the reduced heat transfer coefficient results in a less than proportional increase in the discharge rate with increasing r_v. The discharging time decreases monotonically with increasing r_v since the corresponding increase in the heat pipe radius causes the solid fronts of two adjacent heat pipes to meet earlier. As a result of the considerable drop in the discharge time, the total energy discharged decreases with increasing vapor core (heat pipe) radius, r_v. Figure 6d also shows an increase in the effectiveness of the heat pipes in augmenting the thermal performance of the system, following the trend of the discharging rate with increasing r_v.

The other parametric effects on the discharging of Module 2 are not plotted here but may be summarized as follows: an increase in r_t was found to slightly increase the PCM discharging rate; however, due to a decrease in the convective heat transfer coefficient between the HTF and the VHP, the effectiveness of the system decreased with increasing tube radius. Similarly an increase in L_m was found to increase the PCM discharging rate and the energy discharged, the reduced heat transfer coefficients due to decrease in cross flow velocity for a fixed $\dot{m}$ notwithstanding, due to increase in the surface area of the tube available for solidification. The effects of L_e and L_c were

found to follow the same trends as observed for discharging of Module 1: due to the increased area of interaction between the heat pipes and the HTF with increase in L_e and the increased surface area of the heat pipes for solidification of the PCM with increase in L_c, the discharging rate and discharging effectiveness were both found to increase with the evaporator and condenser lengths. The effect of wick thickness on the discharging cycle followed the same trend as r_v; the discharge rate and the discharging effectiveness increased with increase in b_w due to decrease in thermal resistance for conduction within the heat pipes, while the discharging time decreased as the melt fronts between the VHPs in the adjacent heat pipes met sooner.

2.7 Optimum Designs

The results presented in Figure 4–Figure 6 were used to identify the parametric combinations from those studied that maximize three performance measures: (1) the energy stored, Q_C (discharged, Q_D); (2) the charging (discharging) effectiveness ε_C (ε_D); and (3) an effective charging (discharging) rate as defined in Section 3, $Q_C\varepsilon_C/t_C$ ($Q_D\varepsilon_D/t_D$). Table 2 lists the parameter combinations that maximize each of the three objectives for charging and discharging of LTES with embedded heat pipes in Module 1 and Module 2 configurations. In each case, the corresponding values of the energy stored or discharged, the effectiveness, the charging or discharging time, and the effective charging or discharging rate are also tabulated. The preferred Module for each objective is highlighted and the maximum values of the objective function are listed in bold face.

It is seen from Table 2a that of the cases studied, the best combination of parameters that maximizes Q_C for Module 1 yields an energy storage during charging of 5.021 MJ (Table 2a.1) whereas the best parameter combination for the same objective for Module 2 results in an energy

storage of only 4.096 MJ (Table 2a.2), suggesting that Module 1 is the preferred configuration for LTES charging from the objective of maximizing energy stored. Similarly, Module 1 with the parameter combination listed in Table 2b.1 is seen to be the configuration that maximizes the charging effectiveness with ε_C = 1.926 compared to ε_C = 1.449 for Module 2 (Table 2b.2). Note, however, that Q_C for Module 1 corresponding to the maximum effectiveness design is only 1.027 MJ (Table 2b.1) compared to 5.021 MJ for the design that maximizes Q_C in Table 2a.1 discussed above, but the charging time is 0.445 h (Table 2b.1), much less than the charging time of 2.156 h (Table 2a.1) for the maximum Q_C design. Table 2c shows that Module 2 with the parameter combination listed maximizes the effective charging rate at 7.542 MJ/h (Table 2c.2) compared to the best combination of parameters for Module 1, which yields 4.446 MJ/h (Table 2c.1) of effective charging rate. The corresponding values of Q_C, ε_C, and t_C for the Module 2 configuration are 4.096 MJ, 1.079, and 0.586 h, respectively (Table 2c.2), which is also the design that maximizes Q_C for Module 2 (Table 2a.2).

Tables 2d–2f point to Module 1 being the best configuration from the objectives of maximizing the energy discharged (Table 2d.1) as well as the discharging effectiveness (Table 2e.1), while Module 2 is seen to yield the maximum effective discharge rate of 3.745 MJ/h (Table 2f.2), a design that also maximizes the discharging effectiveness (Table 2e.2). The designs identified in Tables 2a–2f pertain to the best combination of parameters that maximize the three objectives for charging and discharging individually. However, in practice, the same system is used for both charging and discharging, and it is of interest to determine the combination of the operational (mass flow rate) and LTES geometric parameters that maximize a combined objective of the overall energy transfer rate during charging and discharging, defined as $P = \left(Q_C / t_C + Q_D / t_D\right)$.

Table 2g presents the designs for Module 1 and Module 2 that maximize the overall energy transfer rate. It is seen that the designs share several common parameter values and differ only in the tube radius, r_t, and the heat pipe radius (through the vapor core radius, r_v). However, Module 2 is seen to yield the higher overall energy transfer rate of 7.961 MJ/h (Table 2g.2), significantly more than the 3.466 MJ/h for Module 1 (Table 2g.1). The total energy stored and discharged for this design is 8.515 MJ, which is much larger than the corresponding value of 2.523 MJ for Module 1. However, the effectiveness (defined as the total energy charged and discharged with the heat pipes relative to the total energy charged and discharged from the tube alone, without any heat pipes) of Module 2 is lower than that for Module 1 (1.118 vs. 1.954) and the total charging and discharging time for Module 2 of 5.15 h is about three times that for Module 1 (1.738 h).

The designs discussed in Table 2 are based on the combinations of parameters culled from the parametric studies that maximize the chosen objectives. Toward identifying the optimum parameters, in general, a numerical optimization was conducted as explained in Section 3. The optimization runs were conducted using 10 different randomly chosen initial conditions on the parameters to ensure that the optimum results reported are not a local optima. Table 3 lists the designs corresponding to the optimization problem formulated by Eq. 12a and Eq. 12b. As in Table 2, the optimum Module for each objective is highlighted and the optimized values of the corresponding objective functions are listed in boldface. It is evident from the results that Module 1 with the parameter values listed in Tables 3a.1 and 3c.1 are the optimum choices for maximizing charging as well as discharging effectiveness with ε_C = 2.727 and ε_D = 3.045, respectively. However, from the viewpoint of maximizing the effective charging or discharging rate, Module 2 with the optimum parameters in Table 3b.2 maximizes the effective charging rate, $Q_C \varepsilon_C / t_C$ = 16.596 MJ/h, whereas Module 1 with the optimum parameters listed in Tables 3d.1 maximizes the

effective discharging rate with $Q_D \varepsilon_D / t_D$ = 4.113 MJ/h (Table 3d.1). Note that Module 2 (Table 3d.2) has an effective discharging rate (4.061 MJ/h) comparable to, although slightly less than, that of Module 1. The difference is within the accuracy of the numerical model, and for practical purposes, the optimal designs for both Modules 1 and 2 may be considered to be equally acceptable. The optimization results in Table 3 suggest that higher effectiveness is obtained for smaller HTF mass flow rate and maximum effective charge/discharge rate is obtained for larger HTF mass flow rate.

It is instructive to note that the optimum configurations for maximizing charging and discharging effectiveness were also obtained to be Module 1 based on their respective best combination of the parametric values from the parametric studies in Table 2; however, the effectiveness values obtained from the numerical optimization are much higher than those from the parametric studies, cf. ε_C = 2.727 (Table 3a.1) and ε_C = 1.926 (Table 2b.1) and ε_D = 3.045 (Table 3c.1) and ε_D = 1.981 (Table 2e.1). For maximizing the effective charging rate, Module 2 was determined to be the best configuration from the parametric studies (Table 2c.2) as also from the numerical optimization (Table 3b.2) with the numerical optimization based design yielding a higher $Q_C \varepsilon_C / t_C$ of 16.596 MJ/h compared to 7.542 MJ/h from the parametric studies (Table 2c.2). The numerical optimization yielded both Modules 1 and 2 as optimal configurations that maximize the effective discharging rate ($Q_D \varepsilon_D / t_D \approx$ 4.061 – 4.113 MJ/h; Tables 3d.1 and 3d.2) compared to the parametric studies based results that suggested Module 2 as the preferred configuration ($Q_D \varepsilon_D / t_D$ = 3.745 MJ/h Table 2f.2).

The numerical optimization was also conducted for determining the optimum values of the LTES geometric parameters for three fixed values of the mass flow rate of the HTF, $\dot{m}$, the only operating parameter considered in this study. The optimization was carried out to maximize the

combined energy transfer rate during charging and discharging, $P = (Q_C/t_C + Q_D/t_D)$, as formulated in Eq. (12b). Table 3e presents the results of the optimization in which the optimum values of P are presented along with the corresponding optimal design of the LTES and heat pipe geometric parameters as a function the HTF mass flow rate, $\dot{m}$, for both Modules 1 and 2. It is seen that the combined energy transfer rate of charging and discharging increases with $\dot{m}$ and that it is higher for Module 2 compared to that for Module 1, for all the mass flow rates considered. From Table 3e, it is found that for $\dot{m} = 2.8$ kg/s, (Table 3e.3 and 3e.4) the optimum configuration for maximizing overall energy transfer rate is Module 2 which is in agreement with the results based on the best combination from the parametric studies in Table 2g; however, the values obtained from the numerical optimization are much higher than those from the parametric studies, cf. P = 11.746 (Table 3e.4) and P = 7.961 (Table 2g.2). Comparing the designs in Table 3e for $\dot{m} = 2.8$ kg/s with those in Table 2g.2, it is seen that the numerical optimizer predicts a higher module length and higher vapor core radius (a trend that is also seen for the other mass flow rates in Table 3e) compared to the parametric study-based results presented in Table 2g.2.

The focus of the present chapter was on a simplified thermal network modeling of the complex configuration of a LTES with embedded heat pipes. Using the model, the important physical characteristics of the system were elucidated through the parametric and optimization studies. The configuration considered had four embedded heat pipes, although in a general implementation, the number and placement of the heat pipes can vary. Furthermore, the present model is limited in its ability to describe the process only until the first instant of any two melt fronts merging, whereas in an actual system, the process could continue until the entire PCM is melted. These limitations and the study of different heat pipe configurations are addressed with a full computational modeling of the system, as explained in Chapter 3 of this dissertation.

Table 2: Optimum designs obtained from parametric studies reported in Chapter 2

Objective	$\dot{m}$ [kg/s]	L_m [m]	r_t [m]	L_e [m]	L_c [m]	r_v [m]	b_w [m]	Q_C [MJ]	ε_C	t_C [h]	$Q_C\varepsilon_C/t_C$ [MJ/h]
a. Maximum Energy Stored, Q_C											
1. Module 1	2.800	0.200	0.250	0.100	0.140	0.007	0.001	**5.021**	1.179	2.156	2.746
2. Module 2	2.800	0.120	0.400	0.100	0.140	0.007	0.001	4.096	1.079	0.586	7.542
b. Maximum Charging Effectiveness, ε_C											
1. Module 1	2.800	0.120	0.250	0.100	0.140	0.038	0.001	1.027	**1.926**	0.445	4.446
2. Module 2	2.800	0.120	0.250	0.100	0.140	0.038	0.001	1.174	1.449	0.284	5.981
c. Maximum Effective Charging Rate, $Q_C\varepsilon_C/t_C$											
1. Module 1	2.800	0.120	0.250	0.100	0.140	0.038	0.001	1.027	1.926	0.445	4.446
2. Module 2	2.800	0.120	0.400	0.100	0.140	0.007	0.001	4.096	1.079	0.586	**7.542**
Objective	$\dot{m}$ [kg/s]	L_m [m]	r_t [m]	L_e [m]	L_c [m]	r_v [m]	b_w [m]	Q_D [MJ]	ε_D	t_D [h]	$Q_D\varepsilon_D/t_D$ [MJ/h]
d. Maximum Energy Discharged, Q_D											
1. Module 1	2.800	0.200	0.250	0.100	0.140	0.007	0.001	**5.414**	1.188	7.614	0.845
2. Module 2	2.800	0.120	0.400	0.100	0.140	0.007	0.001	4.418	1.157	4.564	1.120
e. Maximum Discharging Effectiveness, ε_D											
1. Module 1	2.800	0.120	0.250	0.100	0.140	0.038	0.001	1.496	**1.981**	1.293	2.292
2. Module 2	2.800	0.120	0.250	0.100	0.140	0.038	0.001	0.898	1.635	0.392	3.745
f. Maximum Effective Discharging Rate, $Q_D\varepsilon_D/t_D$											
1. Module 1	2.800	0.120	0.250	0.100	0.140	0.038	0.001	1.496	1.981	1.293	2.292
2. Module 2	2.800	0.120	0.250	0.100	0.140	0.038	0.001	0.898	1.635	0.392	**3.745**
Objective	$\dot{m}$ [kg/s]	L_m [m]	r_t [m]	L_e [m]	L_c [m]	r_v [m]	b_w [m]	Q_C+Q_D [MJ]	ε	t_C+t_D [h]	$P=(Q_C/t_C+Q_D/t_D)$ [MJ/h]
g. Maximum Overall LTES Energy Transfer Rate (Combined Charging and Discharging), P											
1. Module 1	2.800	0.120	0.250	0.100	0.140	0.038	0.001	2.523	1.954	1.738	3.466
2. Module 2	2.800	0.120	0.400	0.100	0.140	0.007	0.001	8.515	1.118	5.150	**7.961**

Table 3: Optimum designs corresponding to the numerical optimization in Chapter 2

Objective	$\dot{m}$ [kg/s]	L_m [m]	r_t [m]	L_e [m]	L_c [m]	r_v [m]	b_w [m]	Q_C [MJ]	ε_C	t_C [h]	$Q_C\varepsilon_C/t_C$ [MJ/h]
a. Maximum Charging Effectiveness, ε_C (Eq. 12a)											
1. Module 1	0.589	0.102	0.393	0.300	0.050	0.018	0.001	0.375	**2.727**	0.633	1.615
2. Module 2	0.590	0.092	0.200	0.279	0.096	0.008	0.004	0.839	1.505	0.566	2.232
b. Maximum Effective Charging Rate, $Q_C\varepsilon_C/t_C$ (Eq. 12a)											
1. Module 1	5.831	0.188	0.200	0.103	0.236	0.038	0.013	4.609	1.631	0.884	8.484
2. Module 2	5.890	0.200	0.400	0.100s	0.243	0.038	0.001	6.730	1.189	0.483	**16.596**
Objective	$\dot{m}$ [kg/s]	L_m [m]	r_t [m]	L_e [m]	L_c [m]	r_v [m]	b_w [m]	Q_D [MJ]	ε_D	t_D [h]	$Q_D\varepsilon_D/t_D$ [MJ/h]
c. Maximum Discharging Effectiveness, ε_D (Eq. 12a)											
1. Module 1	0.589	0.142	0.203	0.129	0.240	0.038	0.001	3.191	**3.045**	3.837	2.532
2. Module 2	4.975	0.119	0.290	0.210	0.171	0.026	0.001	2.942	1.633	2.102	2.285
d. Maximum Effective Discharging Rate, $Q_D\varepsilon_D/t_D$ (Eq. 12a)											
1. Module 1	5.878	0.162	0.200	0.116	0.243	0.038	0.011	4.364	2.364	2.509	**4.113**
2. Module 2	4.357	0.194	0.400	0.100	0.243	0.038	0.027	7.148	1.526	2.688	4.061
Objective	$\dot{m}$ [kg/s]	L_m [m]	r_t [m]	L_e [m]	L_c [m]	r_v [m]	b_w [m]	$P=(Q_C/t_C+Q_D/t_D)$ [MJ/h]			
e. Maximum Overall Energy Transfer Rate, P (Eq. 12b)											
1. Module 1	0.589	0.144	0.283	0.202	0.152	0.038	0.001	3.306			
2. Module 2	0.589	0.200	0.399	0.101	0.243	0.038	0.026	**6.811**			
3. Module 1	2.800	0.200	0.260	0.157	0.183	0.036	0.032	5.121			
4. Module 2	2.800	0.200	0.399	0101	0.129	0.038	0.005	**11.746**			
5. Module 1	5.890	0.200	0.200	0.097	0.243	0.038	0.030	6.782			
6. Module 2	5.890	0.200	0.400	0.100	0.187	0.038	0.001	**15.757**			

2.8 Nomenclature used in Chapter 2

A area, m^2

b thickness, m

c_p specific heat, J/kg-K

E thermal element

h convective heat transfer coefficient, W/m^2K

HHP horizontal heat pipe

ΔH_f latent heat of fusion of PCM, J/kg

k thermal conductivity, W/m-K

$\dot{m}$ mass flow rate, kg/s

ℓ_i thermal element length in the direction of heat transfer, m

L length, m

Pr Prandtl number

Q_C energy stored in the LTES with heat pipes, J

Q_D energy discharged from LTES with heat pipes, J

$Q_{C,0}$ energy stored in the LTES without heat pipes, J

$Q_{D,0}$ energy discharged from LTES without heat pipes, J

Q_t energy stored (discharged) near the tube, J

Q_{HP} energy stored (discharged) near heat pipes, J

r radius, m

R_i thermal resistance, K/W

Ra Rayleigh number

Re Reynolds number

r radial location, m

s melt front, m

S_L width of the module, m

S_T height of the module, m

T temperature, K

T_m melting temperature, K

t time, s

V volume, m^3

VHP vertical heat pipe

Subscripts and Superscripts

a adiabatic

c condenser

C charging

D discharging

e evaporator

HTF heat transfer fluid

HP heat pipe

i element i

m module

nc onset of natural convection

PCM phase change material

t tube

w wick

Greek Symbols

α thermal diffusivity, m^2/s

β thermal expansion coefficient, K^{-1}

ε effectiveness

μ dynamic viscosity, Pa-s

ρ density, kg/m^3

Chapter 3: Computational Studies on a Latent Thermal Energy Storage Unit Module with Integral Heat Pipes

This chapter presents a transient three-dimensional computational analysis of a shell-and-tube LTES embedded with heat pipes is performed for melting (charging) and solidification (discharging) to determine the position of melt front, energy stored and an effectiveness of the heat pipe embedded configurations as a function of time. The influence of the number and orientation of heat pipes and the configuration of the system are analyzed to identify designs that lead to improved effectiveness.

3.1. Introduction

The simplified thermal network modeling of the complex configuration of a LTES with embedded heat pipes developed in Chapter 2 is limited in its ability to capture the buoyancy driven natural convection flow pattern within the molten PCM prevalent during melting of phase change material (PCM), which requires detailed computational modeling. Numerous studies analyzing the melting/solidification of PCM in LTES have been reported in the literature, some of which are reviewed here. Ng et al. [8] investigated the melting of PCM stored in a cylindrical annulus using finite element method and showed the existence of recirculation cells representative of natural convection within the PCM, which were modeled by the Boussinesq approximation. Trp [38] investigated numerically a two-dimensional model of a shell-and-tube LTES configuration and quantified the thermal performance by analyzing the temperature distributions within the PCM. Guo and Zhang [16] analyzed numerically the performance of an LTES system with KNO_3-$NaNO_3$ mixture as the PCM. The performance enhancement when the PCM is interspersed with

aluminum foils was quantified in [16] by analyzing the time evolution of the liquid fraction within the PCM. Khodadadi and Hosseinizadeh [18] simulated two-dimensional melting and solidification of a PCM mixed with copper nanoparticles, in which the natural convection effects were included by means of the Boussinesq term. Farid et al. [39] presented a brief review on the materials used as PCM for LTES.

Several articles ranging in model complexity of heat pipes are found in the literature. Zuo and Faghri [40] presented a simple network model of heat pipe based on the heat conduction within the wall and the wick, but neglecting the effects of the vapor core, and showed that the results compared favorably with the profiles obtained from the two-dimensional model developed by Cao and Faghri [28] for a sodium-stainless-steel heat pipe. Sobhan et al. [41] simulated a two-dimensional transient operation of flat heat pipes accounting for all the mechanisms occurring within. Kaya and Glodak [42] presented a detailed three-dimensional model of heat pipe and analyzed its transient operation.

It is clear from the foregoing discussion that although studies on the analysis of LTES and heat pipes have been reported separately, the enhancement in the performance of a LTES with integral heat pipes in PCM is not fully explored. The objective this chapter is to conduct a detailed three-dimensional computational study of the shell and tube LTES with embedded heat pipes. Considering various configurations of the HTF flow relative to the PCM as well as different heat pipe locations and orientations, the performance of this integrated system is systematically analyzed during charging and discharging operations, to elucidate the complex interplay between the governing heat transfer and fluid dynamics phenomena. Based on the studies, optimum orientation of heat pipes and design parameters of the system obtained for maximizing targeted performance measures of the LTES system are presented in this chapter.

3.2 Modeling

The LTES configuration considered in the study consists of a rectangular array of tubes of outer radius r_t and wall thickness b_t with a horizontal center-to-center spacing S_L and a vertical center-to-center spacing S_T enclosed in a shell. Figure 7 illustrates two different configurations based on the locations of the PCM and the HTF in the LTES. In the configuration shown in Figure 7a, referred to as Module 1, the HTF flows within the tube surrounded by the PCM, while in the configuration depicted in Figure 7b, referred to as Module 2, the PCM is contained within the tube over which the HTF flows transverse to the tube axis. Heat pipes are placed through the tube walls at m circumferential locations and are spaced by a distance L_m along the tube length. The periodic configuration of the heat-pipe-embedded tube-in-shell geometry allows for identification of a representative three-dimensional rectangular volume element of dimensions $S_T \times S_L \times L_m$ as shown in Figure 7c for the analysis. In both configurations, the heat pipes are placed in such a way that the center of the adiabatic sections of the heat pipe coincides with the wall of the tube in contact with the HTF to ensure that for a given design configuration, the surface area of the heat pipes exposed to the HTF remains the same in both modules. Figure 7d shows a schematic of the longitudinal cross section of a heat pipe of radius r_{HP} identifying the internal components and the associated dimensions.

The flow of the HTF is considered incompressible and the properties of the PCM are considered to be constant in both the solid and the liquid phases. The PCM is treated as a pure substance, which undergoes phase change at a constant temperature. The natural convection effects are modeled by the Boussinesq approximation. The melting and solidification processes within the PCM are modeled by the enthalpy-porosity technique as explained in [43], [44]. In this approach, the solid-liquid interface is represented by a numerical mushy region, which is approximated as a

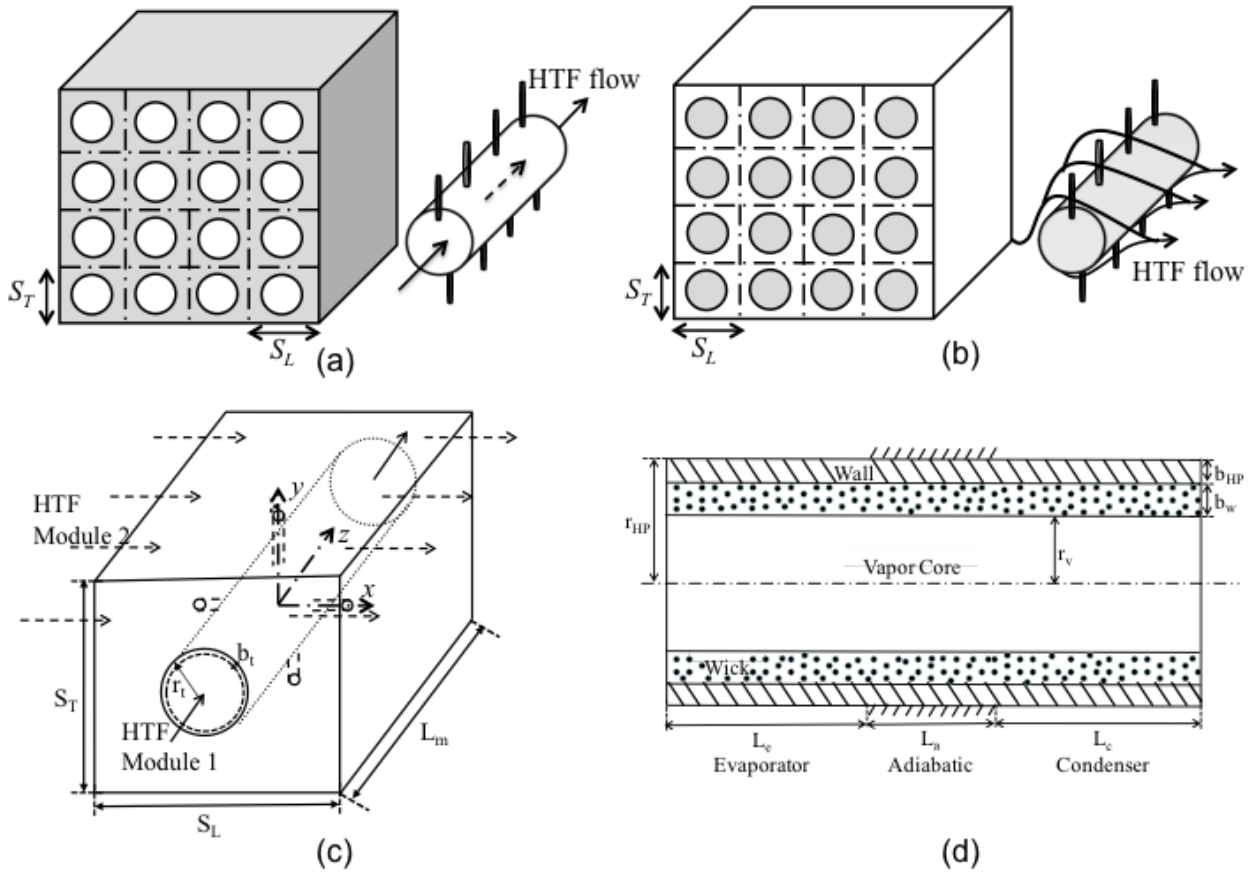

Figure 7: Schematic illustration of LTES (shaded areas denote PCM) with embedded heat pipes: (a) Module 1 configuration, (b) Module 2 configuration, (c) unit cell and (c) heat pipe cross section.

porous medium wherein the porosity in each cell is set equal to the cell liquid fraction, γ, which takes the value of 1 for a fully liquid region, 0 for a solid region, or $0 < \gamma < 1$ for a partially solidified region (mushy zone).

Based on the foregoing assumptions, the coupled system of continuity, momentum and energy equations governing the three-dimensional processes in both the HTF and the PCM are as follows:

$$\nabla.(\rho\vec{V}) = 0 \tag{14}$$

$$\rho\frac{D\vec{V}}{Dt} = -\nabla p + \nabla.\vec{\tau} + S_g \tag{15}$$

$$\rho c_p \frac{DT}{Dt} = \nabla.(k\nabla T) + S_h \tag{16}$$

where ρ is the phase density, k is the thermal conductivity, p is the pressure, t denotes time, T is the temperature, $\vec{V}$ denotes the superficial velocity vector with components u, v, and w in the x-, y- and z-directions (Figure 7c), respectively, and $\vec{\tau}$ is the stress tensor. The momentum equation incorporates a source term for natural convection as $S_g = \rho\vec{g}$ for the HTF, where $\vec{g}$ is the gravity vector = 0 ms^{-2} in the x- and z- directions and = 9.81 ms^{-2} in the y- direction, and $S_g = \rho\vec{g}\beta(T - T_{ref}) - A(\gamma)\vec{V}$ for the PCM, in which the first term is the Boussinesq approximation and the second term includes a porosity function, $A(\gamma) = C(1-\gamma)^2/(\gamma^3 + \varepsilon)$, to mimic the Carman-Kozeny equation for flow through porous media (which ensures zero velocity in the fully solid region and normal liquid flow in the fully liquid region), where, $\varepsilon = 0.001$ is a small computational constant to avoid division by zero, and C is a constant reflecting the morphology of the melting front, set to be 1.6×10^6 as defined by Brent et al. [44]. Based on the enthalpy formulation of the porous medium for a pure substance, the latent heat source term is incorporated in the energy equation as $S_h = \frac{\partial \Delta H}{\partial t}$, where the change in latent enthalpy takes the value of, $\Delta H = \gamma h_{sl}$ for $T < T_{\mathrm{m}}$ and $\Delta H = \gamma h_{sl}$ for $T > T_m$ where h_{sl} is the latent heat content of the PCM.

The modeling of heat pipe follows the simplified equivalent thermal resistance network description developed by Nithyanandam and Pitchumani [45], which accounts for the conduction within the wick and the heat pipe wall, but neglects the effects of evaporation and condensation within the vapor core and advection of the working liquid within the capillary. The mathematical details of the network model are omitted here for brevity but may be found in [45]. The thermal resistance network model was implemented in the present work based on its computational

simplicity without loss of accuracy as reported in [45]. In the present implementation, the effective wick thermal conductivity was calculated using an expression for the effective thermal conductivity [24] as $k_{eff} = \frac{k_l[(k_l + k_s) - (1-\phi)(k_l - k_s)]}{[(k_l + k_s) + (1-\phi)(k_l - k_s)]}$ while the effective heat capacity was expressed as $(\rho c)_{eff} = (1-\phi)(\rho c)_s + \phi(\rho c)_l$, where ϕ is the wick porosity and the subscripts *s* and *l* represent the solid phase of the wick namely, stainless steel, and the liquid phase of the wick, sodium, respectively.

The inlet boundary conditions were specified to be the mass flow rate and the inlet temperature of the HTF, and the outlet was described as an outflow boundary condition for both Module 1 and Module 2, which imposes a zero normal gradient for all flow variables except pressure thus characterizing a fully-developed flow. For Module 1, periodic boundary conditions were imposed on the top and bottom faces of the three-dimensional unit cell surrounding the tube in Figure 7a while the rest of the faces surrounding the PCM were set to be symmetric. For Module 2, the top and bottom faces of the three-dimensional unit cell surrounding the transverse flow of the HTF (Figure 7b) are set to have periodic boundary conditions while the front and back faces of the PCM were set to be symmetric. The tube wall adjoining both PCM and HTF was prescribed as a coupled boundary condition.

Table 1 presents the geometrical and physical parameters used in the simulations of the LTES with embedded heat pipes, where the dimensions listed are representative of those used for large-scale energy storage [34]. Mercury-Stainless steel heat pipe is used for the present analysis [24] while the HTF and PCM materials are Therminol and KNO_3, respectively [34]. Apart from the geometrical and physical parameters listed in Table 1, the other input parameters to the simulations include the inlet mass flow rate and inlet temperature of HTF which were set at 2.89 kg/s and 664

K for Module 1 and 0.706 kg/s and 664 K for Module 2, respectively, which correspond to the total mass flow rate resulting in the generation of 80 MW_e solar power using Therminol [34].

The complete three-dimensional model of the system described above was implemented in a commercial finite-volume based computational fluid dynamics solver, FLUENT. The thermal network modeling of heat pipes as presented in ref. [45] and the source terms for the momentum and energy equations as explained above was implemented in FLUENT through a user-defined function. The computational grid was built of hexahedral elements (typically 110,000 elements) with optimal mesh size determined based on a systematic grid refinement process. In order to accurately predict the liquid fraction in the fixed grid enthalpy-based procedure, the latent heat content of each computational cell, ΔH_p in conjunction with the temperature predicted by Eq. (3), was updated at each iteration within a time step. In the present case, the enthalpy iterative updating scheme takes the following form as reported in [44] for a pure PCM, which melts at constant temperature:

$$\Delta H_i^{n+1} = \Delta H_i^n + \frac{a_i}{a_i^0} \lambda c_p \left[T_i^n - F^{-1}(\Delta H_i^n) \right] \tag{17}$$

In the above equation, a_i is the coefficient of T_i for the nodal point i in the discretized equation of the energy equation for PCM, which is obtained directly from the FLUENT interface, n is the iteration number, λ is a relaxation factor, which is set to 0.05 for the present case, F^{-1} is the inverse of latent heat function which takes the value of T_m for a pure substance, and $a_i^0 = \rho \Delta V_i / \Delta t$ in which ΔV_i is the volume of the computational cell centered on the grid point i and Δt is the time step used in the simulation. The SIMPLE algorithm was used for the pressure-velocity coupling and the time step in the calculation was set at 0.5 s since further decrease to 0.05 s did not show any noticeable changes in the transient results for the melt fraction throughout the whole process.

At each time step during the simulation, residual convergence values of 10^{-5} and 10^{-3} were imposed for the momentum and continuity equations respectively, and a value of 10^{-8} was used for the energy equation. All simulations were conducted on a Dell Power Edge R610 computer, which features two 3.30 GHz quad core Intel Xeon processors, and the simulation times ranged from 24–150 h of CPU time.

From the numerical simulations, the contours of the melt front at different instants of time, and the instantaneous energy stored within the PCM obtained as outputs were used to explore the performance of the two different modules (Modules 1 and 2 as in Figure 7a and b) of the LTES for different number and orientation of heat pipes. The energy charged (discharged) by the PCM at any instant of time is composed of sensible energy and latent energy components calculated as the summation of energy stored in all the PCM thermal elements which can be determined from the following expressions:

$$Q_{C(D)} = \sum_{i=1}^{n} \left[\rho_{PCM} c_p (T_i - T_m) + \rho_{PCM} \Delta H_i \right] \times \Delta V_i, T_i > T_m \tag{18a}$$

$$Q_{C(D)} = \sum_{i=1}^{n} \left[\rho_{PCM} \Delta H_i \right] \times \Delta V_i, T_i < T_m \tag{18b}$$

where, $Q_{C(D)}$ represents the energy stored (discharged) at any instant of time and T_m denotes the melting temperature of PCM and n denotes the total number of discretized cell volumes in the computational grid. The different configurations studied and the corresponding results are discussed in the following Section.

3.3 Model Validation

The computational model is validated by comparing the simulated results obtained for melting of PCM in an axisymmetric domain with the experimental results from Jones et al. [46]. The details of the geometry and the properties of *n*-eicosane PCM can be found in Ref. [46]. Figure 8a

and b presents the melt front locations at different times of melting for different charging temperatures of T_H = 343 K and T_H = 318 K, respectively. It is observed that the melt front locations obtained from the numerical simulation (solid lines) compare well with the experimental results (triangular marks). The deviations observed between the melt front locations obtained from the numerical simulation and the experimental results in Figure 8b could be attributed to several factors such as experimental errors and uncertainties, not accounting for the expansion of wax in the numerical simulation, and use of an adiabatic top boundary condition in the numerical simulation when there is finite heat loss through the top of the enclosure [46]. It can be observed from Figure 8c that the numerical results (solid lines) obtained for the transient evolution of liquid melt volume fraction of the PCM for different charging temperatures of T_H = 343 K and T_H = 318K compare well with the experimental data reported in Ref. [46].

The different arrangements of heat pipes in the LTES system considered in the present study are illustrated in Figure 9. For an LTES system embedded with m = 2 heat pipes, there are two possible arrangements namely, the two heat pipes being oriented either vertically as in Figure 9a, referred to as 2-VHP in this study, or horizontally, as in Figure 9b, referred to as 2-HHP in this study. For an LTES with m = 3 heat pipes, again two different arrangements are considered: a tri-star pattern as depicted in Figure 9c (referred to as 3-*HP) and a Y-pattern as in Figure 9d (referred to as 3-YHP). With 4 heat pipes in the LTES, the arrangement considered, referred to as 4-HP, is as shown in Figure 9e. The simulations were performed for charging as well as discharging processes for a maximum period of 12 hours each, which is assumed to be the average length of a day for which hot HTF is available and the average duration during which solar energy is unavailable and energy is to be discharged from the LTES. The results obtained from the numerical simulations for Module 1 and Module 2 with heat pipes installed in the arrangements as

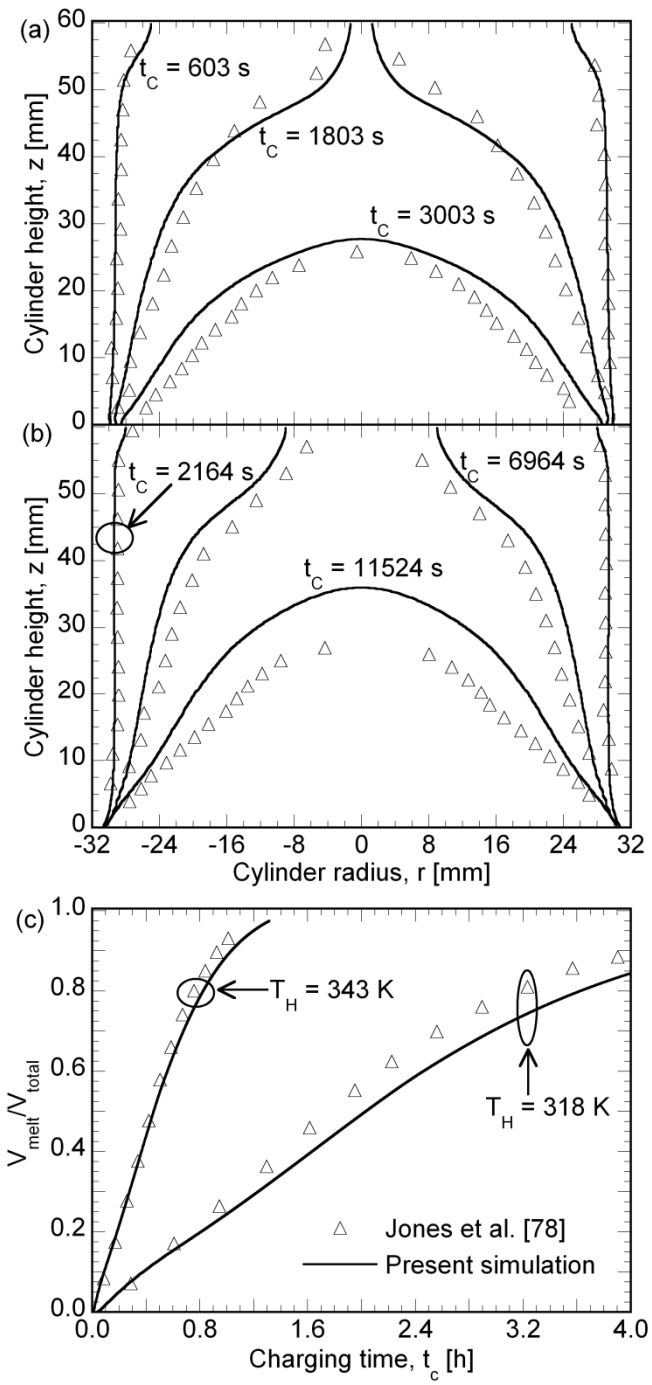

Figure 8: Comparison of the melt front locations from the present simulations (solid lines) with Jones et al. [46] (triangular markers) for charging temperature T_H = (a) 343 K, and (b) T_H = 318 K and, (c) Comparisons of the present simulations (solid lines) of the time evolution of (c) liquid melt volume fraction for T_H = 343 K and T_H = 318 K with the data from Jones et al. [46] (triangular markers).

portrayed in Figure 9a–e are discussed below, first for charging (Section 3.3) and then for discharging (Section 3.4).

3.4 LTES Charging

Figure 10–c presents the contours of the PCM melt volume fraction and the stream lines of flow fields within the molten PCM at various instants of time during the charging process for Module 1 without any embedded heat pipes. This arrangement serves as a reference for comparison with the simulations of Module 1 with heat pipes to establish the degree of heat transfer augmentation in the presence of heat pipes. The end views of the PCM melt volume fraction contour on the vertical diametral axis along the plane A-A' (to the left of each subfigure) and the horizontal diametral axis along the plane B-B' (to the bottom of each subfigure) are also shown in Figure 10a. The solid PCM in the enclosure outside the tube is represented by the light shaded area while the white areas in the enclosure outside the tube represent the molten PCM formed during charging. Figure 10a portrays the melt front at t = 3 h, where it can be seen that the melting of the PCM is aided by the formation of Rayleigh-Benard convection currents within the melt that occurs as a result of the temperature difference between the heated wall and the relatively cold solid phase. The PCM melt fraction at the end of 3 hours is 18.89 %. From Figure 10b, it can be seen that at t = 8 h, the natural convection current within the molten PCM are formed completely. Thus, the lighter melt at the bottom of the tube rises along the hot tube wall to the top, being heated in the process, and upon descending along the cold solid PCM exchanges thermal energy, thus entraining more fluid and forming a clockwise (counterclockwise) vortex in the melt region to the right (left) of the tube. The recirculation ensures relatively faster melting of the PCM at the top of the tube compared to the bottom and the molten PCM volume fraction at the end of 8

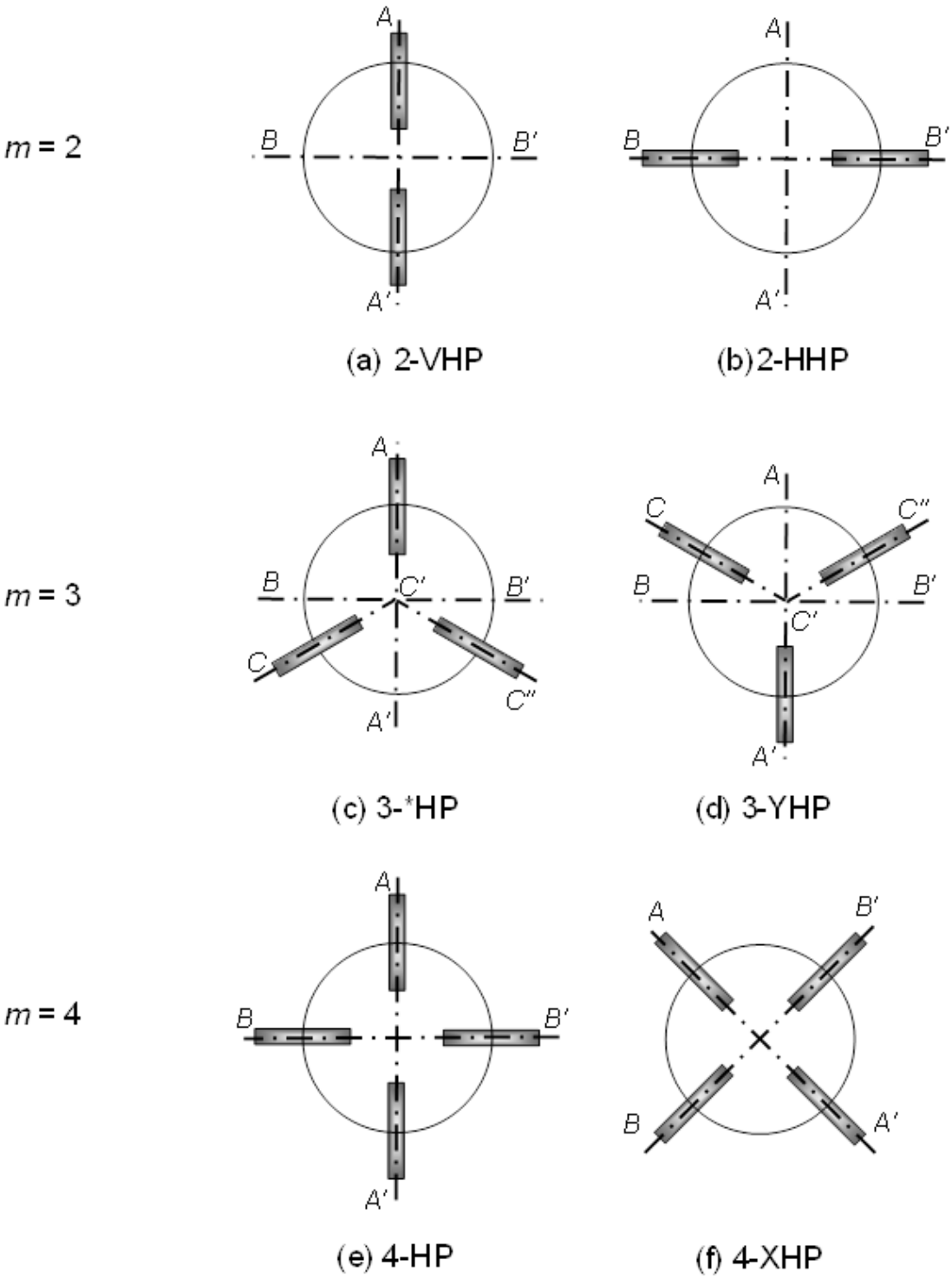

Figure 9: Schematic illustration of the different arrangement of heat pipes: (a) 2 vertical heat pipes (2-VHP) (b) 2 horizontal heat pipes (2-HHP) (c) 3 heat pipes (3-*HP) (d) 3 heat pipes (3-YHP) and (e) 4 heat pipes (4-HP).

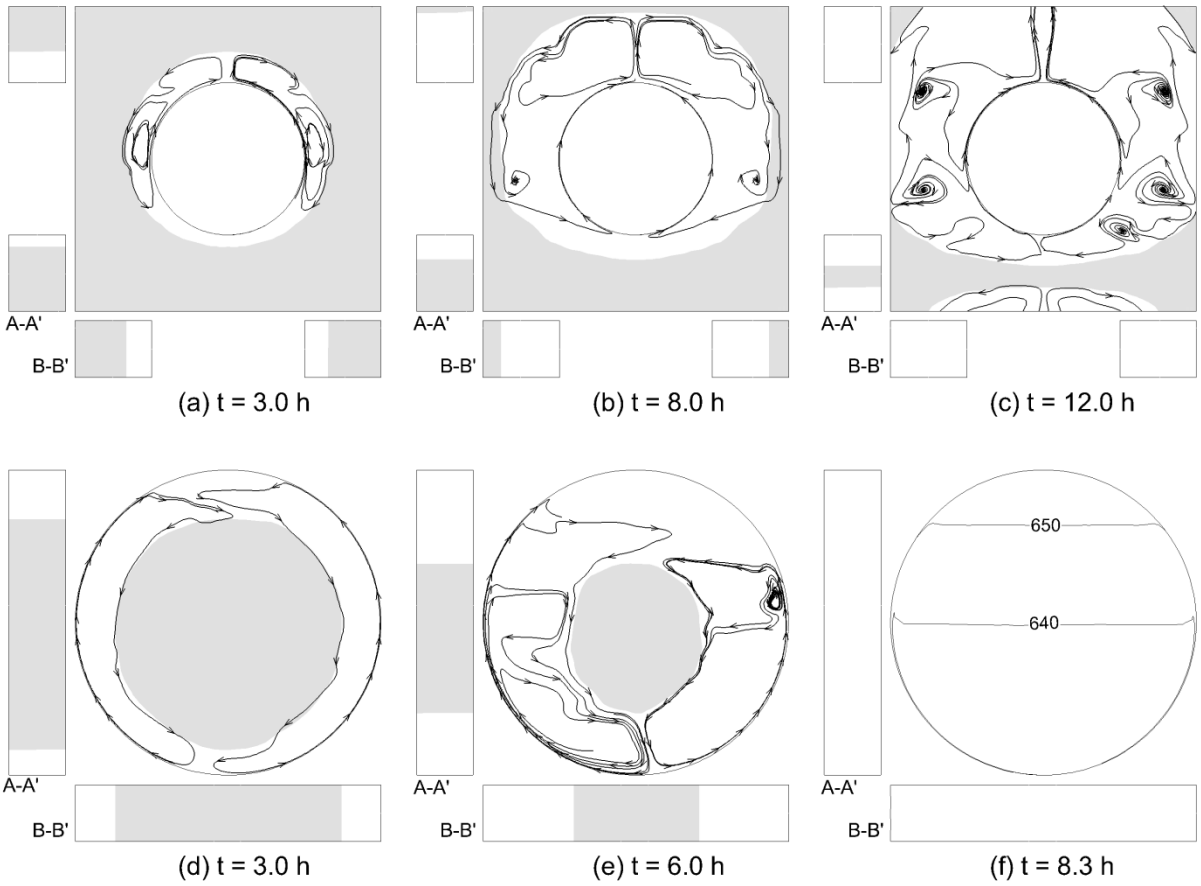

Figure 10: Contours of PCM melt volume fraction (shaded areas denote solid PCM) and streamlines of flow within the molten PCM at various time instants during charging for Module 1 (a)–(c) and Module 2 (d)–(f)

hours is 54.82 %. The snapshot at t = 12 h in Figure 10c shows that more PCM from the top is liquefied and enters the neighboring unit cell above, which is also seen by the emergence of molten PCM at the bottom of the unit cell captured as a result of the periodic boundary condition imposed on the top and bottom faces of the unit cell. The molten PCM below the tube remains at a slightly lower temperature compared to the rest of the molten PCM as there is insufficient cold solid PCM for the formation of Rayleigh-Benard recirculation cells along the circumference of the tube. The total PCM melt fraction at t = 12 h, the maximum time for charging, is 83.65 %. Note

that the PCM melting is symmetric about the vertical diametral axis throughout the charging process.

Similarly, Figure 10d–f presents contours of the molten PCM fraction at various time instants for the charging of Module 2 without any embedded heat pipes. As in the case of Module 1 in Figure 10a–c, the arrangement without heat pipes serves as a reference for comparison of the results for Module 2 with heat pipes discussed later in this Section. In this configuration, the PCM is enclosed within the tube, and the HTF flows transverse to the tube axis. Figure 10d shows that at t = 3 h, the natural convection cells formed extend from the bottom of the tube to the top forming a clockwise vortex to the left and an anti-clockwise vortex to the right of the tube resulting in a PCM melt volume fraction of 46.64 %. With progression of time, the convection cells were found to be stronger, due to the smaller height of the PCM region and, in turn, the smaller length of the convection cells. For the same reason, the Rayleigh-Benard convection cells are seen to extend all the way from the bottom of the tube to the top of the tube. It is to be noted that the local heat transfer coefficient varies along the circumference of the tube, with the heat flux from the HTF being the highest at the top and bottom of the tube diametral cross section. As a result, thermal stratification sets in, as seen in Figure 10e at t = 6 h, which restricts the natural convection cells to extend until the top of the tube with the PCM melt volume fraction reaching 83.56 %. The isothermal contour lines at the end of the charging process in Fig. 4f shows the different thermally stable stratified layers without any recirculation. Complete melting was attained at 8.33 hours as shown in Figure 10f. Note that, in general, there is no line of symmetry in this case owing to the effect of gravity in the vertical direction and the circumferentially varying heat transfer coefficient along the tube surface which is highest at the top and lowest at the point where the horizontal diametral axis of the tube intersects the tube surface in Figure 10d–f.

The time evolution of the molten PCM fraction contours for charging of Module 1 with 2-VHP (Figure 9a) is shown in Figure 11a–c. The end views on the vertical diametral axis depicting the melting around the two heat pipes along the plane A-A' in Figure 9a and the horizontal diametral axis portraying the melting along the plane B-B' in Figure 9a are also shown. It is seen from Figure 11a that at t = 2 h, the convection cells carry the hot, lighter molten PCM from the bottom along the outer circumference of the hot tube, being heated in the process and on reaching the top heat pipe a small counterclockwise (clockwise) recirculation cell is formed to the left (right) of the hot heat pipe. The formation of recirculation is also attributed to the rapid turning of the flow in response to the blockage imposed by the solid PCM at the top of the unit cell. It is found that the PCM around the top heat pipe melts faster and enters the unit cell to the top, which is also observed at the bottom of the domain due to the periodically repeating nature of the geometry. As seen from the end view along the plane A-A', the melt front around the top heat pipe has completely melted at t = 2 h. Rayleigh-Benard convection cells promote good mixing within the molten PCM and thermal

stratification is not observed. The molten PCM volume fraction at this instant was calculated to be 18.68 %. As time progresses, the melt front between the adjacent unit cells at the top and bottom conjoin to form a single recirculation zone with flow field extending form the bottom of the domain to the top of the domain which is seen at t = 5 h in Figure 11b. As the melt fronts from the adjacent unit cell coalesce the temperature within the molten PCM drops slightly as the cold molten PCM accumulated near the bottom of the tube diffuses to the rest of the system. The molten PCM volume fraction corresponds to 32.91 % at the end of 3 hours. The PCM was completely melted at 8.25 hours as portrayed in Figure 11c.

Figure 11d–f depicts the time variation of the PCM melt fraction contours during charging of

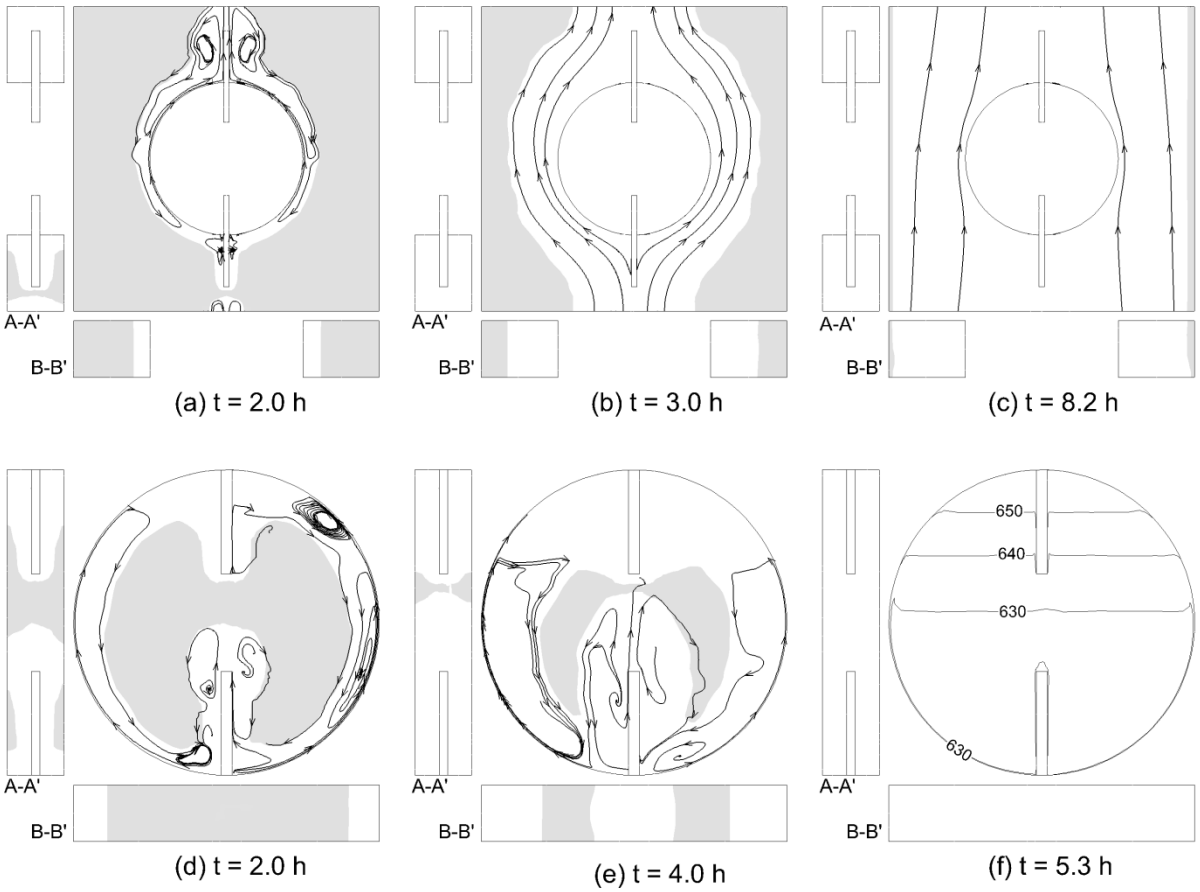

Figure 11: Contours of PCM melt volume fraction (shaded areas denote solid PCM) and streamlines of flow within the molten PCM at various time instants during charging for Module 1 (a)–(c) and Module 2 (d)–(f) embedded with 2-VHP.

Module 2 embedded with 2-VHP (as in Figure 9b). Also shown are the end views on the vertical diametral axis (to the left of each subfigure) as well on the horizontal diametral axis (bottom of each subfigure) along a plane normal to the page, represented by A-A' and B-B', respectively, in Figure 9a. Figure 11d, at t = 2 h, shows that the flow field has similar characteristics as the case with no heat pipes but also exhibits additional recirculation cells in the vicinity of the heat pipes. It is observed that the recirculation zone is stronger in the melt front formed near the VHP located at the bottom. This is attributed to the existence of a thermally stable stratified layer in the PCM stored near the top of the tube where the motion of the molten PCM

due to natural convection is restricted and heat transfer between the HTF and PCM due to conduction prevails. Consequently, the convection currents from the VHP at the bottom do not extend all the way to the top of the PCM resulting in a reduced melting rate near the VHP at the top as observed along the plane A-A' in Figure 11d and e. At t = 4 h, which is illustrated in Figure 11e, it is observed that the solid PCM near the top of the tube is completely molten as the recirculation cells which get heated in the process of ascending from the bottom of the tube transfer greater amount of thermal energy to the solid PCM at the top due to higher temperature gradient between the cold solid PCM and the hot, lighter melt. As the molten PCM descends, losing heat in the process, the temperature gradient progressively decreases and the solid PCM at the bottom does not melt faster. The amount of PCM melt fraction available at t = 4 h corresponds to 84.43 %. With further progression of the charging process, the intense convection effects circulate the hot melt from the bottom along the walls of the tube to the top of the solid PCM aiding the melting process and simultaneously thickening the thermally stratified molten layer at the top of the tube, as seen from the isothermal contour lines in Figure 11f for t = 5.31 h. Overall the PCM melting is complete at 5.31 h for Module 2 embedded with 2-VHP.

Figure 12a–c show the phase distribution during melting of PCM in Module 1 embedded with 2 horizontal heat pipes (Figure 9b) at 4 h, 9 h and 12 h respectively. The contour at the bottom depicts the melt front in the vicinity of heat pipes along a plane normal to the page as seen from the top (B-B' in Figure 9b). Figure 12a, which represents the volume fraction contours at a time instant of 4 hours shows that a higher amount of molten PCM is formed above the heat pipes due to convection assisted melting. The molten PCM volume fraction is calculated to be 36.58 %. No recirculation cells were observed along the condenser section of the horizontal heat pipes due to the absence of gravitational force in that direction to facilitate convection cells. The convection

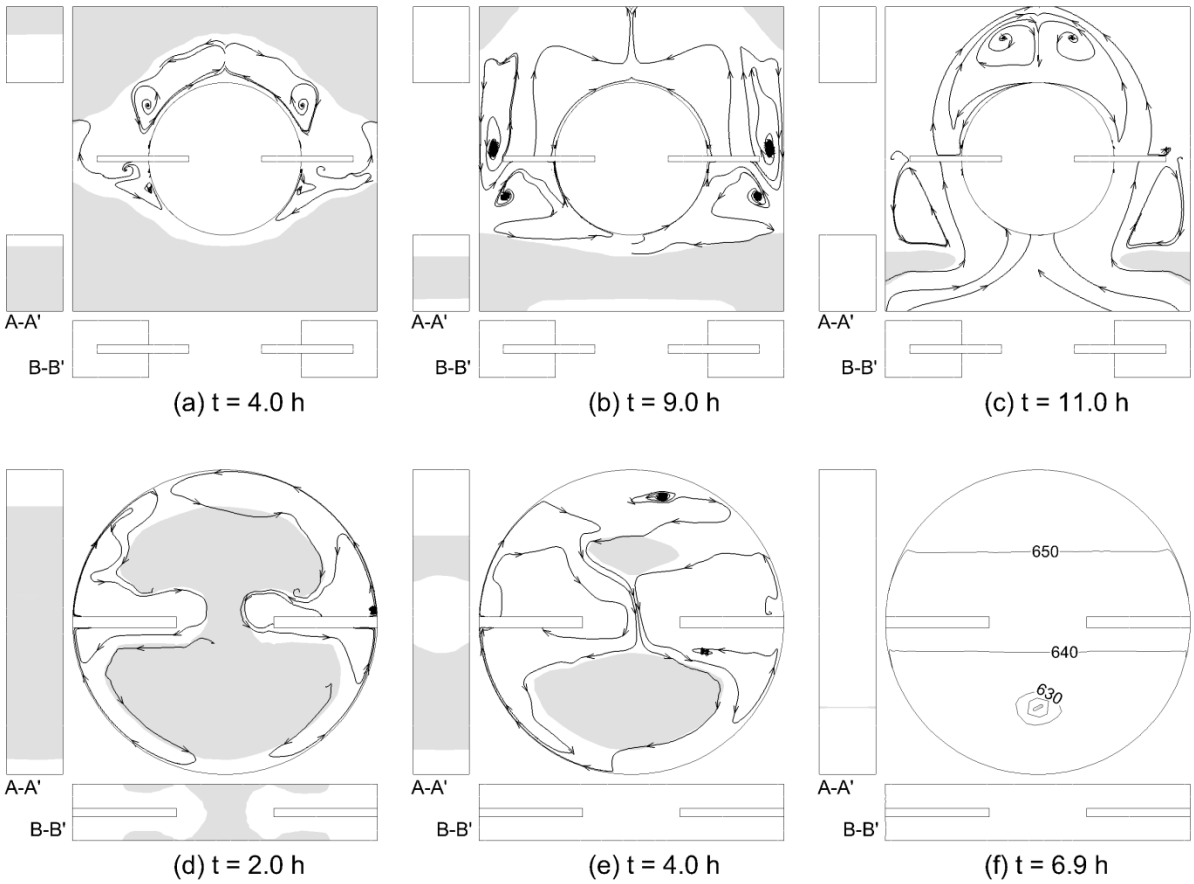

Figure 12: Contours of PCM melt volume fraction (shaded areas denote solid PCM) and streamlines of flow within the molten PCM at various time instants during charging for Module 1 (a)–(c) and Module 2 (d)–(f) embedded with 2-HHP.

currents are seen to be less stronger in the bottom half of the tube owing to the predominant viscous forces over buoyant forces. As time progressed to t = 9 h, the molten PCM from the upper portion of the tube enters the top unit cell (Figure 12b). It was observed that the PCM below the tube remained at a relatively lower temperature than that above the tube due to the accumulation of cold molten PCM as a result of gravity and the absence of free convection currents due to unavailability of cold solid PCM for the molten PCM to descend. The PCM melt fraction at the end of t = 9 h is 78.49 %. As the time progressed to the end of the charging cycle (t = 11 h), two recirculation free convection cells were formed around below the heat pipes and the melt fronts of

all the unit cells in the vertical domain merged to enhance the melting rate of the PCM (Fig 6c). Due to the reduction in the quantity of solid PCM, a weaker temperature gradient exists in the liquid PCM, which results in weaker natural convection currents. The liquid volume fraction that has been melted in this case at 11 hours is 97.74 % as portrayed in Figure 12c. Overall the PCM melting is complete at 11.30 h for Module 1 embedded with 2-HHP.

Figure 12d–f represents the liquid fraction contour plots of the molten PCM in Module 2 embedded with two horizontal heat pipes. At t = 2 h, convection cells were found to be formed spiraling around the length of the horizontal heat pipe as reflected in the amplified magnitude of melting near the middle of the tube in Figure 12d. The PCM melt fraction at this time instant is observed to be 43.16 %. From Figure 12e, which represents the state of the system at t = 4 h, it is observed that the convection currents formed at the top of the tube increases in strength while in the bottom PCM the temperature has not increased much for buoyancy forces to dominate over the viscous forces. Hence some amount of cold molten PCM, which descends down due to gravity, accumulates at the bottom of the tube. A larger amount of solid PCM is observed below the heat pipes than above due to the same reasons as stated above. The total molten PCM volume fraction at this time instant is observed to be 78.43 %. With progression of time, the convection cells circulate from the bottom along the tube to just below the top of the solid PCM found above the heat pipes as restricted by the thermal stratification observed in the upper half of the PCM. The convection currents move along the periphery of the cold solid PCM at the top enhancing the melting process before returning to the solid PCM at the bottom thus entraining more molten PCM due to the subsequent melting of the cold solid PCM. Complete charging of the PCM was achieved at 6.88 hours which is longer compared to Module 2 embedded with 2-VHP due to the absence of

longer recirculation cells along the length of the condenser section in HHP owing to the absence of gravity in the horizontal direction unlike in the case of VHP.

Figure 13a–c represent the liquid fraction contour plots of the molten PCM for various instants of time in Module 1 embedded with three heat pipes at an angle of 120^{o} to each other (Figure 9c) referred to as 3-*HP. This arrangement is chosen to investigate the augmentation in the thermal performance of LTES due to embedding more heat pipes in the bottom to improve the conduction-dominated melting in the lower region of LTES as opposed to the already efficient convection-dominated melting in the top layer of LTES. The contour at the bottom depicts the melt front in the vicinity of heat pipes along a plane normal to the page as seen from the top (C'-C" in Figure 9c). Figure 13a presents the mass fraction contour plot at a time instant of 2 hours with molten PCM volume fraction of 20.82 %. Six natural convection cells were observed, two in the vicinity of either side of the top heat pipe, two extending from the heat pipes at the bottom to the top of the tube forming an anti-clockwise and clockwise vortex to the right and left of the tube, respectively, and the other two on either side of the inclined heat pipes at the bottom. The amount of molten PCM at the end of 2 hours was obtained to be 0.02 m^3 compared to 0.018 m^3 in the case of 2-VHP arrangement, which implies higher melting rate of the PCM in the presence of 3-*HP. As melting continues, the melt front from the bottom unit cell meets with the melt front in the current unit cell and the flow field extends from the bottom to the top of the domain as observed in Figure 13b for a time instant of t = 5 h. The molten PCM fused at a later time (t = 4.33 h) compared to 2-VHP arrangement (t = 2.05 h), despite the presence of two heat pipes in the bottom half of the domain, due to shorter distance between the heat pipe and the bottom unit cell in the case of the 2-VHP arrangement. As a result, the amount of molten PCM at the same instant for the 2-VHP arrangement was 0.052 m^3 compared to 0.045 m^3 for the 3-*HP arrangement. The

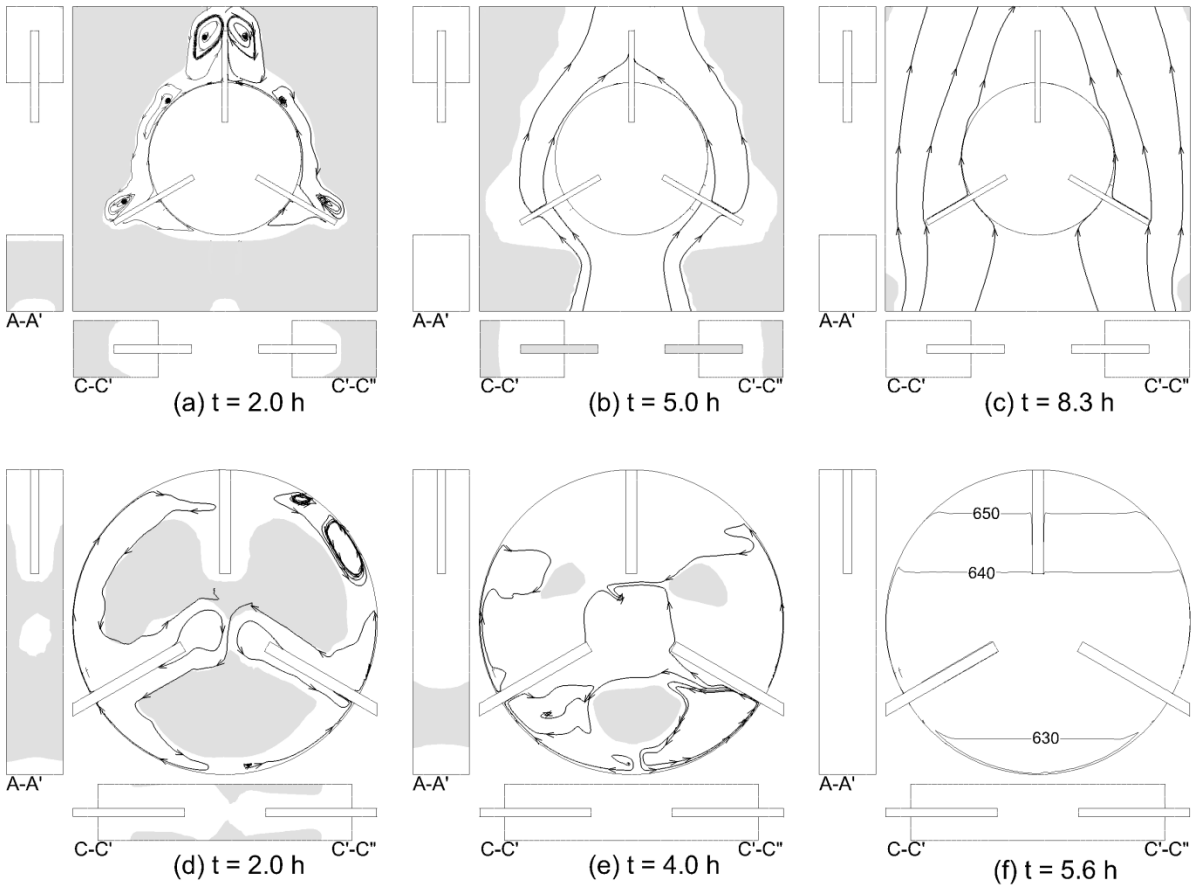

Figure 13: Contours of PCM melt volume fraction (shaded areas denote solid PCM) and streamlines of flow within the molten PCM at various time instants during charging for Module 1 (a)–(c) and Module 2 (d)–(f) embedded with 3-*HP.

streamline of the molten PCM flow field as observed for the time period of 8.31 hours (Figure 13c) extended from the PCM in the bottom region to the top of the domain and enhanced the melting rate of the PCM. Thus, it was observed from Figure 13b and c that even though the heat pipe in the lower region enhances the convection dominated melting of the PCM, the heat pipes should be placed closer to the bottom of the domain for efficient melting of the PCM. Complete melting of the PCM was attained at 8.31 hours, which is slightly longer compared to the 8.25 h for the 2-VHP arrangement.

Figure 13d–f represents the same for Module 2 at various instants of time. Overall, two recirculation cells are observed in this configuration at a time instant of t = 2 h (Figure 13d) on either side of the heat pipes located at the bottom. The molten PCM was found to rise along the tube from its bottom getting heated in the process and on reaching the top of the PCM descends down along the solid PCM. While descending, thermal energy acquired during ascension of the molten PCM is transferred to melting the solid PCM, thus entraining more molten PCM as it descends down and on reaching the heat pipe located at the bottom it rises up again along the condenser of the heat pipe before descending to the bottom of the tube to complete the recirculation loop. As the convection currents rise along the top portion of the heat pipe located at the bottom and descends towards the bottom of the tube, a localized vortex is formed as some of them rise along the lower portion of the hot heat pipe. In contrast to the two heat pipe arrangements (Figure 9a and b), thermal stratification is observed only at a later time due to efficient mixing of the molten PCM by the natural convection currents. The PCM melt fraction at the end of 2 hours is calculated to be 49.06 %. From Figure 13e, it was observed that the localized convection cells formed between the two bottom heat pipes is stronger compared to the convection cell extending from the bottom to the top heat pipe. This can be attributed to the shorter distance of travel and subsequently faster generation of liquid melt in the vicinity of heat pipes located at the bottom. Thus, for Module 2, embedding three heat pipes in 3-*HP arrangement quickens the charging of PCM by inducing natural convection currents in the bottom region of the PCM also (Figure 13e) in contrast to the predominantly conduction-dominated melting of the PCM in the bottom region of Module 1 (Figure 13a). For Module 2, the melting of the PCM completed at 5.62 h, which is longer compared to 5.31 h for the 2-VHP arrangement due to the obstruction imposed on the natural convection currents by the presence of an additional heat pipe.

The performance of the LTES with 3 heat pipes embedded in a Y-pattern as illustrated in Figure 9d is depicted in Figure 14a–c as contours of the melt fraction for Module 1 at the time instants of 3 hours, 6 hours and 8.3 hours, respectively. In all, four natural convection cells were observed at the initial times. The longest natural convection cells formed in Figure 14a on either side of the tube corresponding to a time instant of t = 3 h extended from the bottom of the domain to the top of the tube with the convection currents rising along the wall of the hot tube to the top and on reaching the lower portion of the inclined heat pipe rises along the hot condenser section before descending to the heat pipe located at the bottom along the liquid-solid interface. Two other natural convection cells were observed on either side of the tube extending from the upper portion of the heat pipes to the top of the tube. As time progressed the convection currents grew stronger but maintained the same pattern of travel. The PCM melt fraction at this time instant was calculated to be 32.05 %. From Figure 14b, it can be observed that embedding two heat pipes in the top half of the domain contributes to progression of the melt front in the direction of orientation of heat pipes in addition to the radial progression of melt front from the tube surface.

Complete melting of the PCM was attained at 8.26 h as observed in Figure 14c, which is slightly quicker compared to 3-*HP arrangement due to the closer proximity of the bottom heat pipe to the bottom of the domain which resulted in slightly faster fusion of the PCM melt fronts with the adjacent unit cell to the bottom. Furthermore, this arrangement can be useful due to the rapid extension of convection currents and subsequent melting in the regions along the direction of the inclined heat pipe located at the top, which normally takes a long time to melt.

Figure 14d–f illustrate the contours of the melt fraction for Module 2 embedded with 3-YHP at the time instants of 1 hour, 3 hours and 5.4 hours, respectively. Figure 14d, which illustrates the contours of the melt fraction at a time instant of 1 hour shows that the volume of molten PCM in

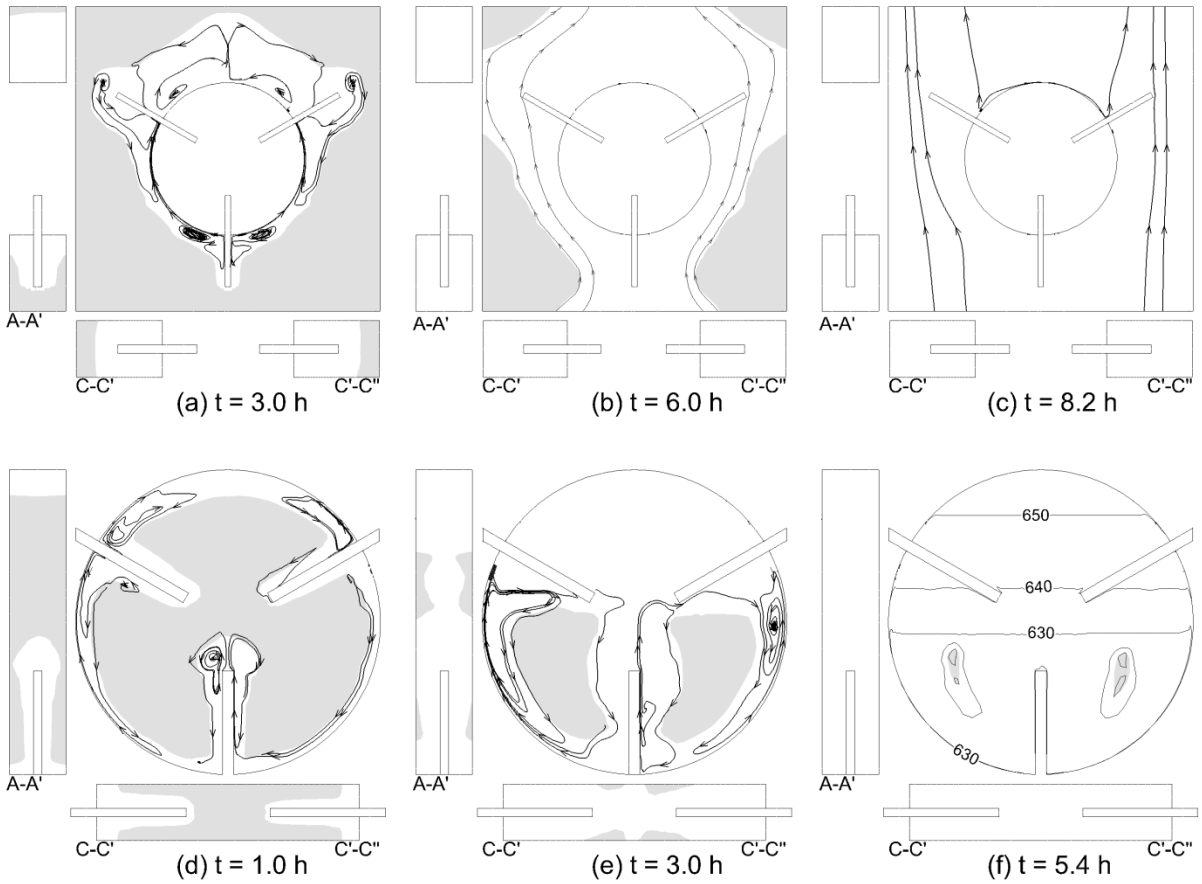

Figure 14: Contours of PCM melt volume fraction (shaded areas denote solid PCM) and streamlines of flow within the molten PCM at various time instants during charging for Module 1 (a)–(c) and Module 2 (d)–(f) embedded with 3-YHP.

Module 2 with 3-YHP arrangement is larger compared to that in the 3-*HP arrangement at a corresponding time. This can be attributed to the enhancement of the already convection-assisted melting above the tube. The convection cells formed between the upper portion of the inclined heat pipes and the top of the tube lead to faster melting of the PCM at the top of the domain and thermal stratification with horizontal layers of relatively cold melt from the top was observed sooner compared to Module 2 with 3-*HP arrangement, implying a higher sensible energy storage compared to the 3-*HP arrangement (Figure 13d). As time progressed, the convection cells between the two inclined heat pipes diminished as the molten PCM at the top of the tube became

thermally stable owing to thermal stratification and at the time instant of t = 3 h corresponding to Figure 14e, only the recirculation cells on either side of the heat pipe located at the bottom was observed giving rise to clockwise (anti-clockwise) vortex to the left (right) of the tube. The PCM was fully melted at 5.41 hours (Figure 14f) compared to 5.62 hours obtained for the 3-*HP (Figure 13f).

Figure 15a–c illustrate the contours of PCM melt fraction at various instants of time for Module 1 embedded with 4 heat pipes (Figure 9e). Initially (Figure 15a), four convection cells were formed in Module 1, which includes the molten PCM circulating from the bottom heat pipe to the horizontal heat pipe on either side of the tube and the molten PCM circulating from the horizontal heat pipe to the top vertical heat pipe on either side of the tube. The increase in the melt rate for Module 1 in increasing the number of heat pipes from three (Figure 13 and Figure 14) to four (Figure 15) is significantly less at a factor of 1.04 compared to the increase in melt rate by a factor of 1.16 in increasing the number of heat pipes from two (Figure 11 and Figure 12) to three (Figure 13 and Figure 14). This is attributed to the fact that in the arrangement with 4-HP the presence of extra heat pipe hampers the flow of natural convection currents, although there is an increase in conduction-dominated melting. Due to the convection-assisted melting in the top region of the tube above the horizontal diametral axis, the solid PCM surrounding the top heat pipe is completely melted as seen from the end views A-A' in Figure 15a–c. Similar amount of molten PCM surrounding the two horizontal heat pipes shown along the plane B-B' reiterates the symmetric melting of PCM along the vertical diametral axis of the domain. As the melt fronts around the tube progressed, they are seen to coalesce with the advancing melt fronts from the adjacent unit cells at the top and bottom (Figure 15b), with the convection currents streaming up from the bottom unit cell due to the periodic geometry of the configuration. The fusion of melt

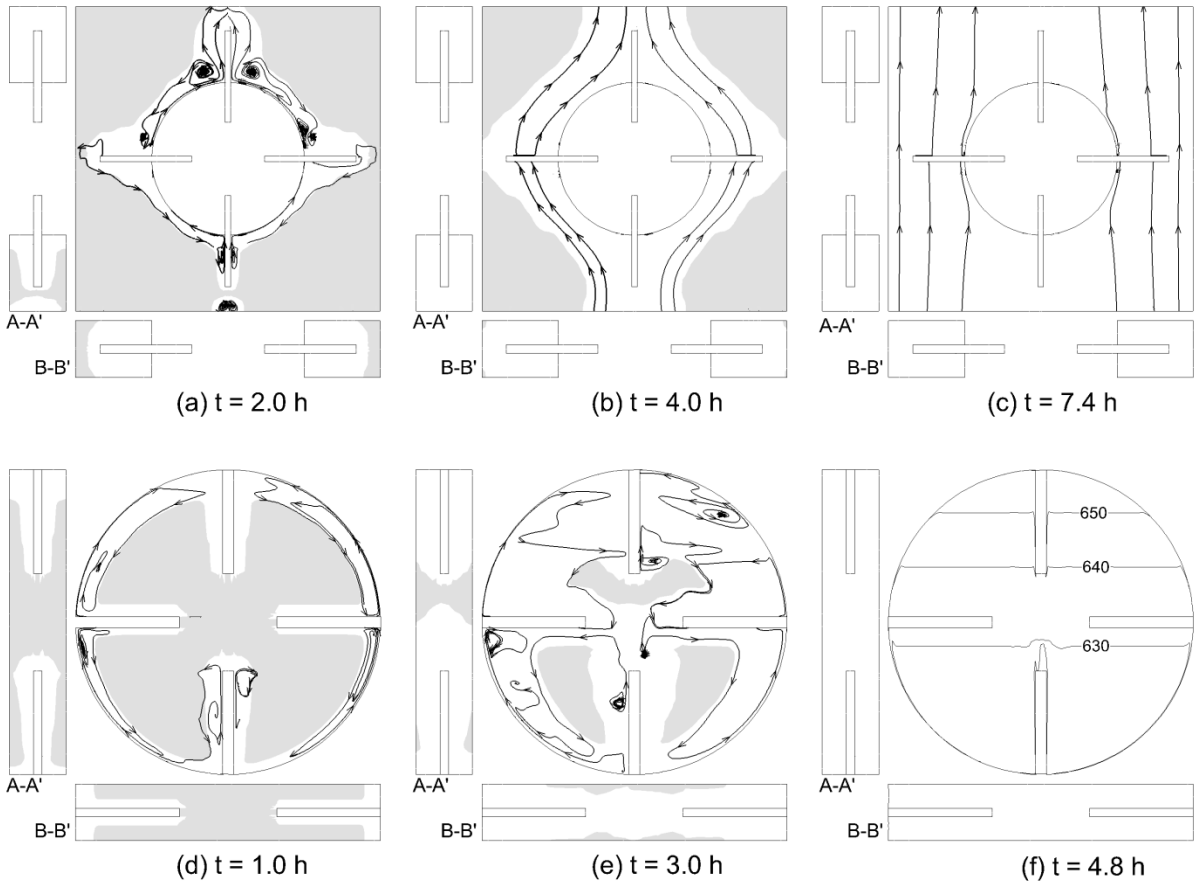

Figure 15: Contours of PCM melt volume fraction (shaded areas denote solid PCM) and streamlines of flow within the molten PCM at various time instants during charging for Module 1 (a)–(c) and Module 2 (d)–(f) embedded with 4-HP.

fronts for the 4-HP arrangement was observed at a slightly later time compared to the 2-VHP arrangement due to the presence of two extra heat pipes obstructing the path of the convection currents. The molten PCM volume fraction at t = 4 h is calculated to be 53.51 %, but following the merging of melt fronts, the flow field pattern amplified in strength, enhancing the melt rate of the PCM and completing charging at t = 7.38 h (Figure 15c). As noted for the other arrangements discussed previously due to the merging of melt fronts from the adjacent unit cells at the top and bottom, thermal stratification is not observed.

Figure 15d–f illustrate the contours of PCM melt fraction at various instants of time for Module 2 embedded with 4 heat pipes. From Figure 15d, it is observed that the melt front in the vicinity of the heat pipe located at the bottom and top has progressed more compared to the melt front adjoining the heat pipe located horizontally due to the higher heat transfer rate between the HTF and the vertical heat pipes. Figure 15e reveals that the natural convection cells between the bottom and the horizontal heat pipes are less intense compared to the natural convection cells between the top and horizontal heat pipes which leads to more melting of PCM at the top than at the bottom. But, due to the thermal stratification near the top heat pipe, the solid PCM is not completely molten as seen from the end view along the plane A-A' in Figure 15e. Unlike in Module 1, the restriction of natural convection currents due to the presence of additional heat pipes was not observed and the increase in the volume of molten PCM between LTES embedded with 4-HP and 3-HP as well as between LTES embedded with 3-HP and 2-HP at t = 3 h is equally observed to be a factor of 1.06. Complete melting of the PCM was achieved at 4.82 h and the contour lines in Figure 15f correspond to the isothermal profile depicting the thermally stable horizontal stratified layers where the motion of molten PCM is restricted.

Figure 11–Figure 15 presented the time evolution of the melt front progression for Modules 1 and 2 with different arrangements of the heat pipes. It is also instructive in examining the variation of energy stored and the charging effectiveness with time. Figure 16a and b depict the time history of energy stored within the PCM and the charging effectiveness of Module 1 for the various arrangements of embedded heat pipes considered (Figure 9). It is observed in Figure 16a that the rate of melting is the highest for LTES embedded with four heat pipes followed by the 2-VHP arrangement. The time histories of the energy stored for the 3-*HP and 3-YHP arrangements are approximately the same. The charging effectiveness is defined to quantify the augmentation in

the performance of LTES system in the presence of heat pipes as, $\varepsilon_C = Q_C / Q_{C,0}$, where Q_C is the energy stored for the case of tube embedded with heat pipes while $Q_{C,0}$ represents the energy stored for the case without any heat pipes. The charging effectiveness was found to follow the relative order with respect to heat pipe arrangement as that in Figure 16a. From Figure 16b it can be seen that the effectiveness starts from a high value due to the earlier onset of melting around the heat pipes compared to melting around the tube, resulting in a high value for the ratio $Q_C / Q_{C,0}$. The effectiveness curve then gradually decreases once the melting of the PCM around the tube also initiates until at a time of approximately 3 minutes when the effectiveness increases sharply. The increase can be attributed to the merging of the melt fronts near the tube and the heat pipes, which amplifies the natural convection currents existing within the molten PCM. After 11 minutes, the effectiveness remains fairly constant until the time instants of 2.05 h, 10.48 h, 4.33 h and 2.10 h for 2-VHP, 2-VHP, 3-*HP, 3-YHP and 4-HP arrangements, respectively, when the effectiveness is observed to increase corresponding to the merging of melt fronts between adjacent unit cells in the top and bottom. At approximately 6 and 7 hours, the effectiveness slightly decreases for the 2-VHP and 4-HP arrangements, respectively, for a short duration owing to the decrease in the sensible energy within the unit cell as cold stream of molten PCM from the bottom unit cell enters the computational domain. Similar characteristics are seen in 3-*HP and 3-YHP arrangements, albeit in a reduced magnitude, which leads to indiscernible change in the effectiveness profiles. This can be attributed to the fact that the melt fronts fuse at earlier times when insufficient volume of molten PCM is formed for it to have an impact on the effectiveness curve. The decrease in effectiveness after the entire PCM is melted is included to signify the culmination of storage of latent energy and start of storage of sensible energy only. The highest charging effectiveness was obtained for Module 1 embedded with 4-HP at 2.00 followed by 2-VHP arrangement with an

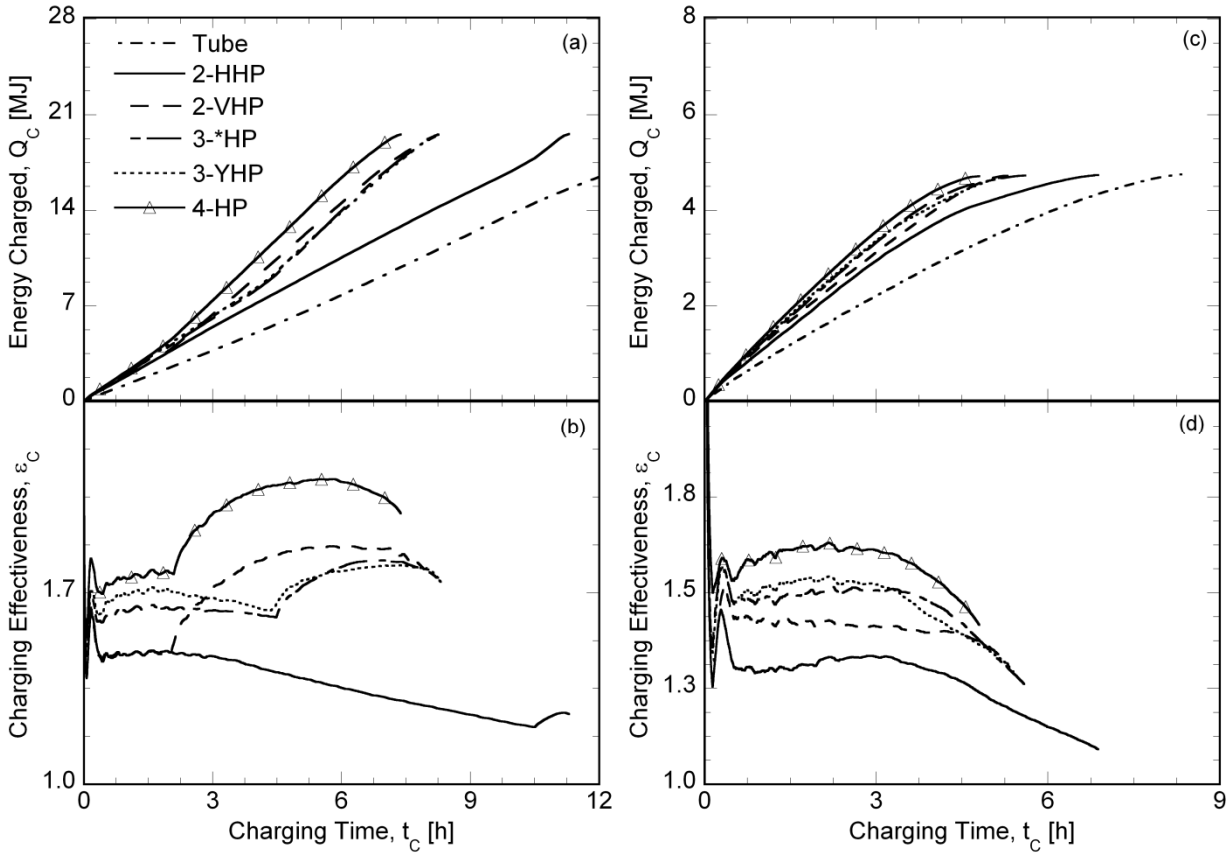

Figure 16: Effect of the arrangement of heat pipes on the energy charged and charging effectiveness for (a, b) Module 1 and (c, d) Module 2.

effectiveness of 1.77 at the end of the charging period.

Figure 16c and d illustrate the time history of energy stored within the PCM and the charging effectiveness of Module 2 for the various arrangements of embedded heat pipes considered (Figure 9). It is observed in Figure 16c that the rate of melting is the highest for LTES embedded with four heat pipes (4-HP) followed by the 3-YHP arrangement. Unlike in Module 1, where the convective heat transfer rate between the HTF and the heat pipes is invariant to orientation, the heat transfer rate between HTF and VHP is higher compared to that between HTF and HHP in Module 2 which manifests as a smaller difference (factor of 1.09) between the energy stored for LTES embedded with 2-HHP and 2-VHP in Module 2 (Figure 16c) compared to 1.18 times obtained between the

same heat pipe arrangements for Module 1 (Figure 16a). The product of the total PCM volume and its latent heat of fusion, h_{sl} yield the maximum latent energy that could be stored in Module 2 to be 4.69 MJ. From Figure 16c, it can be observed that the energy stored for the LTES with various heat pipe arrangements is higher than 4.69 MJ due to the storage of sensible energy in addition to the latent thermal energy storage. It was observed that LTES embedded with 2-HHP stores a greater amount of energy due to the longer charging time and, consequently, a larger sensible energy storage. The melting rate of the 4-HP arrangement is only slightly higher than the 3-HP arrangement due to the obstruction to the flow of natural convection currents owing to the presence of additional heat pipe as explained before. From Figure 16d, it is also observed that the effectiveness curves follow the same variations as observed for Module 1. It is observed that the effectiveness remains at higher value throughout most of the charging process, but decreases at the end when the percentage of sensible energy stored also increases. This suggests that it is reasonable to stop the charging process when the effectiveness starts to decrease, which occurs at approximately t = 3h for all the arrangements, at which time the effectiveness values are 1.41, 1.33, 1.51, 1.52 and 1.61 for the 2-VHP, 2-HHP, 3-*HP, 3-YHP and 4-HP arrangements, respectively. The effectiveness values at the end of the charging period in Figure 16d are seen to decrease to 1.31, 1.09, 1.26, 1.29 and 1.42 for the 2-VHP, 2-HHP, 3-*HP, 3-YHP and 4-HP arrangements, respectively. Overall, the effectiveness of Module 1 embedded with 4-HP is found to be the highest ε_C = 1.42, at the end of the charging period. It is also observed that though the fraction of the volume that has melted in the case of Module 2 is far greater than in Module 1, the latent energy stored in Module 2 over a period of 12 hours is slightly lesser than that in Module 1 implying a smaller melt volume.

3.5 LTES Discharging

Discharging of the energy available in the PCM to the HTF results in the solidification of the PCM. Figure 17a–f represent the melt fraction contours of the solidification of PCM in a LTES after 12 hours for the six different arrangements of the heat pipes. The solidification of the PCM in Module 1 configuration is observed to be uniform adjoining the tube as well as around the heat pipes. This is primarily due to the absence of natural convection effects within the solidified PCM and the purely conduction dominated solidification which accounts for the very slow discharging rate of the PCM compared to the charging rate. Since the orientation of heat pipes does not affect the surface heat transfer coefficient between the heat pipe and the HTF in the case of Module 1, it was found that the solidification rate of the PCM was a function of the number of heat pipes embedded within the LTES only. The solid PCM fraction at the end of 12 h discharging was calculated to be 17.58 % for a tube with no heat pipe (Figure 17a), 20.09 % for both 2-HP arrangements (Figure 17b and c), 21.75 % for both 3-HP arrangements (Figure 17d and e) and 23.31 % for the 4-HP arrangement (Figure 17f). Also, the progressive increase in the solidification rate with the addition of each extra heat pipe is approximately the same, again due to the conduction- dominated solidification of PCM. It was also observed that the solid PCM around the heat pipes is sub-cooled to 585 K while the solidified PCM around the tube is sub-cooled to nearly the same temperature as the HTF. This implies that the steady state temperature of the heat pipes is well above the HTF temperature, which restricts the sub-cooling of the solid PCM within its vicinity.

Figure 18a–f represents the solid regions (shaded areas) at the end of the 12 hour discharging period for Module 2, and for the six arrangements with or without heat pipes. The solidification of the PCM is once again seen to be uniform throughout the solid fraction adjoining the tube and

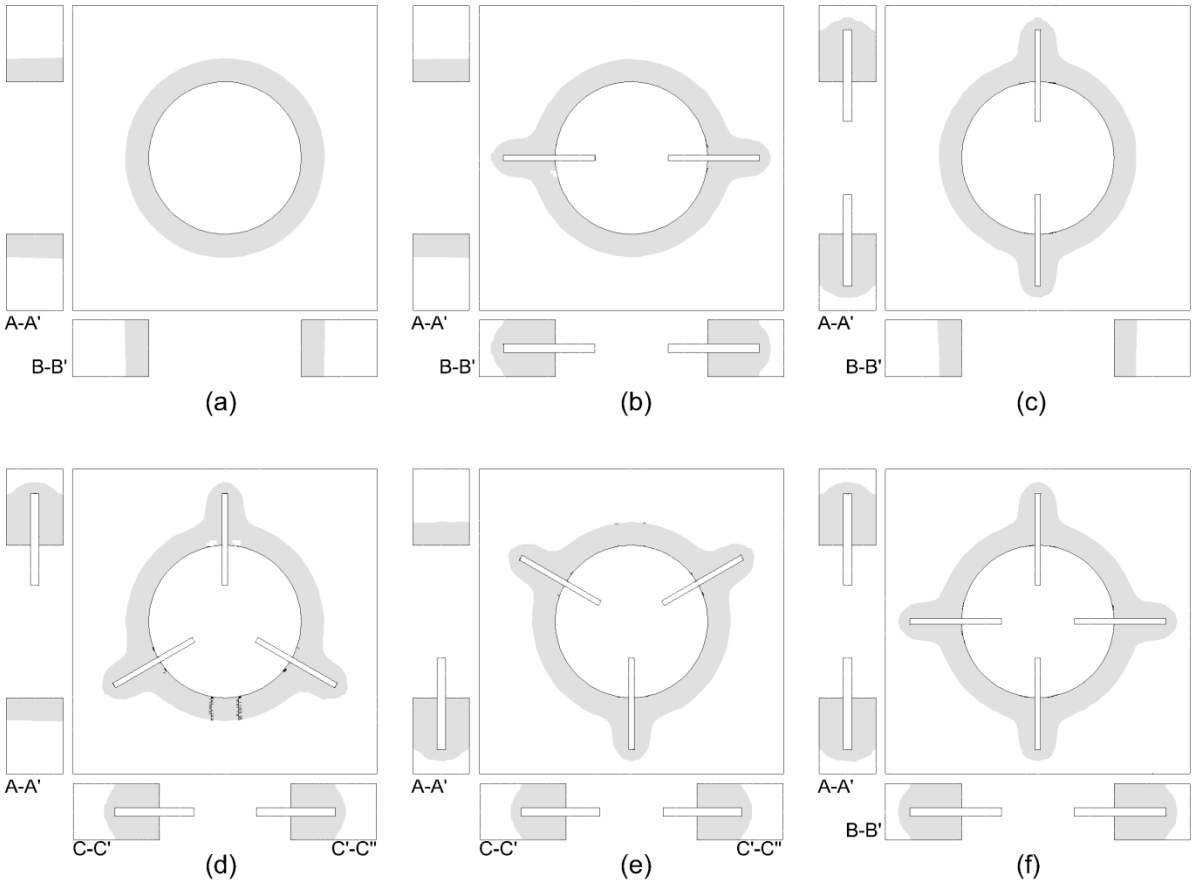

Figure 17: Contours of PCM melt volume fraction (shaded areas denote solid PCM) at t = 12 h during discharging for Module 1 embedded with (a) no heat pipes, (b) 2-HHP, (c) 2-VHP, (d) 3-*HP, (e) 3-YHP and (f) 4-HP.

around the heat pipes due to the conduction-dominated solidification of PCM. It was found that the fraction of solid PCM at the end of the 12 hour discharging period was 55.05 % for the LTES embedded without any heat pipes (Figure 18a), 62.46 % for the 2-HHP arrangement (Figure 18b), 66.06 % for the 2-VHP arrangement (Figure 18c), 70.40 % for the 3-HP arrangements (Figure 18d and e) and 73.26% for the 4-HP arrangement (Figure 18f). The difference in the solid fraction at the end of the discharging cycle between the 2-HHP and the 2-VHP arrangements occurs due to the difference in surface heat transfer coefficient as a result of the different orientations of the heat pipe with respect to the direction of gravity. It is observed that the horizontal heat pipes experience

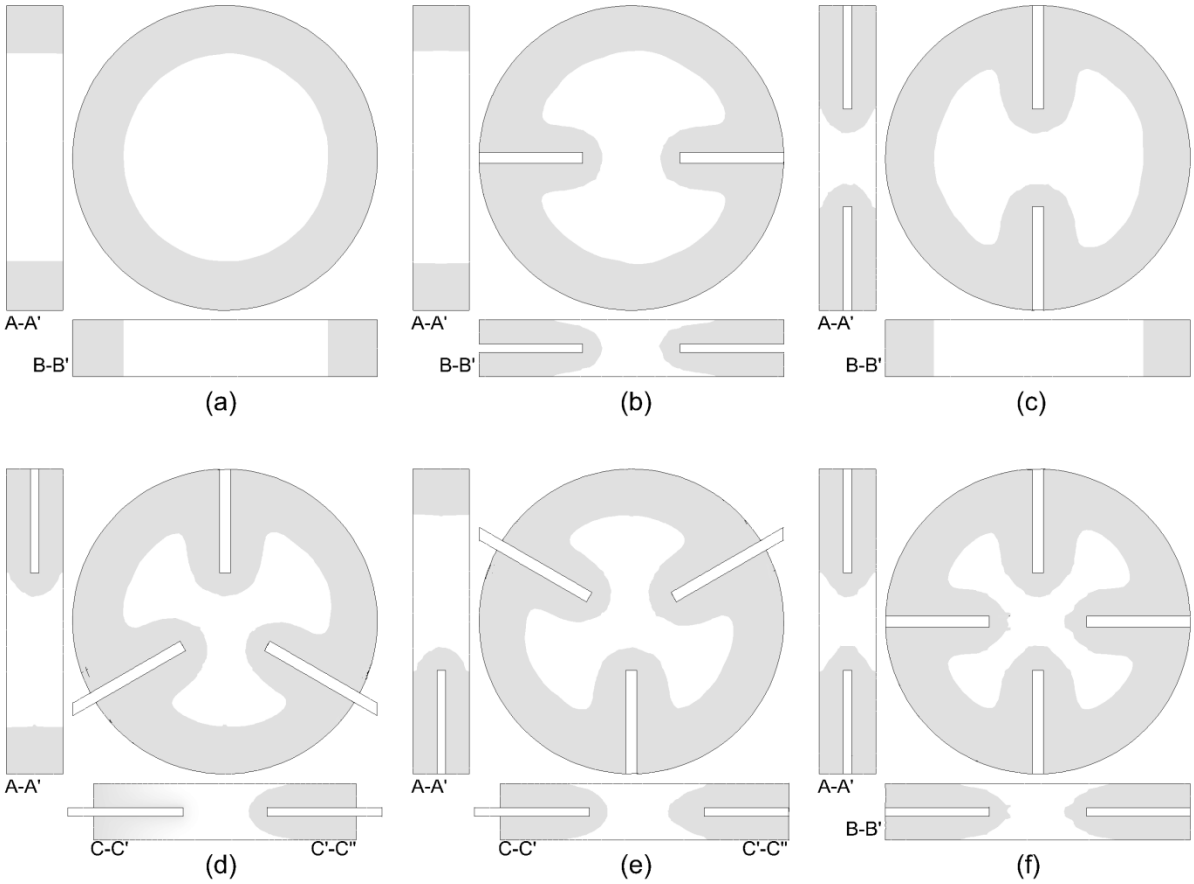

Figure 18: Contours of PCM melt volume fraction (shaded areas denote solid PCM) at t = 12 h during discharging for Module 2 embedded with (a) no heat pipes, (b) 2-HHP, (c) 2-VHP, (d) 3-*HP, (e) 3-YHP and (4) 4-HP.

a smaller surface heat transfer coefficient from the HTF compared to the VHP and hence the solidification rate of the 2-VHP arrangement is higher compared to that of a 2-HHP. No difference is observed in the overall solid fractions in Figure 18d and e between the two different 3-HP arrangements because even though the geometry is rotated about the tube axis by 180^{o}, both the arrangements consist of a heat pipe oriented vertically in the direction of gravity and two inclined heat pipes oriented at an angle of 60^{o} on either side of the vertical diametral axis; resulting in the same surface heat transfer coefficients experienced by the heat pipes in both 3-HP arrangements.

Figure 19 illustrates the time history of the energy discharged and the discharging effectiveness for the different arrangements of heat pipes in both Modules 1 and 2. From Figure 19a and b it is observed that the solidification rate and the discharging effectiveness is highest for the 4-HP arrangement followed by the 3-HP arrangement in Module 1 which is also reflected in the results obtained for Module 2 as portrayed in Figure 19c and d, respectively. In the case of the 2-HP arrangements, the solidification rate is found to be higher for LTES embedded with 2-VHP inModule 2 (Figure 19c). This is due to the relatively larger heat transfer coefficient for heat pipes oriented perpendicular to the HTF flow in the case of Module 2. The latent energy discharged for the 4-HP arrangement in Module 2 over a period of 12 hours (Q_D = 3.45 MJ) is lesser than that in Module 1 (Q_D = 4.57 MJ) due to smaller total solid volume in spite of the higher solid fraction. The effectiveness variation starts from a high value due to the fact that the solid fraction adjoining the heat pipes develops faster when no substantial solid fraction is formed along the tube. The effectiveness curve decreases sharply and then reaches a constant value. Unlike in charging, the sharp increase in effectiveness characterizing the start of free convection effects is not observed in Figure 19b and d due to the conduction-dominated solidification of PCM while a gradual increase in the discharging effectiveness is observed for various configurations of LTES at a time instant of approximately 1.5 h. This can be attributed to the sub-cooling of the solid PCM adjoining the tube when the PCM around the heat pipes is only sub-cooled to a lesser degree, resulting in the discharging effectiveness rising gradually. Of all the heat pipe arrangements, in Figure 19b and d, it was found that 4-HP arrangement provided the highest effectiveness of ε_D = 1.32 for both Modules 1 and 2 at the end of the 12 hour discharging period.

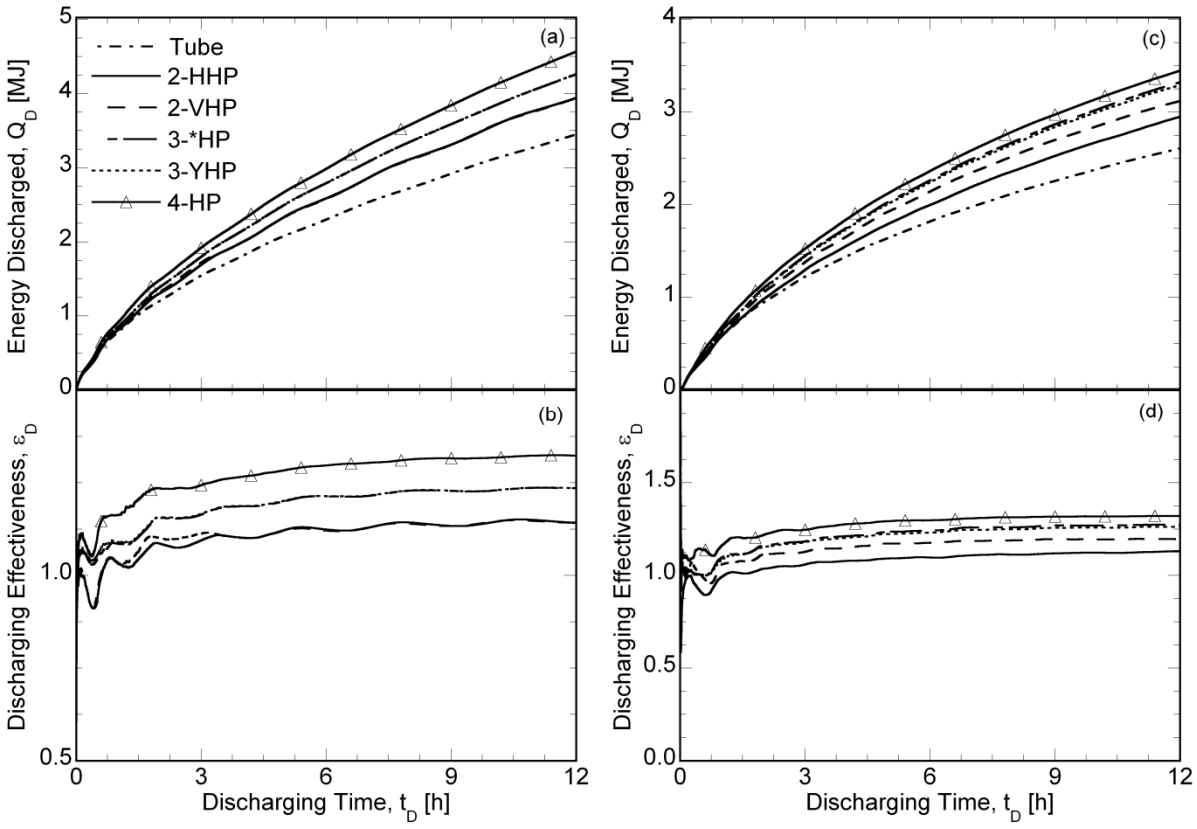

Figure 19: Effect of the arrangement of heat pipes on the energy discharged and discharging effectiveness for (a, b) Module 1 and (c, d) Module 2.

3.6 Optimum Designs

It is instructive to compare the thermal performance of both the modules for all the different types of heat pipe arrangements considered in this study to arrive at an overall best configuration for the storage. To this end, the various configurations and heat pipe arrangements considered are compared in term of three objectives: (1) power charged (discharged), P_C (P_D) defined as the ratio of the total energy stored (discharged) to the charging (discharging) time, (2) the power charged (discharged) per unit volume of the PCM, P_C''' (P_D'''), and (3) power charged (discharged) per unit volume of the PCM per unit heat pipe, $\overline{P_C'''}$ ($\overline{P_D'''}$), which are presented in Table 4. The preferred

Module for each objective is highlighted in italics and the corresponding maximum values of the objective function are listed in bold face.

For both charging and discharging, it was found that though the energy stored (discharged) at the end of charging (discharging), and correspondingly the power charged (discharged) is higher for Module 1, the power density and the power density per unit heat pipe favors Module 2. For charging in Module 1, it was observed that the power charged and power density is greater for the 4-HP arrangement, P_C = 2.65 MJ/h (Table 4a.1) and P_C''' = 27.52 MJ/h-m^3 (Table 4b.1), while the power density per unit heat pipe is greater for the 2-VHP arrangement with $\overline{P_C'''}$ = 12.30 MJ/h-m^3 (Table 4c.1). For discharging in Module 1, the power density is highest for 4-HP arrangement with P_D''' = 3.95 MJ/h-m^3 (Table 4b.1), and the maximum power density per unit heat pipe was found to be equal for both the 2-HP arrangements cf. $\overline{P_D'''}$ = 1.71 MJ/h-m^3 (Table 4c.1). In the case of Module 2, the power charged (discharged) and the charging (discharging) power density were highest for the 4-HP arrangement with P_C (P_D) = 0.98 (0.29) MJ/h (Table 4a.2) and P_C''' (P_D''') = 41.90 (12.40) MJ/h-m^3 (Table 4b.2), respectively, while the charging (discharging) power density per unit heat pipe was greatest for the 2-VHP arrangement, $\overline{P_C'''}$ ($\overline{P_D'''}$) = 18.96 (5.54) MJ/h-m^3 (Table 4c.2). This suggests that though adding heat pipes improved the rate of storage and discharge of energy in the LTES, the 2-VHP arrangement provided the best thermal enhancement per unit heat pipe due to the limited obstruction of the recirculation cells formed in the molten PCM region, as seen from a comparison of the values of $\overline{P_C'''}$ and $\overline{P_D'''}$ for both Modules 1 and 2. Overall, in order to design LTES with high energy transfer capability per charging (discharging) time, Module 1 with 4-HP arrangement is preferred with P_C = 2.65 MJ/h, P_D = 0.38 MJ/h (Table 4a.1) while for maximizing the power density Module 2 embedded with 4-HP is preferred,

Table 4: Optimum configurations obtained from the computational study in Chapter 3

	Charging					*Discharging*				
Objective	*2-HHP*	*2-VHP*	*3-*HP*	*3-YHP*	*4-HP*	*2-HHP*	*2-VHP*	*3-*HP*	*3-YHP*	*4-HP*
a. Maximum power charged (discharged), P_C (P_D)										
1. ***Module 1***	1.74	2.37	2.36	2.37	**2.65**	0.33	0.33	0.36	0.36	**0.38**
2. Module 2	0.69	0.89	0.84	0.88	0.98	0.25	0.26	0.28	0.27	0.29
b. Charging (Discharging) Power density, P_C''' (P_D''')										
1. Module 1	18.06	24.59	24.50	24.61	27.52	3.42	3.42	3.74	3.74	3.95
2. ***Module 2***	29.40	37.92	35.85	37.56	**41.90**	10.65	11.08	11.95	11.52	**12.40**
c. Power density per unit heat pipe, $\overline{P}_C'''$ ($\overline{P}_D'''$)										
1. Module 1	9.03	12.30	8.17	8.20	6.88	1.71	1.71	1.25	1.25	0.99
2. ***Module 2***	14.70	**18.96**	11.95	12.52	13.97	5.33	**5.54**	3.98	3.84	3.10

which yields P_C''' = 41.90 MJ/h-m^3 and P_D''' = 12.40 MJ/h-m^3 (Table 4b.2). In terms of power density per unit heat pipe, Module 2 embedded with 2-VHP yields the highest values at $\overline{P_C'''}$ = 18.96 MJ/h-m^3 and $\overline{P_D'''}$ = 5.54 MJ/h-m^3. The findings of the present study detailed the enhancement in the melting rate of PCM embedded with heat pipes of different orientations for two different configurations of LTES. Future studies will involve a more detailed modeling and analysis of large scale LTES with embedded heat pipes for integration with a CSP plant and subjected to repeated charging and discharging cycles as discussed in Chapter 4 of this dissertation.

3.7 Nomenclature used in Chapter 3

b thickness [m]

c_p specific heat [J/kg-K]

h convective heat transfer coefficient [W/m-K]

h_{sl} latent heat of fusion of PCM [J/kg]

ΔH latent enthalpy [J/kg]

i nodal point

k thermal conductivity [W/m^{2}K]

L length [m]

m number of heat pipes

$\dot{m}$ mass flow rate [kg/s]

n number of computational cell volume elements

P_C power charged [MJ/h]

P_D power discharged [MJ/h]

P_C''' charging energy density [MJ/h-m^3]

P_D''' discharging energy density [MJ/h-m^3]

$\bar{P}_C'''$ charging energy density per unit heat pipe [MJ/h-m^3]

$\bar{P}_D'''$ discharging energy density per unit heat pipe [MJ/h-m^3]

Q_C energy stored in the LTES with heat pipes [MJ]

Q_D energy discharged from LTES with heat pipes [MJ]

$Q_{C,0}$ energy stored in the LTES without heat pipes [MJ]

$Q_{D,0}$ energy discharged from LTES without heat pipes [MJ]

r radius [m]

S_L width of the module [m]

S_T height of the module [m]

T temperature [K]

T_m melting temperature [K]

t time [s]

u x-component velocity [m/s]

v y-component velocity [m/s]

w z-component velocity [m/s]

Subscripts and Superscripts

a adiabatic

c condenser

C charging

D discharging

e evaporator

HP heat pipe

m module

t tube

w wick

Greek Symbols

α thermal diffusivity [m^2/s]

β thermal expansion coefficient [K^{-1}]

ε effectiveness

φ wick porosity

μ dynamic viscosity [kg/m^2-s]

ρ Density [kg/m^3]

γ liquid fraction

Chapter 4: Analysis and Design of a Latent Thermal Energy Storage System with Embedded Gravity Assisted Heat Pipes

This chapter presents a transient numerical model of the present problem is solved and the influence of the design and operating parameters on the dynamic charge and discharge performance of the system is analyzed to identify operating windows that satisfy the SunShot Initiative targets, which include, storage cost less than \$15/kWh$_t$, round-trip exergetic efficiency greater than 95% and charge time less than 6 hours for a minimum discharge period of 6 hours.

4.1 Introduction

The numerical analysis reported in Chapters 2 and 3 for a shell and tube LTES configuration with embedded heat pipes [25], [45], [47] is performed for a single unit module of a large LTES system for single charge and discharge process to provide a quick estimate of the qualitative trends in the performance with respect to the various operational and design parameters. However, LTES integrated to a CSP plant is subjected to repeated sequence of charge and discharge process. A sequence of charge and discharge process is referred to as one cycle and repeated cycles may limit the charge or discharge rate of the LTES system. It is important to understand the dynamic thermal behavior of the LTES with embedded heat pipes (HP-TES) in order to design the storage system for a CSP plant operation.

In developing large scale thermal storage technologies for integration with a CSP plant operation, round-trip energy efficiency is often cited as a key metric of performance; however it is in fact most critical that exergetic efficiency be very high to ensure that heat quality is maintained after storage [48]. Previous investigations focused on LTES have shown that cascading several

PCM's in the order of their decreasing melt temperatures from the hot HTF inlet side can result in higher heat transfer rates, as well as improved exergetic efficiency due to a more uniform temperature difference between the hot and cold media [13], [14], [49]. In 2011, the US Department of Energy launched the SunShot Initiative and has put forth an aggressive research and development (R&D) plan to make CSP technologies cost-competitive with other energy generation sources on the grid by the end of the decade [50]. According to the SunShot vision study, the optimal design of a HP-TES system for integration into CSP plants should have round-trip exergetic efficiency greater than 95% and storage cost less than \$15/kWh$_t$ for a minimum (maximum) discharge (charge) period of 6 h. Integrating a thermal storage system to a CSP plant with the aforementioned characteristics along with technological breakthroughs in other subsystems of the CSP plant has the potential to reduce the levelized cost of electricity generated from CSP to as low as 6 ¢/kWh comparable to fossil-fueled electric power generation.

While modeling of the LTES system with heat pipes has been reported in the literature and provides insight on HP-TES operation [45], [47], designing a large scale LTES system with embedded heat pipes for high temperature power tower CSP plant has not been investigated in the literature. Also, a systematic study to quantitatively determine the optimal design parameters for the dynamic performance of the HP-TES system subjected to constraints dictated by the power plant operation is lacking in the previous studies. In view of this, large scale latent thermal energy storage (LTES) system embedded with gravity-assisted heat pipes is considered in the present study. Gravity assisted heat pipes, which have a simple screen mesh wick to promote uniform liquid distribution within the heat pipes are considered in this chapter due to the low cost and they depend on gravitational force for the return of condensate to the hot temperature (evaporator) end. A transient numerical model of the large scale HP-TES system is developed in this chapter and the

influence of the design and operating parameters on the dynamic charge and discharge performance of the system is analyzed to identify operating windows that satisfy the SunShot Initiative targets, which include, storage cost less than \$15/kWh$_t$, round-trip exergetic efficiency greater than 95% and discharge time less than 6 hours for a maximum charge duration of 6 hours. Based on the parametric studies and specified constraints on the minimum exergetic efficiency, maximum storage capital cost and minimum discharge time, operating windows are identified on the HTF flow velocity as a function of the various design parameters for non-cascaded and cascaded HP-TES system configurations. Overall, a methodology for model based design and optimization based on the systematic parametric studies and consideration of the SunShot requirements [50] on the dynamic operation of the system is presented in this chapter.

4.2 HP-TES Numerical Model

The HP-TES system configuration considered in the present model is shown in Figure 20a. The HTF flow to the storage system is divided equally among the n_d channels where the heat transfer between the HTF and PCM takes place. The schematic of one channel of the heat pipes embedded LTES (HP-TES) system is also shown in Figure 20a. As observed from the front view of the channel in Figure 20c, the height of the channel is represented as H_d, length of the system is represented as L_d while the height of the PCM section is represented as H_p. During charging, hot HTF enters the bottom channel from the left at x = 0 m (Figure 20c) transferring heat to the PCM through the bottom channel wall and heat pipes while cold HTF during discharging enters the top channel from the right at $x = L_d$ (Figure 20a). The channel width is represented by W_d as shown in the side view (Figure 20d). The air gap is provided to accommodate the volumetric expansion of the PCM during melting. A top view of a channel in a HP-TES system showing the arrangement of

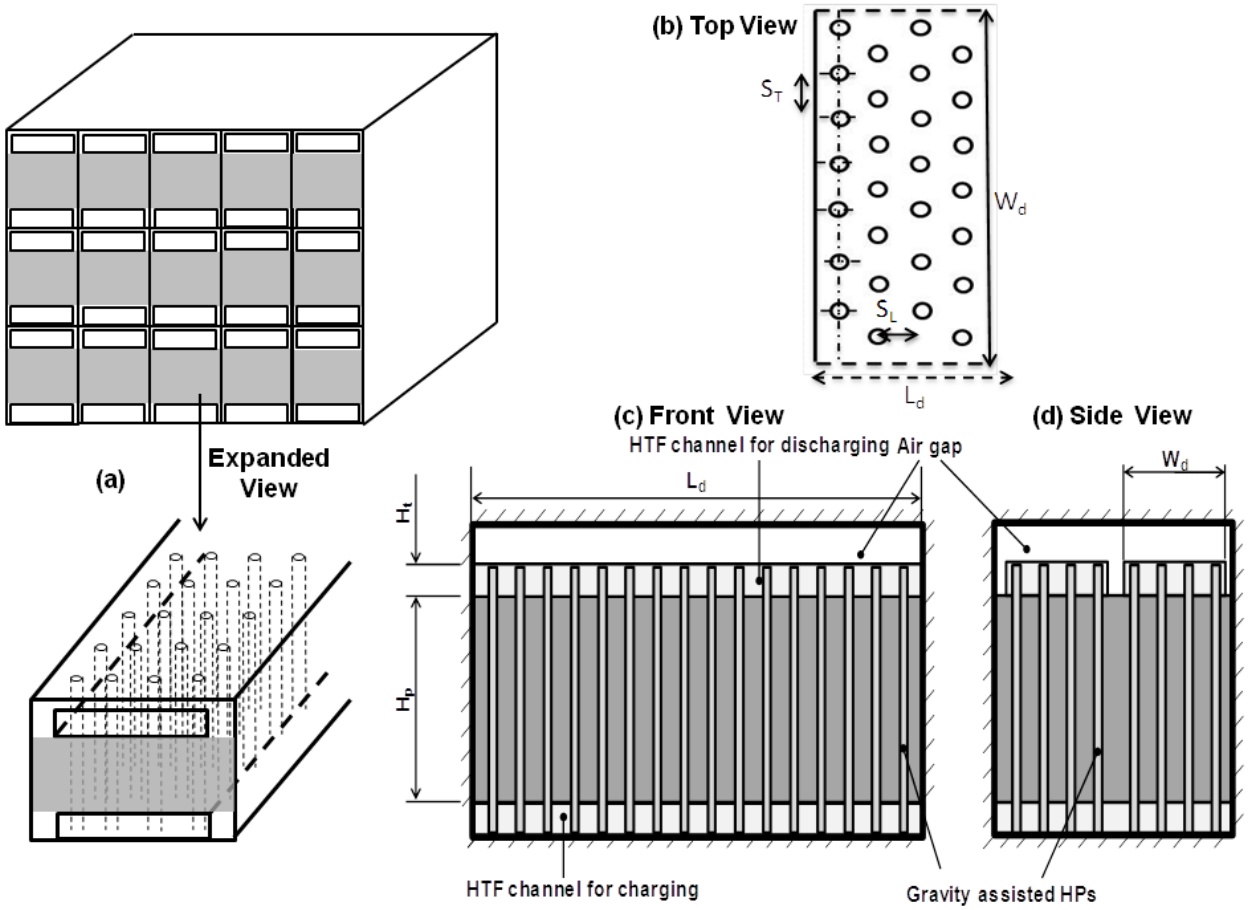

Figure 20: Schematic illustration of: (a) gravity heat pipes embedded latent thermal energy storage system (HP-TES) and an expanded view of HP-TES channel, and (b) top, (c) front and (d) side view of HP-TES channel

heat pipes along the channel length and across the channel width, W_d is depicted in Figure 20b. The transverse pitch, S_T in Figure 20b represents the spacing between adjacent heat pipes across the channel width while the longitudinal pitch S_L in Figure 20b represents the spacing between adjacent heat pipes along the channel length. The arrangement of the heat pipes is staggered in the form of an equilateral triangle such that the transverse and longitudinal pitches are related by $S_L = S_T \times \cos\left(\pi/6\right)$.

The physical phenomena governing the phase change rate of the PCM in the LTES system described in Figure 20 are: forced convection between the HTF and the heat pipes and between the HTF and the channel; conduction within the wick and the walls of the heat pipes; evaporation and condensation heat transfer in the vapor core of the heat pipes; conduction within the tube wall material; free convection within the liquid PCM adjoining the tube and the heat pipes during melting; and conduction within the solid PCM adjoining the tube and heat pipes during solidification.

The governing equation for the HTF along the length of the channel based on conservation of energy can be written as:

$$\rho_f c_f V_i \frac{\partial T_f}{\partial t} + \rho_f c_f V_i U_f \frac{\partial T_f}{\partial x} = \dot{Q}_d + n_{HP}\dot{Q}_{HP} \tag{19}$$

where the subscript *f* represents the HTF. The density and specific heat of the HTF are represented by ρ_f and c_f, respectively while the HTF temperature and volume of the control volume '*i*' are represented by T_f and V_i, respectively in Eq. (19). Two heat transfer pathways between the HTF and the PCM exists, one through the channel wall ($\dot{Q}_d$) and the other through the heat pipes ($\dot{Q}_{HP}$) and the number of heat pipes in each control volume is represented by n_{HP}. The notation U_f in Eq. (19) represents the velocity of the HTF. The spatial variation of HTF is accounted for by discretizing the channel length into n_x rectangular thermal volume elements in the *x*-direction. The transient operation of the heat pipes and the PCM involving heat transfer from the HTF to the PCM through the channel walls and the heat pipes for each of the n_x rectangular thermal elements are solved using a thermal resistance network model as depicted in Figure 21 to calculate $\dot{Q}_{HP}$ and $\dot{Q}_d$. The resistance network approach to solve for the transient operation of the heat pipes is reported in [45], [51] and is repeated here in a concise manner.

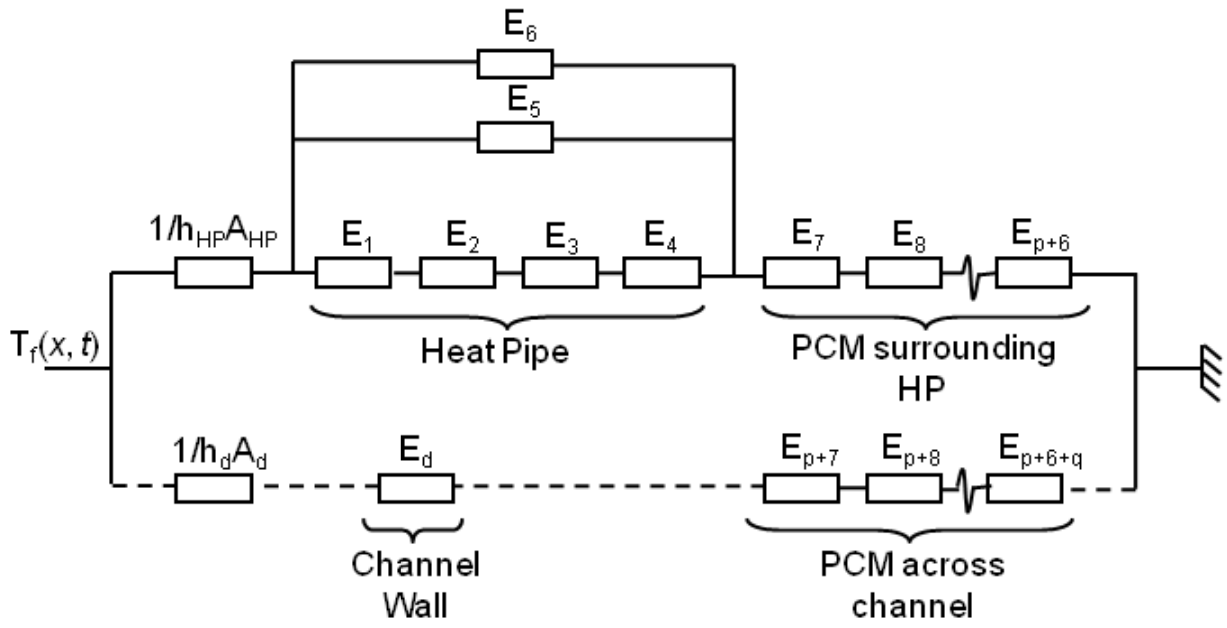

Figure 21: Thermal resistance network of HP-TES system.

Figure 21 shows the thermal resistance network for the HP-TES system. Thermal energy is transferred between the HTF at temperature T_f (x, t) (Eq.(1)) and the liquid (solid) PCM through the heat pipes (the solid lines of the network in Figure 21) and the channel wall (the dashed lines of the network in Figure 21), which are represented in Figure 21 as two parallel thermal resistance networks from the HTF to the PCM.

For any thermal element E_i in the network, Figure 21, an overall energy balance dictates that the rate of increase of thermal energy stored in the control volume equals the difference in the rate at which thermal energy enters the control volume and the rate at which thermal energy leaves the control volume, which can be represented in mathematical form as:

$$\rho_i c_{p,i} V_i \frac{dT_i}{dt} + \rho_i h_{sl,i} V_i \frac{d\gamma_i}{dt} = \left[\frac{(T_{i,1} - T_i)}{R_{i,1}} - \frac{(T_i - T_{i,2})}{R_{i,2}} \right] \tag{20}$$

where the density, specific heat and volume of the element E_i are represented by ρ_i, $c_{p,i}$ and V_i, respectively, the first and second terms within square brackets on the right hand side of Eq. (20)

represent the rates of energy transferred in to and out of the thermal element, respectively, in which, the temperatures $T_{i,1}$ and $T_{i,2}$ represent the surface temperatures at either end of the heat conductor element, and T_i denotes the temperature at the middle of the thermal element (Figure 21). h_{sl} represents the latent heat of fusion of the PCM denoted by elements E_7-E_{p+q+6} (Figure 21) and takes the values of zero for the remaining thermal elements, while γ represents the PCM melt fraction. The last term on the left hand side of Eq. (20) represents the latent heat evolution of the PCM, which is modeled using the fixed-grid enthalpy approach as presented by Voller et al. [43].

The resistances for the heat pipe elements represented by thermal elements E_1–E_6 in Figure 21 are detailed in Ref. [45] and are not discussed here in the interest of brevity. The resistances for the PCM region across the channel wall represented by elements E_{p+7}–E_{p+6+q} can be represented as $R_{i,1} = R_{i,2} = \frac{\ell_i}{k_i A_i}$, where $\ell_i = \frac{(L_a - w_d)}{q}$ is the thickness of each discretized element in the *y*-direction (Figure 20) in which q represents the number of discretized planar elements across the channel length for an adiabatic heat pipe length of L_a, k_i is the thermal conductivity of PCM and A_i is the cross-sectional area of the element (after accounting for area reduction due to the heat pipes) normal to the flow direction: $A_i = \left\{ \frac{W_d L_d}{n_x} - n_{HP} \pi R_{HP}^2 \right\} \ell_i$. The thermal resistances for heat conduction elements (E_7–E_{p+6}), representing the PCM in the annular region surrounding the condenser section of the heat pipes for maximum theoretical radius, r_{max} of $r_{max} = S_T \sqrt{\sin(\pi/3)/\pi}$, are evaluated based on an analysis of the radial conduction heat transfer through the elements as explained in Ref. [45]. The subscript p in E_{p+6} denotes the number of discretized radial elements surrounding the heat pipes determined based on a grid sensitivity study. The thermal element, E_d

represents the channel wall. A derivation of the resistance network modeling was reported in Chapter 2.

The convection heat transfer coefficients (h_t and h_{HP}) and the *enhanced* thermal conductivity of the PCM (k_i for i = 7–11 and 13–17) due to the free convection effects during charging are implemented using appropriate correlations from the literature ensuring their applicability over the range of dimensionless parameters considered in this study. For HTF flow inside the rectangular channel, the correlation provided by Gnielinski [29], which is valid over a large Reynolds number range including the transition region, is used to determine h_t. Forced convection heat transfer also occurs between the HTF and the evaporator sections of the heat pipe. Since the HTF flows normal to the axis of the circular heat pipe, the Zukauskas correlation [29] developed for a staggered tube bank in cross flow is used to define h_{HP}.

The buoyancy driven natural convection currents during the PCM melting cannot be captured using the thermal resistance network model but the increase in the rate of progression of the melt front is captured by an enhanced thermal conductivity of the PCM melt. During the charging cycle, the thermal conductivity of the PCM elements, k_i for i = 7–(p+6) and (p+7)–(p+6+q) (Figure 21), is replaced by an enhanced thermal conductivity to account for the natural convection effects in the augmenting the heat transfer. The natural convection effects during the melting of PCM are modeled using empirical correlations to determine the *enhanced* thermal conductivity of the PCM melt front (k_i for i = 7–(p+6) and (p+7)–(p+6+q)). Two types of melt domain shapes can be formed. The first domain is nominally planar adjacent to the channel wall and the effective conductivity is evaluated using the correlation in Ref. [29]. The second type in the annular region of the heat pipes is a predominantly vertical melt domain consisting of hot inner cylinder and a surrounding nominally circular cold surface. For the vertical melt domain, since the thickness of

the liquid layer is very small initially, heat transfer across the liquid layer occurs primarily by conduction although ultimately, convection becomes important as the melt region expands. Therefore, heat transfer through the melt is calculated by evaluating both (i) a conduction heat transfer rate and (ii) a rate associated with use of a correlation for free convection in a vertical annulus [32]. The expression that yields the largest heat transfer rate was used in the computations.

The energy charged (discharged) by the PCM at any instant of time is composed of sensible energy and latent energy components calculated as the summation of energy stored in all the PCM thermal elements which can be determined from the following expressions:

$$Q_d = \sum_{i=p+7}^{p+6+6} \left[\rho_p c_p (T_i - T_D) + \rho_p h_{sl} \gamma_i\right] \times \left[\pi \left(r_{i,2}^2 - r_{i,1}^2\right) W_d \ell_i - n_{HP} \pi R_{HP}^2 \ell_i\right] \tag{21a}$$

$$Q_{HP} = \sum_{i=7}^{p+6} \left[\rho_p c_p (T_i - T_D) + \rho_p h_{sl}\right] \times \left[\pi \left(r_{i,2}^2 - r_{i,1}^2\right) L_c\right] \tag{21b}$$

where the energy stored (discharged) within (from) the melt (solid) front of the PCM in the vicinity of the channel and heat pipes are represented by Q_d and Q_{HP}, respectively and the terms within the second set of square brackets in the above expressions represent the volume of each element V_i and L_c is the condenser length of the heat pipes. The heat transfer rate between the HTF and the PCM through the channel wall and heat pipes as required in Eq. (19) can be calculated from $\dot{Q}_d = Q_d / \Delta t$ and $\dot{Q}_{HP} = Q_{HP} / \Delta t$ where Δt is the time step size.

The coupled system of governing equations is solved by implicit method and the convective term appearing in Eq. (19) is discretized using the second-order upwind differencing scheme. The iterative residuals are converged to the order of 10^{-10} at each time step and a grid interval size of 0.2 m along the channel length such that $n_x = 5 \times L_d$ and a time step of 30 s is chosen after examining the results of grid sensitivity study. Based on grid sensitivity study, a total of p = 10 planar thermal elements and q= 10 radial thermal elements are chosen to discretize the PCM across

the channel width and surrounding the heat pipes. For a channel length of L_d = 40 m, the complete system including the HTF, heat pipes, channel wall and PCM is discretized into 54000 thermal volume elements for which the temperature and melt fraction is solved for. Sodium-Stainless steel heat pipe is used for the present analysis [24] while solar salt (60 wt. % $NaNO_3$ and 40 wt. % KNO_3) is used as the HTF [50]. Table 5 lists the geometrical and thermophysical properties of the heat pipe and HTF used in the simulations. The key PCM property parameter that is considered in this study is the melt temperature of PCM. The other design parameters that are considered in this study are the longitudinal spacing between the heat pipes, length, width and height of the channel, the condenser and evaporator length of the heat pipes. The default values corresponding to the design variables are listed in Table 5. The default PCM thermophysical properties chosen for this study are in par with the molten salt PCM values reported in the literature [52].

4.3 HP-TES Storage Cost Model

The storage cost of the HP-TES system, α is calculated assuming that the system is designed for integration with a 100 MW_e (270.58 MW_t) power plant operation. The mass flow rate required to meet the design thermal power output corresponds to 635.18 kg/s. For the default HP-TES system design configuration as listed in Table 5 and for HTF flow velocity of 2.53 mm/s, which corresponds to a mass flow rate of, $\dot{m}$ = 1 kg/s (Table 5) through a single channel, a total of 636 channels is required to meet the power requirement.

The storage cost of HP-TES system can be expressed as the ratio of summation of storage material cost (HTF and PCM), container cost, heat pipes cost, overhead cost and the total storage capacity of the LTES. The overhead cost, accounting for the miscellaneous costs such as electrical, instrumental, piping, valves and fitting costs is assumed to be 10% of the storage material,

Table 5: Default geometrical parameters and thermophysical properties of heat pipes, HTF and PCM considered in Chapter 4

a. Heat Pipe and channel Parameters			
Heat pipe radius, r_{HP} [m]	0.009	Channel width, W_d [m]	0.800
Heat pipe wall thickness, b_{HP} [m]	0.001	Channel height, H_d [m]	0.250
Heat pipe wick thickness, b_w [m]	0.001	Channel wall thickness, w_d [m]	0.003
Wick porosity, φ	0.900	Channel length, L_d [m]	30.0
Condenser length, L_c [m]	0.800	Longitudinal spacing, S_L [m]	0.040
Evaporator length, L_e [m]	0.200	PCM storage height, H_p [m]	0.834
Adiabatic length, L_a [m]	0.042		
Wick thermal conductivity, k_i [W/m-K] (i = 2,3,5)	46.05		
Wick heat capacity, $\rho_i c_{p,i}$ [J/m^3-K] (i = 2,3,5)	2.06×10^6		

b. Other Properties	PCM	HTF (Solar Salt)	Stainless Steel
Density, ρ [kg/m^3]	1975.5	1975.5	7900
Thermal conductivity, k [W/m-K]	0.5	0.55	20.1
Specific heat, c_p [J/kg-K]	1500	1500	559.9
Dynamic viscosity, μ [Pa-s]	0.002	0.002	–
Melting temperature, T_m [^{o}C]	503	–	–
Thermal expansion coefficient, β[K^{-1}]	200×10^{-6}	–	–
Latent heat of fusion, h_{sl} [kJ/kg]	213	–	–

container and heat pipes cost. The storage material cost can be calculated as: $\left\{\rho_f \left(W_d L_d H_d - n_{HP} L_e \pi R_{HP}^2\right) C'_{HTF} + \rho_p \left[W_d L_d H_p - N_{HP}(L_c + L_a)\pi R_{HP}^2\right] C'_{PCM}\right\} \cdot n_d$ where the PCM cost per unit mass (C'_{PCM}) is assumed to be \$0.75/kg [52] and the HTF cost per unit mass (C'_{HTF}) used inthe molten salt power tower CSP plant is taken to be \$1.23/kg [53]. The heat pipes cost is calculated as $n_{HP} \cdot C_{HP}$. The unit cost of a heat pipe with a sintered metal powder wick is obtained from Ref. [54] to be \$5 for total of 100 heat pipes and is available at a discounted pricing for quantities greater than that. Also, the gravity assisted heat pipes only require simple screen mesh wicks for which the cost is even lower and a unit cost of \$2, similar to that of thermosyphon cost [55] is assumed in the present analysis. The LTES container cost encompasses the material cost of the stainless steel (321 SS), foundation cost and the insulation cost: $2 \cdot \rho_{SS} L_d w_t \left(H_t + W_t\right) \cdot C'_{SS} + 2 \cdot L_d \left(H_t + W_t\right) \cdot C''_I + W_t L_d \cdot C''_F$ where the subscript *SS* refers to stainless

steel, the density of which is taken as $\rho_{SS} = 7{,}900 kg/m^3$ and w_t refers to the thickness of the storage tank, which is assumed to be 0.038 m. The cost per kg of stainless steel is obtained to be \$5.43/kg from [56] , the calcium silicate insulation cost is assumed to be \$235/m^2 [57], and the foundation cost is taken as \$1,210/m^2 [2]. The cost values reported here are consistent with the values of two-tank molten salt thermal storage system reported in [57]. The height of the storage system, H_t (Figure 20c) is taken as 20 m, and the storage width W_t, required to accommodate the n_d channels can be calculated from the dimensions of the channel considered. The HTF channel cost comprises the material and the welding cost and can be calculated from: $\rho_{SS} L_d W_t w_d n_d \times C'_{SS} + n_d L_d \times C_W$, where the welding cost, C_W is taken as \$20.45 per unit length of the channel as reported in Ref. [55]. Employing the above cost rates, for a two-tank molten salt thermal storage system shows a total cost of \$26.72/kWh$_t$, which is almost equal to the cost of \$27/kWh$_t$ employed in SAM [58].

4.4 Performance Metrics

The dynamic performance of a HP-TES system installed in CSP plants subjected to partial charge and discharge process is of primary interest to the designer, which is analyzed in the present study. The HTF exiting the system during discharging (charging) is fed into the power block (solar field) for superheat steam generation (thermal capture). The strong dependence of the power block Rankine cycle efficiency on the incoming HTF temperature [58] requires the termination of discharge process when the HTF exit temperature reaches a certain minimum discharge cut-off temperature, T'_D. The charging cut-off temperature determines the extent to which the HP-TES system can be charged. This value is limited by the maximum flow rate achievable by the HTF pumps that pump HTF through the tall receivers. The relationship between

these parameters is not easily determined. Generally, a high discharge temperature will force a high flow rate through the receiver, which increases parasitic and thermal losses while increasing the capacity of the storage. In the present study, T'_C and T'_D are selected to be 400 C and 500 C respectively representative of restrictions imposed on power tower CSP plant operation [58].

The HP-TES is subjected to cyclic charge and discharge process until a periodic quasi-steady state is reached, when the variations in performance metrics and model output from one cycle to another are less than 0.5%. During the cyclic operation, the charging temperature profile of the first process becomes the initial condition of the subsequent discharge process which in turn becomes the initial condition of the next charge process and so on. The numerical computation started from a charge process with hot HTF entering from the left of the channel, $x = 0$ at $T = 574^\circ C$. Charging is continued until the temperature of the cold HTF exiting the tank at $x = L_d$ from the bottom of the channel and entering the solar field reached $400^\circ C$ or until the charge time of 6 hours. This is followed by the discharging process with cold HTF entering from the right of the top channel, $x = L_d$ at $T = 290^\circ C$, which is continued until the temperature of the HTF exiting the channel at $x = 0$ m reaches $500^\circ C$. Typically, it requires four cycles of operation for the system to reach quasi-steady state for the range of parametric values considered in this study.

The inputs to the model are the various design parameters listed in Table 5, HTF inlet mass flow rate and the inlet HTF temperature during charging (T_C = 574 $^\circ$C) and discharging (T_D = 290 $^\circ$C). The model outputs include the spatial, temporal variation of the HTF and PCM temperature; spatial and temporal variation of the melt fraction within the PCM. The key performance metrics analyzed in the present study are the steady state discharge time, t_D [h], storage capital cost per unit thermal energy, α [\$/kWh$_t$], the steady state exergy efficiency, ζ and the overall exergetic

efficiency, ζ averaged over the entire cyclic operation of the HP-TES until it reaches steady state. The exergetic efficiency of the storage system is defined as [48]:

$$\zeta = \frac{\int_{t_C}^{t_D} \dot{m}_f c_f \left\{ T_f(x=0,t) - T_D - T_{ref} \ln\left(\frac{T_f(x=0,t)}{T_D} \right) \right\} .dt}{\int_{0}^{t_C} \dot{m}_f c_f \left\{ T_C - T_f(x=L_d,t) - T_{ref} \ln\left(\frac{T_C}{T_f(x=L_d,t)} \right) \right\} .dt} \tag{22}$$

where $\dot{m}_f$ is the mass flow rate of HTF and T_{ref} is the reference or ambient temperature which for the purpose of the analysis is assumed to be 300 K [48]. The term, T_{f} (x = 0) in the numerator refers to the exit temperature of the HTF through the top channel at the left of the HP-TES system during discharging while the term T_{f} ($x = L_{\text{d}}$) in the denominator refers to the temperature of the HTF exiting the bottom channel at the right of the LTES, which is the outlet for charging. The numerical model presented in this section forms the basis of the parametric studies discussed in Section 4.4.

4.5 Results and Discussion

Figure 22a shows the longitudinal variation of HTF temperature at the end of charging and discharging of each cycle for non-cascaded HP-TES system with default parametric values. As observed from Figure 22a, the storage system reaches a quasi-steady state at the end of cycle 4 as seen from the negligible variation in the HTF temperature and magnitude and variation between cycles 3 and 4. The same phenomenon of the achievement of cyclic periodicity is also observed for 2-PCM and 3-PCM cascaded HP-TES systems as portrayed in Figure 22e and i respectively. Figure 22b and c depicts the temporal evolution of the HTF (solid lines) and the average PCM temperature (dashed lines) along the length of the non-cascaded HP-TES system with default parametric values for charging and discharging, respectively during the fourth (periodic) cycle of

operation. The temperature profile at time t = 0 h in Figure 22b, corresponds to the end of the discharge process of the previous (third cycle), which is clearly evident by the fact that the HTF temperature at x = 0 m (discharge outlet) remains at $500^{\circ}C$, corresponding to the discharge cut-off temperature. There is as much as 5% temperature difference between the HTF in the channel and the PCM at any axial position. The constant temperature zones at the top and bottom of Figure 22b at t = 3.0 h correspond to the high and low temperatures, respectively. The constant temperature zone in between the two regions corresponds to the PCM melt temperature, implying latent heat exchange, while the sloped temperature lines between the constant PCM melt temperature and the high temperature zone and the low temperature zone refers to sensible heat exchange between HTF and PCM (Figure 22b). Although the exit temperature of the HTF at x = 30 m does not reach the charging cut-off temperature ($T_C^{'} = 400^{\circ}C$), charging is concluded at the maximum charge time of 6 h (Figure 22b). Figure 22c shows the subsequent discharge process and the temperature profile of the HTF and PCM at t = 0 h is similar to the temperature profile at the end of the charge process in Figure 22b. At t = 3.3 h, the HTF exit temperature decreases from the highest temperature as all the hot HTF stored during the previous charge process is dispatched and the energy stored in the PCM at the highest temperature is extracted. Subsequently, the HTF exit temperature reaches the discharging cut-off temperature at t = 6.6 h and the discharge process is terminated. The conduction dominated PCM solidification results in a longer discharging time compared to charging in spite of the higher thermal drive force (T_D-T_m) for PCM solidification. Figure 22d, portraying the temporal variation of melt fraction within the PCM during the cyclic discharge process shows a latent utilization of14.95%, which can be visualized as the area occupied between the melt fraction contours at the start (t = 0 h) and end (t = 6.6 h) of discharge process in Figure 22d.

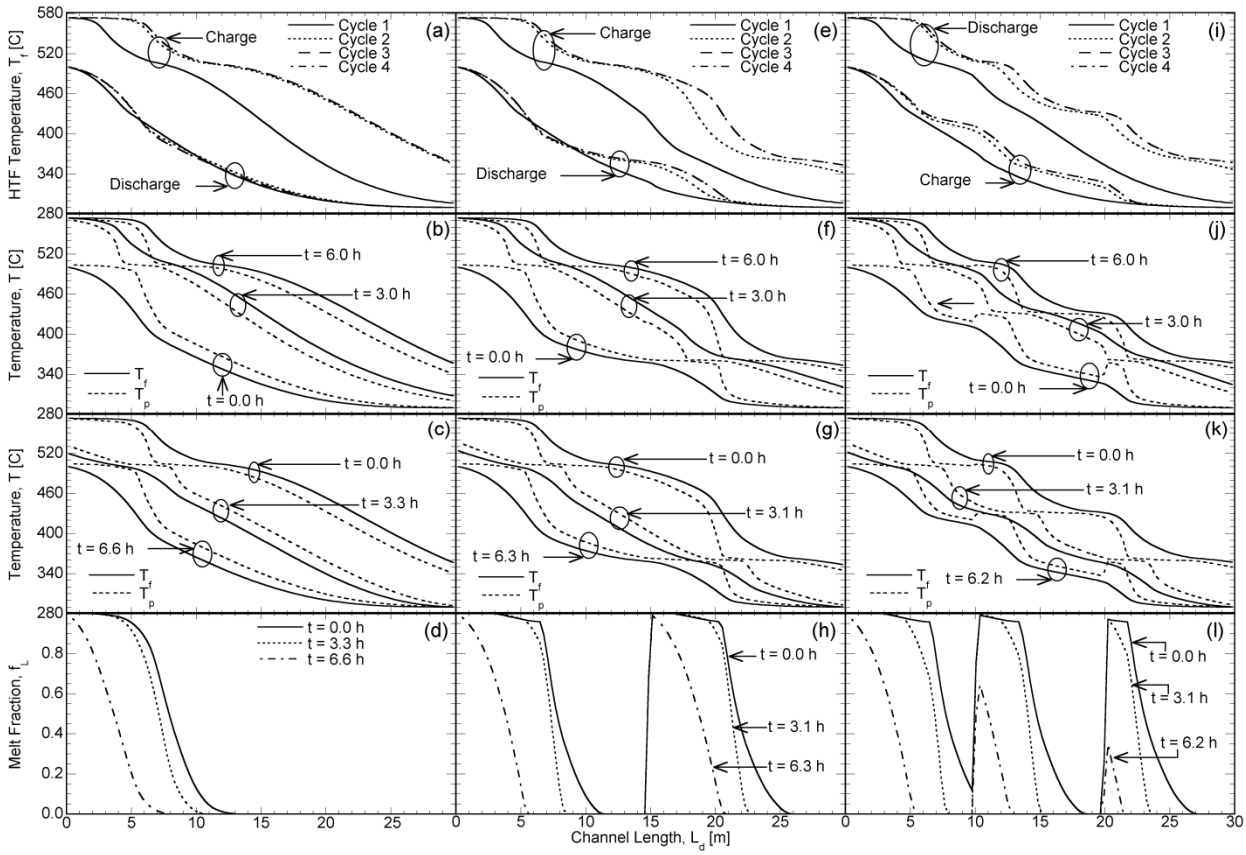

Figure 22: Axial distribution of HTF temperature, at the end of each successive charging and discharging cycles for (a) 1-PCM, (e) 2-PCM and (i) 3-PCM cascaded HP-TES system configurations. Temporal evolution in the axial distribution of HTF (solid lines) and PCM (dotted lines) temperature during the charging and discharging process, respectively of cycle 4 for (b, c) 1-PCM, (f, g) 2-PCM and (j, k) 3-PCM cascaded HP-TES system configurations. Temporal evolution in the axial distribution of PCM melt fraction during the discharge process of cycle 4 for (d) 1-PCM, (h) 2-PCM and (l) 3-PCM cascaded HP-TES system configurations.

In the same manner, Figure 22f–g and Figure 22j–k represents the temporal temperature profile of the HTF and PCM during the charge and discharge process of 2-PCM and 3-PCM cascaded configuration, respectively. For 2-PCM and 3-PCM cascaded configurations the entire length of the channel is divided equally into two and three zones, respectively. Similar trends as found in non-cascaded HP-TES system is observed except that two and three constant melt temperature zones are observed in Figure 22f–g and j–k respectively, corresponding to the number of different

PCM's installed in the system. For instance, at t = 3.0 h and 6.0 h in Figure 22f and g, constant melt temperature zones at $T_{m,L}$ = 503 C and $T_{m,L}$ = 361 C corresponding to the melt temperature of the left and right zone are observed, while constant temperature zones at $T_{m,,L}$ = 503 C, $T_{m,M}$ = 432 C, $T_{m,R}$ = 361 C corresponding to the top, middle and bottom zones, respectively are seen in Figure 22j and k at t = 3.0 h and 6.0 h. The discharge process is faster in comparison to 1-PCM non-cascaded configuration due to better utilization and heat transfer rate between the HTF and PCM. This is clearly evident from the discharge time of 2-PCM and 3-PCM cascaded configuration, t_D = 6.3 h (Figure 22g) and t_D = 6.2 h (Figure 22k) compared to t_D = 6.6 h (Figure 22c) for the 1-PCM non-cascaded configuration. The improvement in the HP-TES system performance is observed to decrease, as the number of PCM's cascaded is increased from two to three. Between the melt fraction contour variations observed for 2- and 3-PCM cascaded configurations in Figure 22h and l, the latent utilization of the system is observed to increase from 26.56 % to 38.15 %, respectively. Although, cascaded configurations show a better latent utilization due to improvement in heat transfer rate between the HTF and PCM, the discharge time decreases, which is supposed to be maximized to meet SunShot requirements. Due to the absence of marked difference in performance metrics with cascading, only non-PCM and 2-PCM cascaded HP-TES systems are explored in this study.

Figure 23a–c presents the steady state discharge time, charge time and exergetic efficiency, respectively of non-cascaded HP-TES configuration for channel length of 20 m and compared with the results obtained for channel length of 40 m in Figure 23d–f. Overall, it is found that the discharge time in Figure 23a and d increases with increase in HTF flow velocity and then decreases, concomitant with the decrease of charge time in Figure 23b and e as the exit temperature during the charging process reaches the cut-off temperature, $T_C^{'}$ before the 6 hour

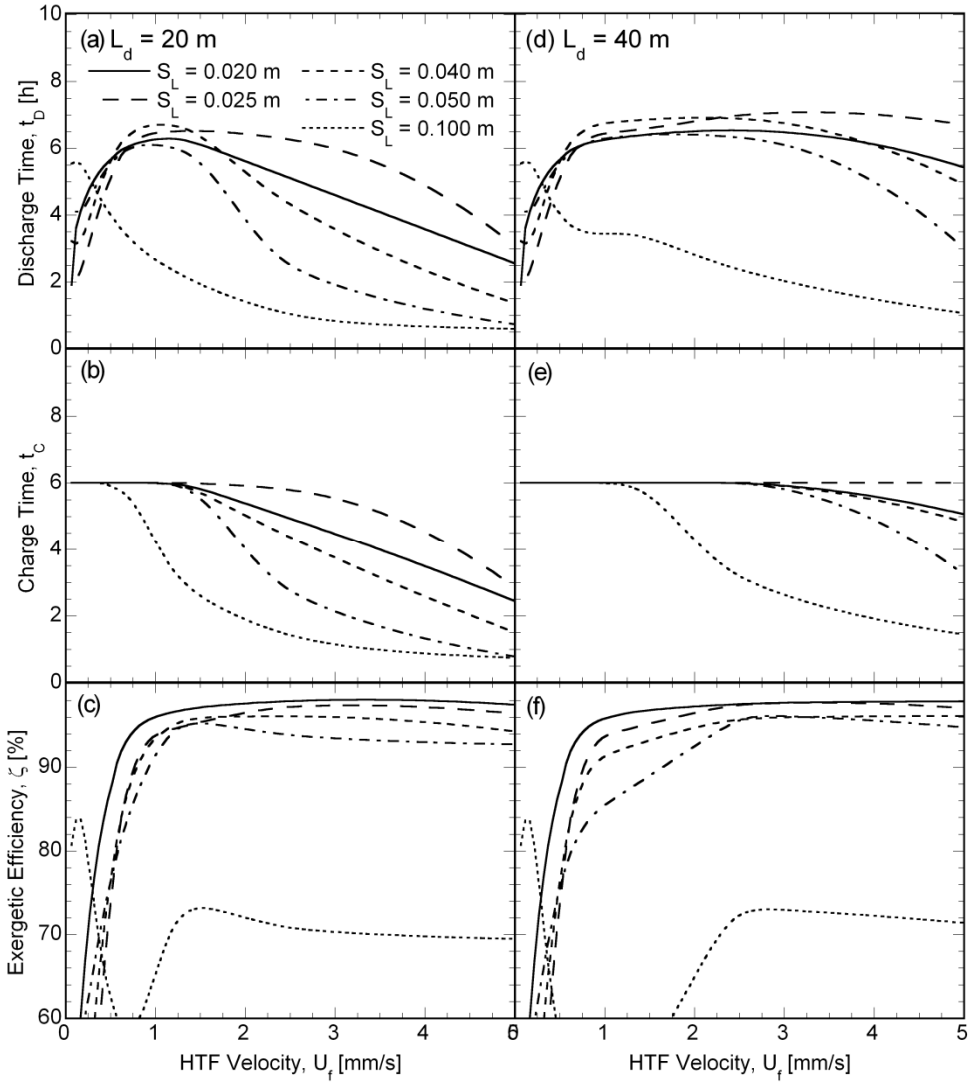

Figure 23: Effect of longitudinal spacing between the heat pipes and HTF flow velocity on (a, d) charge time, (b, e) discharge time, (c, f) exergetic efficiency for channel lengths of 20 m and 40 m, respectively for non-cascaded HP-TES system.

charge duration. As the longitudinal spacing between the heat pipes increases from 0.020 m to 0.025 m, the discharge time greater than 6 h is found for higher HTF flow velocities due to increase in storage capacity as a result of the reduction in the number of heat pipes. With further increase in longitudinal spacing between the heat pipes and subsequent reduction in the number of heat pipes, not enough heat pipes are present for efficient heat exchange between the HTF and PCM and the discharge time is found to be greater than 6 hours only for narrow region of low HTF

velocities. However, it is instructive to note that the highest discharge time (t_D = 6.75 h) is obtained for a longitudinal spacing of 0.04 m for HTF flow velocity of 1.27 mm/s. With increase in channel length, as observed from Figure 23d, the HTF velocity at which the discharge time is maximum increases, resulting in a broad band of mass flow rate for which the discharge time of HP-TES system is greater than 6 hours. The broader bandwidth obtained for longer channel lengths can be addressed by observing that the charge time in Figure 23e decreases from 6 hours only at higher HTF velocities due to increase in flow length (storage capacity) as a result of which the charge cut-off temperature is attained before the 6 hour maximum charge duration. The highest discharge time of t_D = 7.02 h is obtained for S_L = 0.025 m, at HTF flow velocity of U_f = 2.53 mm/s (Figure 23d).

The exergetic efficiency follows the same trend as the discharge time in that it increases with increase in HTF velocity, reaches a maximum and then decreases to almost a constant value for a given longitudinal spacing as portrayed in Figure 23c and f. At lower HTF flow velocities, the exergy charged is higher (longer charge time), while as the charging cut-off temperature is reached for higher HTF flow velocities, the exergy charged is relatively lower leading to a higher exergetic efficiency at higher HTF flow velocity. Smaller longitudinal spacing and hence a closer spacing between the heat pipes shows better exergetic efficiency, due to the concomitant increase in heat exchange rate between the HTF and PCM with large number of heat pipes, resulting in a uniform temperature difference between the HTF and PCM. The exergetic efficiency reaches a constant value at higher HTF flow velocities, due to equal discharge and charge times as observed from Figure 23a and b, respectively. Due to the shorter residence time of the incoming HTF in the HP-TES system at higher flow velocities, heat exchange between the HTF and PCM hardly occurs and eventually the discharge time of the HP-TES system is equal to the time taken for the fluid to

travel the length of the channel at the velocity specified by the HTF mass flow rate and the cross section area of the channel. For a given HTF flow velocity, the convective heat transfer co-efficient for a heat pipe bank decreases from S_L = 0.04 m to S_L = 0.05 m. A combination of large number of heat pipes and a higher heat transfer co-efficient leads to a higher exergetic efficiency with decrease in S_L for any given mass flow rate (Figure 23c and f). Figure 23c shows that the exergetic efficiency decreases monotonically with HTF flow velocity for all the values of S_L. For any given HTF velocity, the exergetic efficiency as observed in Figure 23c and f, is higher for a small S_L due to the large number of heat pipes per unit channel length improving the heat transfer rate between the HTF and PCM leading to slower decay of HTF exit temperature and subsequent delivery of high quality energy for power generation.

Since the discharge time and the exergetic efficiency are of primary interest to the designer, the variations in steady state discharge time and exergetic efficiency for different values of condenser length (L_c), channel height (H_d) and evaporator length (L_e) respectively are plotted as function of the HTF flow velocity in Figure 24 for a channel length of 30 m. Figure 24a and d illustrates the steady state discharge time and exergetic efficiency of the non-cascaded HP-TES system for different values of condenser length. It is observed that the discharge time increases with increase in Reynolds number from a low to intermediate value, reaches a maximum and then decreases with further increase in Reynolds number. For a given Reynolds number, the discharge time is found to increase with increase in condenser length. As the condenser length increases, the surface area for melting and solidification of the PCM in contact with heat pipes increases leading to an improved heat transfer rate between the HTF and PCM and concomitantly longer discharge time is reported. Hence the maximum discharge time increases with increase in condenser length as seen in

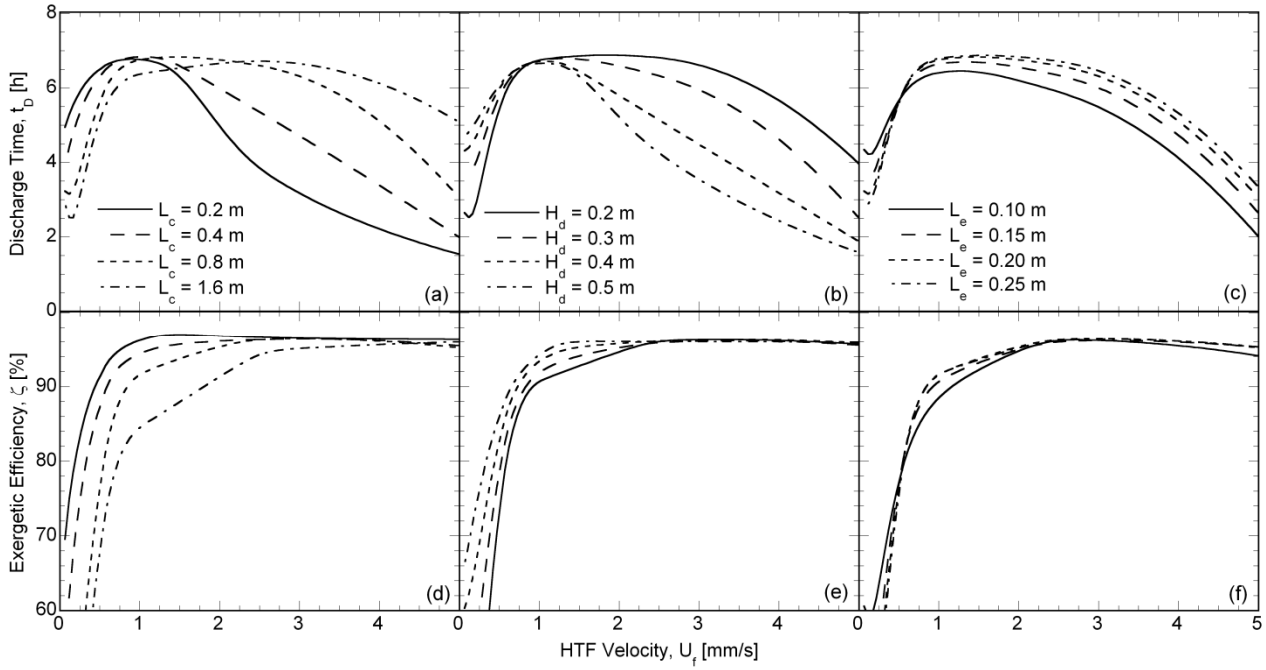

Figure 24: Variation in charge time and exergetic efficiency, respectively for different (a, d) condenser lengths, (b, e) channel heights and (c, f) evaporator lengths with HTF flow velocity for non-cascaded HP-TES system of channel length 30 m.

Figure 24a. Also, it is observed that with increase in condenser length the HTF flow velocity at which the discharge time is maximum increases, resulting in a broad band of mass flow rate for which the discharge time of HP-TES system is greater than 6 hours. The exergetic efficiency follows the same trend as the discharge time in that it increases with increase in HTF velocity, reaches a maximum and then decreases to almost a constant value for a given condenser length as portrayed in Figure 24d. At lower HTF velocity, the exergy charged is higher, while as the charging cut-off temperature is reached for higher HTF velocity, the exergy charged is relatively lower leading to a higher exergetic efficiency at higher HTF velocity. For higher HTF velocity, smaller condenser length shows better exergetic efficiency, due to the reduced thermal resistance to heat transfer, albeit, the smaller surface area of interaction.

For a given HTF flow velocity, with increase in channel height (Figure 24b) and channel width, the mass flow rate increases. Hence, with increase in channel height, the convective heat transfer coefficient increases resulting in a faster discharge time at higher HTF flow velocities. But at lower HTF velocity (U_f < 1 mm/s), when the convective heat transfer coefficient is low, it is observed that discharge time increases with increase in channel height due to higher thermal inertia. Smaller channel height possess wider band of Reynolds number with discharge time greater than 6 h and the discharge time is found to be the higher for a smaller channel height, which correspond to smaller mass flow rate per unit channel and longer residence time of the incoming HTF for heat exchange with PCM. For the same reasons, the exergetic efficiency in Figure 24d shows the same variations and is higher for a smaller channel height. The increase in channel width (not illustrated here) does not have an impact on the discharge time and exergetic efficiency due to the increase in the number of heat pipes as well to accommodate the increase in PCM volume. The discharge time increases with increase in evaporator length (Figure 24c) due to increase in surface area of interaction between the HTF and heat pipes for convective heat transfer. At lower HTF velocities, when the convective heat transfer coefficient is low, the discharge time decreases with increase in evaporator length due to decrease in storage capacity as a result of reduced HTF volume, which is occupied by larger heat pipes. The exergetic efficiency portrayed in Figure 24e shows similar variations as the discharge time due to the aforementioned reasons. Among all the design parameters, namely channel height (H_d), channel width (W_d), channel length (L_d), longitudinal spacing (S_L), evaporator (L_e) and condenser length (L_c), studied for non-cascaded, 2-PCM cascaded and 3-PCM cascaded configurations, the highest discharge time of t_D = 7.02 h is obtained for non-cascaded configuration for S_L = 0.025 m with exergetic efficiency of 97.59% and latent utilization of 18.74 % compared to t_D = 6.93 h obtained for 2-PCM cascaded

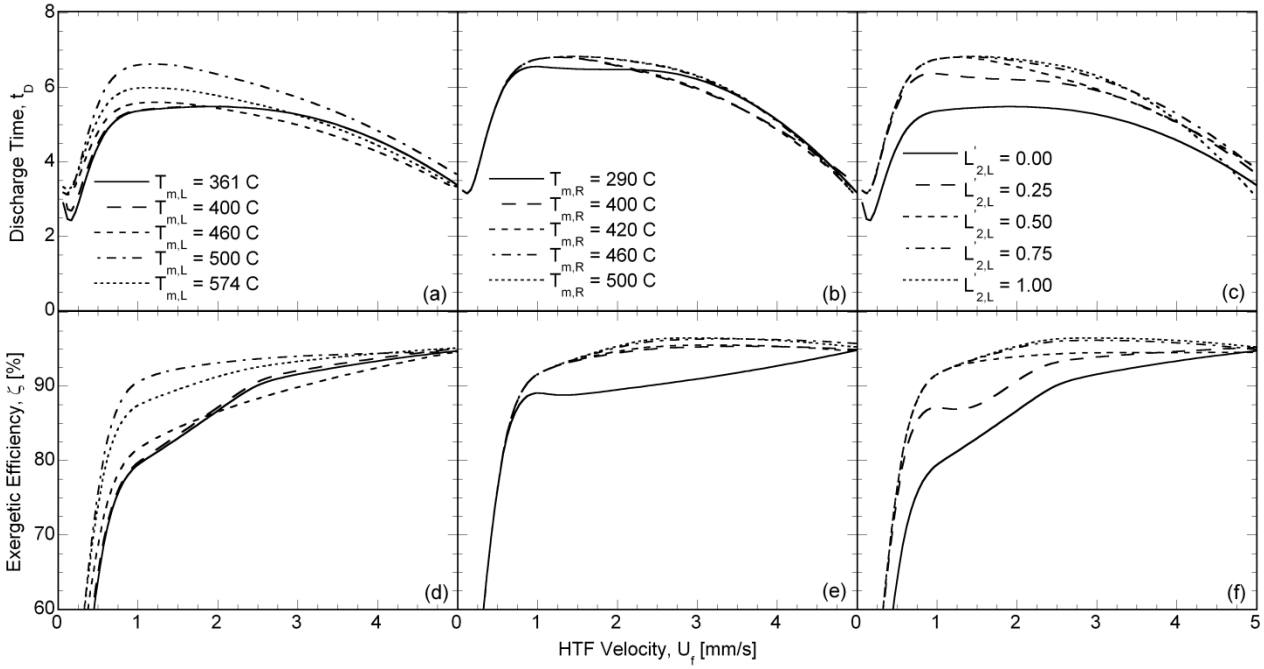

Figure 25: Variation in charge time and exergetic efficiency, respectively for different (a, d) left zone PCM melt temperature, (b, e) right zone PCM melt temperature and (c, f) left zone length fraction with HTF flow velocity for 2-PCM cascaded HP-TES system of channel length 30 m.

configuration with exergetic efficiency of 96.38% and latent utilization of 20.37 % for channel length of 40 m.

Figure 25a–d presents the variations in discharge time and exergetic efficiency for different PCM melt temperatures at the left and bottom zones for a 2-PCM cascaded HP-TES system. Note that the PCM melt temperature at the left zone is varied between the default bottom zone PCM melt temperature ($T_{m,B}$ = 361 C) and the hot HTF temperature, T_C in Figure 25a and b while the bottom zone melt temperature is varied between T_D and the default left zone PCM melt temperature ($T_{m,T}$ = 503 C) in Figure 25c and d. It is observed that significant changes are observed in the variation of left zone melt temperature in that the highest discharge time increases with increase in PCM melt temperature between 361 C to 503 C and then decreases with further increase in PCM melt temperature between 574 C (Figure 25a). The decrease can be attributed to

the absence of driving force for melting the PCM, which manifests as the temperature difference between T_C and T_m, thus resulting in low latent utilization. At higher velocities, $U_f > 4.5$ mm/s, the effect of cascading in improving the heat exchange rate is observed as the bottom zone melt temperature of 375 C cascaded with the default left zone PCM melt temperature of 503 C shows a higher discharge time $t_D = 3.78$ h compared to non-cascaded configuration ($t_D = 2.88$ h) with PCM melt temperature of 503 C. Similarly, the maximum discharge time obtained for PCM melt temperature of 290 C at the bottom zone is less due to the absence of driving force for PCM solidification.

Concomitant to the trends observed for the discharge time, the exergetic efficiency in Figure 25b and d is found to increase with increase in PCM melt temperatures at the left and bottom zone, respectively. Figure 25e and f shows that the highest discharge time and the exergetic efficiency are obtained when the total channel length is filled with high melt temperature PCM, indicative of left zone length fraction of $L'_{2,L} = 1.0$. However, the advantage of cascading is realized only for higher velocities, when the discharge time is observed to be greater for intermediate left zone length fractions other than 1 and 0 as observed for $U_f > 3.8$ mm/s in Figure 25c. In light of the SunShot requirements of discharge time greater than 6 hours, the cascaded configuration shows similar highest discharge compared to non-cascaded configuration. For instance, the highest discharge time of a 2-PCM cascaded HP-TES system with the high and low PCM melt temperatures distributed in the ratio of 0.75:0.25 from $x = 0$ m (Figure 20c) for $L_d = 40$ m and $U_f = 2.53$ mm/s, is 6.9 h, which is the same as that obtained for a non-cascaded HP-TES system.

Figure 26a–d represents the storage cost for different design parameters namely, condenser length, channel height, channel width and longitudinal pitch respectively. In Figure 26 it is seen that for a given power plant capacity, the storage capital cost, α decreases with decrease in HTF

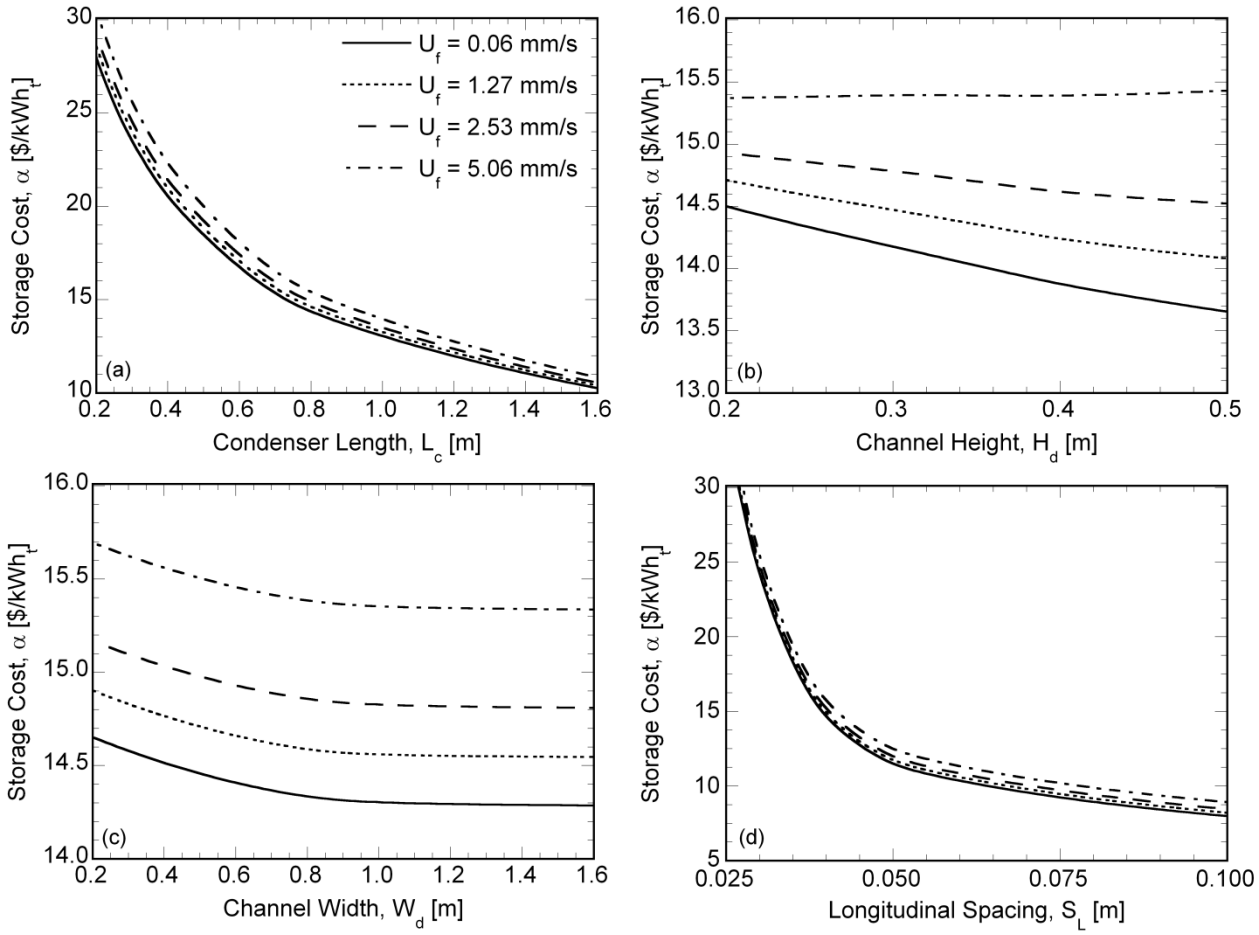

Figure 26: Variation in storage cost with (a) condenser length, (b) channel height, (c) channel width and (d) longitudinal spacing between the heat pipes for different HTF flow velocities.

flow velocity, albeit, an increase in the number of channels. This is due to the simultaneous increase in total capital cost of the system and the energy storage capacity of the HP-TES system with decrease in HTF velocity (decrease in HTF mass flow rate per channel) as the number of channels increase. As shown in Figure 26a, with increase in condenser length, L_c the height of the PCM unit, H_p also increases, leading to an increase in the amount of energy stored (increase in PCM mass) and decrease in α. It is observed from Figure 26d that the storage cost decreases with increase in channel height for smaller flow velocities while for faster HTF flow velocity, the storage costs increases with increase in channel height. For a given velocity, an increase in the

Table 6: Cost of various components of HP-TES system

	H_d = 0.2 m		H_d = 0.5 m	
	U_f = 1.27 mm/s	U_f = 5.06 mm/s	U_f = 1.27 mm/s	U_f = 5.06m m/s
No. of channels, n_d	1588	397	636	159
No. of heat pipes, n_{HP}	27250080	6812520	10913760	2728440
HP-TES width, W_t [m]	67.2	16.8	36.8	9.6
HP-TES height, H_t [m]	20	20	20	20
PCM material cost [US $MM]	54.22	13.56	21.72	5.43
HTF material cost [US $MM]	17.34	4.33	19.01	4.75
Heat pipes cost [US $MM]	109.00	27.25	43.66	10.91
Container cost [US $MM]	28.45	9.34	14.18	5.81
Overhead cost [US$MM]	10.00	2.73	5.49	1.60
Total capital cost [US$MM]	219.01	57.20	104.05	28.51
Storage capacity [MWh]	14884.49	3721.12	7388.58	1847.15
Storage cost [$/kWh$_t$]	14.71	15.37	14.08	15.43

channel height results in a decrease in the number of channels due to the increase in mass flow rate in a unit channel. Concomitantly, the storage capital cost decreases with increase in channel height as the volume and energy storage capacity of the PCM decreases, notwithstanding an increase in the material cost for channel construction. For a better understanding of the observed trend, a detailed capital cost breakdown of the various components of HP-TES is provided in Table 6. From Table 6, it is observed that for a given channel height, the total capital cost of the HP-TES system decreases with increase in HTF flow velocity. This is attributed to the decrease in the number of channels and the resultant number of heat pipes. However, for the channel height of 0.5 m, the capital cost decreases only by a factor of 3.69 for an increase in the storage capacity by a factor of 4, resulting in an increase in the storage cost expressed on a kWh$_t$ basis.

For a given channel width, the storage cost, α is found to increase with increase in HTF flow velocity as presented in Figure 26c. This is attributed to the increase in mass flow rate in a unit duct with increase in HTF flow velocity, resulting in a decrease in the number of channels and concomitant decrease in the stored energy. Hence the storage cost per unit kWh$_t$ increases with

increase in HTF flow velocity, notwithstanding a decrease in the total capital cost. It is noteworthy that the storage capital cost per unit kWh_t decreases with increase in channel width, reaches an optimal minimum, and remains constant with further increase in channel width. With increase in channel width for a given HTF flow velocity, the HTF mass flow rate in a unit duct increases resulting in a decrease in the total number of channels required to meet the rated power capacity of the CSP plant. This causes a decrease in the total capital cost of the system from W_d= 0.1 m to 0.4 m, resulting in a decrease in the storage cost per unit kWh_t as observed from Figure 26c. A decrease in S_L leads to an increase in the number of heat pipes, thus resulting in an increase in the storage cost (Figure 26d). For instance the number of heat pipes in a unit duct increases from 2586 for S_L = 0.10 m to 68641 for S_L = 0.02 m and concomitantly, the storage cost increases due to the combined effect of decrease in PCM volume (storage capacity) and increase in storage capital cost. The increase in capital cost with increase in channel length is negligible due to the increase in the energy stored combined with increase in total cost (PCM material, heat pipes, HTF channel, Container cost). As the evaporator length increases, the storage cost increases due to decrease in the HTF volume and the storage capacity of the HTF in the channel. Since the observed decrease is relatively insignificant, it is not illustrated here.

Based on the parametric studies shown in Figure 23–Figure 26, Figure 27 and Figure 28 present the design windows on the HTF flow velocity, U_f, which identify the regions where $t_D \geq 6h$, $\zeta \geq 95\%$ and $\alpha \leq 15 kWh_t$ can be achieved (the shaded areas) as a function of the different design parameters for non-cascaded and 2-PCM cascaded HP-TES system respectively. From Figure 23–Figure 25, it is seen that for any design parameter, there exists a lower and upper bound on the discharge time, which are represented, by solid and dotted lines, respectively in Figure 27. Similarly the long-dashed and short-dashed lines in Figure 27 represent the lower and upper

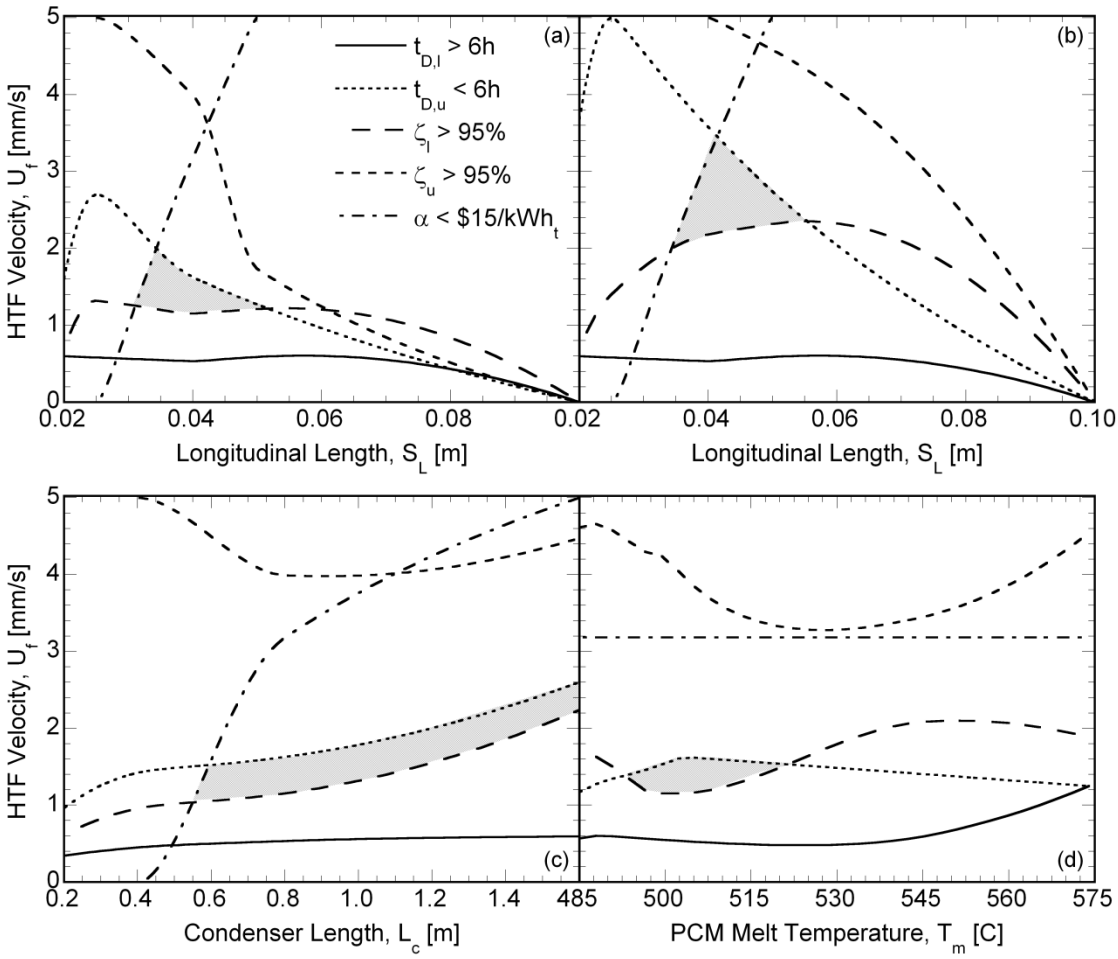

Figure 27: Operating windows as function of longitudinal spacing between the heat pipes for channel lengths of (a) 20 m and (b) 40 m. Operating windows for a channel length of 20 m as function of (c) condenser length and (d) PCM melt temperature for non-cascaded HP-TES system.

bounds on the HTF velocity subject to the constraint of minimum exergetic efficiency and the chain-dashed line forms the upper bound subject to the constrains on the maximum storage capital cost. Values of the HTF flow velocity for the corresponding design parameter that lie inside the operating window will ensure that the minimum exergetic efficiency, the minimum discharge time and the maximum storage capital cost are within the prescribed limits that correlate to desired overall HP-TES system performance.

Figure 27a and b shows the feasible operating regime (shaded area) of the HP-TES system as a function of the longitudinal spacing between the heat pipes, which meets the SunShot requirements for two different channel lengths, viz. L_d = 20 m and L_d = 40 m, respectively. The feasible design window of operation is constrained between the upper bound on the discharge time, lower bound on the exergetic efficiency and the upper limit on the storage cost of the HP-TES system. At longitudinal spacing of 0.025 m, as observed from Figure 27a and b, the broader regions of operating window on the HTF velocity can be realized. However, the unit cost of the heat pipes restricts operation of the HP-TES system at small longitudinal spacing due to an exponential increase in the number of embedded heat pipes. It is also observed that the band between the upper bound on discharge time and lower limit on exergetic efficiency decreases for S_L = 0.02 m, due to decrease in the storage capacity as a result of the increase in number of heat pipes that take up the PCM volume. With increase in channel length, as seen from Figure 27b for L_d = 20 m, operation of the HP-TES system at high HTF flow velocities is possible due to the increase in storage capacity of the HP-TES system.

Figure 27c shows the feasible design window of operation for variations in condenser length as bounded by the upper limits on discharge time, storage cost and lower limit on exergetic efficiency. Due to the increase in storage cost beyond \$15/kWh$_t$ the HP-TES system cannot be operated with heat pipes of condenser length less than ~ 0.5 m, due to the decrease in storage capacity of the HP-TES system. As the condenser length increases, the feasible bandwidth on the HTF velocity narrows down due to decrease in the exergetic efficiency as observed in Figure 24d due to the increase in conduction-dominated resistance to PCM solidification. Figure 27d provides important information on the selection of PCM based on melt temperature for integrating a HP-TES system to CSP plant. Essentially, the PCM melt temperature should have a PCM melt

temperature within -10 C and +20 C from the discharge cut-off temperature to satisfy the SunShot goals.

Figure 28a and b presents the design window obtained for 2-PCM cascaded configuration for various right zone PCM melt temperatures (closest $x = L_d$) and variations in right zone length fraction, respectively. No feasible design window could be obtained by varying the left zone PCM melt temperature closest to the inlet of the hot HTF side while maintaining the right zone PCM melt temperature at the default value, $T_{m,R} = 361$ C. Feasible operating regimes are obtained when the PCM selected to fill the right zone has a melt temperature in excess of 410 C due to the decrease of exergetic efficiency below 95 % for PCM melt temperatures less than 410 C. This effect can also be observed for variations in right zone length fraction in Figure 28b, which shows that at least 65% of the total volume of the PCM unit volume along the channel length from the inlet of the hot HTF side should be filled with PCM at the highest melt temperature to satisfy SunShot requirements. The storage cost assumed in this study does not change with PCM melt temperature and hence the feasible design window of operation is bound between the upper limit on discharge time and the lower limit on exergetic efficiency. The design window of operation for 2-PCM cascaded HP-TES is seen to favor PCM with higher melt temperatures due to the increase in exergetic efficiency with increase in PCM melt temperature.

A further goal of the present study is to find and report the optimum design parameters, which maximizes the discharge time (t_D), maximizes the exergetic efficiency, ξ and minimizes the storage cost per unit thermal energy, α within the operating window for the non-cascaded and 2-PCM cascaded HP-TES systems considered. The optimization scheme considered in this study serves as an illustrative example to introduce the methodology for using physics based models for system design and optimization. Table 7 lists the parameter combinations that maximize the

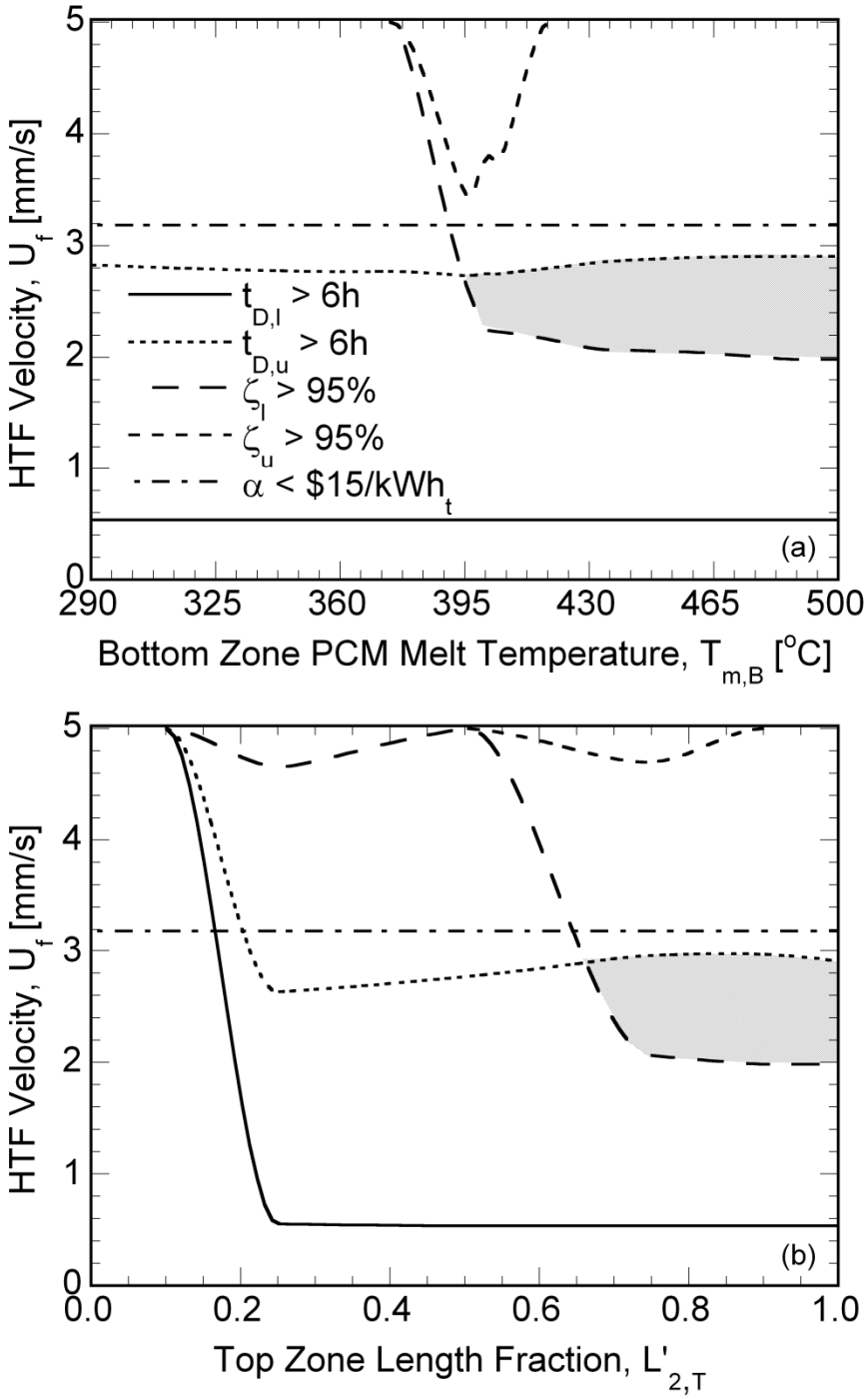

Figure 28: Operating windows as functions of (a) bottom zone PCM melt temperature and (b) left zone PCM length fraction for 2- PCM cascaded HP-TES system of channel length, 30 m.

discharge time and exergetic efficiency and minimizes the storage cost, provided the SunShot constraints are satisfied. Since the default PCM melt temperature chosen for the non-cascaded

configuration in the present analysis yielded the maximum discharge time, the values tabulated for non-cascaded configuration serve to identify the optimum design configuration of the HP-TES system. The maximum values of the objective function are listed in bold face and the preferred design configuration is highlighted in Table 7.

For channel lengths of 20 m and 40 m, the maximum discharge time is obtained for the largest evaporator length of L_e = 0.25 m considered in the present study (Table 7.a.1) with the rest of the parameters at the default values. For the intermediate channel length of 30 m, the best design was obtained for smaller channel height of H_t = 0.2 m. As observed from Table 7, the HTF flow velocity corresponding to the best design point increases with increase in channel length. The longest discharge time is obtained for channel length of 40 m cf. t_D = 6.95 h (Table 7a.1). Parametric studies of 2-PCM cascaded configurations reveal that the best design configuration depends on the optimal length fractions of each PCM zone and the design that yielded the highest discharge time required a higher fraction of the channel length filled with PCM of high melt temperature. The best design configuration with highest discharge time of t_D = 6.9 h for the 2-PCM cascaded HP-TES system requires that the left and right zones filled with high and low melt temperature PCM, respectively be split in the ratio of 0.75:0.25 (Table 7a.2 for L_d = 40 m). The best design configuration for maximum exergetic efficiency (Table 7b) and minimum storage capital cost (Table 7c) also shows that non-cascaded PCM configuration yielded the best design configuration. The maximum exergetic efficiency is obtained for an intermediate channel length of 30 m for both non-cascaded and 2-PCM cascaded configuration. The lowest storage cost for non-PCM cascaded configuration is obtained for a condenser length of 1.6 m cf. \$10.56/kWh$_t$ (Table 7c.1) due to increase in storage capacity as a result of increase in PCM volume with increase in L_c (H_p). Thus Table 7 provides optimum design parametric values to maximize the discharge time,

Table 7: Optimum design obtained from operating windows for HP-TES system design based on SunShot requirements

Objective			T_d [°C]	L'	H_d [m]	W_d [m]	S_L	L_e [m]	L_c [m]	t_C [h]	t_D [h]	U_f [mm/s]	α [$/kWh$_t$]	ζ [%]
a. Maximum Discharge Time, t_D [h]														
1. 1-PCM (Non-Cascaded)	L_d = 20 m	-	503.00	-	0.250	0.800	0.040	0.250	0.800	6.000	6.833	1.266	14.614	95.262
	L_d = 30 m	-	503.00	-	0.200	0.800	0.040	0.200	0.800	6.000	6.817	2.531	14.934	96.248
	L_d = 40 m	-	503.00	-	0.250	0.800	0.040	0.250	0.800	6.000	**6.950**	2.531	14.614	95.650
2. 2-PCM (Cascaded)	L_d = 20 m	Top Bottom	503.00 361.00	0.900 1.000	0.250	0.800	0.040	0.200	0.800	6.000	6.750	1.266	14.614	95.925
	L_d = 30 m	Top Bottom	503.00 361.00	0.900 1.000	0.250	0.800	0.040	0.200	0.800	6.000	6.600	2.531	14.886	96.438
	L_d = 40 m	Top Bottom	503.00 361.00	0.750 0.250	0.250	0.800	0.040	0.200	0.800	6.000	**6.900**	2.531	14.886	95.843
b. Maximum Exergetic Efficiency, ζ [%]														
1. 1-PCM (Non-Cascaded)	L_d = 20 m	-	503.00	-	0.250	0.800	0.040	0.200	1.600	6.000	6.167	2.531	14.531	96.683
	L_d = 30 m	-	500.16	-	0.250	0.800	0.040	0.200	0.800	6.000	6.233	2.531	14.856	**97.215**
	L_d = 40 m		503.00	-	0.250	0.800	0.040	0.100	0.800	6.000	6.500	2.531	14.810	96.638
2. 2-PCM (Cascaded)	L_d = 20 m	Top Bottom	503.00 361.00	0.900 1.000	0.250	0.800	0.040	0.200	0.800	6.000	6.750	1.266	14.614	95.925
	L_d = 30 m	Top Bottom	503.00 361.00	0.900 1.000	0.250	0.800	0.040	0.200	0.800	6.000	6.600	2.531	14.886	**96.438**
	L_d = 40 m	Top Bottom	503.00 361.00	0.750 0.250	0.250	0.800	0.040	0.200	0.800	6.000	6.900	2.531	14.886	95.843
c. Minimum Storage Cost, α [$/kWh$_t$]														
1. 1-PCM (Non-Cascaded)	L_d = 20 m	-	503.00	-	0.250	0.800	0.040	0.200	1.600	6.000	6.167	2.531	**10.559**	96.683
	L_d = 30 m	-	503.00	-	0.500	0.800	0.040	0.200	0.800	6.000	6.700	1.266	14.474	96.106
	L_d = 40 m		503.00	-	0.250	0.800	0.040	0.200	1.600	6.000	6.400	5.062	10.853	96.638
2. 2-PCM (Cascaded)	L_d = 20 m	Top Bottom	503.00 361.00	0.900 1.000	0.250	0.800	0.040	0.200	0.800	6.000	6.750	1.266	**14.614**	95.925
	L_d = 30 m	Top Bottom	503.00 361.00	0.900 1.000	0.250	0.800	0.040	0.200	0.800	6.000	6.600	2.531	14.886	96.438
	L_d = 40 m	Top Bottom	503.00 361.00	0.500 0.500	0.250	0.800	0.040	0.200	0.800	6.000	6.283	2.531	14.787	95.789

exergetic efficiency and minimize the α within the operating window of the HP-TES system for both non-cascaded and 2-PCM cascaded HP-TES configuration.

The best configurations obtained from the parametric studies (Figure 23–Figure 26) and the design windows (Figure 27 and Figure 28) reported in Table 7 are obtained from varying one parameter at a time with the rest of the parameters at the design values. It is imperative that an optimization procedure varying all the design parameters simultaneously is followed in order to find the optimum distribution of PCM melt temperature and other design parameters while also achieving the SunShot targets, which will be the subject of future study. Further, the storage performance model will be coupled with a CSP plant performance model to analyze the impact of HP-TES system on the CSP plant performance in future studies.

4.6 Nomenclature used in Chapter 4

c_p	specific heat [J/kg-K]
C'	cost per unit mass [$/kg]
C''	cost per unit area [$/m^2]
h	convective heat transfer coefficient [W/m-K]
h_{sl}	latent heat of fusion of PCM [J/kg]
H	height [m]
i	nodal point
k	thermal conductivity [W/m^{2}K]
L	length [m]
$\dot{m}$	mass flow rate [kg/s]
n	number

Q energy [J]

r radius [m]

S_L longitudinal spacing [m]

S_T transverse spacing [m]

T temperature [K]

T_m melting temperature [K]

t time [s]

U velocity [mm/s]

w thickness [m]

W width [m]

Subscripts and Superscripts

a adiabatic

c condenser

C charging

d channel

D discharging

e evaporator

HP heat pipe

d channel

w wick

x computational cells in x-direction

Greek Symbols

α thermal diffusivity [m^2/s]

β	thermal expansion coefficient [K^{-1}]
φ	wick porosity
μ	dynamic viscosity [kg/m^2-s]
ρ	Density [kg/m^3]
γ	liquid fraction

Chapter 5: Analysis of a Latent Thermocline Storage System with Encapsulated Phase Change Materials

This chapter presents a transient, numerical analysis of a molten salt, single tank latent thermocline energy storage system (LTES) is performed for repeated charging and discharging cycles to investigate its dynamic response. The influence of the design configuration and operating parameters on the dynamic storage and delivery performance of the system is studied to identify configurations that maximize utilization of the storage system. Based on the parametric studies, guidelines are derived for designing a packed bed PCM based storage system for CSP plant operating conditions.

5.1 Introduction

This chapter considers another promising approach to improving the heat transfer rate between the HTF and PCM, through increasing the heat transfer area by encapsulating the PCM mixture in small capsules. For example, PCM stored in capsule diameters of 10 mm offer surface area of more than 600 square meters per cubic meter of capsules [59].

The configuration of a single-tank thermal storage system packed with spherical capsules containing PCM is considered in this chapter. The working of a encapsulated PCM based thermal energy storage (EPCM-TES) system in a CSP plant fundamentally involves the exchange of heat between a heat transfer fluid (HTF) and the packed bed of spherical PCM capsules during the charging and discharging processes. During charging, hot HTF from the solar receiver enters the EPCM-TES system from the top and transfers heat to the PCM, thus effecting the melting of PCM at a constant temperature. The cooled HTF exits from the bottom of the tank to return to the solar field, completing a closed loop of the HTF flow. During discharging, a cold fluid is pumped from

the bottom of the EPCM-TES packed bed, resulting in the solidification of the PCM within the capsules as heat is drawn from the PCM to the fluid, and the hot fluid exiting the top of the tank is directed to generate steam to drive a turbine to produce electricity. Buoyancy forces ensure stable thermal stratification of hot and cold fluids within the tank during both charging and discharging processes. The charging process takes place during the day when solar energy is available while energy is discharged whenever the sun is not available or when there is a peak demand in electricity. As in the case of any latent thermal energy storage system integrated to a CSP plant, repeated cycles subjected to partial charging and discharging processes may limit the rate of phase change of PCM and decrease the utilization of the tank with time. It is imperative to understand the dynamic thermal behavior of the packed-bed EPCM-TES in order to design the storage system for a CSP plant operation.

Numerous works on the numerical modeling of sensible heat storage in packed beds are found in the literature [60–65]. As a pioneering work, Schumann et al. [61] presented the first numerical study on modeling of the packed bed, which is widely adopted in subsequent studies. The model enables prediction of the temporal and axial variation of the HTF and filler bed temperatures in a thermocline tank. Yang and Garimella [62] presented a computational fluid dynamics model to analyze the performance of thermocline storage system filled with quartzite rocks for use in parabolic trough CSP plants, and more recently, Yang and Garimella [63] explored the cyclic behavior of sensible thermocline storage system. For a given mass flow rate of the HTF, the cycle efficiency was concluded to be intimately influenced by the filler particle diameter and tank radius. Van Lew et al. [64] adopted the Schumann model [61] to analyze the performance of thermocline energy storage system embedded with rocks as filler material. Li et al. [65] extended the model developed in [64] to develop design charts for thermocline energy storage system design and

calibration. Hänchen et al. [66] employed Schumann's model [61] to discuss the effects of particle diameter, bed dimensions, fluid flow rate and the solid filler material on the dynamic performance of thermocline storage system. Uniform charging and discharging times were considered and the efficiency of the system as a function of cycles was monitored.

Ismail and Henriquez [67] numerically investigated the influence of the working fluid inlet temperature, the working fluid flow rate and the material of a spherical capsule of 77 mm diameter on the PCM solidification process. Felix Regin et al. [68] and Singh et al. [69] presented brief reviews of the work performed on thermocline storage system with PCM capsules. Felix Regin et al. [70] also reported on the modeling of thermocline energy storage system with embedded PCM capsules. The modeling follows the Schumann formulation [61] except that the dependent variable for the energy equation of the filler bed was enthalpy instead of temperature. The resistance developed during the solidification phase change process was accounted for by a decrease in the heat transfer coefficient between the HTF and the filler bed. Wu and Fang [71] analyzed the discharging characteristics of a solar heat storage system with a packed bed of spherical capsules filled with myristic acid as PCM. The influence of the HTF mass flow rate, inlet temperature and the porosity of packed bed were studied.

The foregoing discussion suggests that although several studies are reported on a thermocline system packed with sensible filler materials, the literature on the performance of a latent thermocline energy storage system is relatively few. To the authors' knowledge, a thorough modeling of solidification and melting process of encapsulated PCM in a thermocline energy storage system and a comprehensive study of the dynamic performance of the system subjected to constraints dictated by the power plant operation is lacking in the previous studies.

To this end, the objectives of the chapter are to develop a detailed model of a thermocline storage system containing spherical capsules filled with PCM and to investigate the influence of the design and operating parameters on the dynamic performance of the system to identify configurations that lead to maximizing system utilization. Based on systematic parametric studies, design guidelines for a latent thermocline storage system with a packed bed of encapsulated phase change materials are established. The results of the study are presented in terms of nondimensional groups for generalized applicability for designing the storage system for both parabolic (low temperature) and power tower (high temperature) CSP plants.

5.2 Mathematical Model

Figure 29a illustrates the schematic of a thermocline storage tank of height H_t and radius R_t packed with spherical capsules filled with PCM. For the sake of clarity in illustration, an ordered arrangement of capsules is depicted in Figure 29a; however, in reality, the packing scheme may vary and the porosity of the packed bed for a fixed diameter of spherical capsules can range from 0.25–0.48. The solid arrows indicate the direction of hot HTF during charging while the dotted arrows indicate the direction of cold HTF flow through the storage system during discharging. The inner radius of the capsules, represented by R_c, is filled with PCM (shaded), while the thickness of the capsule wall is denoted by b, as depicted in Figure 29b.

The flow of the HTF is considered incompressible and the PCM is assumed to be homogeneous without any impurities and isotropic on the physical properties. The outer surface of the insulated thermocline tank is considered to be adiabatic and the HTF flow is assumed to be radially invariant and only along the axis of the tank, which was also confirmed from a detailed computational analysis of the system, that is not discussed here. The temperature variation in the

thermocline tank is considered to be axisymmetric, whereas the temperature is considered to vary radially inside the encapsulated PCM region. The transient heat transfer in the axisymmetric domain of the packed bed is coupled with the transient radial heat transfer in the PCM to determine the spatial and temporal temperature variation along with the melt interface location. Thermal expansion and shrinkage of PCM in the spherical capsules is not accounted for in the present study and the density of solid and liquid phase of the PCM is considered to be same. Thermal conduction between the spherical PCM capsules in contact is neglected because of the large contact resistance. The melting and solidification processes within a PCM are modeled by the enthalpy-porosity technique as introduced by Voller et al. [43]. By this approach, the porosity in each cell is set equal to the liquid fraction, f_L, in the cell, which takes either the value of 1 for a fully liquid region, 0 for a solid region, or $0 < f_L < 1$ for a partially solidified region (mushy zone).

Based on the foregoing assumptions, the governing energy equations for the HTF temperature, T_f, and the encapsulated PCM temperature, T_p, are as follows:

$$\varepsilon \rho_f c_f \frac{\partial T_f}{\partial t} + \rho_f c_f U \frac{\partial T_f}{\partial z} = k_f \frac{\partial^2 T_f}{\partial z^2} + \frac{3(1-\varepsilon)}{4\pi (R_c + b)^3} \frac{T_{p,r=R_c} - T_f}{RT_1 + RT_2} \quad (23)$$

$$\rho_p \left(c_p + h_{sl} \frac{\partial f_L}{\partial T_p} \right) \frac{\partial T_p}{\partial t} = \frac{1}{r^2} \frac{\partial}{\partial r} \left(k_{p,eff} r^2 \frac{\partial T_p}{\partial r} \right) \quad (24)$$

where $RT_1 = b \big/ 4\pi k_w R_c (R_c + b)$ and $RT_2 = 1 \big/ 4\pi h (R_c + b)^2$ in Eq. (1) denote the thermal resistance offered by radial heat conduction in the capsule wall and convective heat transfer between the HTF and filler phase, respectively. The terms ρ, c, k and T correspond to density, specific heat, thermal conductivity, and temperature, respectively, of either the HTF denoted by subscript *f* or the

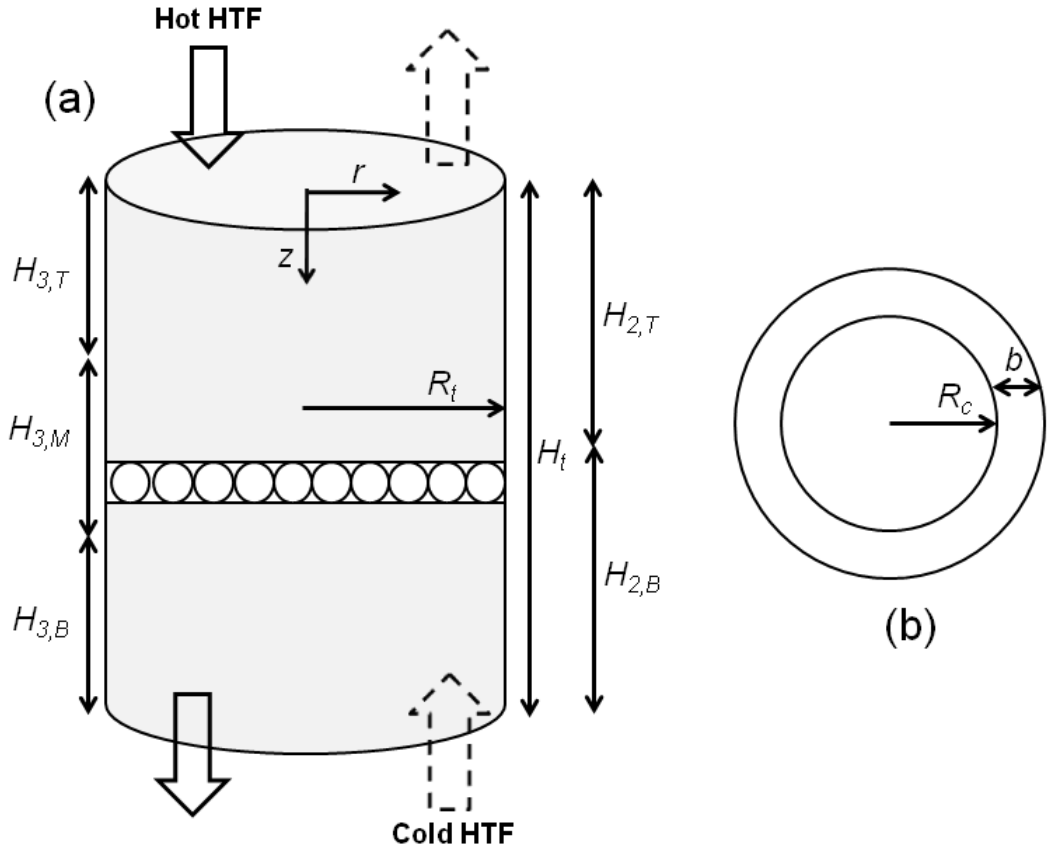

Figure 29: Schematic illustration of: (a) latent thermocline storage system (LTES), (b) capsule cross-section.

encapsulated PCM denoted by subscript *p*, h_{sl} denotes the latent heat of fusion of the PCM, *t* denotes time, *U* represents the superficial velocity of the heat transfer fluid entering the packed bed storage system, *h* represents the convective heat transfer coefficient between the HTF and PCM capsules and ε denotes the porosity of the packed bed. The term, $T_{p,r=R_c}$ on the right hand side of Eq. (23) denotes the PCM temperature calculated at the inner surface of the PCM capsules as shown in Figure 29b.

The circulation of liquid due to buoyancy-driven natural convection currents during the melting of PCM are modeled using an enhanced effective thermal conductivity of the PCM melt

front, $k_{p,eff}$, evaluated using the empirical correlation in [72], which covers both the conduction and convection regimes and is expressed as $k_{p,eff} = k_p \times Nu_{conv}$, where k_p is the molecular thermal conductivity of PCM and Nu_{conv} is calculated using [72]:

$$Nu_{conv} = 1.16 f(\mathrm{Pr}) \left(\frac{D_o - D_i}{2D_i} \right)^{1/4} \frac{Ra^{1/4}}{\left\{ \left(D_i / D_o \right)^{3/5} + (Do / Di)^{4/5} \right\}^{5/4}} \qquad (25)$$

$$f(\mathrm{Pr}) = \frac{2.012}{3 \times \left[1 + (0.492/\mathrm{Pr}_p)^{9/16} \right]^{4/9}}$$

The correlation is valid for a wide range of Prandtl (Pr_p) number and Rayleigh number (Ra) of the PCM. The term D_o–D_i appearing in Eq. (25) represents the thickness of the liquid layer formed during melting of PCM. Since the thickness of the liquid layer is very small initially, heat transfer across the liquid layer occurs primarily by conduction although, ultimately, convection becomes important as the melt region expands. Therefore, heat transfer through the melt is calculated by evaluating both (1) a conduction heat transfer rate using k_p and (2) a rate associated with the use of $k_{p,eff}$ for free convection in a spherical enclosure. The expression that yields the largest heat transfer rate was used in the computations.

In order to generalize the model and the corresponding results, Eqs. (23) and (24) are non-dimensionalized as follows:

$$\varepsilon \frac{\partial \theta_f}{\partial t^*} + \mathrm{Re}_H \mathrm{Pr}_f \frac{\partial \theta_f}{\partial z^*} = \frac{\partial^2 \theta_f}{\partial z^{*2}} + \frac{3 \times (1-\varepsilon)}{(R_c^* + b^*)^3} \times \frac{(\theta_{p,r^*=R_c^*} - \theta_f)}{\left\{ \frac{b^*}{k_w^* \times R_c^* \times (R_c^* + b^*)} \right\} + \left\{ \frac{2}{Nu \times (R_c^* + b^*)} \right\}} \qquad (26)$$

$$(1+\psi\frac{\partial f_L}{\partial \theta_p})\frac{\partial \theta_p}{\partial t^*}=\frac{k_p^*\times Nu_{conv}}{\lambda}\frac{\partial}{\partial r^*}\left(r^{*2}\frac{\partial \theta_p}{\partial r^*}\right) \tag{27}$$

where the non-dimensional parameters are defined as follows:

$$\begin{aligned}
&z^*=\frac{z}{H_t};\ r^*=\frac{r}{H_t};\ t^*=\frac{k_f\times t}{\rho_f c_f H_t^2};\ b^*=\frac{b}{H_t};\ R_c^*=\frac{R_c}{H_t};\ \theta_f=\frac{T_f-T_D}{T_C-T_D};\ \theta_p=\frac{T_p-T_D}{T_C-T_D}\\
&\psi=\frac{h_{sl}}{c_p(T_C-T_D)};\lambda=\frac{\rho_p c_p}{\rho_f c_f};\ k_w^*=\frac{k_w}{k_f};\ k_p^*=\frac{k_p}{k_f};\ \mathrm{Re}_H=\frac{\rho_f\cdot U\cdot H_t}{\mu_f};\ \mathrm{Pr}_f=\frac{\mu_f c_f}{k_f}\\
&Nu=\frac{hH_t}{k_f}=2+2.87\left[(R_c^*+b^*)\mathrm{Re}_H\right]^{1/2}\mathrm{Pr}_f^{1/3}+0.098(R_c^*+b^*)\mathrm{Re}_H\mathrm{Pr}_f^{1/2}
\end{aligned} \tag{28}$$

in which, the interstitial Nusselt number, *Nu*, thermally couples the HTF with the spherical PCM capsules, and is given by the above expression obtained from Galloway and Sage [23]. The other characteristic nondimensional parameters that appear in Eq. (26) are the Reynolds number, Re_{H}, Prandtl number of the HTF, Pr_{f} and the inverse Stefan number of the PCM, ψ. Subscripts *C* and *D* correspond to the hot inlet HTF temperature during charging and the cold inlet HTF temperature during discharging, respectively. Note that hot HTF enters the tank at $z^* = 0$ during charging and the exit temperature of the HTF corresponds to an axial position of $z^* = 1$ and vice-versa during discharge.

Further, the boundary conditions during the charging and discharging process are specified as

$$\theta_f(z^*=0)=1,\ \frac{\partial\theta_f}{\partial z^*}(z^*=1)=0;\ \textit{Charging}$$

$$\theta_f(z^*=1)=0,\ \frac{\partial\theta_f}{\partial z^*}(z^*=0)=0;\ \textit{Discharging}$$

$$k_p^*\frac{\partial\theta_p}{\partial r^*}(r^*=R_c^*,0<z^*<1)=\frac{\left[\theta_p(R_c^*,z^*)-\theta_f(z^*)\right]/R_c^*}{\left[\frac{b^*}{k_w^*(R_c^*+b^*)}\right]+\left[\frac{2R_c^*}{Nu(R_c^*+b^*)}\right]} \tag{29}$$

$$\frac{\partial\theta_p}{\partial r^*}(r^*=0,0<z^*<1)=0$$

The numerical simulations start with a charge process assuming that the tank is completely discharged initially, resulting in the following initial conditions for the HTF and the PCM phase:

$$\theta_f=0;\ \theta_p=0 \tag{30}$$

The complete set of governing equations is discretized using the finite volume approach and the melting/solidification of the PCM is modeled using the fixed-grid enthalpy method as presented by Voller et al. [43]. In order to accurately predict the liquid fraction in the fixed grid enthalpy-based formulation, the liquid fraction in each computational cell, in conjunction with the temperature, θ_p, predicted by Eq. (27) for the encapsulated PCM, should be updated at each iteration within a time step. In the present case, the enthalpy iterative updating scheme of the liquid fraction takes the following form for a pure PCM, which melts at constant temperature:

$$\psi f_{L(i)}^{n+1}=\psi f_{L(i)}^{n}+\frac{a_i}{a_i^0}\delta\left[\theta_{p(i)}^{n}-F^{-1}(f_{L(i)}^{n})\right] \tag{31}$$

In the above equation, a_i is the coefficient of θ_i for the radial nodal point i in the discretized energy equation of the PCM, n is the iteration number, δ is a relaxation factor, which is set to 0.01

for the present case, and F^{-1} is the inverse of latent heat function which takes the value of θ_m for a pure substance.

The coupled system of governing equations in their nondimensional form is solved using an implicit method with the diffusive and convective fluxes discretized using hybrid differencing scheme, the convective-diffusive fluxes in the HTF governing equation (Eq. (26)) discretized using the power-law scheme, and the diffusive fluxes in the PCM governing equation (Eq. (27)) discretized using central differencing scheme [73]. After a systematic grid refinement study, the thermocline tank was discretized into 200 equally spaced intervals in the axial direction and the encapsulated PCM within the spherical capsules was discretized into 10 uniform zones in the radial direction. The nondimensional time step chosen for the study was $\Delta t^* = 5\times10^{-10}$. The iterative residuals at each time step are converged to the order of 10^{-11} to eliminate iterative errors from the solution.

5.3 Model Inputs and Outputs

The numerical model allowed for studying all the physical heat transfer processes that occur within the system namely, the convective heat transfer between the HTF and the filler phase, the radial thermal conduction in the wall, the conduction in the solid PCM, and conduction and natural convection within the liquid PCM. The outputs from the model comprise the transient axial variation of temperature in the HTF, the transient radial variation of temperature and the melt fraction contour of PCM within the capsule at any axial location. The transient total energy available within the system ($Q_T = Q_S + Q_L$) is composed of sensible energy (Q_S) and latent energy

(Q_L) components, calculated as the summation of energy stored in all the PCM capsules and the HTF, which can be determined from the following expressions:

$$Q_S = \pi R_t^2 \sum_{j=1}^{p} \left[\varepsilon \rho_f c_f (T_{f(j)} - T_C) \Delta z + \sum_{i=1}^{q} \frac{(1-\varepsilon)(T_{p(i,j)} - T_C) \rho_p c_p V_i \Delta z}{V_c} \right] \tag{32a}$$

$$Q_L = \sum_{j=1}^{p} \sum_{i=1}^{q} \frac{(1-\varepsilon)\pi R_t^2 \rho_p h_{sl} f_{L(i,j)} V_i \Delta z}{V_c} \tag{32b}$$

where *i* represents the radial node at any axial location, *j*, *p* and *q* denotes the total number of discretized finite volumes in the axial direction of the tank and radial direction of the capsules, respectively. V_c and V_i denotes the volume of the spherical capsules and the discretized volume of the radial node '*i*', respectively; and Δz represents the discretized length of the nodes in the axial direction of the LTES. The corresponding nondimensionalized sensible energy and latent energy components are calculated as:

$$Q_s^* = \frac{Q_s}{\rho_f c_f \pi R_t^2 H_t (T_C - T_D)} = \sum_{j=1}^{p} \left[\varepsilon \theta_{f(j)} \Delta z^* + \sum_{i=1}^{q} \frac{(1-\varepsilon)\theta_{p(i,j)} V_i^* \Delta z^* \lambda}{(R_c^* + b^*)^3} \right] \tag{33a}$$

$$Q_L^* = \frac{Q_L}{\rho_f c_f \pi R_t^2 H_t (T_C - T_D)} = \sum_{j=1}^{p} \sum_{i=1}^{q} \left[\frac{(1-\varepsilon)\psi f_{L(i)} V_i^* \Delta z^* \lambda}{\left(R_c^* + b^*\right)^3} \right] \tag{33b}$$

The nondimensional operating and design parameters analyzed in the present study are the Reynolds number, Re_H, the capsule radius, R_c^*, the capsule wall thickness, b^*, inverse Stefan number, ψ, and the melt temperature, θ_m. The results of the study are presented and discussed in the following section.

5.4 Model Validation

The validity of the model developed in Section 5.2 is examined by comparing the axial variation of the HTF temperature at different time instants obtained from the present simulation with experimental data reported by Pacheco et al. [74] for a small pilot scale, 2.3 MWh_t sensible thermocline storage tank. The results of the comparison are presented in Figure 30a. The model developed to study latent thermocline energy storage system in the previous section can be used to analyze sensible thermocline energy storage system by setting the the inverse Stefan number of the filler material, ψ, to 0 in Eq. (27) so that the second term on the left side vanishes. In the experimental studies [74], a eutectic molten salt of $NaNO_3$ + KNO_3 and Quartzite rocks were used as the HTF and filler material, respectively, for which the thermophysical properties are reported in [74]. In Figure 30a, the markers denote the experimental results while the lines denote the corresponding results obtained from the present simulation. The initial condition of the HTF axial temperature profile, at t = 0.0 h in Figure 30a, corresponds to the final charging state of the first cycle, which was carried out for 2 hours from a fully discharged state. With the flow of cold HTF into the tank, at $z^* = 0$, the preexisting hot fluid in the tank flows out at $z^* = 1$. Simultaneously, heat exchange between the Quartzite rocks and the cold HTF takes place, which is characterized by the sloped line from $\theta_f = 0$ to $\theta_f = 1$ observed at t = 0.5 h in Figure 30a. As time progresses, the temperature of the fluid exiting the tank gradually decreases as all the preexisting hot fluid in the tank is discharged and the cold HTF which entered the tank at t = 0 h starts to discharge. Since not all the energy is transferred from the filler material to the cold HTF, the temperature of the HTF exiting the tank, $\theta_f(z^* = 1)$, starts to decrease gradually, as observed at t = 1.5 h and 2 h in Figure 30a. Since the experiment is not carried in a controlled environment, the temperature profiles show some scatter. The agreement between the experimental and numerical results is satisfactory to

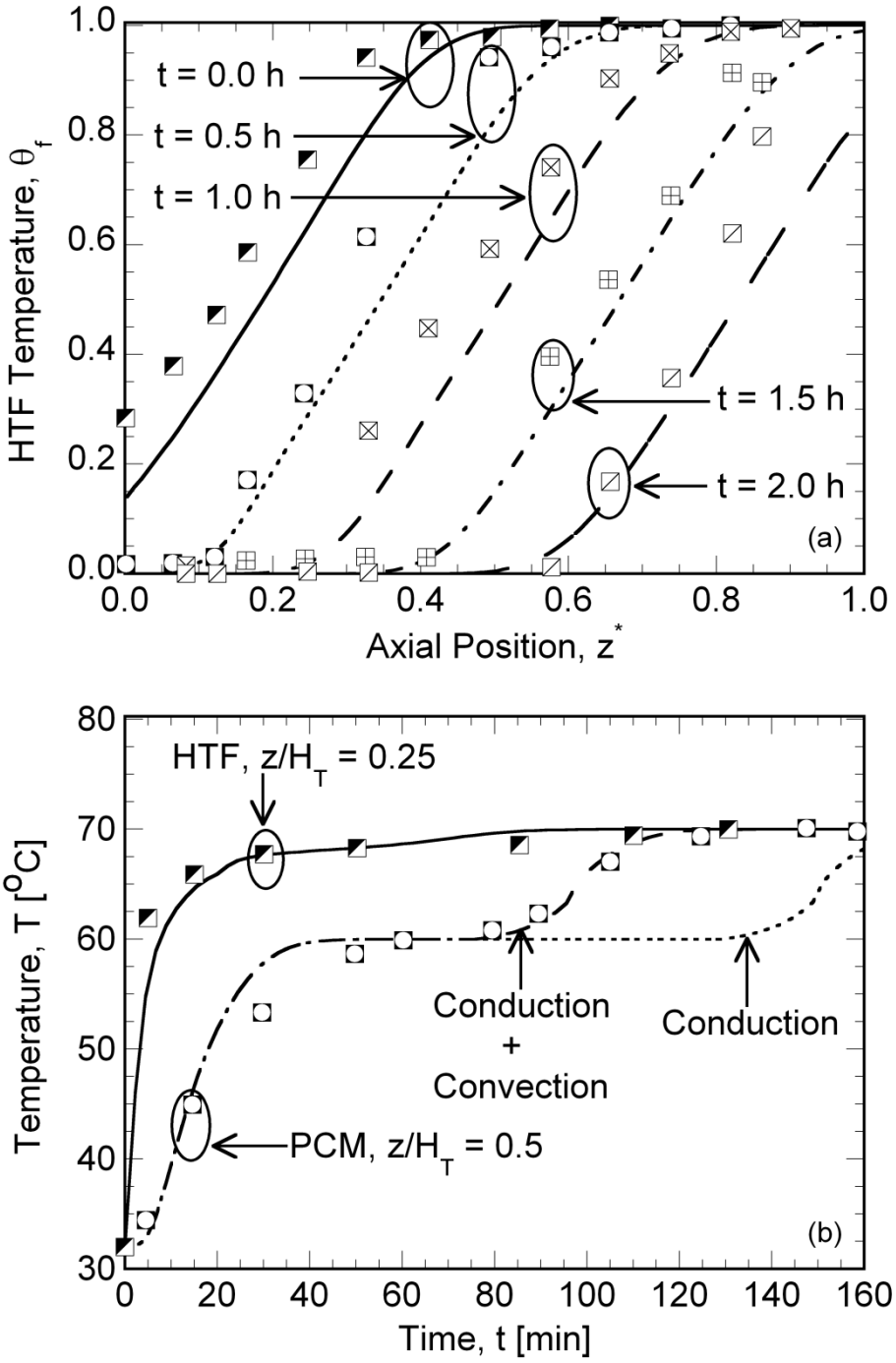

Figure 30: Comparison of the (a) axial HTF temperature variation from the present simulations (lines) with the experimental data from Pacheco et al. [74] (markers), (b) the temporal HTF and PCM temperature variation from the present simulations (lines) with the experimental data from Nallusamy et al. [75] (markers).

within the uncertainty in the experimental tests, the properties of materials considered and the numerical simulation.

Figure 30b shows the comparison of the temporal variation of the HTF temperature at z/H_t = 0.25 and the PCM temperature inside the spherical capsules at z/H_t = 0.5, obtained from the numerical simulation, with experimental data of Nallusamy et al. [75]. The experimental results correspond to the operation of a packed bed thermocline system filled with spherical capsules of diameter 55 mm. The capsules were filled with paraffin wax, which melts at 60 $^{\circ}$C and water was used as the HTF. It is observed from Figure 30b that the prediction of the PCM melting rate with the present convection-assisted model leads to a sound agreement with the experimental data than accounting for only conduction within the PCM inside the spherical capsules, which predicts a slower melting rate relative to the observed experimental data. This result points to the importance of accounting for the buoyancy-driven natural convection effects during the charging process, which was incorporated in the present study using an effective thermal conductivity of the PCM, as discussed in the previous section.

The close agreement of the numerical simulations with the experimental results confirms the reliability of the model, which forms the basis of the parametric studies presented and discussed in Sections 5.4 and 5.5.

5.5 Single Charge and Discharge

The effects of the various design and operating parameters on the performance of the system subjected to a single charging and discharging cycle are discussed first. The range for each of the operating and design parameters included in this study is determined from a literature review of various PCM properties, as shown in Table 8, such that the default parametric combination is

Table 8: Operating and design parameters considered in Chapter 5 for encapsulated PCM TES

Parameters	Symbol	Design Intervals
Reynolds Number	Re_H	$5000 \leq \mathrm{Re}_H \leq 50000$
Capsule Radius	R_c^*	$0.00025 \leq R_c^* \leq 0.0025$
Capacitance Ratio	λ	$0.500 \leq \lambda \leq 2.000$
PCM Melt Temperature	θ_m	$0.000 \leq \theta_m \leq 1.000$
Inverse Stefan number	ψ	$0.000 \leq \psi \leq 2.000$

$R_c^* = 0.001$; $\mathrm{Re}_H = 5000$; $b^* = 5\times10^{-8}$; $\psi = 0.5$; $\theta_m = 0.75$; $\mathrm{Pr}_f = 5$; $\lambda = 1$; $k_w^* = 1$; $k_p^* = 1$. The Prandtl number chosen for the study corresponds to that of molten salt HTF used in CSP plants. The initial state of the system corresponds to a fully charged state for the discharging process and a fully discharged state for the charging process. The performance of LTES is quantified in terms of the discharge efficiency of the tank defined as, $\eta_D = \int_{t^*=0}^{t^*=t_D} \left(\frac{\theta_f(z^*=0) - \theta_D}{\theta_C - \theta_D} \right)$.

Figure 31a presents the axial HTF temperature distribution (solid line) and the PCM melt fraction (dashed line) inside the tank at various time instants during the charge process for PCM melt temperature of $\theta_m = 0.5$ with the rest of the design parameters at the default values. The tank is initially in a fully discharged state with the HTF and the PCM filler capsules kept at the cold temperature, $\theta_f = \theta_p = 0$, and the PCM in solid state (Figure 31a). At $t^* = 0$, hot HTF is introduced into the tank at $z^* = 0$, which results in the heat exchange between the incoming hot HTF and the cold solid PCM stored in the spherical capsules, resulting in the melting of PCM. At $t^* = 2.0\times10^{-5}$, it is observed that until the axial position of $z^* = 0.25$, the PCM stored inside the spherical capsules completely melts and reaches the inlet temperature of the hot HTF. The HTF temperature

distribution presented in Figure 31a at $t^* = 2.0\times10^{-5}$ consists of four zones as also reported in [62]: (1) a constant low-temperature zone ($\theta_f = 0$) near the bottom of the tank (z^* = 1), (2) a constant high-temperature zone ($\theta_f = 1$) which prevails near the top of the tank (z^* = 1), (3) a constant melt-temperature zone ($\theta_f = \theta_m$) and (4) two intermediate heat exchange zones ($\theta_m < \theta_f < 1$ and $0 < \theta_f < \theta_m$). In the constant low- and high-temperature zones, the molten salt and PCM capsules are in thermal equilibrium; in the heat exchange zones, sensible energy transfer between the PCM capsules and the HTF occurs; and in the constant melt-temperature zone, latent energy transfer between the HTF and PCM takes place. The constant low temperature zone is clearly observed in the HTF temperature profile at $t^* = 2.0\times10^{-5}$ (Fig. 3a). As time progresses, at $t^* = 4.0\times10^{-5}$ in Figure 31a, it is found that the temperature of the HTF exiting the tank at z^* = 1, increased from 0 to 0.2 as all the initial cold fluid is completely discharged and the incoming hot fluid, which exchanges thermal energy with the PCM filler materials, starts to discharge.

Figure 31b shows the HTF temperature profile at various time instants during the discharge process. The HTF and the PCM filler capsules are initially kept at the high temperature corresponding to a fully charged state, $\theta_f = \theta_p = 1$, and the PCM is in molten state (Figure 31b). At t^* = 0, cold HTF at $\theta_f = 0$ is introduced into the tank at z^* = 1, which results in the heat exchange between the incoming cold HTF and the molten PCM stored in the spherical capsules, resulting in the solidification of the PCM radially inward into the spherical capsules. The axial temperature variation of the HTF follows the same discussions as in the charging process. Due to the small capsule radius considered ($R_c^* = 0.001$), natural convection currents in the molten PCM does not have any significant effect on the charge rate and as a result, the total time taken to charge the

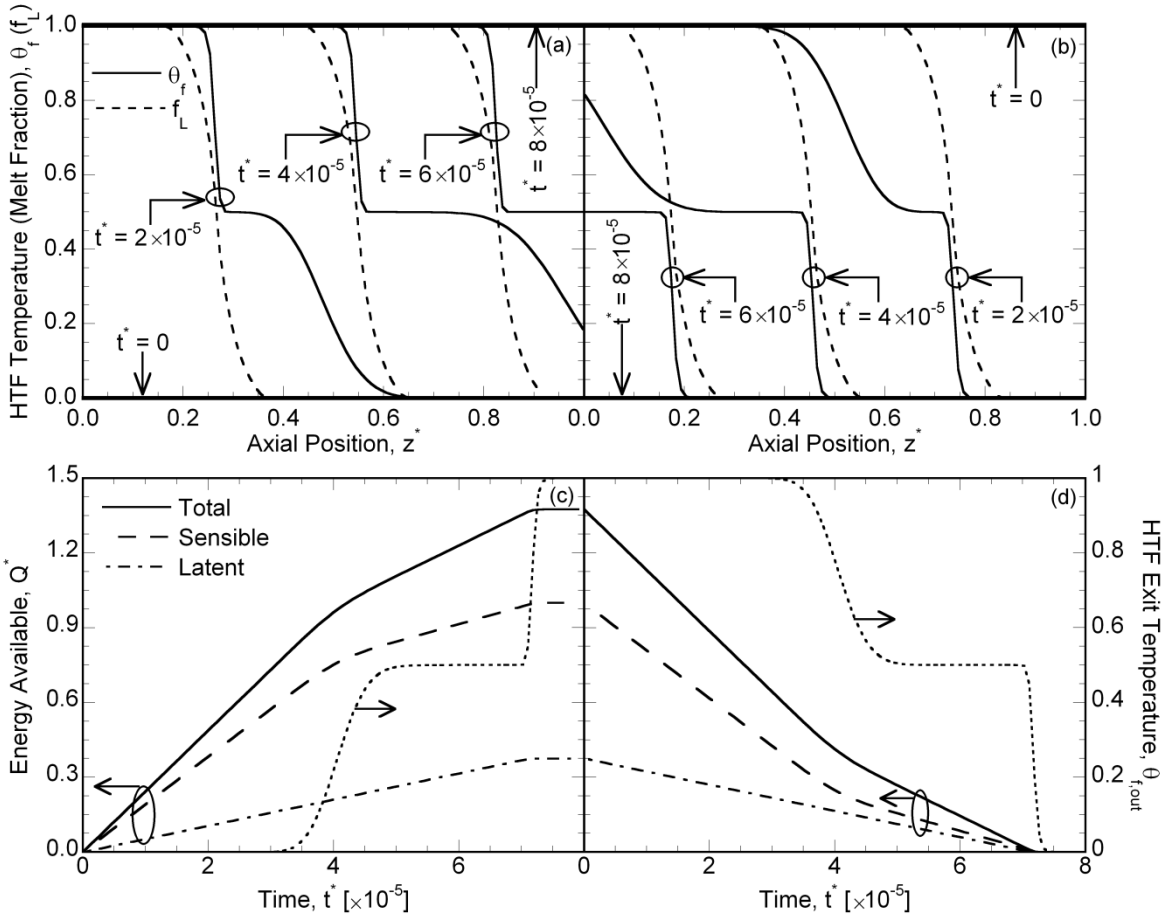

Figure 31: Time evolution of axial HTF temperature and PCM melt fraction profiles during (a) charging and (b) discharging,and time variation of the HTF exit temperature, $\theta_{f,out}$, and total energy available, Q^*, in the LTES during (c) charging and (d) discharging, respectively.

system was the same as that to discharge the system, i.e., $t_C^* = t_D^* = 8.0\times10^{-5}$, for the combination of parameters listed at the beginning of this subsection.

Figure 31c presents the temporal variations of the exit temperature of the HTF (θ_f at $z^* = 1$) depicted by dotted line and the accumulation, Q^*, of total (solid line), sensible (dashed line), latent energy (dotted-dashed line) in the thermocline system during the entire charging process, for the

default parametric values as presented at the beginning of Section 5.4. The sensible, latent and total energy available in the LTES can be calculated from Q_s^* in Eq. (33a), Q_L^* in Eq. (33b) and $Q_s^* + Q_L^*$. The exit temperature of the HTF is observed to gradually increase at $t^* = 3.5\times10^{-5}$ when the hot fluid which entered the tank at $t^* = 0$ and exchanged thermal energy with the cold PCM capsules starts to exit from the bottom of the tank. Ideally, considering infinite heat transfer rate between the HTF and the PCM capsules, the hot HTF entering the tank should transfer 100% of its thermal energy to the cold solid PCM capsules, and the exit temperature of the HTF should follow a step curve increasing from 0 to 1 after all the PCM capsules are completely charged. However, due to the conduction and convection resistances limiting the heat transfer rate between the HTF and PCM capsules, the HTF temperature gradually increases from 0 to θ_m and stays at θ_m until the bulk of the PCM at the top portion of the tank changes phase from solid to liquid after which the temperature increases from θ_m to 1 (Figure 31c). From the temporal variation of the total energy stored in the tank, as plotted in Figure 31b, it is observed that the charge rate slightly decreases at approximately $t^* = 4.5\times10^{-5}$ when the HTF exit temperature is governed by the melting of the PCM. The latent energy storage rate is slower than sensible energy storage rate as observed from the slope of the sensible energy and latent energy curves in Figure 31c. At $t^* = 4.5\times10^{-5}$, latent energy storage rate dominates as reflected in a decrease in the total energy storage rate. Similar to the charge process, the temporal variations of the energy available in the tank and the exit temperature of the HTF during the discharge process (θ_f at $z^* = 1$) is presented in Figure 31d. Since the PCM melt temperature, $\theta_m = 0.5$ is exactly mid-way between the charge and the discharge temperature of the incoming HTF fluid, and no convection assistance is observed during charging, the exit temperature and the energy available during the discharge process shown in

Figure 31d exhibits a reverse variation of the corresponding curves illustrated in Figure 31c. The discharge efficiency, η_D, can be visually interpreted as the ratio of the area under the HTF exit temperature curve in Figure 31d with respect to the total plot area.

Figure 32 portrays the time required to charge and discharge the thermocline tank and also the corresponding discharge efficiency for the various nondimensional operating and design parameters of the system namely, the Reynolds number (Figure 32a), capsule radius (Figure 32c) and porosity (Figure 32d). The driving force for melting (solidification) is the difference between the hot (cold) HTF temperature and the PCM melt temperature. In Figure 32, the charge time is higher than the discharge time because for the default melt temperature of $\theta_m = 0.75$, the driving force for solidification is greater than that for melting. It can be observed from Figure 32a that with increase in Reynolds number, the charge time as well as the discharge time decrease. The trend can be explained by the fact that for a given capsule size, the Nusselt number, which governs the heat transfer rate between the HTF and the PCM capsules, increases with increase in Reynolds number (Eq. (28)), leading to a faster storage and extraction of energy. However, the discharge efficiency decreases with increase in Re_{H} due to the faster decrease of the exit temperature with increase in Reynolds number, as seen in Figure 32b during the discharge process. This, in turn, corresponds to a smaller area under the temperature time curve, leading to a decrease in discharge efficiency with increase in Re_{H}.

An increase in capsule radius is accompanied by an increase in the Nusselt number (Eq. (28)), which signifies efficient convective heat transfer between the HTF and PCM capsules, due to the increase in surface area of interaction. Simultaneously, the conduction (RT_1) resistance, as defined in Eq. (23), within the PCM capsules also increases resulting in a slower extraction of both latent

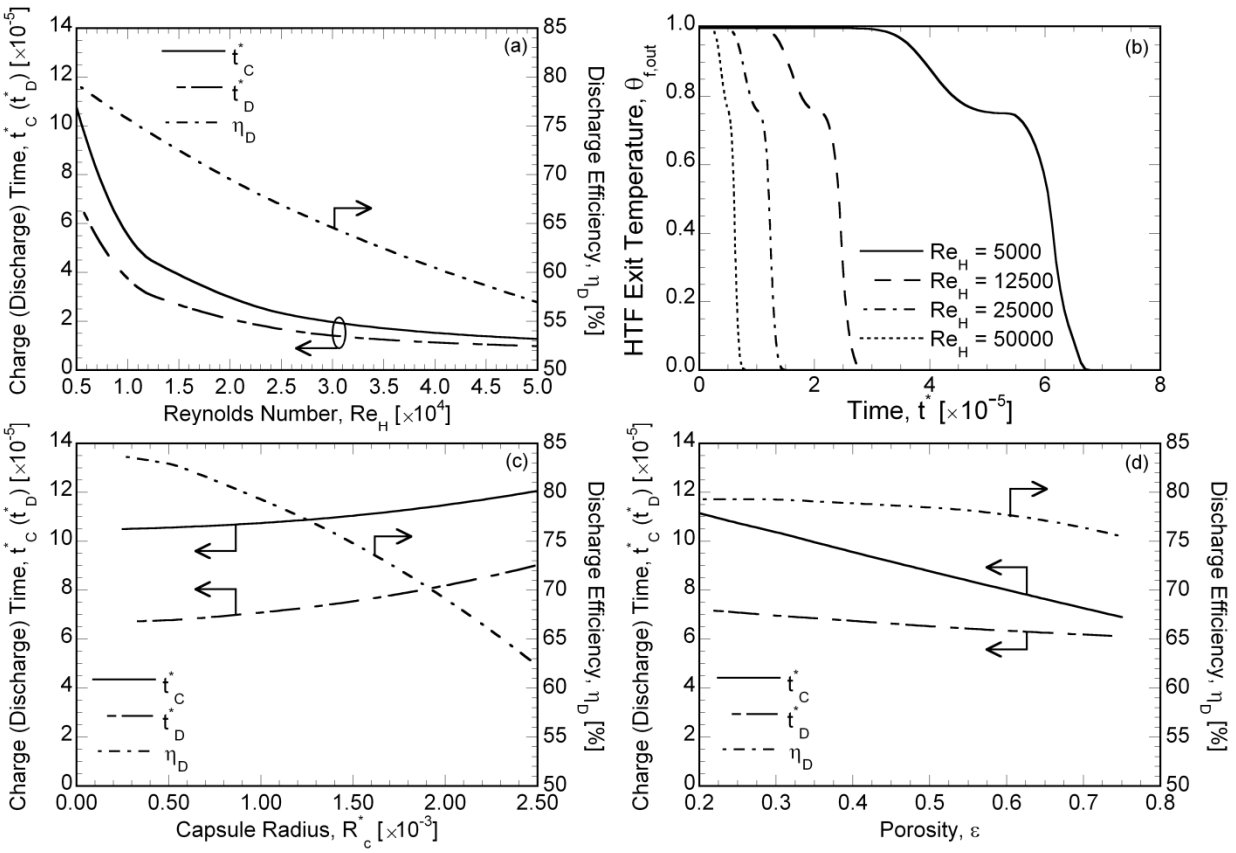

Figure 32: Variation of (a) charge time, discharge time and discharge efficiency with Reynolds number, (b) HTF exit temperature with time for various Reynolds numbers, and charge time, discharge time and discharge efficiency with (c) capsule radius and (d) porosity.

and sensible energy from the interior of PCM capsules. This leads to a subsequent increase in the charge and discharge time leading to a decrease in discharge efficiency with increase in capsule radius, as illustrated in Figure 32c. The difference between the charge and discharge time decreases with increase in capsule radius from $t^*_C - t^*_D = 3.78\times10^{-5}$ for $R^*_c = 0.00025$ to 3.03 for $R^*_c = 0.0025$. This is due to the enhancement in the PCM melting rate during charging assisted by the buoyancy driven natural convection currents. From Figure 32c, it is also found that the critical capsule radius beyond which the buoyancy driven natural convection current effects in the molten PCM are important correspond to $R^*_c = 0.001$ with $t^*_C - t^*_D = 3.66\times10^{-5}$.

With increase in porosity, the charge and discharge time of the thermocline tank decreases as illustrated in Figure 32d. The decrease in charge and discharge time with increase in porosity can be explained by the fact that a smaller number of capsules are present inside the tank for thermal energy exchange with the HTF. With increase in porosity, the sensible energy extraction rate increases while the latent energy extraction rate decreases due to the increase in HTF volume and reduction in the number of PCM capsules respectively. This leads to a faster decrease in the exit temperature of the HTF followed by the discharge of pre-existing hot HTF in the tank, thus leading to a decrease in discharge efficiency with increase in porosity for the default PCM melt temperature of $\theta_m = 0.75$. For low PCM melt temperatures, $\theta_m < 0.5$, the discharge efficiency is found to increase with increase in porosity (not illustrated here) due to the larger area under the temperature-time curve, similar to that illustrated for different Reynolds number in Figure 32b. However, as seen in Figure 32d, the porosity has a minimal effect on the discharge efficiency compared to the rest of the parameters. For a porosity of 1, which is not plotted here, the total volume of the tank will be occupied by the HTF leading to equal charge and discharge time dictated by the velocity of HTF flow and the tank height, as seen by the faster approach of charge time to the discharge time value at higher porosity in Figure 32d.

From Figure 33a, it is seen that as the capacitance ratio increases, since the thermal inertia increases, the corresponding slower temporal variation of PCM temperature, θ_p, leads to a slower energy charge and discharge rate or equivalently, longer charge and discharge times. On the other hand, only a slight decrease in the discharge efficiency is observed because with increase in capacitance ratio, the thermal capacitance increases and the exit temperature of the HTF decreases slowly, which compensates for the longer charge and discharge times. Figure 33b shows the influence of inverse Stefan number on the charge and discharge times and discharge efficiency of

the tank. With increase in inverse Stefan number, the PCM has a larger amount of latent energy (Eq. (33b)), which increases the latent thermal inertia of the system, and results in a longer charge and discharge time. The discharge efficiency initially increases from $\eta_D = 64.04\%$ for $\psi = 0$, which corresponds to a sensible thermocline storage system, to $\eta_D = 80.84\%$ for a inverse Stefan number of 1, after which it decreases again to $\eta_D = 79.6\%$ for $\psi = 2$. For high inverse Stefan number, the discharge efficiency does not decrease as much as the increase in the discharge time, because the HTF exit temperature remains at the PCM melt temperature for a longer time with increase in inverse Stefan number, which compensates for the longer discharge time.

From Figure 33c, it is observed that the discharge time is higher than the charge time PCM melt temperature less than 0.5 because the temperature difference between the external cold HTF temperature and the PCM melt temperature decreases with decrease in PCM melt temperature. The effect of PCM melt temperature beyond $\theta_m = 0.5$ on the discharge time is observed to be insignificant. The converse trend is observed in Figure 33c for the charge time in that the charge time is higher than the discharge time for PCM melt temperature greater than 0.5 and the relative immunity for $\theta_m < 0.5$. For instance, the discharge time in Figure 33c decreases from $t_D^* = 7.91\times10^{-5}$ for $\theta_m = 0.5$ to $t_D^* = 6.44\times10^{-5}$ for $\theta_m = 1.0$. For $\theta_m = 0.0$ ($\theta_m = 1.0$) during the discharge (charge) process the temperature difference between the cold (hot) HTF and the PCM melt temperature to drive the solidification (melting) of the PCM is zero which results in zero extraction of latent energy. However, the discharge efficiency is obtained to be the lowest at $\theta_m = 0.25$ ($\eta_D = 52.32\%$) when the discharge time is the highest, because the exit temperature of the HTF will stay at the low PCM melt temperature for the longest period of time. The discharge efficiency of the tank is found to be the highest for a melt temperature equal to the hot HTF

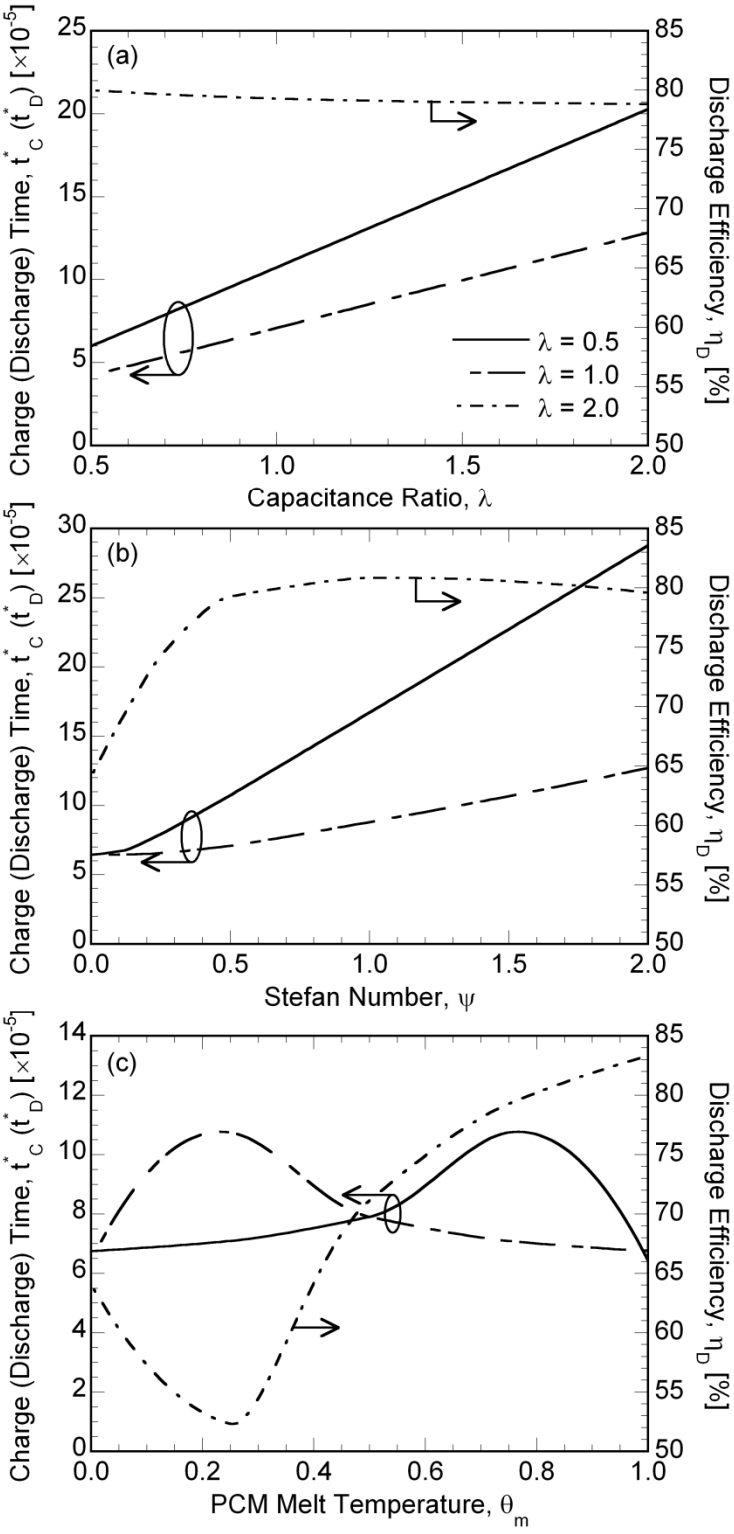

Figure 33: Variation of charge time, discharge time and discharge efficiency with (a) capacitance ratio, (b) inverse Stefan number and (c) PCM melt temperature.

temperature because the exit temperature of the HTF will stay at the highest temperature for a long time corresponding to the latent energy extraction. The effects of k_p^* and k_w^* on the LTES performance metrics are found to be insignificant and are not reported here. Among the plots in Figure 32 and Figure 33, the highest discharge efficiency is obtained to be $\eta_D = 83.32\%$ for $\theta_m = 1$ (Figure 33c), with other parameters held at the default values mentioned earlier in this subsection, which is significantly higher than $\eta_D = 64.04\%$ corresponding to a sensible thermocline tank with the same parametric values.

5.6 Cyclic Charging and Discharging

When designing a storage tank for a CSP plant, the dynamic behavior of the LTES subjected to repeated charge and discharge process is of primary interest. Initially the tank is kept in a fully discharged state as established by Eq. (30). The cyclic charge and discharge process of the LTES differs from the single charge and discharge process considered in Section 5.4 in that the initial conditions for subsequent charge and discharge processes are not the fully discharged or charged states, as considered in Section 5.4, but, instead, are the final states of discharge or charge at the end of the previous cycle. The performance of the LTES is analyzed following repeated charge and discharge processes until a periodic state is established, when the variations from one cycle to another is less than 0.5%.

The dynamic behavior and design of a latent thermocline storage system is assessed with respect to the following operating considerations of molten salt power tower CSP plants. In a molten salt power tower plant, the storage fluid as well as the working fluid of the power block is

the same and hence, the mass flow rate of the HTF depends on the CSP plant thermal power output requirement, P_t, and can be expressed as

$$P_t = \dot{m}_f \, c_f (T_C - T_D) = \rho_f c_f U \pi R_t^2 (T_C - T_D) \tag{34}$$

where, U is determined from the power plant output assuming that the HTF temperature always enters the power block at T_C. The baseline volume of a LTES, V_t ($V_t = \pi R_t^2 H_t$) can be found out from the following relation

$$Q_{cap} = V_t \left[\varepsilon \rho_f c_f (T_C - T_D) + (1-\varepsilon) \rho_p c_p (T_C - T_D) + (1-\varepsilon) \rho_p h_{sl} \right] \tag{35}$$

where Q_{cap} denotes the storage capacity of LTES based on an ideal thermocline.

In an effort to generalize the system performance and design a thermocline tank for any given discharge power and storage capacity, Eqs. (34) and (35) are non-dimensionalized as

$$P_t^* = \frac{P_t}{\left(k_f \pi H_t (T_C - T_D) \right)} = \beta^2 \, \mathrm{Re}_H \mathrm{Pr}_f \tag{36a}$$

$$Q_{cap}^* = \frac{Q_{cap}}{\rho_f c_f \pi H_t^3 (T_C - T_D)} = \beta^2 \left[\varepsilon + (1-\varepsilon)\lambda + (1-\varepsilon)\lambda\psi \right] \tag{36b}$$

where $\beta = \frac{R_t}{H_t}$. The analysis is presented here for $\beta = 1$, although other values of β will not affect the performance of the thermocline since the governing equations (Eqs. (26) and (27)) of the LTES are independent of β. Based on the given power plant power requirement and the storage operation duration, β merely appears as a scaling factor for increasing or decreasing the storage capacity of the plant and determining the Reynolds number. In this study, the Prandtl number of the fluid is not changed while the Reynolds number of the HTF is adjusted to explore the performance of the thermocline tank designed for various power plant requirements.

It was pointed out in Section 5.4 that the exit temperature of the HTF decreases (increases) after a period of time during discharging (charging). Commonly in CSP plants, the HTF exiting the tank during discharging (charging) is fed into the power block (solar field) for superheated steam generation. The strong dependence of the power block cycle efficiency on the working fluid temperature [58] requires the termination of discharge process when the HTF exit temperature reaches a certain *minimum* dimensionless cut-off temperature, $\theta_D^{'}$. Similarly, the material temperature limitations of the heat transfer fluid and the solar receiver dictate a *maximum* cut-off temperature, $\theta_C^{'}$, for the HTF exit temperature of the thermocline system during charging. If the exit temperature exceeds this value, a high flow rate is needed through the receiver in order to keep the temperature of the receiver and HTF in the receiver within allowable limits. The high flow rate, in turn, increases parasitic and thermal losses [58]. In the present study, $\theta_C^{'}$ and $\theta_D^{'}$ were set to be 0.39 and 0.74, respectively, representative of the requirements of a 115 MW turbine in a CSP plant operation [58].

The performance metrics used to characterize the dynamic behavior of the system in the present work are the cyclic total utilization, $U_T = \left(Q_{S,D}^* + Q_{L,D}^*\right) \big/ Q_{cap}^*$, and the latent utilization, $U_L = Q_{L,D}^* \big/ Q_{cap,L}^*$, where $Q_{S,D}^*$ ($Q_{L,D}^*$) denotes the sensible (latent) energy discharged in a cycle, which is obtained by subtracting the sensible, Q_S^* (latent, Q_L^*) energy available within the system defined in Eq. (33) of Section 5.3 at the end of the discharging process, from the total (latent) energy available within the system at the end of the charging process of the corresponding cycle. The term Q_{cap}^* represents the total energy storage capacity of LTES as defined in Eq. (36b) while $Q_{cap,L}^*$ accounts for only the latent energy capacity of the LTES, which can be denoted as $Q_{cap,L}^* = (1-\varepsilon)\lambda\psi$. A third performance metric namely, the useful thermal energy discharged by

the system is defined as, $Q^*_{cap,u} = Q^*_{cap} \times U_T$ was also used to quantify the performance of the storage system. Numerical simulations were conducted for various combinations of design and operating parameters listed in Table 8, to analyze the effects of total utilization, U_T, latent utilization, U_L, and useful thermal energy discharged, $Q^*_{cap,u}$, of the LTES at its periodic steady state.

Figure 34 shows the cyclic behavior of the axial temperature distribution of the HTF, θ_f, and the melt fraction distribution of the PCM inside the spherical capsules subjected to four cycles of the charging and discharging process. The layout of the figure is such that each row of plots represents one cycle of charging and discharging, and within each row the first and second plots represent the axial temperature profile evolution with time during charging and discharging, respectively, whereas the third and fourth plots denote the transient melt fraction profile variation during charging and discharging, respectively. The axial HTF temperature and PCM melt fraction profiles illustrated in Figure 34 correspond to a dimensionless PCM melt temperature of 0.5 and Reynolds number of 25,000 with the rest of the parameters retaining the values listed in Section 5.4. In cycle 1, Figure 34a–d, initially, at $t^* = 0$, the tank is in a completely discharged state and the PCM is in the solid phase as denoted by the coincidence of the HTF temperature and PCM melt fraction curve with the *x*-axis in Figure 34a and c, respectively. In Fig. 6a, as charging continues, hot HTF flows from $z^* = 0$, and exchanges energy with the PCM stored inside the spherical capsules resulting in the melting of PCM. As illustrated for Figure 31, the HTF temperature distribution at anytime instant consists of two heat exchange zones: a constant melt temperature zone, high- and

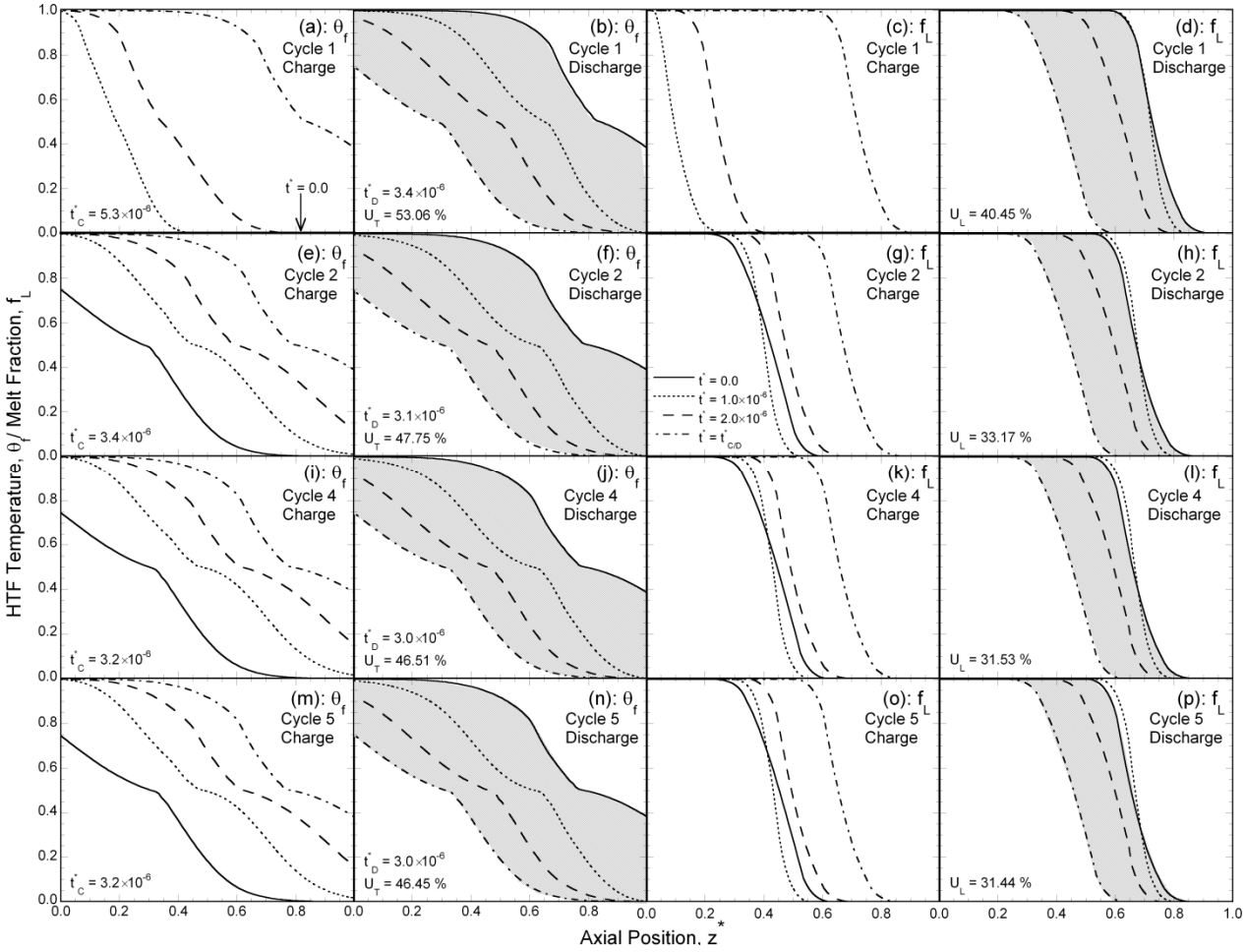

Figure 34: Temporal evolution in the axial distribution of HTF temperature, and PCM melt fraction during repeated charging and discharging cycles: HTF temperature variation during cycle 1 (a) charging and (b) discharging and PCM melt fraction variation during cycle 1 (c) charging and (d) discharging; HTF temperature variation during cycle 2 (e) charging and (f) discharging and PCM melt fraction variation during cycle 2 (g) charging and (h) discharging; HTF temperature variation during cycle 4 (i) charging and (j) discharging and PCM melt fraction variation during cycle 4 (k) charging and (l) discharging; HTF temperature variation during cycle 5 (m) charging and (n) discharging and PCM melt fraction variation during cycle 5 (o) charging and (p) discharging. The legends are included in Fig. 34g.

low- temperature zones. Charging continues until the exit temperature of the HTF at $z^* = 1$ reaches the cut-off temperature, $\theta_C^{'} = 0.39$, during which time the total molten PCM volume fraction in Figure 34c corresponds to 0.77. During the cyclic operation, the final charging temperature and melt fraction profile of the first process, depicted by chain dashed lines in Figure 34a and c,

respectively, becomes the initial condition, $t^* = 0$, of the subsequent discharge process, as depicted by the solid lines in Figure 34b and d, respectively. During the discharge process, cold HTF flows from $z^* = 1$, extracting thermal energy from the PCM inside the spherical capsules, thereby resulting in the solidification of PCM. As cold HTF flows from $z^* = 1$, the pre-existing hot HTF at the end of the previous charge process (solid line in Figure 34b) exits the tank at $z^* = 0$, followed by the discharge of the HTF that has extracted energy from the PCM. For a given design configuration, the nondimensional time taken for the inlet HTF to traverse the entire height of the tank is $\varepsilon/(\mathrm{Re}_H \mathrm{Pr}_f)$, obtained by substituting $t = \varepsilon U / H_t$ for the definition of t^* in Eq. (28), which for the current design configuration yields 2×10^{-6}. Correspondingly, at $t^* = 2\times10^{-6}$ in Figure 34b, the HTF temperature exiting the tank at $z^* = 0$, decreases as the incoming HTF that exchanges thermal energy with the PCM starts to discharge. The discharging process continues until the exit temperature of the HTF, θ_f, at $z^* = 0$ reaches $\theta_D' = 0.74$ and the corresponding axial PCM melt fraction distribution is depicted in Figure 34d. The percentage of shaded area in Figure 34b and d provide a representation of the total utilization, U_T, and latent utilization, U_L, of the LTES system, which are seen to be 53.06% and 40.45%, respectively. The dimensionless charge and discharge times are noted to be, respectively, $t_C^* = 5.3\times10^{-6}$ and $t_D^* = 3.4\times10^{-6}$.

Figure 34e shows the charging process of cycle 2, the initial temperature distribution of which corresponds to the final distribution of the discharge process of cycle 1 (Figure 34b). As the initial condition for charging of cycle 2 corresponds to a partially discharged LTES system compared to a fully discharged LTES in cycle 1 (Figure 34a), the total charge time for cycle 2 is less than that obtained for cycle 1. As the total time taken for the HTF to traverse the entire height of the tank is 2×10^{-6}, the exit temperature of the HTF starts to increase as the pre-existing cold HTF is

completely discharged and the inlet hot HTF starts to discharge after exchanging energy with the PCM. On the other hand, the exit temperature of the HTF for cycle 1 at $t^* = 2\times10^{-6}$ in Figure 34a does not increase yet, due to the exposure of inlet hot HTF to a completely discharged LTES which results in the discharge of HTF at low temperature even after the complete discharge of pre-existing cold fluid. After the culmination of charge process when the exit temperature of the HTF at $z^* = 1$ reaches the cut-off temperature, $\theta_C^{'}$, discharge process commences until the HTF exit temperature at $z^* = 0$ reaches $\theta_D^{'}$, as presented in Figure 34f, resulting in a total utilization, U_T, of 47.75%, about 10% lower than the 53.06% (Figure 34b) at the end of cycle 1 The corresponding charge time and discharge times are $t_C^* = 3.4\times10^{-6}$ (Figure 34e) and $t_D^* = 3.1\times10^{-6}$ (Figure 34f), which are less than the corresponding times in cycle 1 (Figure 34a and b). The solid line in Figure 34g represents the melt fraction contour at the start of cycle 2 charging which is the same as melt fraction curve at the end of discharging of cycle 1 (chain-dashed line in Figure 34d). As seen from the solid line in Figure 34g solid PCM exists between $z^* = 0$ and $z^* = 0.6$. From Figure 34b, it is seen that the HTF between $z^* = 0.35$ and $z^* = 1.0$ is below the PCM melt temperature, which results in further solidification of the PCM until the hot HTF from $z^* = 0$ is convected to that position. Hence, the axial melt front moves further to the left for a brief period of time from the start of cycle 2 charging before it moves right due to melting, which results in the crossing of melt fraction contour at $t^* = 0$ and $t^* = 1\times10^{-6}$. The latent utilization of the LTES at the end of cycle 2 decreases to 33.17% (Figure 34h) from 40.45% obtained for cycle 1 (Figure 34d).

Subsequent charge and discharge processes are carried out until the LTES reaches a periodic state, defined such that the total and latent utilization of the LTES, each changes by less than 0.5% between two consecutive cycles. Figure 34i (Figure 34j) and Figure 34m (Figure 34n), which show

the temporal evolution of axial HTF temperature distribution during charging (discharging) of cycles 4 and 5, respectively, follows the same description as cycles 1 and 2. Figure 34j and n reveals that the difference in total utilization of the LTES between cycle 4 and 5 is 0.13% and from Figure 34l and p, it is observed that the change in latent utilization of the LTES between the two cycles is 0.29%, reflecting the attainment of periodic state. The charge and discharge times are also seen to be nearly invariant with cycles at $t_C^* = 3.2\times10^{-6}$ (Figure 34i and m) and $t_D^* = 3.0\times10^{-6}$ (Figure 34j and n). It requires at most five cycles of operation for the system to achieve periodic state for the various range of parametric values considered in the present study (Table 8). Overall, it is seen from Figure 34 that a completely discharged initial state during the first cycle results in a higher utilization and the utilization of the LTES decreases in the subsequent cycles. It is instructive to note that the design of the LTES for CSP plants should be based on the utilization of the system obtained at the periodic cycle and the performance of the LTES is explored only after cyclic periodicity is achieved.

Figure 35a–d illustrates the influence of capsule radius, capacitance ratio, inverse Stefan number and PCM melt temperature, respectively, on the utilization of the thermocline storage system for different Reynolds. Figure 35a portrays the total and latent utilization of the LTES system calculated for different Re_{H} and different non-dimensional capsule radius, R_c^*. It is clear from Figure 35a that utilization decreases with increase in Re_{H} and R_c^*. At the higher values of the Reynolds number, a longer flow time is required for the exchange of thermal energy between the HTF and PCM, which results in an expansion of the heat exchange zone. Also, the constant melt-temperature zone is observed to reduce in length as the Reynolds number increases, implying lesser extraction of latent energy from the PCM. As explained before, the area between the charge

and discharge temperature profile is a visual representation of the total utilization of the system, which is found to decrease with increase in Reynolds number for any capsule radius. It is observed

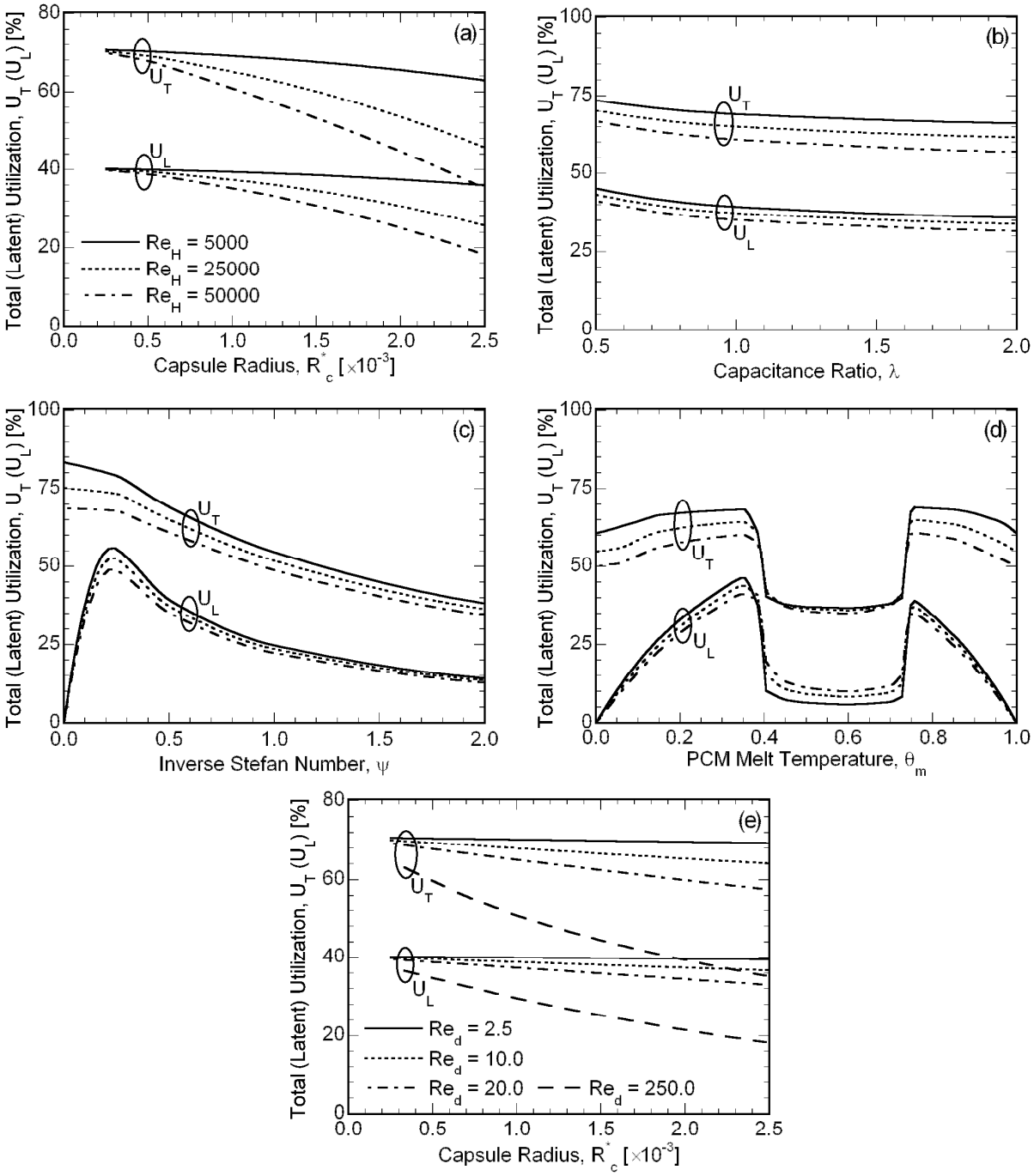

Figure 35: Effects of (a) capsule radius, (b) capacitance ratio, (c) inverse Stefan number and (d) PCM melt temperature on total and latent utilization of the latent thermocline energy storage

system for different Reynolds numbers, Re_H, and (e) effect of capsule radius on total and latent utilization for different Reynolds numbers based on capsule diameter, Re_d

that increasing R_c^* results in an expansion of the heat exchange zone and restricts the formation of constant melt-temperature zone as illustrated for the axial HTF temperature distribution in Figure 34, thus resulting in a decrease in total and latent utilization is observed. This is attributed to the fact that for a given height of the tank, increasing the capsule radius, results in an increased resistance to the conduction dominated PCM solidification, which occurs during discharge process limiting the heat exchange rate between the HTF and PCM. Figure 35a highlights the important effects of the Reynolds number and capsule radius, R_c^* on the design of a latent thermocline storage system. For very small capsule radius, R_c^*, between 2.5×10^{-4} and 6.0×10^{-4}, negligible variation in total and latent utilization is observed with increase in R_c^* and Re_H. Hence, capsule radii as large as 6 mm and 12 mm can be used in LTES of height 10 m and 20 m, respectively, for enhanced system performance.

It is observed from Figure 35b that the total utilization and latent utilization of the system decreases with increase in capacitance ratio. With increase in capacitance ratio, the slope of the heat exchange zone increases while the extent of the constant low temperature zone and constant high temperature zone decreases in the axial melt fraction distribution as explained for Figure 34. This can be explained with reference to high thermal inertia posed to the temporal variation of the PCM temperature resulting in a slower extraction of thermal energy from the PCM inside spherical capsules. For a given capacitance ratio, the total and latent utilization is observed to decrease with increase in Reynolds number as a result of insufficient residence time of the incoming cold/hot inlet HTF inside the tank and slower heat exchange between the HTF and spherical PCM capsules,

notwithstanding the increase in Nusselt number. The discharging cut-off temperature is reached quicker for higher Re_{H} as the heat exchange zone expands and contributes to low total utilization. Figure 35c illustrates the total and latent of the LTES as a function of the inverse inverse Stefan number and Re_H. From Figure 35c, it is found that the total utilization, $U_T = \left(Q^*_{S,D} + Q^*_{L,D}\right) \big/ Q^*_{cap}$, of the LTES is highest for inverse Stefan number of 0, which corresponds to a filler material with zero latent heat storage capacity or a sensible thermocline storage system. This is attributed to the low total storage capacity of the system, Q^*_{cap}, as $\psi = 0$, which can be readily observed from Figure 35c with the latent utilization value being zero for $\psi = 0$. As inverse Stefan number increases from 0 to 0.23, it is observed from Figure 35c that the total utilization of the system decreases linearly corresponding to the increase in Q^*_{cap}, while the latent utilization of the system is found to increase in Figure 35c. Beyond $\psi = 0.23$, both the total utilization and latent utilization of the LTES, portrayed in Figure 35c, decreases with increase in inverse Stefan number due to higher thermal inertia concomitant with the increase in latent energy density of the PCM.

Figure 35d reveals that the total and latent utilization is observed to follow a non-monotonic trend with variations in PCM melt temperature for different Reynolds number. For any given Reynolds number or non-dimensional power, the total utilization of the system is found to be significantly higher for PCM with θ_m either between $0 < \theta_m \le \theta'_C$ or between $\theta'_D \le \theta_m \le 1$ (Figure 35d). The two peaks in the latent utilization of the system ($\theta_m = 0.34$ and $\theta_m = 0.76$) are observed for PCM melt temperatures within the above-mentioned constraints (Figure 35d). However, from Figure 35d, it can also be found that the latent utilization of the system decreases from the peak value to zero at PCM melt temperatures of 0 and 1, due to insufficient temperature difference between the PCM melt temperature and incoming HTF temperature to drive the solidification and

melting of PCM, respectively. Within the aforementioned temperature constraints, it is observed that the latent utilization decreases with increase in Reynolds number primarily due to the shorter residence time of the incoming hot and cold HTF to melt and solidify the PCM, respectively (Figure 35d). For PCM melt temperature outside the constraints, $\theta_C^{'} < \theta_m < \theta_D^{'}$, high latent energy utilization is not realized in Figure 35d, and the latent utilization is found to be the least for higher Re_H. At such low latent utilization, it is clear that only a portion of the PCM adjoining the capsule wall is involved in the phase change process and the LTES is in operation for a short duration only due to faster approach of cut-off temperatures. So the heat exchange rate between the HTF and PCM governs the phase change process and hence the latent utilization ratio is observed to be higher for high Reynolds number. Since latent energy is a small portion of the total energy, the total utilization of the LTES is governed by the residence time of the incoming HTF and U_T is

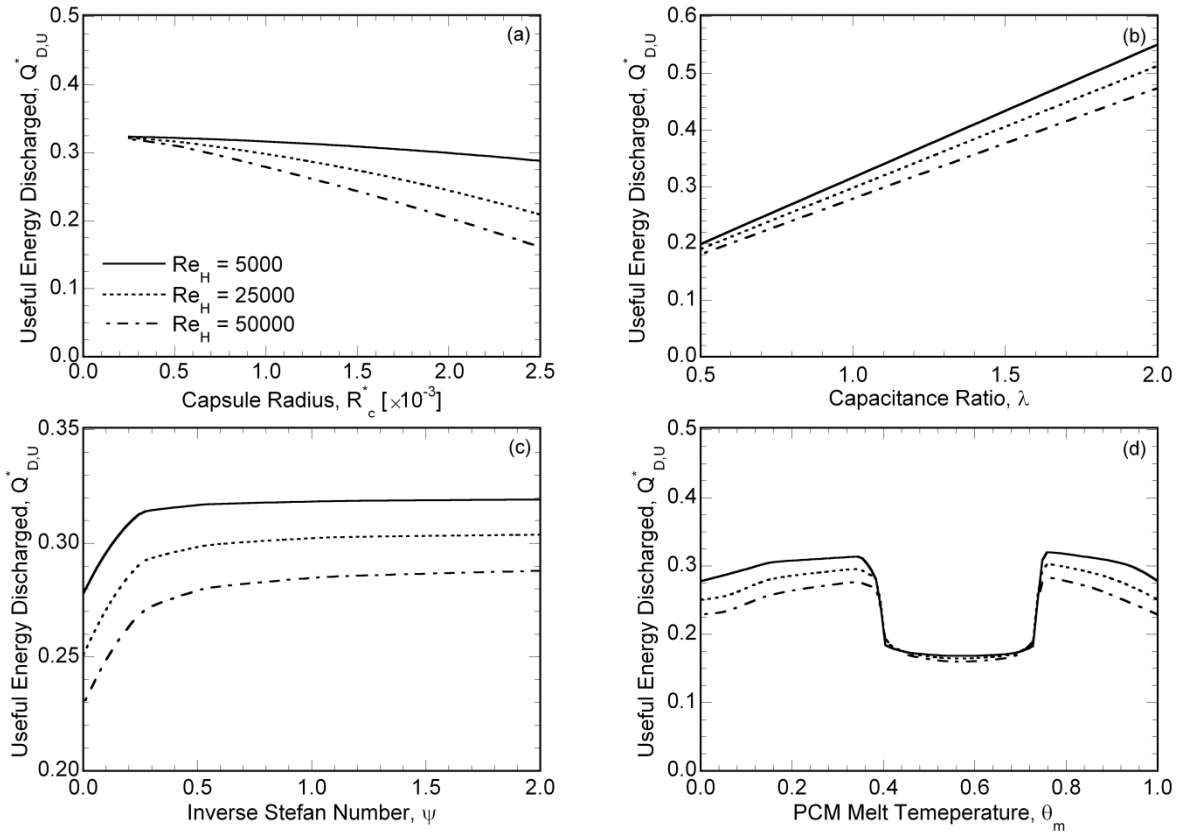

Figure 36: Effects of (a) capsule radius, (b) capacitance ratio, (c) inverse Stefan number and (d) PCM melt temperature on total useful energy discharged by the latent thermocline energy storage system for different Reynolds numbers.

higher for lower Re_{H} even for $\theta_C^{'} < \theta_m \leq \theta_D^{'}$ (Figure 35d). The highest total (latent) utilization of the thermocline between PCM melt temperature constraints of $0 \leq \theta_m \leq \theta_C^{'}$ and $\theta_D^{'} \leq \theta_m \leq 1$ are obtained as 68.43% (46.54%) for $\theta_m = 0.34$ and 69.14 % (39.42 %) for $\theta_m = 0.76$, respectively, for Re_{H} = 5,000, while between $\theta_C^{'} < \theta_m < \theta_D^{'}$ the highest total (latent) utilization is obtained as 43.26% (20.31%) for $\theta_m = 0.4$ and Re_{H} = 50,000. The Reynolds number for a packed bed is usually based on the diameter of the spherical capsules expressed as $\mathrm{Re}_d = \dfrac{\rho_f U(2\times R_c)}{\mu_f}$ which is related to Re_{H} as defined in Eq. (28) by $\mathrm{Re}_H = \dfrac{\mathrm{Re}_d}{2\times R_c^*}$. Figure 35e shows the variation in total and latent utilization with capsule radius for different Reynolds number based on the capsule diameter, Re_{d}. For instance, at Re_{d} = 250 and $R_c^* = 0.0025$, Re_{H} corresponds to 50,000 and it is observed that the total and latent utilization values obtained from Figs. 35a and e comply with each other. The purpose of this plot is to identify if any valuable information can be obtained. For the maximum Reynolds number, Re_{H} = 50000 considered in this study, Re_{d} corresponds to 50 and 250, respectively for non-dimensional capsule radii of 0.00025 and 0.0025, respectively, which shows that the flow within the packed bed is within the laminar regime. The qualitative trends observed in the variations of total and latent utilization with capsule radius for different Re_{H} and Re_{d} as portrayed in Figs. 35a and e are similar.

Figure 36 illustrates the influence of various design and operating parameters on the total useful energy discharged by the thermocline storage system for different Reynolds number (plant power requirements). The variation in capsule radius and PCM melt temperature does not alter the storage capacity of the LTES. Hence, the total useful energy discharged follows the same trend as the utilization trends illustrated in Figure 36a and d for variations in capsule radius and PCM melt temperature, respectively. With increase in capacitance ratio—albeit the decrease in utilization (Figure 35b)—the useful thermal energy discharged (Figure 35b) increases because of increase in system storage capacity as calculated from Eq. (36b). From Figure 36b, it is observed that the effect of Reynolds number on the useful thermal energy discharged for a given capacitance ratio is found to be less significant at lower capacitance ratio concomitant with change in slope in the total utilization slope curve at lower total utilization. Concomitant with increase in energy storage capacity and latent utilization of the system with increase in inverse Stefan number from $\psi = 0$ to $\psi = 0.23$ the total useful energy discharged also increases. Notwithstanding the decrease in total utilization and the latent utilization beyond $\psi = 0.23$ in Figure 35c, the useful thermal energy discharged illustrated in Figure 36c remains the same, because with increase in inverse Stefan number the storage capacity of the storage system also increases (Eq. 36). So, the opposing trends of increase in storage capacity and decrease in total utilization nullify to yield an almost constant useful thermal energy delivery from inverse Stefan number of 0.23 to 2.0. It is observed that the latent utilization of the system is maximum at inverse Stefan number of 0.23 (U_L = 55.85%) in Figure 35c, beyond which no significant increase in total useful energy discharged is observed in Figure 36c and hence can be safely regarded as the optimum inverse Stefan number value for the current default parametric configurations.

The studies discussed so far pertain to varying one parameter at a time with the rest of the parameters kept constant. In order to find the LTES design configuration on the best combination of the dimensionless parameters that maximizes the various performance metrics, numerical simulations were run for $4 \times 3 \times 16 \times 4 \times 4$ different combinations of the five parameters, Reynolds number, capacitance ratio, PCM melt temperature, inverse Stefan number and capsule radius, respectively, for a total of 3,072 cases. Due to the highly nonlinear dependence of utilization on PCM melt temperature sixteen values were chosen to resolve the trends with higher accuracy. Table 9 presents the designs on the combinations of dimensionless parameters culled from the comprehensive parametric studies that maximize the chosen objectives: (1) the useful thermal energy discharged, $Q^*_{cap,u}$; (2) the total utilization, U_T; and (3) the latent utilization, U_L, for different Reynolds number. In each case, the corresponding values of the useful thermal energy discharged and the total and latent utilization values are also tabulated, with the maximum values of the objective function listed in bold face. It is seen from Table 9a that of the cases studied, the best combination of parameters that maximizes $Q^*_{cap,u}$ results in a useful thermal energy discharge of 0.563 (Table 9a.1). Also, it is observed that the maximum thermal energy discharged corresponds to the combination of high capacitance ratio, high inverse Stefan number, small capsule radius and a PCM melt temperature of 0.85, which is within the high temperature range, $\theta'_D \le \theta_m \le 1$. Another important observation is that the total and latent utilization of the LTES corresponding to maximum $Q^*_{cap,u}$ are rather low.

Similarly, the parameter combination listed in Table 9b is seen to be the configuration that maximizes both total and latent utilization. The PCM melt temperature corresponding to the highest utilization for all the thermal power outputs is found to be 0.35, which is within the low

Table 9: Optimum design for EPCM-TES obtained from comprehensive parametric studies

Objective	R_c^*	ψ	θ_m	λ	$Q^*_{cap,u}$	U_T	U_L
a. Maximum Useful Energy Discharged, $Q^*_{cap,u}$							
1. P^*_t = 25000	0.00025	2.000	0.850	2.000	**0.563**	35.586	16.764
2. P^*_t = 62500	0.00025	2.000	0.850	2.000	**0.562**	35.475	16.698
3. P^*_t = 125000	0.00025	2.000	0.850	2.000	**0.560**	35.313	16.614
4. P^*_t = 250000	0.00025	2.000	0.850	2.000	**0.556**	35.090	16.505
b. Maximum Utilization, $U_T(U_L)$							
1. P^*_t = 25000	0.00025	0.25	0.350	0.500	0.199	**83.098**	**68.546**
2. P^*_t = 62500	0.00025	0.25	0.350	0.500	0.199	**82.926**	**68.342**
3. P^*_t = 125000	0.00025	0.25	0.350	0.500	0.198	**82.667**	**68.135**
4. P^*_t = 250000	0.00025	0.25	0.350	0.500	0.197	**82.254**	**67.825**

temperature range, $0 \le \theta_m \le \theta_D^{'}$. This is due to the requirement of higher temperature difference between the incoming cold fluid temperature and the PCM melt temperature during the discharge process, resulting in a high latent utilization. On further inspection, it is found that low capacitance ratio and low inverse Stefan number maximize system utilization (Table 9b), which is in contrast to the results obtained for maximum total energy discharged (Table 9a). Note that the maximum total thermal energy discharged and the maximum system utilization marginally decrease with increase in thermal power output. For low thermal power output, the fluid interacts with the PCM capsules for a long time and, correspondingly, the highest maximum useful energy discharged and maximum total utilization and latent utilization are obtained for $\mathrm{Re}_H = 5000$, c.f. $Q^*_{cap,u} = 0.563$ (Table 9a.1) and $U_T = 83.10\%, U_L = 68.55\%$ (Table 9b.1).

As presented, the total utilization of LTES is closely related to PCM melt temperature, inverse Stefan number, capacitance ratio, capsule radius and Reynolds number. The numerical

results can be correlated with a maximum deviation less than 5% and mean squared error less than 3.6×10^{-4} by the following nonlinear relationship:

$$U_T = \left[\left(a_1\theta_m^2 + a_2\theta_m + a_3\right) + a_4\lambda^{\left(a_5(\mathrm{Re}_H/1000)+a_6R_c^*\right)} + a_7\ln(\psi)\right]\cdot e^m, 0<\theta_m<\theta_C^{'} \text{ and } \theta_D^{'}<\theta_m<1 \qquad (37)$$

where $m = -a_8R_c^*(\mathrm{Re}_H/1000) + a_9(\mathrm{Re}_H/1000) + a_{10}R_c^*$ and e represents the exponential function. The coefficients a_1, a_2, and a_3 for PCM melt temperature within the temperature constraint $0\le\theta_m\le\theta_C^{'}$ ($\theta_D^{'}\le\theta_m\le1$) are obtained to be –0.6906 (–3.4142), 0.4947 (5.7774), 0.2039 (–2.1585), respectively, while a_4,…,a_{10} are obtained to be 0.309, –0.004, –163.1, –0.1755, 5.69, 0.0012, and –59.6, respectively. The power law dependence on capacitance ratio in Eq. (37) reflects the monotonic increase in total utilization with increase in capacitance ratio (Figure 35b), while the logarithmic dependence on the inverse Stefan number captures the quick rate of decrease in utilization initially after which it levels out with increase in inverse Stefan number as portrayed in Figure 35c. The exponential dependence of utilization on Reynolds number and capsule radius corroborates with the trends observed in Figure 35a, which shows an exponential decrease in utilization for higher capsule radius and Reynolds number. Within the aforementioned temperature constraints, the utilization is found to increase first and then decrease as illustrated in Figure 35d which is captured by the polynomial function in melt temperature. The correlation of total utilization for PCM melt temperatures between $\theta_C^{'}\le\theta_m\le\theta_D^{'}$ is not derived due to the low total utilization of the LTES as presented in Figure 35d.

5.7 Design Example

Based on the foregoing discussion, a procedure for designing a thermocline tank packed with PCM capsules is presented in this section. The storage fluid (HTF) and the PCM selected for the

purpose of illustration are a binary sodium/potassium salt mixture (60% $NaNO_3$ + 40% KNO_3) [50] and eutectic mixture of Li_2CO_3(20)–60Na_2CO_3–20K_2CO_3 [52], respectively. The dimensionless melt temperature, capacitance ratio, Prandtl number and inverse Stefan number for the selected combination of HTF and PCM are 0.915, 0.718, 5.45 and 0.574, respectively. The charge and discharge temperatures of the solar salt for the power plant operation are considered to be 574 $^{\circ}$C and 290 $^{\circ}$C respectively [50], typical of molten salt power tower operation. For a given power plant operation, the thermal discharge power requirement, P_t and the useful thermal energy storage (discharge) capacity, Q^*_{cap}, are pre-determined by the nameplate capacity. For a known capsule radius, the recommended design procedure is detailed below for dimensionless charging and discharging cut-off temperatures of 0.39 and 0.74, respectively.

1. Calculate the volume of the tank, V_t, required to meet the required thermal storage (discharge) capacity, $Q_{cap,u} = Q_{cap} \times U_T$ from Eq. (35) assuming a total utilization of U_T = 1 for the first iteration. The ideal LTES generally has a small volume requirement.
2. Choose the tank height based on the soil bearing capacity of the location and with the calculated tank volume, V_t, calculate the radius of the tank, R_t, and β appearing in Eqs. 36a and b. From the chosen tank height, the non-dimensional capsule radius, $R^*_c = R_c / H_t$ can also be calculated.
3. Calculate the nondimensional thermal discharge power, P^*_t, and the nondimensional useful thermal energy, $Q^*_{cap,u} = Q^*_{cap} \times U_T$, from Eqs. 36a and b, respectively.
4. Calculate Re_H from the known P^*_t, Pr_f and determine U_T from Eq. (37).
5. With the new U_T values, repeat steps 1-4 until the newly obtained U_T closely matches the previous iteration value.

6. The final R_t is the required tank radius.

Table 10 presents some examples of designing a latent thermocline based energy storage based on the procedure outlined above for various power plant requirements. For comparison, the results obtained from the numerical values and that of sensible thermocline storage system, which employ Quartzite rocks as the filler material are also listed in Table 10. Two different heights of the tank based on the soil bearing capacity are considered. For instance based on the analysis in [76], the soil in Barstow, California could withstand a maximum structure height of 15 m, which is one of the potential CSP installation sites. Examples in Table 10 show the tank radius required for different PCM capsule radius. The deviation between the tank radius values obtained from numerical simulations and the correlation (Eq. (37)) is found to be less than 2%. Generally, it is observed that for a given storage capacity time, with increase in thermal power output, the radius of the tank required increases due to higher storage capacity. Also, the tank radius increases with increase in capsule radius because of lesser utilization with increase in R_c^* as observed from the trends in Figure 35. The use of small sized PCM capsules reduces the tank radius greatly, due to higher system utilization, which not only reduces the material cost for tank construction but also decreases the surface area for heat loss to the environment. Also, it is found that at least 34% reduction in the tank radius is observed for LTES compared to sensible thermocline storage system for the various thermal power requirements listed in Table 10. Overall, the results in this section illustrate a methodology for analyzing a latent thermocline storage system corresponding to CSP plant operation requirements, and provide important design guidelines in a dimensionless form, valid for any combination of PCM and HTF. The modeling presented in this chapter is extended to include a detailed exergy analysis and optimization as well as analysis of cascaded latent thermocline storage systems in Chapter 6.

Table 10: Design example results obtained from numerical simulations for EPCM-TES system

Case No.	P_t [MW]	Q_{cap} [MW-h]	R_c [m]	H_t [m]	R_t [m]		
					Simulations	Correlation [Eq. (15)]	Sensible
1	500	3000	0.0075	10	18.436	18.538	24.871
2	500	3000	0.001	10	18.584	18.800	25.003
3	500	3000	0.002	10	19.409	19.851	25.672
4	500	3000	0.0075	15	15.039	15.023	20.295
5	500	3000	0.001	15	15.153	15.211	20.393
6	500	3000	0.002	15	15.795	15.950	20.915
7	1000	6000	0.0075	10	26.072	26.217	35.172
8	1000	6000	0.001	10	26.281	26.587	35.359
9	1000	6000	0.002	10	27.449	28.073	36.306
10	1000	6000	0.0075	15	21.268	21.246	28.701
11	1000	6000	0.001	15	21.430	21.512	28.840
12	1000	6000	0.002	15	22.338	22.556	29.578

5.8 Nomenclature used in Chapter 5

b capsule wall thickness [m]

c specific heat [J/kg-K]

f_L liquid fraction

h convective heat transfer coefficient [W/m^2-K]

h_l latent heat of fusion of PCM [J/kg]

H height [m]

k thermal conductivity [W/m-K]

$\dot{m}$ mass flow rate [kg/s]

Nu Nusselt number

P_e electrical power output [MW$_e$]

Pr Prandtl number

P_t thermal power output [MW_t]

Q energy [MJ]

R radius [m]

Re Reynolds number

t time [s]

T temperature [K]

T_m melting temperature [K]

Greek Symbols

ε porosity of the packed bed

μ dynamic viscosity

ρ density

Subscripts and Superscripts

c capsule

cap storage capacity

C charging

D discharging

f heat transfer fluid

L latent

p phase change material

S sensible

t tank

T total

eff effective

Chapter 6: Design and Optimization of a Encapsulated PCM Thermal Storage System

This chapter builds on the encapsulated PCM thermal energy storage (EPCM-TES) system model developed in Chapter 5 to investigate the influence of the design and operating parameters on the dynamic energy and exergy performance of the EPCM-TES system. Based on the parametric studies operating windows are developed that satisfy the SunShot Initiative targets [35], which include, storage cost less than \$15/kWh$_t$, round-trip exergetic efficiency greater than 95% and charge time less than 6 hours for a minimum discharge period of 6 hours. The operating regimes are identified as a function of the various design parameters for cascaded and non-cascaded EPCM-TES systems. A further contribution of the study involves finding the optimum combination of design and operating parameters of the EPCM-TES system subject to the aforementioned constraints for successful deployment in CSP plants. Overall, this study illustrates a methodology for design and optimization of encapsulated PCM thermal energy storage system (EPCM-TES) for a CSP plant operation.

6.1 Model Inputs and Outputs

The non-dimensional operating and design parameters analyzed in the present study are the Reynolds number, Re_{H}, capsule radius, R_c^*, inverse Stefan number, ψ, and the melt temperature, θ_m. The default case pertains to $R_c^* = 0.001$; $\mathrm{Re}_H = 25000$; $b^* = 5\times10^{-8}$; $\psi = 0.5$; $\theta_m = 0.75$; $\mathrm{Pr}_f = 5$; $\lambda = 1$; $k_w^* = 1$; $k_p^* = 1$; $\varepsilon = 0.25$. For the 2-PCM cascaded EPCM-TES, the default non-dimensional melt temperature at the top and bottom zone pertains to $\theta_{m,T} = 0.75$ and $\theta_{m,B} = 0.25$, respectively, and the default PCM melt temperature at the mid zone for 3-PCM cascaded

configuration taken as $\theta_{m,M} = 0.50$ for 3-PCM cascaded configuration. The non-dimensional height of each individual zone (Figure 29) in cascaded configuration is defined as $H^*_{p,q} = H_{p,q} / H_t$ where p denotes the number of cascades and subscript q denotes either T (top zone), M (mid zone) or B (bottom zone). The numerical model presented in Chapter 5 forms the basis of the parametric studies discussed in Section 6.3 and is also used in a numerical optimization of the EPCM-TES system as formulated in Section 6.4.

6.2 Performance Metrics

Since the dynamic behavior of the storage system subjected to partial charge and discharge process is of primary interest to the designer, repeated charging and discharging process are carried out until a periodic state is achieved. The performance of the EPCM-TES system is analyzed following repeated charge and discharge processes until a periodic state is established, when the variations from one cycle to another is less than 0.5% as explained in Chapter 5.

The exergetic efficiency of the EPCM-TES defined as the ratio of exergy recovered by the HTF during discharging to the exergy gained by the HTF during charging of the periodic cycle [48]:

$$\zeta = \frac{\int_{t_C}^{t_D} \left\{ T_f(z=0,t) - T_D) - T_{ref} \ln\left(\frac{T_f(z=0,t)}{T_D} \right) \right\} .dt}{\int_{0}^{t_C} \left\{ T_C - T_f(z=H_t) - T_{ref} \ln\left(\frac{T_C}{T_f(z=H_t)} \right) \right\} .dt} \tag{38}$$

where T_{ref} is the reference or ambient temperature which for the purpose of the analysis is assumed to be 300 K [48]. The term, T_{f} (z = 0, t) in the numerator refers to the exit temperature of the HTF at the top of the thermocline storage tank during discharging while the term T_{f} ($z = H_{\mathrm{t}}$, t) in the denominator refers to the temperature of the HTF at the bottom of the EPCM-TES system,

which is the outlet for charging. The exergetic efficiency cannot be calculated in terms of non-dimensional variables because the logarithmic term in the denominator always tends to infinity, since the non-dimensional variable of T_D, viz. θ_D as defined in Eq. (38) equals zero. Hence the charge (T_C) and discharge (T_D) temperatures for the calculation of exergetic efficiency are considered to be 574 ^oC and 290 ^oC, respectively [50], typical of molten salt power tower operation. Typically, at least five cycles are required for the storage system to achieve the periodic state for the range of parametric values considered in the present study.

6.3 Parametric Studies

Figure 37 illustrates the cyclic behavior of the axial temperature distribution of the HTF, θ_f, subjected to five cycles of the charging and discharging process for 2-PCM and 3-PCM cascaded EPCM-TES system. The cyclic variation in the axial HTF temperature distribution for a non-cascaded EPCM-TES system is explained in Chapter 5. The axial HTF temperature profiles illustrated in Figure 37 correspond to an inverse Stefan number of 0.25 and capacitance ratio of 0.5, top, mid and bottom zone PCM melt temperatures of 0.9, 0.5 and 0.1, respectively and a capsule radius of $R_c^* = 0.0015$. The rest of the parameters retain the default values listed in Section 6.1. Figure 37a and b shows the axial temperature distribution of the HTF, θ_f in a 2-PCM cascaded EPCM-TES system at various instants of time during the charge and discharge process respectively for cycle 1 while Figure 37i and j represents the same for 3-PCM cascaded EPCM-TES system. Initially at $t^* = 0.0$, the tank is in a completely discharged state and the PCM is in the solid phase (Figure 37a and i), while hot HTF enters the EPCM-TES storage system at $z^* = 0$. At time $t^* = 2.0\times10^{-6}$, in Figure 37a and i it is observed from $z^* = 0$ to $z^* = 0.1$ that the hot HTF

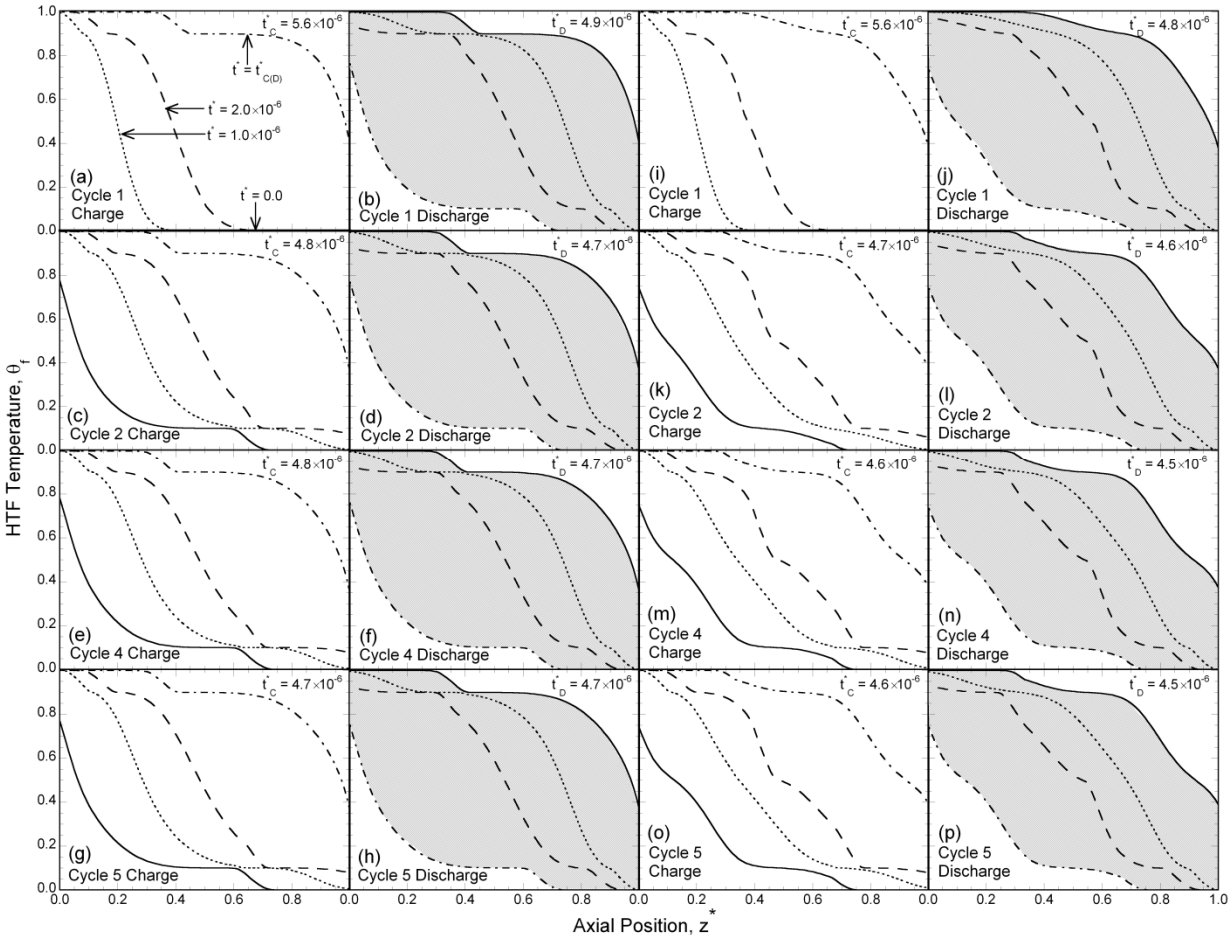

Figure 37: Temporal evolution in the axial distribution of HTF temperature, during repeated charging and discharging cycles for (a–h) 2-PCM and (i–p) 3-PCM cascaded EPCM-TES system.

exchanges energy with the PCM and reaches the highest temperature, $\theta_f = 1$, while from $z^* = 0.15$ to $z^* = 0.25$, the energy extracted from the HTF is utilized in melting the PCM while from $z^* = 0.6$ to $z^* = 1$, no energy exchange has taken place and the system is at the initial state.

The sloped line between $\theta_f = 1$ and constant melt temperature zone ($\theta_m = 0.9$); and between the constant melt temperature zone and $\theta_f = 0$ reflects the sensible energy transfer from the hot HTF to PCM in the liquid and solid phase respectively. As charging proceeds the HTF temperature

at the exit of thermocline storage system, $z^* = 1$ reaches the charging cut-off temperature, $\theta_C^{'}$ at $t^* = 5.6\times10^{-6}$. The charging process is followed by the discharge process, – during night and cloudy conditions – which is continued until the temperature of the HTF exiting the tank (θ_f at $z^* = 0$) and entering the power block reaches 0.74 ($\theta_D^{'}$). During the cyclic operation, the charging temperature profile of the first process becomes the initial condition of the subsequent discharge process which in turn becomes the initial condition of the next charge process and so on. Hence the discharge temperature profile at $t^* = 0.0$ in Figure 37b is the same as the temperature profile at $t^* = 5.6\times10^{-6}$ in Fig. 3a. The percentage of the shaded area in Figure 37b and j shows a visual representation of the total utilization of the system, as defined in Chapter 5, which denotes the percentage of total (sensible and latent) energy discharged from the cycle.

In Figure 37c, two constant temperature zones, one between $z^* = 0.2$ and $z^* = 0.3$ at $\theta_f = 0.9$ corresponding to the PCM melt temperature at the top zone and the other between $z^* = 0.7$ and $z^* = 1.0$ at $\theta_f = 0.1$ corresponding to the PCM melt temperature at the bottom zone are observed for $t^* = 2.0\times10^{-6}$ (dashed line). Comparing Figure 37a and c, it is observed that the temperature profile at $t^* = 0.0$ in Figure 37c corresponds to the temperature profile of the HTF at the end of the previous discharge process (Figure 37b) while $t^* = 0.0$ in Fig. 3a corresponds to a fully discharged state. Also, total charge time during the second cycle is observed to be $t_C^* = 4.8\times10^{-6}$ (Figure 37c) compared to $t_C^* = 5.6\times10^{-6}$ during cycle 1 (Figure 37a). Similarly the total discharge time during cycle 2 is $t_D^* = 4.7\times10^{-6}$ (Figure 37d) compared to $t_D^* = 4.9\times10^{-6}$ during cycle 1 (Figure 37b). Subsequent cycles were carried out until the HTF axial temperature distribution within the tank reached a cyclic periodic state independent of the initial condition as seen by the negligible

variation in the charge and discharge times between cycles 4 and 5 indicated in Figure 37e–h. The total utilization of the system decreases from 75.77% in cycle 1 to 72.85% in cycle 4 and 72.80% in cycle 5.

Following the presentation format for 2-PCM cascaded EPCM-TES, for a 3-PCM cascaded configuration, three constant temperature zones are observed at $t^* = 2.0\times10^{-6} - \theta_f = 0.9$, $\theta_f = 0.5$, and $\theta_f = 0.1$ – corresponding to the PCM melt temperatures at the top, middle and bottom zones, respectively in Figure 37k and l. The total system utilization for a 3-PCM cascaded configuration at the periodic cycle (Figure 37o and p) is 88.28% with lower charge ($t_C^* = 4.6\times10^{-6}$) and discharge time ($t_D^* = 4.5\times10^{-6}$) compared to 2-PCM cascaded EPCM-TES system. The total utilization of the system decreases from 75.97% in cycle 1 to 69.74% in cycle 4 and 69.63% in cycle 5. In spite of the low total utilization compared to 2-PCM cascaded EPCM-TES system, the latent utilization of the system defined as the ratio of latent energy discharged to the latent storage capacity of the EPCM-TES system, as defined in Chapter 5, is obtained to be 98.59% for 3-PCM cascaded compared to 71.85% obtained for 2-PCM cascaded EPCM-TES system. Hence cascading improves the uniformity of temperature difference between the HTF and PCM resulting in efficient PCM solidification, resulting in a faster charge and discharge time for all the cycles in Figure 37i–p.

Figure 38a–e shows the axial charge and discharge temperature profile of the HTF inside the EPCM-TES at the end of the final cycle (periodic state) for various Re_H, R_c^*, λ, ψ, θ_m of non-cascaded EPCM-TES system respectively and Figure 38f shows the same for bottom zone height , $H_{t,B}^{'}$ of 2-PCM cascaded EPCM-TES system. The range of the Reynolds number and the non-

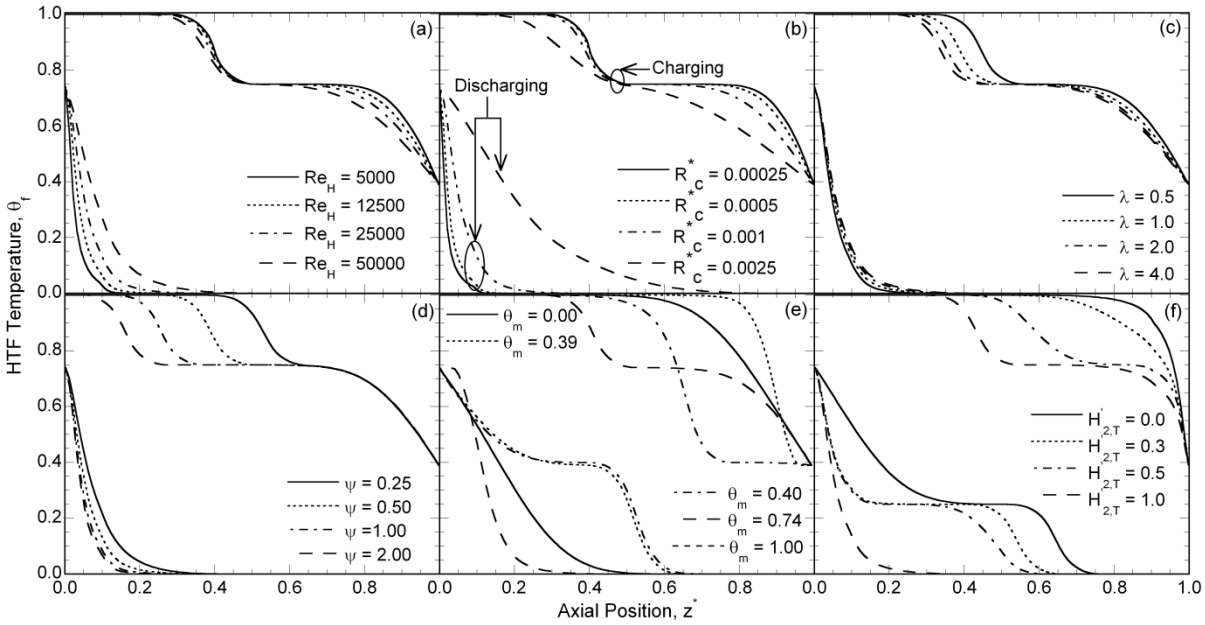

Figure 38: Parametric study of (a) Reynolds number (b) capsule radius, (c) capacitance ratio, (d) Stefan number, (e) PCM melt temperature on the axial HTF temperature at the end of final charging and discharging process for non-cascaded and (f) top zone height on 2-PCM cascaded EPCM-TES system.

dimensional capsule radius values chosen for this study corresponds to the practical design of a EPCM-TES system for CSP plant. The effect of Re_H on the axial charge and discharge temperature profile of the HTF illustrated in Figure 38a shows that with increase in Re_H, the area between the axial HTF temperature variation at the end of the charge and discharge process of the final cycle reduces, reflecting a decrease in the total system utilization. As Re_H increases, the residence time of the incoming HTF in the EPCM-TES system is shorter leading to a decrease in the heat exchange between the HTF and PCM, notwithstanding, an increase in the convective heat transfer coefficient with increase in Re_H. From Figure 38b, it is observed that increasing R_c^* results in an expansion of the heat exchange zone and restricts the formation of constant melt-temperature zone implying negligible latent utilization of the system. This is attributed to the fact that

increasing the capsule radius, results in an increased resistance to the thermal conduction within the PCM stored inside the capsules — albeit an increase in the convective heat transfer coefficient (Eq. (28)) and surface area — which limits the heat exchange rate between the HTF and PCM.

The effect of capacitance ratio, λ, on the axial temperature profile of the HTF temperature at the final (periodic) cycle is plotted in Figure 38c. It is observed that with increase in capacitance ratio, the extent of the constant low temperature zone and high temperature zone decreases. This can be explained with reference to high thermal inertia posed to the temporal variation of the PCM temperature inside spherical capsules for high capacitance ratio, resulting in a slower extraction of thermal energy from the filler materials. Figure 38d portrays the effect of inverse Stefan number on the quasi-steady HTF temperature profile for thermocline storage system operation. Similar to the effect of capacitance ratio, higher inverse Stefan number leads to lesser system utilization due to the high thermal inertia imposed on the temporal variation of melt fraction in the PCM. The total system utilization decreases with increase in λ and ψ, from 70.28% at $\lambda = 0.5$ to 61.66% at $\lambda = 2.0$ and 73.55% at $\psi = 0.25$ to 36.46% at $\psi = 2.0$, respectively. Although the total utilization decreases, it is found that the non-dimensional total energy discharged, product of energy storage capacity of the system and the total system utilization, during the final cycle increases from 0.19 to 0.51 for increase in λ from 0.5 to 2.0. For increase in ψ from 0.25 to 2.0, the total energy discharged increases from 0.29 to 0.30 only, due to higher volumetric system storage capacity. Correspondingly, the discharge time increases with increase in capacitance ratio and inverse Stefan number.

Figure 38e presents the effect of PCM melt temperature on the axial HTF temperature profile at the end of charge and discharge process during the final cycle (periodic state). Figure 38e shows

that possessing a melt temperature between the low temperature and charge cut-off temperature, $0 < \theta_m \le \theta_C^{'}$ or between the discharge cut-off temperature and high temperature, $\theta_D^{'} \le \theta_m < 1$ extends the operation of the thermocline storage system. This can be readily understood by observing the HTF temperature profile at the end of charge and discharge process for a PCM melt temperature of $\theta_m = 0.4$, which falls outside the aforementioned ranges. The total utilization of the thermocline system with PCM of melt temperature $\theta_m = 0.4$ amounts to 42.37% while the total utilization of the thermocline system with PCMs of melt temperature, $\theta_m = 0.39$ and $\theta_m = 0.74$ are 60.22% and 60.16% respectively. The highest total utilization is observed for PCM of melt temperature $\theta_m = 0.75$. The temperature profiles for $\theta_m = 0.0$ and $\theta_m = 1.0$ falls on top of one another and is not discernible in Figure 38e. Figure 38f illustrates the effect of varying the top zone height, $H_{2,T}^{'}$ on the axial HTF temperature profiles at the end of charge and discharge process for a 2-PCM cascaded configuration. By varying the height of the top zone, it is found that the total utilization is highest at 80.19% when the height of the EPCM-TES system is divided equally between the high and low melt temperature PCMs in the top and bottom zones, respectively. Similar observation is observed for a 3-PCM cascaded configuration (not illustrated here) in that the total utilization of the system is highest when the height of the thermocline storage system, H_t is divided equally among the three PCMs with melt temperatures of 0.25, 0.50 and 0.75 in the top, middle and bottom zones, respectively.

With the overview of the thermal transport process illustrated in Figure 37 and Figure 38, the model is further used in a parametric study to evaluate the performance of the thermocline storage system over a wide range of design and operating conditions. In this study, three quantities obtained from the numerical model namely, the charge time, discharge time and the exergetic

efficiency as detailed in Section 6.2 are examined for various design and operating parameters to evaluate the thermocline storage performance.

Figure 39a–f illustrates the effect of the non-dimensional parameters on the various performance metrics of the storage system namely, the charge time, discharge time and exergetic efficiency for a non-cascaded thermocline storage system configuration. From Figure 39a and b, it is observed that charge time and discharge time decreases with increase in Reynolds number and capsule radius due to the shorter residence time of the incoming HTF with increase in Re_{H} for effective heat exchange between the HTF and PCM and increase in thermal conduction resistance in the PCM with increase in R_c^*, respectively. Figure 39c illustrates the effect of capsule radius and Reynolds number on the exergetic efficiency of the system. It is observed that for a capsule radius of $R_c^* = 0.00025$, the influence of Reynolds number on the exergetic efficiency is not pronounced while for larger diameter capsules, the exergetic efficiency decreases with increase in Reynolds number. The variation in performance metrics are illustrated for the effect of capacitance ratio on the charge time, discharge time and exergetic efficiency of thermocline storage system in Figure 39d–f. For a given Reynolds number the charge time and discharge time is found to increase with increase in capacitance ratio due to the increase in volumetric heat capacity of the system (Figure 39d and e). The same observations are found with exergetic efficiency although the roles are reversed in that it is found that exergetic efficiency is greater for system with smaller capacitance ratio (Figure 39f). This is attributed to the fact that even though the charge and discharge times are longer for a higher capacitance ratio, concomitant with increase in storage capacity, the HTF exit temperature is at the PCM melt temperature ($\theta_m = 0.75$) for longer portion of discharge process

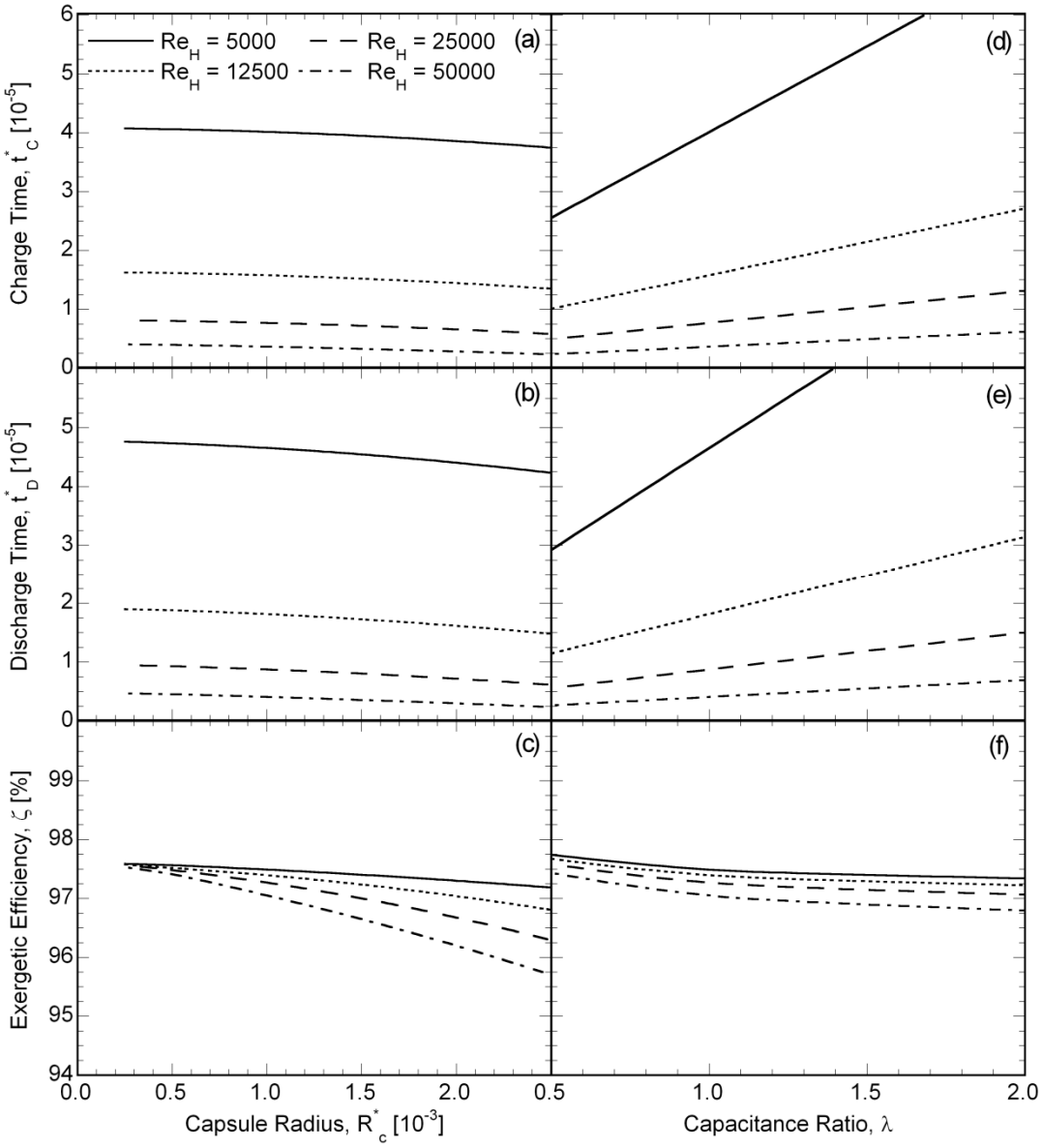

Figure 39: Variation in (a, d) charge time, (b, e) discharge time and (c, f) exergetic efficiency with capsule radius and capacitance ratio, respectively of non-cascaded EPCM-TES system for different Reynolds number.

compared to the system with smaller capacitance ratio.

Figure 40a–c portrays the various performance metrics of the EPCM-TES system as a function of Re_H calculated for different inverse Stefan number, ψ. It is observed that the charge

and discharge time increases with increase in inverse Stefan number, albeit to a reduced order of magnitude (Figure 40a and b). This can be explained with reference to the observations in Figure 39d in that — notwithstanding the decrease in total system utilization with increase in inverse Stefan number — the total energy discharged marginally increases leading to a meager increase in the charge and discharge time (Figure 40a and b). Comparing Figure 40a and b it can be inferred that the effect of inverse Stefan number on the discharge time is more pronounced than on charge time. It is primarily due to the fact that the default PCM melt temperature value chosen ($\theta_m = 0.75$) leads to slower PCM melting due to weaker driving force for melting ($\Delta\theta_C = \theta_C - \theta_m$). For the same reasons, the charge time in Figure 40a is found to be faster than the discharge time in Figure 40b because the cut-off temperature is attained faster for lower Reynolds number. At higher Reynolds number, both the charge and discharge time is approximately the same, due to the shorter residence time of the incoming HTF within the thermocline tank owing to faster velocity inlet. For any given Reynolds number, it is found from Figure 40c that the exergetic efficiency decreases with increase in inverse Stefan number. At higher inverse Stefan number, longer discharge time at the PCM melt temperature, which is lesser than the high temperature ($\theta_f = 1.00$) leads to larger exergy destruction and hence reduced exergetic efficiency.

Figure 40d-f illustrates the variation of charge time, discharge time and exergetic efficiency with Reynolds number for various PCM melt temperatures. At any given Reynolds number, the charge time is found to increase from $\theta_m = 0.00$ to $\theta_m = 0.39$, which is the charging cut-off temperature. This is clearly evident in the inset figure of Figure 40d and can be explained by the fact that the driving force for PCM melting which manifests as the temperature difference between the incoming hot HTF and the PCM melt temperature decreases leading to slower charge rate.

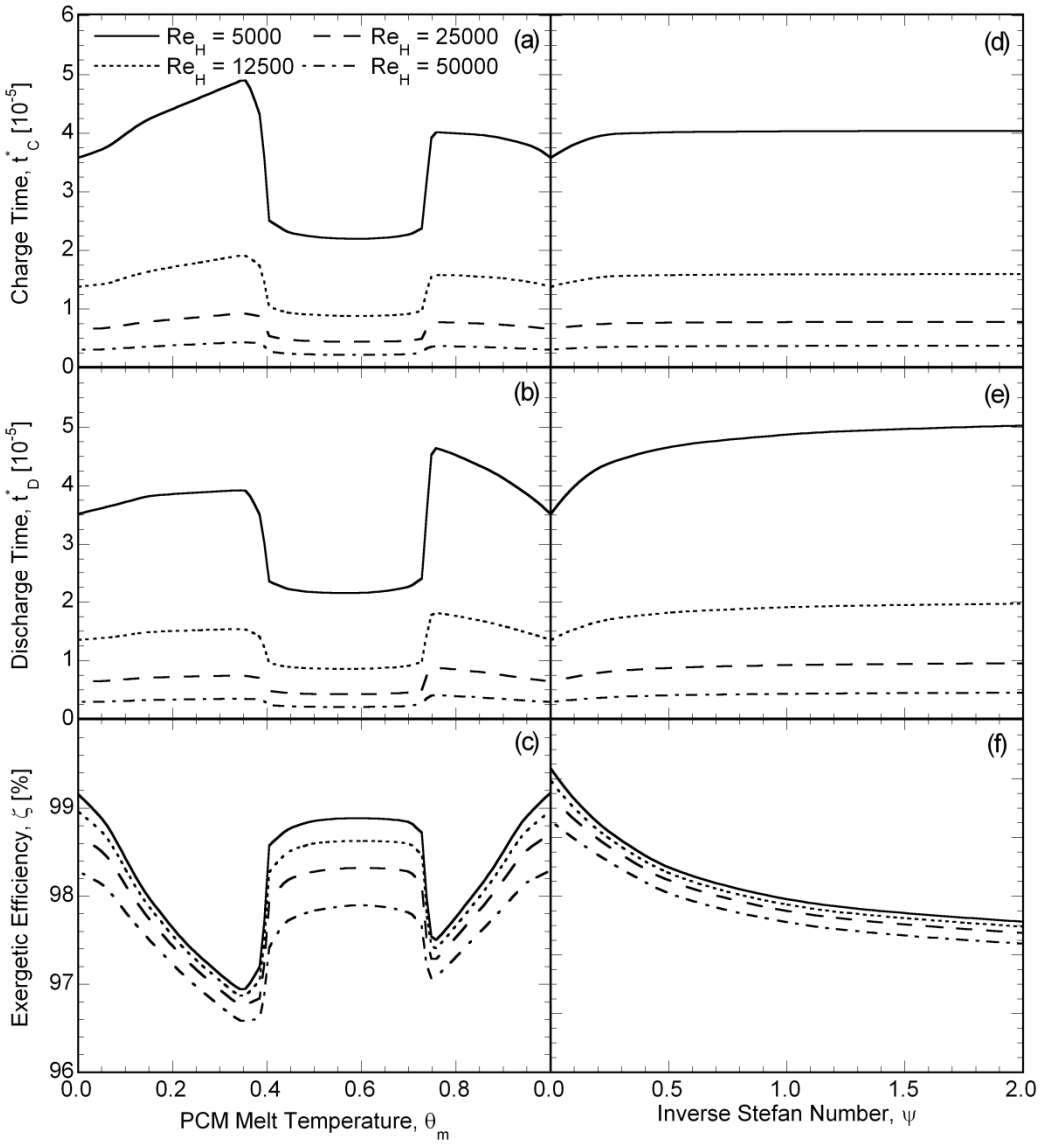

Figure 40: Variation in (a, d) charge time, (b, e) discharge time and (c, f) exergetic efficiency with inverse Stefan number and PCM melt temperature, respectively of non-cascaded EPCM-TES system for different Reynolds number.

Also, for $\theta_m = 0.00$, discharge process does not lead to PCM solidification and hence the thermocline storage system works only in the sensible regime during the cyclic operation. This is also confirmed by calculating the latent utilization of the system, defined as the amount of latent energy extracted from the system to the total latent energy capacity of the system, which amounts

to zero. The aforementioned reason also applies for $\theta_m = 1.00$ with the only difference being no driving force exists for PCM melting during charge process. It is seen that for $\theta_m = 0.40$, the charge time is faster due to insignificant system utilization as it falls outside the low temperature and charge cut-off temperature range, $0 < \theta_m \le \theta_C^{'}$ and the discharge cut-off temperature and high temperature range, $\theta_D^{'} \le \theta_m < 1$. This leads to insufficient sensible and latent utilization of the system for optimum performance of the thermocline storage system.

The same trend can also be observed in the discharge time for PCMs with melt temperature between $\theta_C^{'} \le \theta_m \le \theta_D^{'}$, which is clearly evident in the inset of Figure 40e. However, comparing the inset plots in Figure 40d and e, opposite trends are observed when the PCM melt temperature increases from 0.00 to 0.39, because the temperature difference between the incoming cold HTF and the PCM melt temperature driving the PCM solidification increases leading to faster discharge time. Hence from Figure 40d and Figure 40e, it can be observed that charge time is maximum at $\theta_m = 0.38$ while the discharge time is maximum at $\theta_m = 0.75$ for any given Reynolds number. The exergetic efficiency is higher for PCMs with melt temperatures of either 0 or 1 because of operation in the sensible regime leading to almost equal charge and discharge time (Figure 40f). For PCM with melt temperature between $\theta_C^{'}$ and $\theta_D^{'}$ the exergetic efficiency is relatively high as clearly seen from the inset plot in Figure 40f because of similar reason as for PCM melt temperatures 0 and 1 in that, predominantly sensible energy transfer takes place compared to latent energy utilization. Even though the exergetic efficiency of PCM's with melt temperatures in the feasible operating range, namely $0 < \theta_m \le \theta_C^{'}$ and $\theta_D^{'} \le \theta_m < 1$, is lesser than the rest, it is to be noted that the exergetic efficiency is still greater than 95%. Also, from the inset plots in Figure 40d–f, it can be observed that charge time, discharge time and exergetic efficiency, respectively,

for any given PCM melt temperature decreases due to the shorter residence time of the incoming HTF concomitant with increase in Reynolds number.

From previous plots, it is observed that the exergetic efficiency for almost all of the parametric values are greater than 95% which was also verified for other parametric combinations as well and hence is not illustrated further on. In the interest of brevity, the charge time is also not plotted further on as it exhibits similar trend as the discharge time for any given Reynolds number and follow the same variations as illustrated for non-cascaded configuration in Figure 39 and Figure 40.

To this extent, Figure 41a and b displays the effect of bottom zone PCM melt temperature and top zone PCM melt temperature, respectively, as a function of Reynolds number for a 2-PCM cascaded EPCM-TES system configuration. It is observed from Figure 41a, that the discharge time increases with increase in bottom zone PCM melt temperature until $\theta_{m,B} = 0.39$, which is the charging cut-off temperature after which it decreases and remains constant. It is observed that the decrease in discharge time as the PCM melt temperature in the bottom zone decreases from charging cut-off temperature to higher melt temperature is not as high as observed for non-cascaded EPCM-TES system configuration (Figure 40e) because of the fact that the PCM melt temperature at the top zone ($\theta_m = 0.75$) extends the system operation. Correspondingly, for the variations of PCM melt temperature at the top zone (Figure 41b), it is observed that the discharge time is higher for PCM's possessing a melt temperature greater than 0.74, which is the discharge cut-off temperature. However, it is seen that with subsequent increase beyond $\theta_{m,T} = 0.8$ in PCM melt temperature at the top zone — for which the discharge time is $t_D^* = 5.26 \times 10^5$ compared to a discharge time of 5.45×10^5 for $\theta_{m,T} = 0.74$ — the discharge time decreases due to impediment in

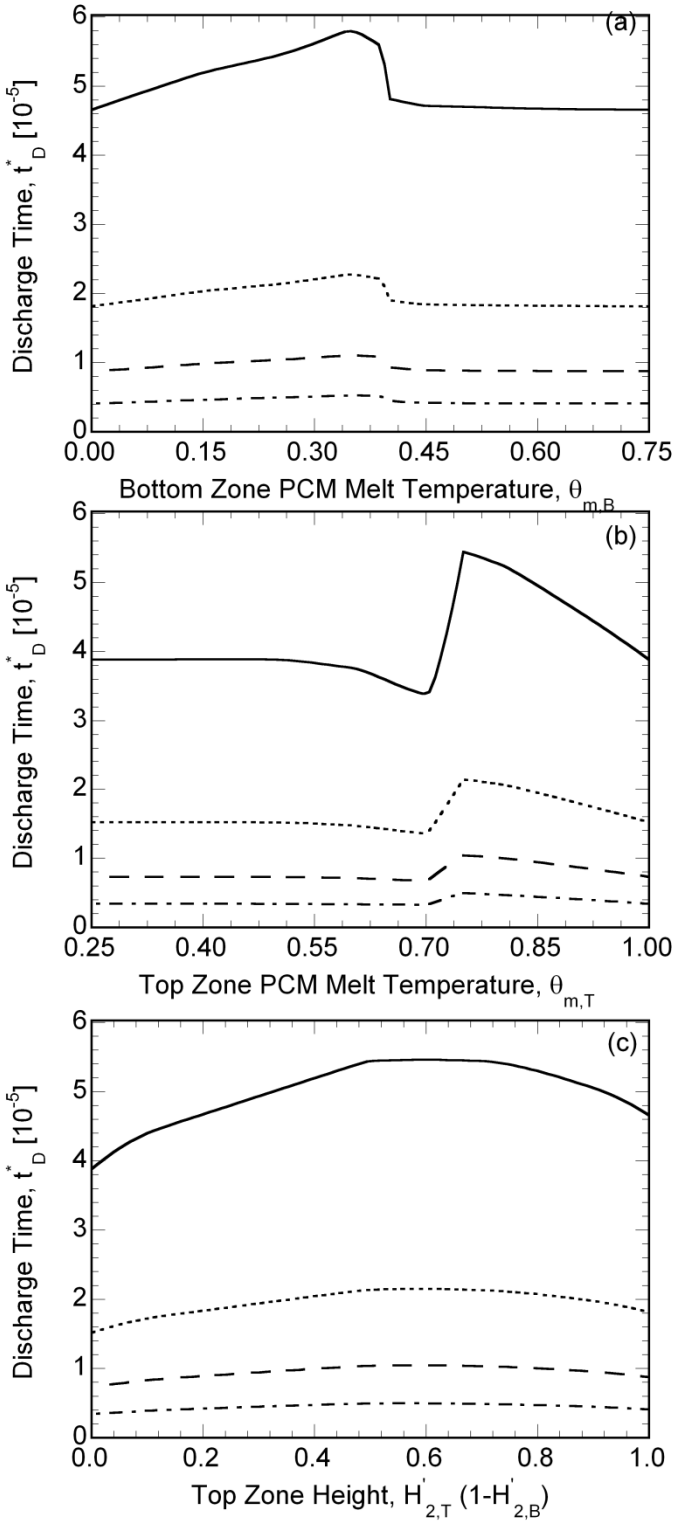

Figure 41: Variation in discharge time with (a) bottom zone PCM melt temperature (b) top zone PCM melt temperature, and (c) top zone height of 2-PCM cascaded EPCM-TES system for different Reynolds number.

the melting of PCM as $\Delta\theta_C$ decreases. The same phenomena can be observed in Figure 41a, although for temperatures below 0.39, due to the decrease in driving force for solidification as $\Delta\theta_D$ ($\Delta\theta_D = \theta_m - \theta_D$) decreases.

Figure 41c shows the effect of varying the height of the top zone in a 2-PCM cascaded EPCM-TES system, $H'_{2,T}$ on the overall performance of the EPCM-TES system. For a top zone height of 1, it is observed that the system follows the characteristics of non-cascaded storage system at the default parametric values. At $H'_{2,T} = 1$, the EPCM-TES system is packed with PCM possessing a melt temperature of $\theta_m = 0.75$ leading to a slower discharge time compared to the charge time for any given Reynolds number. The effect of top zone height on the discharge time in Figure 41c shows that as the zone height increases, the discharge time increases, gradually until $H'_{t,T} = 0.5$ (equally divided zones) after which it gradually decreases as the system configuration tends to a non-cascaded EPCM-TES system configuration at $H'_{t,T} = 1$. Correspondingly, the cyclic exergetic efficiency at the periodic state is higher for $H'_{t,T} = 1$, with EPCM-TES system packed with PCM capsule melting at $\theta_m = 0.75$ (not illustrated here). Even though, the exergetic efficiency is higher for a non-cascaded configuration with PCM melting at 0.75 ($H'_{t,T} = 1$), it should be noted that a 2-PCM cascaded configuration, with $H'_{2,T} = 0.5$ possesses higher total and latent utilization, and higher discharge time. For instance at $\mathrm{Re}_H = 5000$, the discharge time of ECPM-TES system is $t^*_D = 5.26 \times 10^5$ with $H'_{2,T} = 0.5$ and the total utilization of 2-PCM cascaded configuration is 84.08% with 98.95% of the energy coming from the latent enthalpy of fusion of the PCM, while the

discharge time of non-cascaded configuration at $H_{2,T}^{'} = 0.5$ is $t_D^* = 4.66\times10^5$ with a total utilization of 69.14% and a latent utilization of 39.42% only.

Figure 42a–c portrays the combined effects of Reynolds number and PCM melt temperature at the top, mid and bottom zone respectively, while Figure 42d–f portrays the combined effects of Reynolds number and height of the top, mid and bottom zone, respectively on the discharge time for a 3-PCM cascaded EPCM-TES system configuration. In Figure 42a, for the top zone default PCM melt temperature of $\theta_m = 0.75$, the discharge time is found to be $t_D^* = 5.86\times10^5$. For melt temperatures below the default, a step decrease in discharge time is observed because the melt temperature falls outside the range, $\theta_D^{'} \le \theta_{m,T} \le 1$, leading to a decrease in latent utilization. For melt temperatures above the default value, the discharge time gradually decreases due to the decrease in driving force for melting as $\Delta\theta_C$ decreases. Figure 42b shows that changing the PCM melt temperature at the middle zone does not significantly affect the discharge time, although the maximum discharge time is achieved for $\theta_{m,M} = 0.50$. This is attributed to the fact that for equally divided 3-zone PCM cascaded configuration; PCM's with equally spaced intervals in melt temperatures lead to a more uniform temperature difference between the hot and cold media. Figure 42c exhibits the same trend as variations in PCM melt temperature at the top zone in that, a step decrease in discharge time is observed when the melt temperature falls outside the range, $0 \le \theta_{m,B} \le \theta_D^{'}$ while the discharge time decreases gradually with decrease in melt temperature due to the decrease in driving force for solidification as $\Delta\theta_D$ decreases.

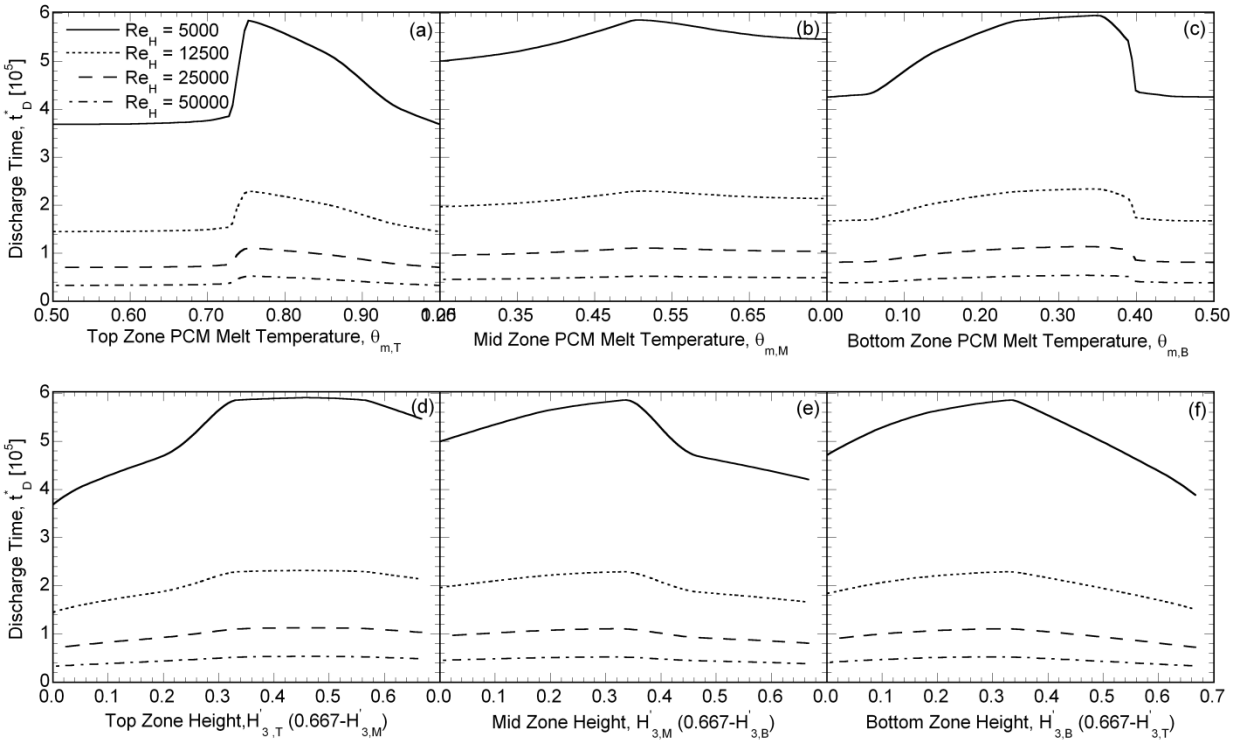

Figure 42: Effect of variation in (a, d) top, (b, e) middle, (c, f) bottom PCM melt temperature and zone height, respectively on discharge time for different Reynolds number of 3-PCM cascaded EPCM-TES system.

Since the height of each of the zones cannot be varied independently, in the present study, the heights of two zones are varied simultaneously to analyze its influence on the performance metrics. For instance in Figure 42d, the heights of the top zone and middle zone are varied simultaneously while the height of the bottom zone is fixed at the default value, which expressed in terms of fraction of the tank height is 0.335. Figure 42d shows that as the fraction of the top zone increases from 0 to 0.2, the discharge time gradually increases while the increase is higher when the fraction of the top zone increases from 0.2 to 0.467. With a top zone height fraction of 0, the thermocline storage system becomes a 2-PCM cascaded configuration with the middle zone occupying 0.667 of the tank height. Since the default PCM melt temperature of the middle zone is 0.5, the latent utilization of the PCM is restricted, and hence the discharge time is the lowest. As

the top zone percentage increases, with PCM possessing a melt temperature of 0.5 — within the limits of $\theta_D^{'} \le \theta_m \le 1$ —, the discharge time increases and when the top zone percentage increases from 0.2 to 0.335 the discharge time increases drastically from 4.76×10^5 to 5.86×10^5, reflecting a uniformity in the temperature difference between the HTF and PCM leading to a better system utilization. However, the discharge time peaks at $H_{3,T}^{'} = 0.467$ ($H3_{t,M}^{'} = 0.200$) with a discharge time of 5.91×10^{-5} although the increase from $H_{3,T}^{'} = 0.335$ is very subtle. The charge time (not illustrated here) followed the same trend as discharge time except that it peaked for a top zone height fraction of 0.335 while it was the lowest for $H_{3,T}^{'} = 0$.

Similarly from Figure 42e, it is found that the discharge time is highest for mid zone height fraction of 0.335 while the charge time was highest for a mid zone percentage slightly less than the default ($H_{3,M}^{'} = 0.335$). Note that the observation is different from that observed in Figure 42d in that the highest discharge time was observed for a top zone height fraction of 0.467 with a corresponding mid zone percentage of 0.2. While varying mid zone percentage to 0.2 in Figure 42e, the top zone percentage remains at the default 0.335 and the bottom zone percentage is reduced to 0.2 which is different from the analysis in Figure 42d. From Figure 42f, it is observed that the discharge time increases with increase (decrease) in bottom (top) zone percentage due to the availability of PCM at melt temperatures between $0 < \theta_m \le \theta_C^{'}$ and $\theta_D^{'} \le \theta_{m,T} \le 1$. The discharge time (Figure 42f) is highest when the top and bottom zone heights are equally distributed implying the significance of having PCMs with melt temperature at both the low and high temperature range below the charging cut-off temperature and above the discharging cut-off temperature, respectively. However, this does not imply that a 2-PCM cascaded configuration is the optimum, since the discharge time of a 3-PCM cascaded configuration is higher ($t_D^* = 1.11 \times 10^5$

) compared to a 2-PCM cascaded configuration ($t_D^* = 1.04 \times 10^5$). Note that even though the configuration is different, at the default parametric values, the energy storage capacity of either of the configurations is same since the inverse Stefan number and capacitance ratio is same across all the zones. It is also observed from Figure 42d–f, the discharge time decreases with increase in Reynolds number for any given zone percentage value. At higher Reynolds number, the mass flow rate is higher. Hence the existing hot fluid in the tank is discharged faster, after which due to insufficient residence time of the cold inlet HTF within the tank, heat exchange between the HTF and spherical PCM capsules do not take place efficiently, resulting in a faster decay of the HTF discharge temperature and contributing to low system utilization. Hence the variations in the discharge time with zone percentage for higher Reynolds number is not pronounced (Figure 42d–f).

6.4 Design Window

Having presented the effects of the non-dimensional parameters on the system performance (Figure 39–Figure 42), it is important to identify system design configurations which satisfy the SunShot targets: (1) discharge time greater than 6 hours, (2) charge time less than 6 hours, (3) exergetic efficiency greater than 95% and a storage cost less than \$15/kWh$_t$. To this extent, properties of molten salt (60% $NaNO_3$+40% KNO_3) and two different tank heights, 15 m and 20 m are considered for which the non-dimensional time pertaining to 6 hours are 1.7232×10^5 and 0.9932×10^5 respectively. In this study, design windows identifying regions, which satisfy the SunShot targets, are presented in the reminder of the section for a power plant operating at a rated capacity of 115 MW$_e$. For a gross cycle conversion efficiency of 42.5%, 270.588 MW$_t$ of thermal

power input is required to deliver power at the rated capacity, for which the mass flow rate of the HTF required is 635.44 kg/s. Hence, for a fixed HTF flow rate, changes in Reynolds number, Re_H corresponds to variations in the tank radius. Also, with the properties of the HTF fixed, the change in capacitance ratio and inverse Stefan number corresponds to variation in density of the PCM and latent heat of fusion respectively.

It is understood from the SunShot vision study [50] that to achieve a levelized cost of electricity of 6 cents/kWh, equivalent to the cost of fossil fueled power plants, improvements to all subsystems within a CSP plant is required which also includes reducing the thermal storage cost from \$27/kWh$_t$ (2-tank sensible storage) to \$15/kWh$_t$. The total cost of thermocline storage system can be expressed as the ratio of summation of storage material cost (HTF and PCM), container cost, encapsulation cost, overhead cost and the total storage capacity of the EPCM-TES system. The overhead cost, accounting for the miscellaneous costs such as electrical, instrumental, piping, valves and fitting costs is assumed to be 10% of the storage material, container and encapsulation cost. The storage material cost can be calculated as: $\left[\rho_p(1-\varepsilon)C_p' + \rho_f \varepsilon C_f'\right]\pi R_t^2 H_t$ where the PCM cost per unit mass (C_p') is assumed to be \$0.75/kg [52] and the HTF cost per unit mass (C_f') used in the molten salt power tower CSP plant is taken to be \$1.23/kg [53]. The EPCM-TES system container cost is calculated as explained in [53], [57], which encompasses the material cost of the stainless steel (321 SS), foundation cost and the insulation cost: $\underbrace{\rho_{SS} H_t \left[\pi(R_t + w_t)^2 - \pi R_t^{\,2} + 2\pi R_t^{\,2}\right] \cdot C_{SS}'}_{Material\ Cost} + \underbrace{\pi R_t^2 \cdot C_F''}_{Foundation\ Cost} + \underbrace{2\pi R_t H_t \cdot C_I''}_{Insulation\ Cost}$, where the subscript *SS* refers to stainless steel, the density of which is taken as $\rho_{SS} = 7900\ kg/m^3$ and w_t refers to the thickness of the tank, which is assumed to be 0.038 m. The cost per kg of stainless steel is obtained to be \$5.43/kg from [56], the calcium silicate insulation cost is assumed to be \$235/m^2 [57], and the

foundation cost is taken as \$1,210/m^2 [57]. The cost values reported here are consistent with the values of two-tank molten salt thermal storage system reported in [2]. The cost of encapsulation is usually measured in terms of cost/kg of capsule and due to lack of information on the effect of capsule radius on the encapsulation cost, it is expressed as $\left(\frac{R_c}{0.005}\right)^{0.3} C'_{encap}$, where the base cost for encapsulating one kg of PCM in a capsule of radius 0.005 m is assumed as \$0.75/kg [77] . The encapsulation cost increases with increase in capsule radius due to higher heat treatment and processing cost. Also, the stronger buoyancy driven natural convection current that will be prevalent inside the molten PCM of larger capsules during the melting process requires a thicker shell material [77].

The plots in Figure 43 presents the storage cost of thermocline storage system as a function of Reynolds number for various parametric values considered. It is to be noted that the density of phase change material and latent heat of fusion of the PCM is varied to reflect the changes in capacitance ratio and inverse Stefan number respectively. It should also be noted that the melt temperature is assumed to not have any effect on the storage cost. Figure 43a–c shows the variation in storage cost as a function of capacitance ratio, capsule radius and inverse Stefan number respectively for a tank height of 15 m. It is observed from Figure 43a that the storage cost decreases with increase in capacitance ratio because the density of the PCM increases and correspondingly, the storage capacity of the tank increases for a given tank dimension. As Reynolds number increases, the storage cost increases because of the decrease in tank radius and the corresponding storage capacity, notwithstanding the increase in material, insulation and foundation cost. In Figure 43b, it is observed that storage cost increases with increase in capsule radius due to increase in encapsulation cost. In the analysis of the effect of inverse Stefan number

on the storage cost it is found that the storage cost decreases with increase in inverse Stefan number which is consistent with the reasoning that the storage capacity of the system increases with increase in latent energy capacity of the PCM. It is to be noted that the storage cost obtained (not illustrated here) is less for a tank height of 20 m, because of the smaller tank radius compared to a tank height of 15 m.

Based on the parametric studies shown in Figure 39–Figure 43, Figure 44a–d presents the design windows on the Reynolds number, Re_H, which identify the regions where $t_D \geq 6h$, $t_C \leq 6h$, $\zeta \geq 95\%$ and $\alpha \leq \$15/kWh_t$ can be achieved as a function of the different design parameters of non-cascaded PCM configuration for a tank height of $H_t = 15m$. Corresponding to the constraint on the minimum discharge time, the upper limits of the Reynolds number for different values of Reynolds number are indicated by the solid line in Figure 44a. Similarly, the dotted line, the long-dashed line and the chain-dashed line are based on the constraints on the maximum charge time, minimum exergetic efficiency and minimum storage cost respectively. In Figure 44a–f, the long-dashed line corresponding to the constraint on the minimum exergetic efficiency falls on the top of the ordinate axis (Re_{H} = 50000) since the criteria is met for all the design parameters as presented in Figure 39–Figure 42. The shaded area identifies regions of operation which satisfy the primary requirements of a thermal storage system and it is seen that for most of the design parameters, there exists an upper bound and lower bound for which the constraints are satisfied. From Figure 44a, it is observed that as capacitance ratio increases the upper bound and lower bound on the Reynolds number increases concomitant with increase in thermal inertia or increase in thermal conduction resistance of the PCM capsules of the packed bed column. Hence, a higher charge and

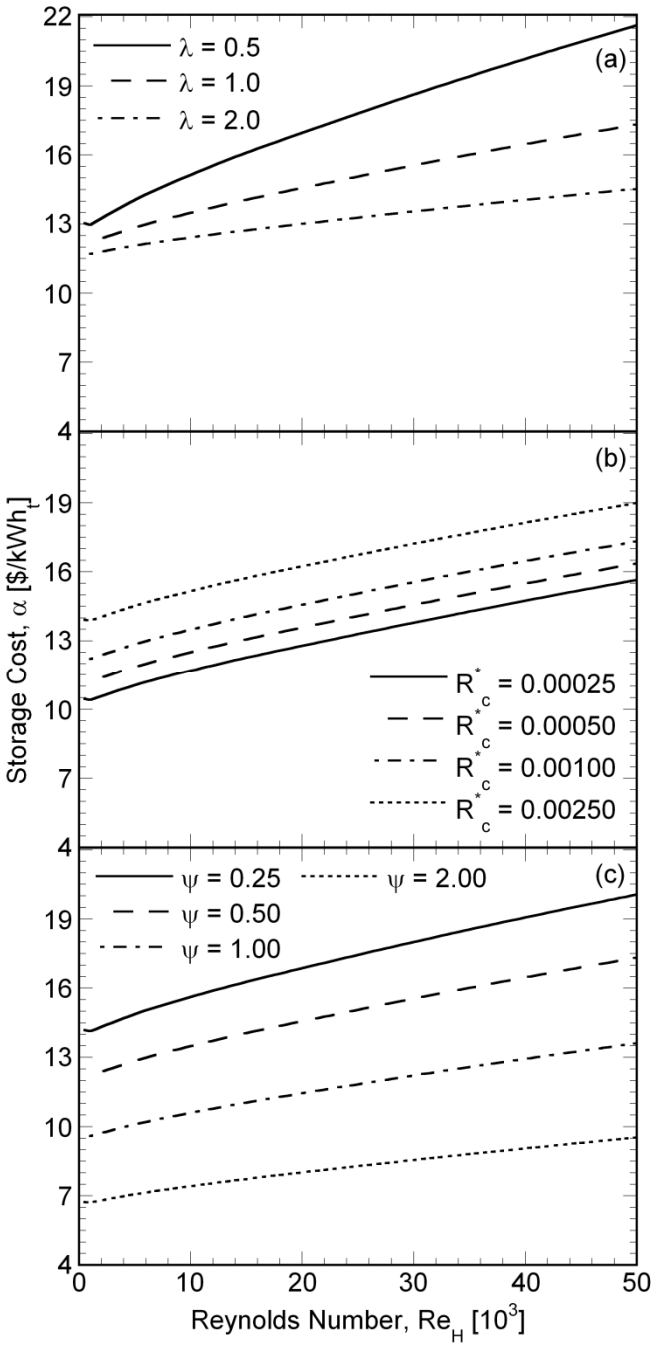

Figure 43: Variation in storage cost with Reynolds number for different (a) capacitance ratio, (b) capsule radius and (c) inverse Stefan number for 15 m tall non-cascaded EPCM-TES system.

discharge time is observed, notwithstanding the shorter residence time of the incoming HTF in the system.

With increase in capsule radius, the design window shrinks to a narrow range as depicted in Figure 44b. The effect of capsule radius on the lower bound (charge time constraint) is not pronounced, due to the fact that melting is assisted by buoyancy driven natural convection currents effecting efficient storage of energy, while the additional thermal conduction resistance accompanied with increase in capsule radius leads to a decrease in the upper bound dictated by the discharge time constraint owing to the conduction dominated solidification (energy retrieval). It is to be noted that the upper bound on the Reynolds number dictated by storage cost (chain-dashed line) decreases with increase in capsule radius as encapsulation cost increases and restricts the operation of tank filled with large capsule radius (Figure 44b). Figure 44c illustrating the effect of inverse Stefan number on the design window shows that lower bound on Re_{H} by the charge time constraint remains unaffected while the upper bound on Re_{H} by the discharge time constraint increases initially and then settles to a constant value. The range of feasible operation of the storage system is broader for higher inverse Stefan number. With increase in inverse Stefan number and thermal inertia of the system, a higher Reynolds number and correspondingly higher heat transfer coefficient is required for efficient heat exchange between the HTF and PCM. While the increase in thermal inertia affects the conduction dominated solidification rate, its influence on the natural convection assisted melting rate is not compelling. From Figure 44d, it is observed that a PCM with low melt temperature possesses a higher charge time compared to the discharge time leading to infeasibility in operation of the thermocline storage system. A very narrow range of feasible operation window is observed for PCM with melt temperatures in the range $\theta_D^{'} \leq \theta_m < 1$. It should be noted that for PCM with melt temperatures close to 1, no window of operation is observed as the driving force for charging operation is zero and the storage system works in the sensible regime with equal charge and discharge time. It should be noted that the effect of PCM melt

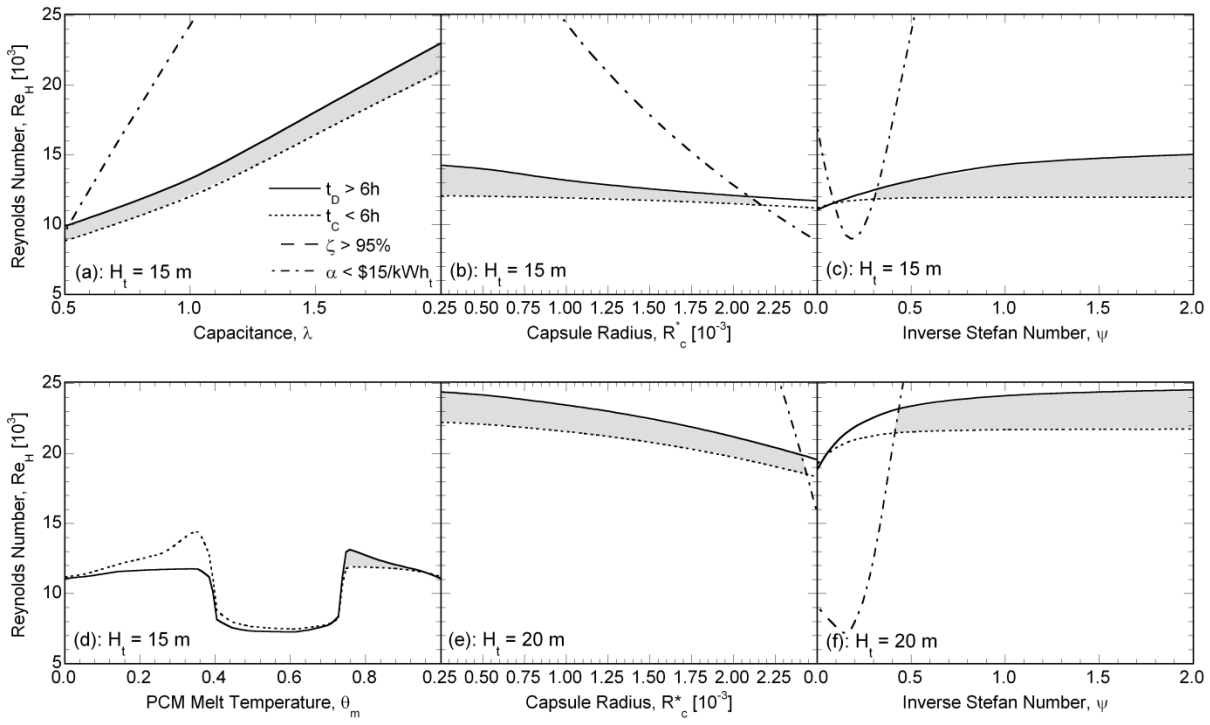

Figure 44: Operating windows as functions of (a) capacitance ratio, (b) capsule radius, (c) inverse Stefan number, (d) PCM melt temperature for 15 m, and (e) capsule radius and (f) inverse Stefan number for 20 m tall non-cascaded EPCM-TES system.

temperature on the design window of operation is studied with the rest of the parameters at the default values and a combinatorial variation of PCM melt temperature combined with another parameter such as inverse Stefan number will lead to a broader area of operation.

Figure 44e and f provides a comparison of the effect of capsule radius and inverse Stefan number on the design window of operation for a tank height of 20 m with respect to a tank height of 15 m portrayed in Figure 44b and c respectively. For a given Reynolds number with increase in tank height, the velocity of HTF flow in the storage system decreases leading to a favorable operation of the thermocline storage system at higher Reynolds number with smaller tank radius. Analyzing Figure 44e and f, extension of the operation of thermocline storage system at higher

Reynolds number is possible for a tank height of 20 m compared to a tank height of 15 m (Figure 44b and c) for various Reynolds number. It should be noted that for a inverse Stefan number lesser than 0.3, the constraint on the storage cost restricts the storage system operation (Figure 44f) in contrast to that observed for a tank height of 15 m (Figure 44c). For conciseness, the effect of capacitance ratio and inverse Stefan number on the performance of a EPCM-TES system tank of height 20 m is not presented, although similar trends are observed in that the feasible operation regime of thermocline storage tank is realized at higher Reynolds number.

Figure 45a emphasizes the effect of varying PCM melt temperature at the bottom zone on the design window of operation. For PCM with melt temperature less than 0.20 and for PCM greater than 0.40 feasible region of operation are observed as portrayed in Figure 45a. From Figure 45a, as PCM melt temperature in the bottom zone increases from zero, the Reynolds number which satisfies the charge time requirement also increases reflecting the fact that higher charge and discharge time is achieved with increase in PCM melt temperature. Even though the discharge and charge time also follows the same trend at a PCM melt temperature of $\theta_m = 0.20$ (Figure 42e) the charge time becomes greater than 6 h leading to infeasible operation of EPCM-TES system between PCM melt temperatures of 0.20 and 0.40 in the bottom zone. At higher PCM melt temperatures, the discharge time is higher while the charge time is smaller because none of the zones possess PCM within the charging cut-off temperature range which can extend the charging operation of thermocline storage system The effect of top zone height fraction on the design window of operation (Figure 45b) shows that the feasible operation region is observed for higher top zone percentages, since a higher percentage of the storage system is packed with PCM of higher melt temperature ($\theta_m = 0.75$). Broader range of design window is observed for a top zone

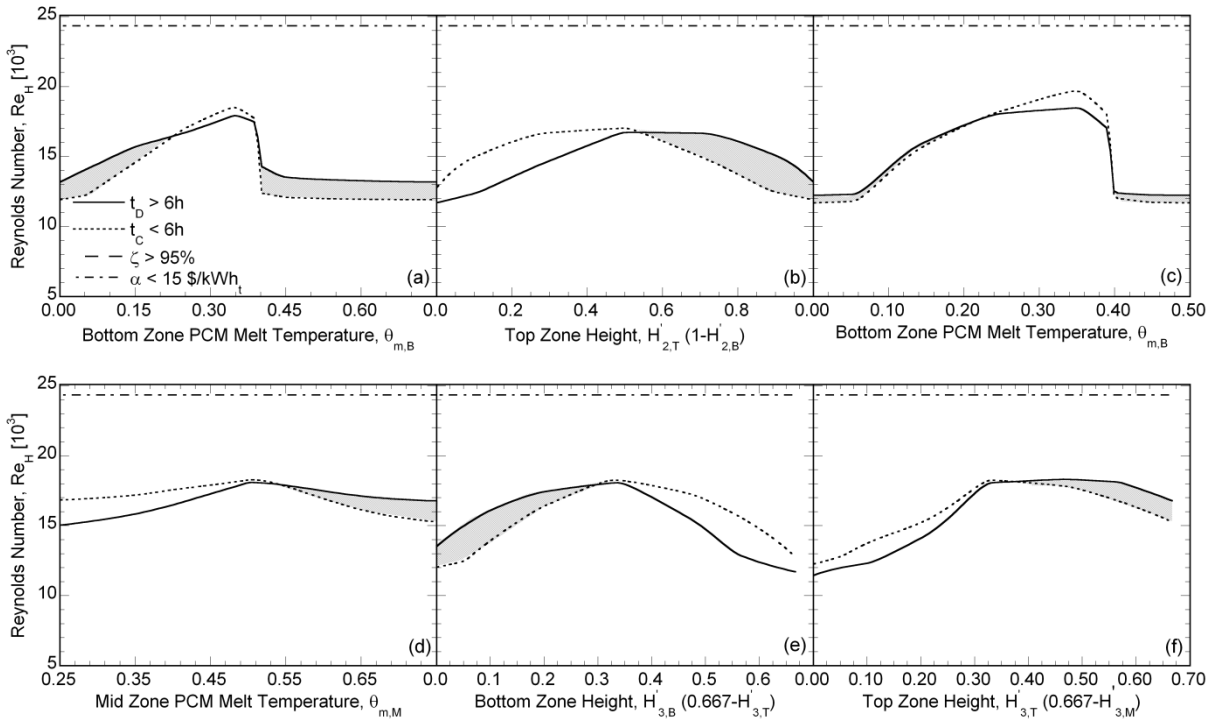

Figure 45: Operating windows as functions (a) bottom zone PCM melt temperature, (b) top zone height of 2-PCM cascaded, and (c) bottom zone PCM melt temperature, (d) top zone PCM melt temperature, (e) bottom zone height and (f) top zone height of 3-PCM cascaded 15 m tall EPCM-TES system.

height fraction of 0.82 while for a top zone height fraction of 0.1, the range of operation decreases reflecting the advantage of a cascaded configuration for a better storage system operation.

Similarly the effect of changing PCM melt temperature in the bottom and mid zone of a 3-PCM cascaded configuration is shown in Figure 45c and d. It is observed from Figure 45c, that for the variations in the PCM melt temperature at the bottom zone feasible operation regions are observed for lower PCM melt temperatures and higher PCM melt temperatures, illustrative of the trends observed for 2-PCM cascaded configuration. Interestingly, the critical melt temperature at which the charge time is greater than the discharge time decreases for a 3-PCM cascaded configuration compared to a 2-PCM cascaded configuration. Figure 45d illustrating the effect of variation in the melt temperature in the middle zone shows that feasible region of operation is

obtained for higher melt temperature PCMs. At the default PCM melt temperature values in the bottom and mid zone, the variation in the PCM melt temperature at the top zone did not yield any feasible region of operation. Figure 45e and f portrays the effect of variation in the bottom and mid zone height on the design window. Figure 45e shows the effect of varying the top zone and mid zone height simultaneously, while fixing the bottom zone height ($H_{3,B}^{'}$) at the default value of 0.335. Feasible region of operation is obtained only when the bulk of the storage system is filled with PCM of higher melt temperature. The above argument is also justified on observing Figure 45f, which shows that simultaneously varying middle and bottom zone PCM melt temperature does not yield significant change in the feasible operation region (Figure 45e) while broader feasible design region is obtained for very small bottom zone height, ($H_{3,B}^{'}$ and large top zone height, $H_{3,T}^{'}$ (Figure 45f).

The effects of other parameters on the design window of operation, though not illustrated here, may be summarized as follows: For cascaded configurations, feasible region of operation is obtained for higher capacitance ratios and inverse Stefan number when the top zone is varied, while feasible region of operation is obtained for low capacitance ratios and inverse Stefan number when the bottom zone is varied. In the case of a 2-PCM cascaded configuration, feasible operation region is observed for higher top zone heights. For 2-PCM cascaded configuration, broader range of design window is observed for a top zone height of 0.82 while for a top zone height of 1.0 the range of operation decreases reflecting the advantage of a cascaded configuration for a better storage system operation. The design windows for a tank height of 20 m are not presented, although similar trends are observed with the feasible operation regime of thermocline storage tank obtained at higher Reynolds number compared to tank height of 15 m.

While meeting the storage system demands is a necessary condition, maximizing the discharge time, exergetic efficiency, overall exergetic efficiency, and minimizing the charge time, storage capital cost is imperative to find the best design configuration of EPCM-TES system within the design window. In view of this, Table 11 lists the combinations of parameters culled from the parametric studies that maximize the chosen objectives: (1) the discharge time, t_D; (2) the charge time, t_C; (3) the overall exergetic efficiency, ζ' and (4) minimizes storage cost, α within the design and operating window of thermocline operation as presented in Figure 44 and Figure 45 for non-cascaded, 2-PCM cascaded and 3-PCM cascaded EPCM-TES system configurations. The overall exergetic efficiency, ζ' defined as the average of exergetic efficiency (Eq. (38)) over the five cycles of operation is selected as a performance metric since the cyclic exergetic efficiency is greater than 95% for almost all the parametric combinations considered. In each case, the corresponding values of charge and discharge time, exergetic and overall exergetic efficiency, and storage cost are also tabulated. The maximum or minimum values of the objective function are listed in bold face.

It is seen from Table 11a that of the cases studied, the best combination of parameters that maximizes t_D for non-cascaded EPCM-TES system yields discharge time of 7.42 h for H = 15 m while (Table 11a.1) whereas the best parameter combination for the same objective for H_t= 20 m results in an discharge time of only 7.38 h (Table 11a.1). Also, it is observed that the maximum discharge time corresponds to case with high inverse Stefan number with the rest of the parameters at the default values. For a 2-PCM cascaded configuration, the optimum design corresponds to a top zone height of 1.0 reflecting a non-cascaded configuration as the optimum configuration with a discharge time of 6.91 h. But, it is important to note that the optimum configurations obtained

from parametric studies pertain to varying the parameters in one zone at a time. For instance, from Table 11a.3, it is observed that for a 3-PCM cascaded configuration, the optimum design corresponds to a inverse Stefan number of 2.0 at the top zone with a discharge time of 6.86 h at a relatively higher Reynolds number, reflecting the need for an optimization procedure to find the optimum distribution of the design across the cascaded zones. Another important observation is that the charge time of the EPCM-TES system corresponding to maximum t_D corresponds to 6 hours for all the EPCM-TES system configurations namely non-cascaded, 2-PCM and 3-PCM cascaded EPCM-TES system for both H = 15 m and H = 20 m which sets the lower bound on the Reynolds number for various design parameters.

Table 11b presents the configurations of the storage system, which provided the minimum charge time and the optimum system configuration are the same as those obtained for maximum discharge time with the minimum charge time obtained for 1-PCM non-cascaded configuration, c.f. $t_C = 4.86\ h$ in Table 11b.1. While it is observed from Figure 39–Figure 40 that the exergetic efficiency of the system at the periodic state is greater than 95% for all the design configurations, a more conservative approach is taken and the system configuration with the highest overall exergetic efficiency is reported. The system with the maximum exergetic efficiency corresponds to a configuration with a larger percentage of tank possessing PCM at the highest melt temperature as observed in Tables 11c.2 and 11c.3. For 2-PCM cascaded configuration the maximum overall exergetic efficiency corresponds to the system with the top zone height at 1.0 while for a 3-PCM cascaded configuration a top zone height of 0.667, which is the highest parametric value explored in the parametric study and the remaining 0.333 the system with a PCM melt temperature of 0.500 reported the highest exergetic efficiency. The highest overall exergetic efficiency was achieved for

non-cascaded system configuration coupled with the smallest capsule size, c.f. $\zeta' = 97.34\%$ in Table 11c.1.

The minimum storage cost for the different configurations of storage system reported in Table 11d corresponds to system with higher inverse Stefan number and hence higher energy storage capacity. Although, higher capacitance ratio also corresponds to higher energy storage capacity, the cost of the PCM material also increases due to increase in PCM mass. The minimum storage cost also corresponds to the upper bound of the design window with higher Reynolds number (smaller radius) and lesser material cost. Among the parametric studies considered in this study, the non-cascaded configuration has the minimum storage cost, c.f. $\alpha = \$\ 7.55 / kWh_t$ in Table 11d.1, since the energy storage capacity is at least 50% higher compared to a 2-PCM cascaded configuration (Table 11d.2) and at least 66.7% higher compared to a 3-PCM cascaded configuration (Table 11d.3).

Table 11: Optimum design obtained for EPCM-TES system from feasible operating windows based on SunShot requirements

Objective			ψ	θ_m	λ	H'	R_c^* (10^{-3})	t_C [h]	t_D [h]	Re_H (10^3)	ζ [%]	α [$/kWht]	ζ' [%]
a. Maximum Discharge Time, t_D^*													
3. 1-PCM (Non-Cascaded)	H = 15 m	-	2.000	0.750	1.000	-	1.000	6.000	7.422	11.983	96.491	7.545	95.461
	H = 20 m	-	**2.000**	0.750	1.000	-	1.000	5.999	**7.376**	21.749	96.407	7.913	94.920
4. 2-PCM (Cascaded)	H = 15 m	Top	0.500	0.750	1.000	1.000	1.000	6.001	6.909	11.933	97.407	13.719	96.668
		Bottom	0.500	0.250	1.000	0.000							
	H = 20 m	Top	0.500	0.750	1.000	1.000	1.000	5.999	6.862	21.571	97.308	14.387	96.234
		Bottom	0.500	0.250	1.000	0.000							
5. 3-PCM (Cascaded)	H = 15 m	Top	2.000	0.750	1.000	0.335	1.000	6.001	6.858	19.147	95.537	11.365	94.599
		Mid	0.500	0.500	1.000	0.335							
		Bottom	0.500	0.250	1.000	0.333							
	H = 20 m	Top	2.000	0.750	1.000	0.335	1.000	5.999	6.815	33.121	95.452	11.963	94.121
		Mid	0.500	0.500	1.000	0.335							
		Bottom	0.500	0.250	1.000	0.333							
b. Minimum Charge Time, t_C^*													
1. 1-PCM (Non-Cascaded)	H = 15 m	-	**2.000**	0.750	1.000	-	1.000	**4.859**	6.001	15.052	96.464	7.725	95.290
	H = 20 m	-	2.000	0.750	1.000	-	1.000	4.893	5.999	24.555	96.384	8.038	94.765
2. 2-PCM (Cascaded)	H = 15 m	Top	0.500	0.750	1.000	1.000	1.000	5.219	6.001	13.197	97.392	13.860	96.607
		Bottom	0.500	0.250	1.000	0.000							
	H = 20 m	Top	0.500	0.750	1.000	1.000	1.000	5.256	5.999	23.468	97.289	14.534	96.150
		Bottom	0.500	0.250	1.000	0.000							
3. 3-PCM (Cascaded)	H = 15 m	Top	2.000	0.750	1.000	0.335	1.000	5.257	6.001	21.377	95.522	11.545	94.515
		Mid	0.500	0.500	1.000	0.335							
		Bottom	0.500	0.250	1.000	0.333							
	H = 20 m	Top	2.000	0.750	1.000	0.335	1.000	5.292	5.999	37.902	95.425	12.229	93.970
		Mid	0.500	0.500	1.000	0.335							
		Bottom	0.500	0.250	1.000	0.333							
c. Maximum Overall Exergetic Efficiency, ζ'													
3. 1-PCM (Non-Cascaded)	H = 15 m	-	0.500	0.750	1.000	-	**2.500**	6.001	7.004	12.082	97.582	11.938	***97.343***
	H = 20 m	-	0.500	0.750	1.000	-	2.500	5.999	6.996	22.240	97.573	12.473	*97.300*
4. 2-PCM (Cascaded)	H = 15 m	Top	0.500	0.750	1.000	1.000	1.000	6.001	6.909	11.933	97.407	13.719	*96.668*
		Bottom	0.500	0.250	1.000	0.000							

5. 3-PCM (Cascaded)	H = 20 m	Top	0.500	0.750	1.000	1.000	1.000	5.999	6.862	21.571	97.308	13.423	*96.234*
		Bottom	0.500	0.250	1.000	0.000							
	H = 15 m	Top	0.500	0.750	1.000	0.667	1.000	6.858	6.001	12.050	97.340	13.732	*96.572*
		Mid	0.500	0.500	1.000	0.333							
		Bottom	0.500	0.250	1.000	0.000							
	H = 20 m	Top	0.500	0.750	1.000	0.667	1.000	6.802	10.669	21.917	97.225	14.414	*96.115*
		Mid	0.500	0.500	1.000	0.333							
		Bottom	0.500	0.250	1.000	0.000							
d. Minimum Storage Cost, α													
1. 1-PCM (Non-Cascaded)	H = 15 m	-	**2.000**	0.750	1.000	-	1.000	6.001	7.422	11.983	96.491	***7.545***	95.461
	H = 20 m	-	2.000	0.750	1.000	-	1.000	5.999	7.376	21.749	96.407	*7.913*	94.920
2. 2-PCM (Cascaded)	H = 15 m	Top	2.000	0.750	1.000	0.500	1.000	6.001	6.820	17.244	95.448	*10.127*	93.75
		Bottom	0.500	0.250	1.000	0.500							
	H = 20 m	Top	2.000	0.750	1.000	0.500	1.000	5.999	6.772	28.678	95.347	*10.582*	93.194
		Bottom	0.500	0.250	1.000	0.500							
3. 3-PCM (Cascaded)	H = 15 m	Top	2.000	0.750	1.000	0.335	1.000	6.001	6.858	19.147	95.537	*11.365*	94.599
		Mid	0.500	0.500	1.000	0.335							
		Bottom	0.500	0.250	1.000	0.333							
	H = 20 m	Top	2.000	0.750	1.000	0.335	1.000	5.999	6.815	33.121	95.452	*11.963*	94.121
		Mid	0.500	0.500	1.000	0.335							
		Bottom	0.500	0.250	1.000	0.333							

The best configurations obtained from the parametric studies (Figure 38–Figure 42) and the design windows (Figure 44 and Figure 45) reported in Table 11 are obtained from varying one parameter at a time with the rest of the parameters at the design values. It is imperative that an optimization procedure varying all the design parameters simultaneously is followed in order to find the optimum distribution of PCM melt temperature and other design parameters while also achieving the SunShot targets, which will be the subject of future study.

6.5 Numerical Optimization

The best configurations obtained from the parametric studies (Figs. Figure 39–Figure 43) and the design windows (Figure 44 and Figure 45) reported in Table 11 are obtained from varying one parameter at a time with the rest of the parameters at the design values. It is imperative that an optimization procedure varying all the design parameters simultaneously is followed in order to find the optimum distribution of PCM melt temperature and other design parameters while also achieving the SunShot targets.

The goal of the optimization is to determine the design parameters of the Latent Thermocline Storage System so as to minimize the storage cost. The optimization is subject to operation constraints on the charge time, discharge time and exergetic efficiency as required by the SunShot Initiative [50]. The decision variables whose optimum values are sought to be determined ranges from 5 variables for a non-cascaded system configuration to 14 variables for a 3-PCM cascaded system configuration. For a 3-PCM cascaded storage system the decision variable are the capacitance ratios, inverse Stefan number, melt temperature of the PCM in each of the three zones, the height ratio of each of the zones, the Reynolds number and the capsule radius. In this

optimization study as explained in Section 6.4, a 100MW_e CSP plant is considered for which the desired flow rate of the HTF is fixed and the optimum Reynolds number pertains to the desired tank radius which minimizes the storage cost and hence is also considered to be a design parameter rather than an operational parameter. The upper and lower bounds of the decision variables considered for the study are listed in Table 12 and the optimization problem can be written mathematically as:

$$\underset{\lambda,\theta,\psi,H_t^{'},R_c^{*},\mathrm{Re}_H}{Mimimize} \quad \alpha \tag{39a}$$

subject to

$$\begin{aligned} g_1 &= t_C - t_{critical} \le 0 \\ g_2 &= t_D - t_{critical} \ge 0 \\ g_3 &= \zeta' - \zeta'_{critical} \ge 0 \end{aligned} \tag{39b}$$

The physical significance of the constraints established by the SunShot Initiative are as follows: The storage system for a CSP plant should be charged in 6 hour period ($t_{crtical}$) which is the equivalent of excess energy available from solar irradiation during the day for a 100 MW_e power plant. Similarly, the storage system should assist in the generation of electricity for more than 6h during the nighttime when solar energy is unavailable. The exergy efficiency takes care of the amount of useful thermal energy charged that can be converted into electricity and should be greater than 95% as dictated by SunShot requirements. Since for the various parameters considered, the exergetic efficiency is greater than 95%, Figure 39–Figure 40, the constraint is imposed on the overall exergetic efficiency.

The optimization problem represented by Eqs. (39a) and (39b) is solved using the Nelder-Mead simplex method [78] combined with a simulated annealing technique to improve the effectiveness of the search [79], [80]. The simplex search method is an algorithm that performs continuous search for selecting a new point during an optimization iteration, which guarantees objective function improvement. A simplex is defined as a convex hull of N + 1 vertices in an N-dimensional space, representing the N decision variables that govern the objective function evaluation. The vertices are ranked, from best to worst, based on the corresponding objective function evaluations and the best vertex is defined as the primary vertex. Since the primary vertex corresponds to a set of decision variables, which corresponds to the lowest objective function evaluation, the finding of a new primary vertex constitutes an improvement to the objective function. The Nelder–Mead simplex method combined with simulated annealing is designed to solve non-linear unconstrained problems. Since the optimization problem in hand has several constraints, g_k, those constraints are incorporated using a penalty method [81] into an augmented objective function to be minimized, such that the optimization problem becomes unconstrained.

For instance, the 14 decision variables in a 3-PCM cascaded thermocline configuration leads to a simplex is formed fourteen-dimensional space and consists of fifteen vertices. Initial guess for the decision variables correspond to one of the vertices, and adding scaled basis unit vectors creates the other fifteen vertices, such that the hyper-surfaces are independent of each other. The cost model (Section 6.4) and the numerical model (Section 5.1) are then invoked to determine the objective function and constraints respectively, corresponding to each vertex at every step of the optimization procedure. Upon completion of the optimization algorithm, the decision variables corresponding to the primary vertex are the optimal decision variable vector and the corresponding objective function value taken as the optimal storage cost, α.

Table 12 lists the designs corresponding to the optimization problems formulated by Eqs. (39a) and (39b). The storage cost obtained for a non-cascaded configuration from the numerical optimization are much lower than those obtained from the parametric studies, cf. $\alpha = 5.79 \$/kWh_t$ and $\alpha = 6.09 \$/kWh_t$ (Table 3a), and $\alpha = 7.55 \$/kWh_t$ and $\alpha = 7.91 \$/kWh_t$ (Table 11d.1) for tank heights of 15 m and 20 m respectively. Similarly, the storage costs obtained for a 2-PCM cascaded EPCM-TES system configuration $\alpha = 5.74 \$/kWh_t$ and $\alpha = 5.99 \$/kWh_t$ (Table 12b) is much lower compared to that obtained from parametric studies, $\alpha = 10.13 \$/kWh_t$ and $\alpha = 10.58 \$/kWh_t$ (Table 11d.2) for tank heights of 15 m and 20 m respectively. On further observation, the optimum values for a 2PCM cascaded configuration is obtained for a configuration with the maximum storage capacity with the highest capacitance ratio and inverse Stefan number (Table 12b). Also, it is observed that the charge time for a 2-PCM cascaded configuration is much lower than the optimum value obtained for non-cascaded EPCM-TES system configuration, cf. $t_C = 5.94\ h$ and $t_C = 5.93\ h$ (Table 12b) compared to 6 hour charge cycle obtained from parametric studies. The storage cost for the 3-PCM cascaded configuration obtained from the optimization studies is relatively higher compared to 2-PCM cascaded configuration (Table 12b and 12c). However, the optimum 3-PCM cascaded configuration gives the highest discharge time among all the cases, cf. $t_C = 6.62\ h$ and $t_C = 6.39\ h$ (Table 12c) for tank heights of 15 m and 20 m respectively. Compared to the result of the parametric studies, the storage cost obtained for the 3-PCM cascaded configuration from the optimization is approximately two times lower. From the optimization study it can be concluded that a 2-PCM cascaded configuration offers the lowest storage cost and 3-PCM cascaded configuration offers the highest discharge and lowest charge times. Further improvement in cascading will lead to only minor improvement as seen from the negligible difference in results between 2-PCM and 3-PCM cascaded configurations.

Table 12: Optimum design of EPCM-TES obtained from optimization study constrained by SunShot requirements

		H_t [m]		ψ	θ_m	λ	H'	R_c^* (10^{-3})	t_C $[h]$	t_D $[h]$	Re_H (10^3)	ζ [%]	α [\$/kWh$_t$]	ζ' [%]
1.	1-PCM	15	-	**2**.000	0.952	2.000	-	0.250	5.968	6.104	13.241	98.976	***5.791***	98.323
		20	-	2.000	0.900	2.000	-	0.250	6.000	6.471	34.750	98.343	6.088	98.000
2.	2-PCM	15	Top	2.000	0.992	2.000	0.515	0.250	5.935	6.402	17.515	98.359	***5.739***	95.963
			Bottom	2.000	0.743	2.000	0.485							
		20	Top	2.000	0.882	2.000	0.613	0.250	5.928	6.380	30.119	97.838	5.989	95.047
			Bottom	2.000	0.509	2.000	0.387							
3.	3-PCM	15	Top	2.000	0.982	2.000	0.220	0.250	5.643	6.618	19.773	96.896	***5.800***	96.666
			Mid	2.000	0.750	2.000	0.428							
			Bottom	2.000	0.608	2.000	0.352							
		20	Top	2.000	0.891	2.000	0.690	0.250	5.930	6.392	33.546	97.404	6.052	96.168
			Mid	2.000	0.557	2.000	0.166							
			Bottom	2.000	0.485	2.000	0.144							

6.6 Nomenclature used in Chapter 6

b capsule wall thickness [m]

c specific heat [J/kg-K]

C' cost per unit mass [$/kg]

C'' cost per unit area [$/m^2]

h convective heat transfer coefficient [W/m^2-K]

h_l latent heat of fusion of PCM [J/kg]

H height [m]

k thermal conductivity [W/m-K]

$\dot{m}$ mass flow rate [kg/s]

Nu Nusselt number

P_e electrical power output [MW]

Pr Prandtl number

P_{th} thermal power output [MW]

Q energy [MJ]

R radius [m]

Re Reynolds number

t time [s]

T temperature [K]

T_m melting temperature [K]

w thickness [m]

Subscripts and Superscripts

c capsule

C	charging
D	discharging
encap	encapsulation
f	heat transfer fluid
F	foundation
I	insulation
L	latent
p	phase change material
SS	stainless steel
t	tank
eff	effective

Greek Symbols

α	storage capital cost [\$/kWh$_t$]
ε	porosity of the packed bed
ρ	density [kg/m^3]
γ	melt fraction
λ	capacitance ratio
μ	dynamic viscosity [kg/m-s]
ψ	inverse Stefan number

Chapter 7: System Analysis of Concentrating Solar Power Plants with Integrated Latent Thermal Energy Storage

In the present chapter, the cost and performance models of an encapsulated phase change material thermal energy storage (EPCM-TES) system and latent thermal storage system with embedded heat pipes (HP-TES) developed in Chapters 4, 5 and 6 are integrated with a CSP power tower system model utilizing Rankine and supercritical carbon-dioxide (s-CO_2) power conversion cycles, to investigate the dynamic TES-integrated plant performance. The influence of design parameters of the storage system on the performance of a 200 MW_e capacity power tower CSP plant is studied to establish design envelopes that satisfy the U.S. Department of Energy SunShot Initiative requirements, which include a round-trip annualized exergetic efficiency greater than 95%, storage cost less than \$15/kWh_t and levelized cost of electricity (LCE) less than 6¢/kWh. From the design windows, optimum designs of the storage system based on minimum LCE, maximum exergetic efficiency, and maximum capacity factor are reported and compared with the results of two-tank molten salt storage system.

7.1 Introduction

Thermal energy storage can significantly increase the capacity factor of CSP plants which, in turn, can reduce the levelized cost of electricity (LCE) produced. The goal of the SunShot Initiative [50] is to reduce the LCE from solar power plants to 6 ¢/kWh without subsidies, by 2020, which would pave way for rapid and large-scale adoption of solar electricity. The SunShot 2020 goal calls for reduction in the upfront investment costs through reduced installation and manufacturing costs, and performance improvements in the various sub-systems of the CSP plant,

some of which include, reducing the optical losses of heliostats, developing storage systems with high volumetric energy density and high exergetic efficiency.

One potential contributor to the reduction in CSP plant capital cost arises from operation at high temperatures (> 650℃) using advanced cycles such as supercritical CO_2 Brayton (s-CO_2) cycle, which offers the potential of high cycle efficiency and reduction in power block cost compared to the currently existing Rankine cycle operation. The supercritical CO_2 cycle can achieve thermal efficiency as high as 55% for turbine inlet temperature and pressure of 850 ℃ and 20 MPa, respectively [82–84]. The main improvement of cycle efficiency comes from compressor work reduction due to a rapid increase of CO_2 density, when it is compressed near the critical point (30.98 ℃, 7.38 MPa) [82–84]. Other benefits of s-CO_2-Brayton cycle include the ability to achieve high efficiency at low temperatures and the high operating pressure allows small sized components (reduction in power block cost). In addition to the reduction in power block cost, operation at high temperatures requires only less volume of HTF material in the solar field, thus offering a reduction in the HTF material cost [50].

In order to achieve the SunShot Initiative goals, a system-driven approach that examines the cost and efficiency of CSP systems is necessary to understand the benefits of CSP with thermal energy storage. The Solar Advisor Model (SAM) [58] developed by the National Renewable Energy Laboratory (NREL) and the Sandia National Laboratories provides the framework to investigate the impact of geographical, geometrical and operating parameters on the performance of various CSP technologies including parabolic trough, molten salt power tower and dish sterling power plants. Purohit and Purohit [85] and Jain et al. [86] investigated the potential application of parabolic trough solar power plant in India using SAM and a sensitivity analysis to evaluate the impact of solar radiation on project economics and performance. Janjai et al. [87] also used SAM

to find the suitable location for the installation of CSP plant in the tropical climate of Thailand. Similar system analysis studies evaluating the performance of parabolic trough solar power plant with two-tank thermal energy storage system are reported in the literature [88–93]. Kolb [93] and Burkhardt et al. [94] have compared the economics and performance of parabolic trough plant with 2-tank and thermocline energy storage system filled with quartzite rocks. Based on the annual power production of the CSP plant, Kolb [93] concluded that the annual performance of parabolic trough power plant with 2-tank and thermocline energy storage system was nearly identical. On the contrary, Burkhardt et al. [94] presented a detailed life cycle assessment of trough CSP plants and concluded that CSP plants equipped with dry-cooling and 12 hours of thermocline thermal energy storage (TES) minimize both greenhouse gas emissions and water consumption.

As per the U.S. Department of Energy SunShot Initiative requirements, the optimal design of a TES for integration into CSP plants should yield a round-trip exergy efficiency greater than 95% and a storage capital cost less than \$15/kWh$_t$ for a minimum discharge period of 6 h [50]. Although the round-trip exergetic efficiency of sensible TES can attain close to 100%, the storage capital cost of current 2-tank sensible TES is reported as \$27/kWh$_t$ [53]. Nevertheless, an optimally designed latent TES has the potential to reach both storage capital cost less than \$15/kWh$_t$ and exergetic efficiency greater than 95%.

The goal of Chapter 7 is to expand on the limited literature and evaluate the performance of power tower CSP plant (net annual energy production, storage capital cost capacity factor and LCE) operating on s-CO_2 cycle with integrated encapsulated PCM based thermal energy storage (EPCM-TES) system explored in Chapters 5 and 6, tank based latent thermal storage embedded with heat pipes (HP-TES), which is described in Chapter 4 and 2-tank sensible storage system. The system analysis studies in the literature have concentrated on parabolic trough CSP plant design

operation based on Rankine cycle integrated with direct/indirect 2-tank sensible energy storage system. However, the SunShot Initiative's projected goal of 6 ¢/kWh by the end of 2020 is expected to be achieved with molten salt power tower CSP plant [50]. In the present study, the feasibility of the latent thermocline energy storage (LTES) system is studied by integrating the physics-based model of the storage system with the performance model of the molten salt power tower CSP plant. The SunShot 2020 goal aims to achieve a LCE of 6 ¢/kWh without subsidies for a 200-MW_e molten salt power tower CSP plant with 14 hours of TES and a capacity factor of 66.6%. To this end, a systematic analysis of the various design configurations of two different types of latent thermal storage systems on s-CO_2 based CSP plant operation is conducted and for the first time, a methodology for deriving design envelopes of the two different types of latent thermal storage system based on the aforementioned constraints is illustrated. Optimum design configuration of the latent thermal storage system based on minimum LCE from the design windows is reported and compared with the CSP-plant operation based on Rankine cycle and 2-tank direct sensible energy storage system in Chapter 7 of this dissertation.

7.2 CSP Plant Performance Model

A schematic of the integration of the LTES in a the power tower CSP plant working on Rankine cycle is shown in Figure 46a for a typical charging operation and Figure 46b shows the discharge operation of a power tower CSP system based on s-CO_2-Brayton cycle. As shown in Figure 46, a power tower CSP plant comprises of five sub-systems namely, the heliostat field, central tower/receiver, power block, cooling tower and TES system. A heliostat field constitutes a series of sun-tracking flat shaped mirrors, which collect thermal energy from the sun and

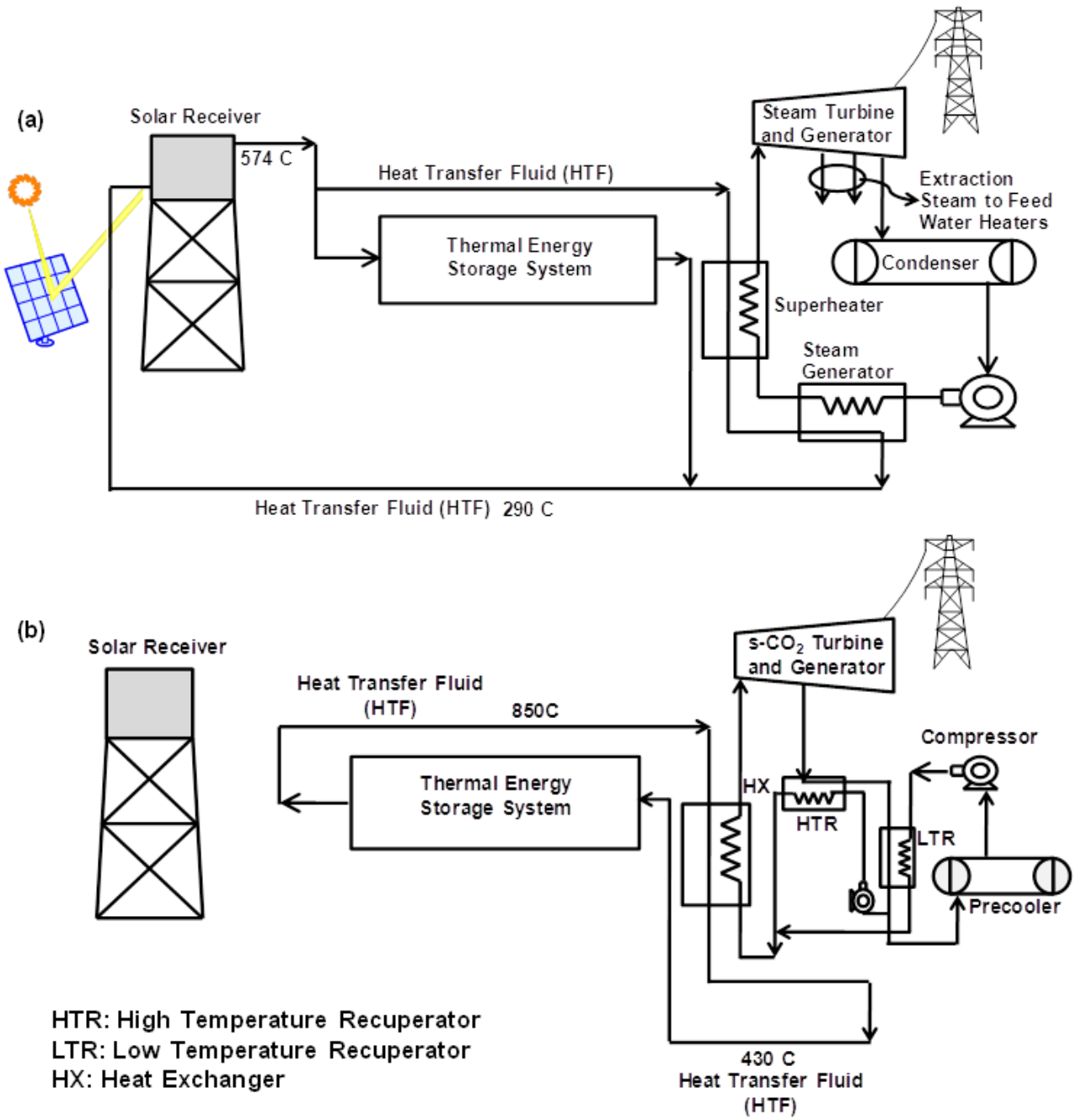

Figure 46: Schematic illustration of: (a) concentrating solar power (CSP) plant integrated with thermal storage system working on steam powered Rankine cycle, (b) CSP plant integrated with thermal storage system working on supercritical carbon-dioxide (s-CO_2) cycle. The molten salt HTF flow path during (a) charging and (b) discharging are also shown.

concentrates onto a central tower/receiver (Figure 46). In the external tower/receiver, molten salt HTF (solar salt) is circulated to absorb the solar thermal energy reflected by the heliostats. The hot HTF exiting the receiver is then fed into the power block which works on either conventional steam Rankine cycle or s-CO_2 based Brayton cycle to convert the thermal energy into electrical energy with a rated cycle conversion efficiency of 41.6% and 55% respectively [50]. The compressor, steam generator, superheater, steam turbine and generator in Fig. 1a make up the Rankine cycle based power block components, while the low- (LTR) and high- temperature recuperators (HTR), compressor, turbine and the generator make up the Brayton cycle based power block components. The inlet temperature and pressure of the steam at the inlet of the turbine in Figure 46a are typically 574 ℃ and 100 bar, respectively, while those for the s-CO_2 cycle in Figure 46b are 850 ℃ and 20 MPa, respectively. The typical operation pressure and temperature of the working fluid of the power cycle at the inlet and outlet of each of the power block components (Figure 46) can be found in Refs. [82] and [83].

The hot steam/s-CO_2 from the turbine exit is fed into a condenser/cooling tower to condense the exhaust steam by rejecting the heat of vaporization to the cooling medium as illustrated in Figure 46. A dry cooling technology is considered in the present study instead of the conventional wet cooling tower owing to high water consumption in spite of the improved performance and lower cost. As illustrated in Figure 46a, excess hot HTF fluid from the receiver outlet is stored in the thermal energy storage, which can be subsequently removed to smooth fluctuations in power output during cloud episodes and to extend power generation after sunset (Figure 46b).

A “process-based” approach, in which a system is modeled from the ”bottom up“ using component masses and process energy flows similar to that implemented in SAM [58], is implemented in the present study. The overall CSP plant performance relies on input from more

detailed process models that provide information regarding the performance of the aforementioned individual components. The dynamic model uses actual weather data at time intervals of one hour and calculates the net electrical energy output at every time step during an entire year, thus simulating the hourly, monthly and annual energy output of a solar thermal power plant [58]. A detailed explanation of the CSP plant performance model is provided in [95] and is not reported here in the interest of brevity. The power block component in SAM calculates the net Rankine cycle conversion efficiency, expressed as a function of the inlet temperature and mass flow rate of the HTF from the solar field, and the ambient temperature, thus properly accounting for the reduction in efficiency during part load conditions. The expression for Rankine cycle efficiency is obtained based on the parametric studies of various operating conditions using a high-fidelity process model as reported in Ref. [95]. It is to be noted that the outputs from SAM have been validated with experimental results obtained from the operation of Solar II CSP plant installed in Daggett, CA. Similar expression for s-CO_2 Brayton cycle efficiency, validated with numerical simulation results of Dostal et al. [82], is reported in Ref. [84], which is used to simulate the performance of CSP plant operation based on s-CO_2 based Brayton cycle.

The two latent thermal energy storage options considered in the model are EPCM-TES and HP-TES, as illustrated schematically in Figure 29 and Figure 20, respectively. The storage integrated CSP plant operates in one of the two modes, namely, charging and discharging, depending on the solar thermal energy resource at the particular hour of the day and the energy available in the LTES. Charging occurs whenever the incident solar thermal energy is in excess to that required by the operation of the power block at the rated capacity. The excess heat (HTF mass flow rate) is directed to the storage system until the exit temperature of the HTF, T_f, at $z = H_t$ (EPCM-TES) and $x = L_d$ (HP-TES) in Figure 29 and Figure 20 reaches a charge cut-off

temperature, $T_C^{'}$, taken to be 400 ℃, which determines the extent to which the TES system can be charged. The charge cut-off temperature value is limited by the maximum flow rate achievable by the HTF pumps in the receiver section. The increase in HTF flow rate through the receiver for higher cut-off temperature increases undesirable parasitic and thermal losses [58]. Discharging occurs during periods of low or no solar insolation to obtain the full rated capacity of the CSP power block. Similar to the charging process, the strong dependence of the power block cycle efficiency on the incoming HTF temperature [58] requires the termination of discharge process when the HTF exit temperature reaches a certain minimum discharge cut-off temperature, $T_D^{'}$ = 500 ℃ and 705 ℃ for Rankine and s-CO_2 based cycles, respectively. The description of the models for the EPCM-TES and HP-TES systems are presented in Chapter 4 and Chapter 5, respectively.

7.3 Model Inputs and Outputs

The complete formulation—including the CSP plant performance model, the storage performance model and the cost model—was implemented in FORTRAN. The model is validated with the results from SAM [58] for a CSP plant with no storage and for a CSP plant with 6 hours of 2-tank direct molten salt storage system. The major inputs for the CSP plant performance model include the weather data of the location, design parameters of the heliostat, receivers, type of cooling tower, power plant output requirement to name a few. The models assume a plant life of 30 years and the geographic location used is Daggett, CA, where the annual DNI is among the highest in the U.S. [94]. Table 14 provides a list of the major input parameters that is used to simulate the performance of CSP plant integrated with Rankine and s-CO_2 cycle. For an exhaustive list of the inputs required for the model the reader is referred to [58]. The HTF used in the CSP plant integrated with Rankine power cycle corresponds to 60% $NaNO_3$-40%KNO_3 (Solar

Salt) while that used in CSP plant integrated with s-CO2 power cycle corresponds to KCl-$MgCl_2$.

In this analysis, a 2-PCM cascaded storage system is assumed, with 75% of the total tank height and total channel length from the hot HTF inlet (Figure 20 and Figure 29) filled with PCM of high melt temperature while the remaining 25% of the volume filled with PCM of low melt temperature. The high melt temperature PCM chosen for this study corresponds to a blend of Li_2CO_3(35%) and Na_2CO_3(65%) for low temperature Rankine based CSP plant while for the high temperature s-CO_2 based Brayton cycle operation, a blend of K_2CO_3(51%)–Na_2CO_3(49%) is chosen. The low temperature PCM for both the configurations is chosen as Li_2CO_3(32%)–K_2CO_3(35%)–Na_2CO_3(33%). The thermophysical properties of the PCM are obtained from Ref. [52] and are listed in Table 13. The selected PCM's are certified with moderate safety hazard rating code. The operating parameters — HTF inlet mass flow rate and HTF inlet temperature depend on the hour of the day, available solar insolation, etc., and is dictated by the CSP plant operation. The influence of the tank radius (R_t), tank height (H_t) and capsule radius (R_c) of EPCM-TES system on the CSP plant performance is reported in the present study, the default values of which are taken to be R_t = 15 m, H_t = 15 m and R_c = 0.5 cm, respectively. Similarly, the influence of HTF channel width (W_d), channel length (L_d) and the longitudinal spacing between the heat pipes (S_L) are the major design parameters of the HP-TES system considered in the present study.

The major outputs from the model are the hourly gross electric output, hourly parasitic loss, hourly inlet temperature of the power block, hourly inlet temperature and mass flow rate of the LTES system, hourly exergy input and output of the LTES system. The hourly net electric output of the plant is calculated by subtratcting the parasitic loss from the hourly gross electric output. The storage pump power, which is a function of the pressure drop in the LTES systems, is also encompassed in the hourly parasitic loss output calaculations. The cyclic annual exergetic

Table 13: Physical parameters of PCM used in the latent thermal storage systems integrated to a CSP plant model

	Li_2CO_3(35%) Na_2CO_3 (65%)	Li_2CO_3(32%)–K_2CO_3(35%)–Na_2CO_3(33%)	K_2CO_3(51%)–Na_2CO_3(49%)
Density, ρ [kg/m^3]	2260	2260	2400
Thermal Conductivity, k [W/m-K]	1.89	2.02	1.73
Specific heat, c_p [J/kg-K]	1640	1650	1635
Melting Temperature, T_m [℃]	505	397	710
Latent heat of fusion, h_{sl} [kJ/kg]	344	276	163
Cost [$/kg]	0.88	0.73	0.24

efficiency of the EPCM-TES and the HP-TES system is defined as the ratio of exergy gained by the HTF during discharging to that gained during charging [48] and are expressed as follows:

$$\zeta_{EPCM} = \frac{\int_{\text{Discharge}} \dot{m}_f(t)\cdot c_f\left[T_f(z=0,t) - T_D - T_{ref}(t)\cdot\ln\left(\frac{T_f(z=0,t)}{T_D}\right)\right].dt}{\int_{\text{Charge}} \dot{m}_f(t)\cdot c_f\left[T_C - T_f(z=H_t,t) - T_{ref}(t)\cdot\ln\left(\frac{T_C}{T_f(z=H_t,t)}\right)\right].dt} \quad (40a)$$

$$\zeta_{HP} = \frac{\int_{\text{Discharge}} \dot{m}_f(t)\cdot c_f\left[T_f(x=0,t) - T_D - T_{ref}(t)\cdot\ln\left(\frac{T_f(x=0,t)}{T_D}\right)\right].dt}{\int_{\text{Charge}} \dot{m}_f(t)\cdot c_f\left[T_C - T_f(x=L_d,t) - T_{ref}(t)\cdot\ln\left(\frac{T_C}{T_f(x=L_d,t)}\right)\right].dt} \quad (40b)$$

where Eqs. (40a) and (40b) pertain to the EPCM-TES and HP-TES systems, respectively, $\dot{m}_f(t)$ is the mass flow rate of HTF in the storage system and $T_{ref}(t)$ is the ambient temperature of the CSP

Table 14: Geometric parameters of CSP plant used in the numerical model

	Rankine	s-CO_2
Heat Transfer Fluid (HTF)	$NaNO_3$-KNO_3 (Solar Salt)	KCl-$MgCl_2$
Design HTF Power Block Inlet Temperature [C]	574	850
Design Conversion Efficiency [%]	41.6%	53.8%
Design Thermal Power [MW_t]	558.25	418.18
Design Mass Flow Rate [kg/s]	4227.23	2103.13
No. of Heliostats	20509	15029
Heliostats Area [km^2]	2.96	2.17
Tower Height [m]	326.67	277.78
Receiver Height [m]	36.8	29.48
Receiver Diameter [m]	23	22.11

location, which also exhibits diurnal variation.

The key performance metrics characterizing the performance of the CSP plant integrated with storage system are the plant capacity factor, β, annual exergy efficiency of the LTES and the levelized cost of electricity (LCE). The capacity factor of a power plant is the ratio of the actual output of a power plant over a period of time and its output if it had operated at full nameplate capacity the entire time [58] while the levelized cost of electricity [57], is defined as $LCE = \frac{(C_I \times CRF + C_{OM})}{(8760 \times \beta)}$ where CRF is the capital recovery factor, β is the capacity factor obtained from the CSP plant performance model, 8760 is the number of hours in a year, C_I represents the total installation cost of the CSP plant expressed in \$/kW_e and C_{OM} represents the

fixed Operation and Maintenance cost. The values for fixed is obtained from [50] as \$40/kW-yr. The total installed costs of 200 MW_e power tower CSP plant without storage as reported in Ref. [50] for Rankine cycle based and s-CO_2 based power block are \$5,672.30/kW_e and \$3,330.90/kW_e to which the storage capital cost as discussed in Sections 4.2 for HP-TES and 6.4 for EPCM-TES are added to obtain the total installed cost of the plant. The decrease in capital cost for s-CO_2 based CSP plant is concomitant with decrease in solar field size, HTF inventory and power block cost with increase in operation temperature and rated cycle conversion efficiency, as observed in Table 14.

7.4 Results and Discussion

The numerical model developed in Section 7.2 is validated with results obtained from SAM [58] and presented in Figure 47. Figure 47a compares the electric output obtained from the present numerical model with the results obtained from SAM for a power tower CSP plant with solar multiple of 2.7 working on Rankine cycle installed in Daggett, california. The solar field for the considered solar multiple consists of 20509 heliostats with tower and receiver heights of 326.7 m and 36.8 m, respectively and a receiver diameter of 23 m. The net (solid line) and gross (dotted line) electric output obtained from the numerical model are plotted along with the corresponding values obtained from SAM which are denoted by open circles and open squares, respectively. The monthly variations observed for both CSP plant without storage and CSP plant integrated with 14 hour two-tank direct storage capacity are consistent with the trends obtained from SAM and the present numerical model closely agrees with the SAM results. The capacity factor, β obtained from the present numerical model for a CSP plant with no storage and with 14 hour two-tank direct molten salt storage capacity are 32.18 % and 66.23 %, respectively, which are within a

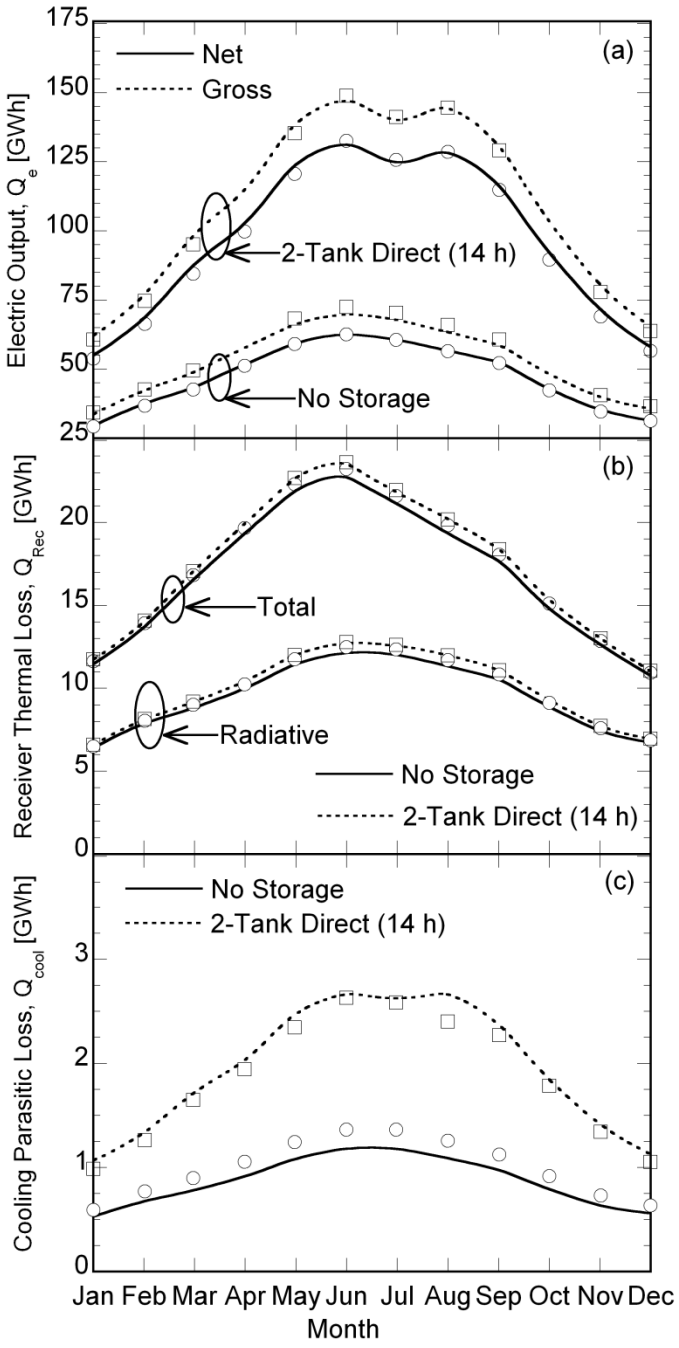

Figure 47: Comparison of the monthly variations in (a) net and gross electric output of CSP plant, (b) total and radiative thermal loss from the receiver, and (c) cooling tower parasitic loss obtained from the present model (solid and dashed lines) with the results from Solar Advisor Model [58] (SAM) (markers) integrated with 2-tank direct molten salt of 14 hours and 0 hour storage capacity.

maximum of 1.5% error from the results obtained from SAM, $\beta = 31.95\%$ and $\beta = 65.23\%$. The increase in error percentage from 0.7% to 1.5% for a no-storage and 2-tank direct storage CSP plant can be attributed to the fact that in the present model the storage system is assumed to be perfectly insulated in contrast to SAM model.

Figure 47b portrays the monthly thermal losses in the receiver. The receivers exposed to high temperatures experience radiative and convective losses. The results obtained from the numerical model for the monthly variations in radiative and total (summation of radiative and convective) losses compare well with the SAM results. The peak total receiver thermal loss obtained for the month of June (peak summer) corroborates with the predictions of SAM. Figure 47c depicts the monthly variations in the cooling parasitic loss, which shows a higher loss during summer (May–August) concomitant with the decrease in efficiency of dry cooling tower with increase in ambient temperature. In general, the results from the model developed in Section 7.2 compares well with the validated SAM results.

Figure 48a shows the net electric output generated by the s-CO_2 based CSP plant of 200 MW_e rated capacity as a function of various months in the year with no storage (chain-dashed line), and for different capsule radius of the EPCM-TES system with R_t = 10 m and H_t = 15 m and a solar multiple of 2.7. The net energy output obtained from the CSP plant increases from the month of January (winter) to the middle of the year (summer) and decreases later in the year toward the end of December (winter). The trend in the monthly net electric power produced is commensurate with the monthly variation in the incident solar thermal energy and the peak net electric power output of 101.9 GWh is obtained during the month of June for a capsule radius, R_c = 0.5 cm. It is observed from Figure 48a that a CSP plant integrated with thermal energy storage yields higher net energy output compared to a plant with no storage system. The net annual electric output obtained from

CSP plant with no storage and with EPCM-TES comprising capsules of radius, R_c = 0.5 cm, which can be calculated as the summation of monthly net electric output for the entire year as presented in Figure 48, are 585.47 GWh and 970.52 GWh respectively. A marginal difference is observed between the capsule radii of 0.5 cm and 2.0 cm, while the net electric output decreases drastically for capsule radius greater than 2.0 cm. This is due to the increase in resistance to the conduction dominated solidification of the PCM, resulting in a slow thermal energy transfer rate between the PCM and HTF. Hence, the discharge cut-off temperature is reached quicker, resulting in a decrease in storage utilization.

Figure 48b shows the monthly net electric output generated from CSP plant operating based on the Rankine cycle. In general, the trends observed are similar to that obtained for CSP plant operating on s-CO_2 cycle, but the net electricity output is less due to the lower cycle conversion efficiency. In addition, for CSP plant operating on s-CO_2 cycle, the monthly parasitic loss—encompassing the pumping power for HTF through power block, receiver and storage, tracking power for heliostats, among others—as presented in Figure 48c for a capsule radius of 0.5 cm, is less than that of CSP plant operating on Rankine Cycle. The energy required to pump HTF through the tall tower/receiver unit, being a major contributor of the parasitic loss, is also plotted in Figure 48c. The monthly tower/receiver pumping energy and the parasitic loss portrayed in Figure 48c vary in the same fashion as the net electric power output (Figure 48a and b). It is observed that the tower/receiver pump energy requirement for s-CO_2 based CSP plant, which operates at the highest temperature of 850 C, is lower than that of Rankine cycle based CSP plant (Table 14), which operates at the highest temperature of 574 C. For the similar rated capacity of the CSP plant, the higher operating temperature of the s-CO_2 cycle based CSP plant requires a lower HTF mass flow rate compared to Rankine cycle based CSP plant, which results in reduced tower/receiver pump

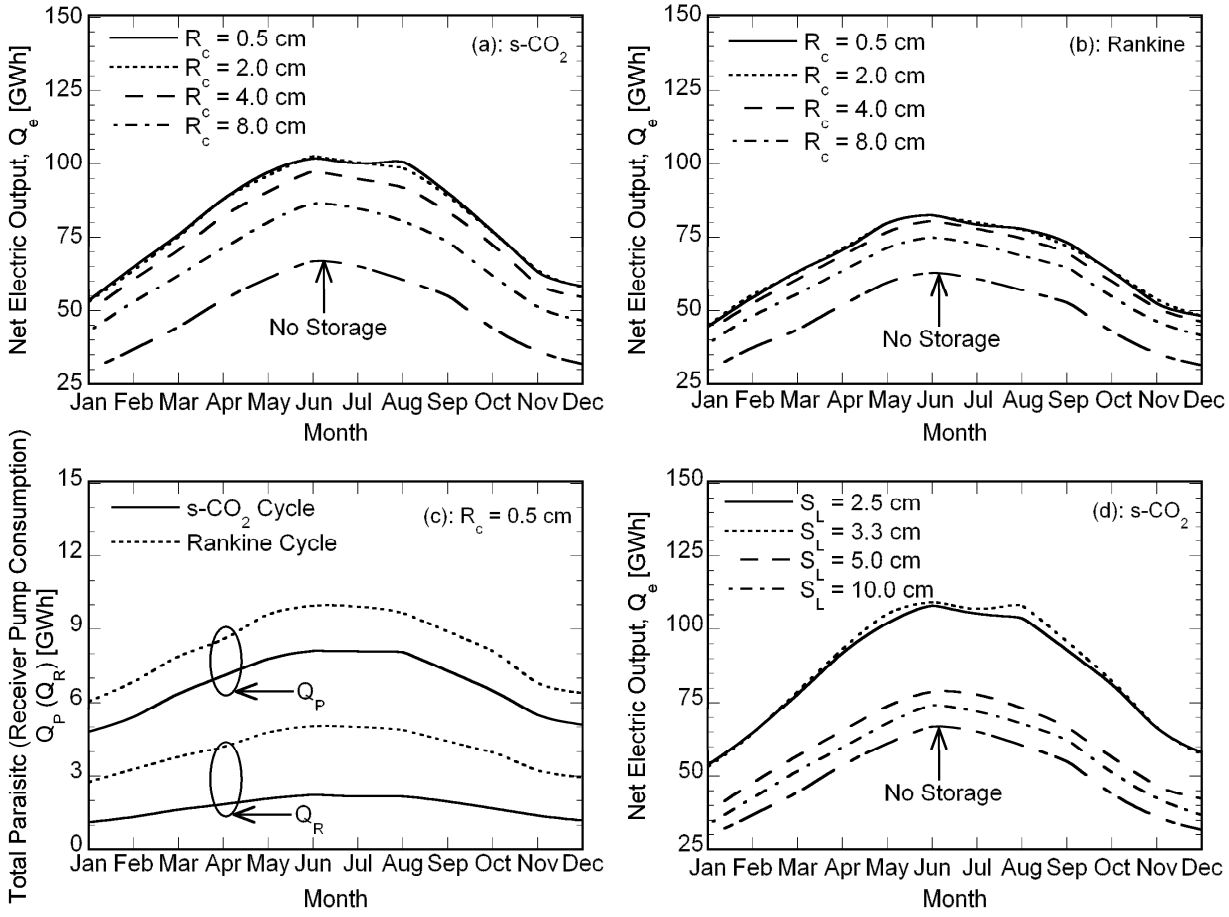

Figure 48: Monthly variations in net electric output for different capsule radius of EPCM-TES system integrated to (a) s-CO_2 powered and (b) Rankine powered CSP plant, and monthly variations in net electric output for different longitudinal spacing between heat pipes of HP-TES system integrated to (a) s-CO_2 powered and (b) Rankine powered CSP plant.

energy requirements, albeit the negligible increase in convection and radiation losses in the receiver. The annual parasitic loss for R_c = 0.5 cm, calculated from Figure 48c as the summation of the parasitic loss at each month for the entire year, is found to be 98.80 GWh, which is higher compared to the parasitic losses for s-CO_2 based CSP plant (79.77 GWh). The total parasitic loss for other capsule radius also follows the same trend depicted in Figure 48c and is not illustrated here.

Similarly, the monthly variations in the net electric output generated from s-CO_2 cycle based CSP plant integrated with HP-TES system with a channel width of W_d = 0.8 m and channel length of L_d = 25 m are presented in Figure 48d for various longitudinal spacing (S_L) between the heat pipes. It is seen from Figure 48d that relative to the system with no storage, the monthly net electric power generated increases with increase in longitudinal spacing (S_L = 2.5 cm and S_L = 3.3 cm) initially and then decreases with further increase in longitudinal spacing between the heat pipes (S_L = 5.0 cm and S_L = 10.0 cm). The effect of heat pipes on the net energy extracted from the PCM and, in turn, the net electricity generated, is governed by two competing considerations: on the one hand, the number of heat pipes, and correspondingly, the heat transfer augmentation for energy extraction during discharging, decreases as the longitudinal heat pipe spacing, S_L, increases; on the other hand, the total storage capacity, and the net electricity output, increases with increasing longitudinal heat pipe spacing, S_L, due to a reduced amount of PCM in the storage tank and the HTF in the channel being replaced by the heat pipe volume. This tradeoff is evident in Figure 48d, where the net electricity output is seen to increase with respect to the system with no storage as S_L increases initially to 3.3 cm. With further increase in S_L, the reduced number of heat pipes available for energy extraction leads to a decrease in the net electricity output. The annual net electricity output of CSP plant is highest for S_L = 3.3 cm at 1021.2 GWh (Figure 48d), although it should be noted that the total storage capacity for the HP-TES is 15.08 h compared to 6.1 h illustrated for thermocline configuration in Figure 48a. A CSP plant with HP-TES and a Rankine cycle power block exhibited the same trend with S_L, except for smaller net output electricity compared to that in Figure 48d. The results are omitted here in the interest of brevity.

Figure 49a and b presents variation of the capacity factor of the EPCM-TES integrated CSP plant with tank radius and capsule radius, for two different tank heights of 10 m and 20 m,

respectively. The results correspond to the thermal energy storage system integrated with a s-CO_2 cycle power block. As the resistance to conduction dominated solidification increases with increase in capsule radius, the utilization of the storage system decreases leading to a decrease in the capacity factor of the CSP plant, as illustrated in Figure 49a and b. From Figure 49c, it is seen that for a tank height of 10 m, the total (latent) energy discharged from EPCM-TES with capsules of radius 0.5 cm amounts to 452.0 (95.5) GWh for a tank radius of 10 m, and 981.4 (150.0) GWh for a tank radius of 20 m, while for a capsule of larger radius, R_c = 8.0 cm, the total (latent) energy discharged amounts to 183.8 (41.03) and 799.0 (153.7) GWh for a tank radius of 10 m and 20 m, respectively. As the difference in the energy discharged between small and large radii capsules diminishes with increase in tank radius, the difference in capacity factor between the smallest and largest capsule radius also decreases as portrayed in Figure 49a. For capsules of small radius, the improvement in the latent energy discharged with increase in tank radius is not as high as that observed for capsules of large radius, due to the decrease in the convective heat transfer coefficient as a result of the low HTF velocity for the same mass flow rate, while the higher residence time of the HTF coupled with the higher surface area available for interaction with HTF in the EPCM-TES system enhances the melting-solidification process of the PCM in large capsule radius.

With increase in the tank radius, and for H_t = 20 m (Figure 49b), the capacity factor for EPCM-TES with a large capsule radius is seen to converge to the capacity factor values obtained for a small capsule radius. The difference in capacity factor between EPCM-TES with capsules of radius 0.5 cm and 8.0 cm is as low as 1.0% for the tank radius of 20 m (Figure 49b) compared to 10.5% difference obtained for the tank radius of 10 m (Figure 49a). This is also in agreement with the trends obtained for the annual total (latent) energy discharged from the EPCM-TES system with increase in tank radius from 10 m to 20 m—785.3 (155.1) GWh to 1001.8 (132.7) GWh for a

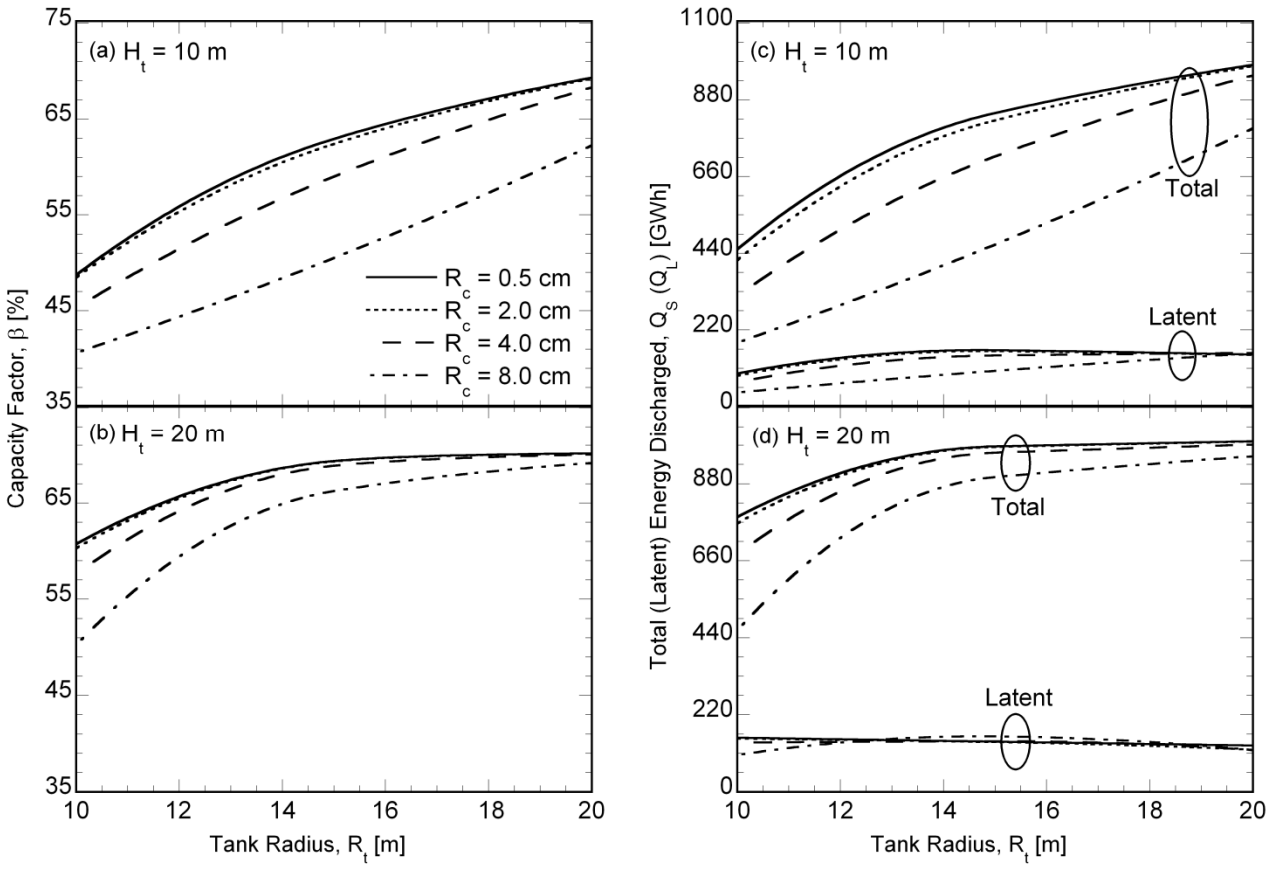

Figure 49: Variations in capacity factor with tank radius and capsule radius of (a) 10 m and (b) 20 m tall EPCM-TES system integrated to a s-CO_2 powered CSP plant and variations in total and latent energy discharged from (a) 10 m and (b) 20 m tall EPCM-TES system integrated to a s-CO_2 powered CSP plant as functions of capsule radius and tank radius.

capsule of radius 0.5 cm and 461.1 (105.5) GWh to 959.1 (119.6) GWh for a capsule radius of 8.0 cm (Figure 49d). Comparing Figure 49c and d, it is observed that with increase in tank height, a larger percentage of energy is extracted in the form of sensible energy from the stored hot HTF and the PCM due to increase in storage capacity (32.4 h at H_t = 20 m and R_t = 20 m), corresponding to which a very small difference is observed in the capacity factor of small and large capsule radius at large tank radius. For a tank height of 20 m, it is seen from Figure 49b that the increase in capacity factor is meager for increase in tank radius greater than 15 m, as the

storage capacity of the tank is much higher compared to the net thermal energy collected by the solar field for the solar multiple of 2.7. The highest capacity factor that can be obtained from the CSP integrated with EPCM-TES corresponds to 70.2% (Figure 49b).

Following the presentation format in Figure 49, Figure 50a and b illustrates the annual capacity factor of a CSP plant based on a s-CO_2 power cycle integrated with a HP-TES system as a function of channel width and longitudinal spacing of heat pipes for channel lengths of 25 m and 30 m. The corresponding annual energy discharged from the storage is presented in Figure 50c and d. As is seen from Figure 50a and c, for a channel length of 25 m, the capacity factor and the energy discharged increase slightly with S_L between 2.5 and 3.3 cm but decrease substantially with further increase in the longitudinal spacing, S_L. In the case of a channel length of 30 m, Figure 50b and d, the capacity factor and the energy discharged are relatively invariant with S_L between 2.5 cm and 3.3 cm and, as for L_d = 25 m, decrease with further increase in the longitudinal spacing, S_L. The decrease in the capacity factor with increase in S_L greater than 3.3 cm, despite increase in storage capacity, is due to reduction in the number of heat pipes and, in turn, a decrease in the heat transfer rate between the HTF and PCM. This is also reflected in Figure 50c and d in that the total discharged from HP-TES system of channel lengths 25 m and 30 m, respectively decreases with increase in longitudinal spacing between the heat pipes for S_L > 3.3 cm. However, for a channel length of 25 m, as illustrated in Figure 50a, the capacity factor is higher for a longitudinal spacing of 3.3 cm compared to 2.5 cm, until channel width of 1.4 m concomitant with higher total energy discharged for S_L = 3.3 cm (Figure 50c). This is attributed to the fact that a closer spacing and hence a large number of heat pipes corresponding to S_L = 2.5 cm results in a reduction in the volume of PCM (storage capacity) for a given dimension of the HP-TES system. For instance, the

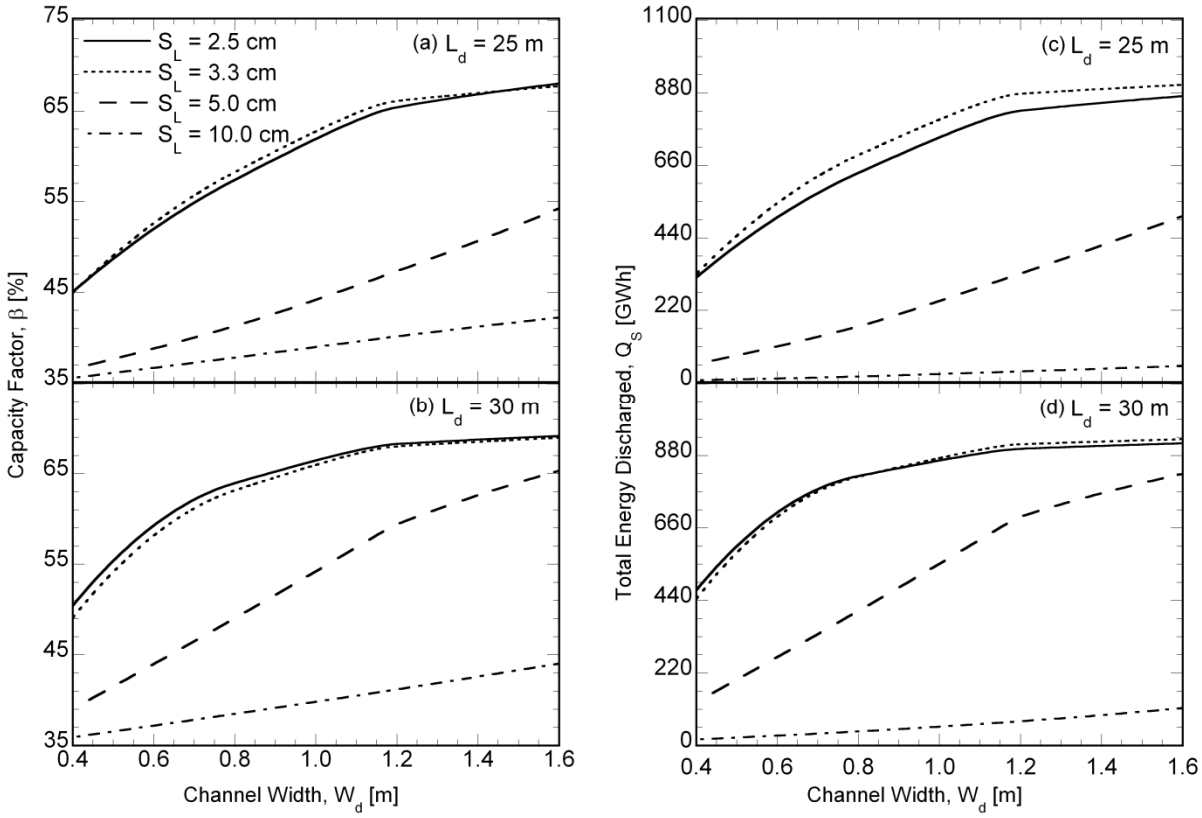

Figure 50: Variations in capacity factor with longitudinal spacing between the heat pipes and channel width of (a) 25 m and (b) 30 m long HP-TES system integrated to a s-CO_2 powered CSP plant and monthly variations in total and latent energy discharged from (a) 25 m and (b) 30 m long HP-TES system integrated to a s-CO_2 powered CSP plant as functions of longitudinal spacing between heat pipes and channel width.

number of heat pipes installed in a channel of length and width 25 m and 0.8 m corresponds to 27,360 and 15,530 for S_L = 2.5 cm and 3.3 cm, respectively, thus reducing the storage capacity by 2.74 h. The capacity factor for channel width greater than 1.4 m is higher for S_L = 2.5 cm, as observed in Figure 50a, in spite of the higher total energy discharged obtained for S_L = 3.3 cm. This is attributed to the higher parasitic energy consumption for S_L = 3.3 cm due to higher utilization of the HP-TES system, which results in a lower capacity factor than S_L = 2.5 cm. In addition, the longer residence time owing to the low velocity of the HTF in the HP-TES system

compensates for the reduction in the storage capacity and hence the capacity factor and energy discharged is higher for S_L = 2.5 cm (Figure 50a and c).

The capacity factor of the CSP plant is also seen to increase with channel width due to the lower velocity of the HTF flow inside wider channels and the increase in total storage capacity (Figure 50a and b). This is also confirmed from the measure of the total energy discharged from the HP-TES system with S_L = 2.5 cm, for increase in channel width from 0.4 m to 1.6 m as observed from Figure 50c and d, which increases from 321.0 GWh to 870.9 GWh for L_d = 25 m and from 472.4 GWh to 917.5 GWh, for a channel length of 30 m. From Figure 50a and b, it is seen that for the design configurations considered, the highest capacity factor of 69.2% is obtained for a channel length and width of 30 m and 1.6 m, respectively with the heat pipes arranged in a longitudinal spacing of 2.5 cm. In Figure 50b, it is seen that the capacity factor a HP-TES with a channel length of 30 m does not increase much with increase in channel width beyond 1.2 m, for which the storage capacity is 22.14 h while for a latent thermocline storage system discussed in Figure 50, the critical storage capacity beyond which further improvement in capacity factor is found to be 18.23 h corresponding to a tank height and radius of 20 m and 15 m, respectively (Figure 50b). Even though the thermocline storage system requires a lower storage capacity to achieve the maximum capacity factor, it is instructive to compare their levelized costs of electricity (LCE) as discussed later in this section.

Figure 51a and b shows the annualized exergetic efficiency of the encapsulated PCM TES as a function of tank and capsule radius for tank of heights 10 m and 20 m, respectively, for a plant operating using the s-CO_2 power cycle. It is observed from Figure 51a that for smaller tank radius, the exergetic efficiency of EPCM-TES filled with capsules of radius 8.0 cm shows higher exergetic efficiency compared to capsules of radius 0.5 cm in spite of the higher capacity factor

obtained for smaller capsule radius as illustrated in Figure 49a. The major driving force for PCM solidification (discharging) is the temperature difference between the cold HTF temperature and the PCM melt temperature while the major drive force for melting (charging) is characterized by the temperature difference between the hot HTF temperature and the PCM melt temperature. For the present configuration with 75% of the EPCM-TES height filled with PCM melting at high temperature, discharge takes place faster than charging. However, the assistance of natural convection in the melting process provides for a better melt rate, albeit the reduced drive force. So, a capsule radius of 2 cm leads to an almost equal rate of charge and discharge for the current system configuration, leading to the higher exergetic efficiency seen in Figure 51a. For small tank radius, the capsules of radius 0.5 cm show poor exergetic efficiency than capsules of radius, R_c = 8 cm, due to the fact that PCM's encapsulated in the larger capsules store energy mostly in the sensible regime with at most 43% less latent energy discharge than the small radii capsules as observed from the latent energy discharge values for tank radius of 10 m in Figure 49c. Nevertheless, it is to be noted that the net annual exergy discharged by the EPCM-TES filled with large capsule radius (R_c = 8.0 cm), which amounts to 476.41 GWh is significantly (45.4%) less than the EPCM-TES with capsule radius of 0.5 cm (1049.28 GWh). For a large tank radius, characterized by low velocity of HTF within the tank, the smaller convection heat transfer coefficient leads to discharge of HTF at high temperatures for a longer duration, resulting in high exergetic efficiency for smaller capsule radius (Figure 51a).

For large tank heights, illustrated in Figure 51b, larger exergetic efficiency is observed for capsules of radius smaller than 4 cm. For a given capsule radius, the exergy efficiency of the LTES system decreases with decrease in tank radius as illustrated in Figure 51a and b. For a given solar multiple, a decrease in EPCM-TES tank radius leads to an increase in HTF velocity, resulting in a

decrease in the residence time of the HTF in the tank. As a result, the exit temperature of the HTF decays faster and, consequently, lower exergetic efficiency is obtained for small tank radius. For H_t = 20 m (Figure 51b), the exergy efficiency increases until a tank radius of 14 m, corresponding to a storage capacity of 15.9 h and then remains constant similar to that observed in the trend for capacity factor, as depicted in Figure 49b. This is attributed to the fact that with further increase in system size, significant portion of the stored thermal energy in the PCM is not utilized and the HTF temperature exiting the storage system and fed into the power block remains at a high temperature.

Figure 51c and d portrays the exergetic efficiency of ECPM-TES system integrated to a CSP plant working on steam powered Rankine cycle. In general, compared to the exergetic efficiency observed in s-CO_2 based CSP plant (Figure 51a and b), lower values are seen in Figure 51c and d due to the relatively low temperature of HTF flow (574 ℃) in the storage and power block. From Figure 51c and d, highest annual exergetic efficiency of 98.1% is noted for EPCM-TES system of height 20 m and radius 20 m filled with capsules of radius 0.5 cm, which is lower compared to 99.4% obtained for ECPM-TES system of the same configuration integrated with a s-CO_2 cycle based CSP plant. For a tank height of 10 m, characterized by higher percentage of latent energy utilization as explained earlier, the highest exergetic efficiency of $\zeta = 96.3\%$ is obtained for capsule and tank radii of 0.5 cm and 20 m, respectively (Figure 51c), in comparison to $\zeta = 98.2\%$ obtained in s-CO_2 based CSP plant (Figure 51a).

The exergetic efficiency of the HP-TES system, plotted as a function of channel width in Figure 51e and f for channel lengths of 25 m and 30 m, show that the heat pipes should be arranged close together to obtain high exergetic efficiency. The exergetic efficiency follows the same trends as the capacity factor in that the exergetic efficiency decreases with increase in

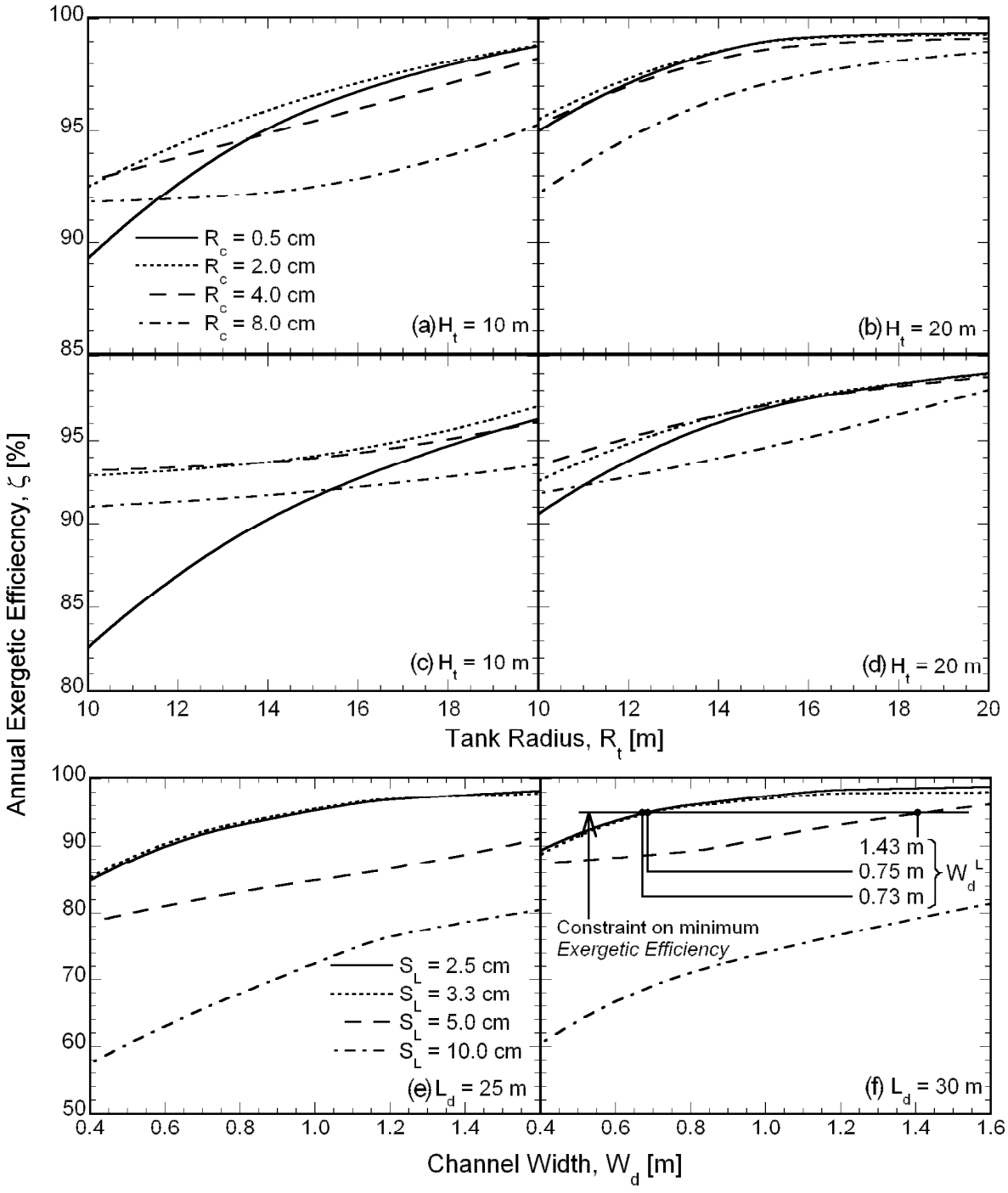

Figure 51: Variations in annual exergetic efficiency with tank radius and capsule radius of (a) 10 m and (b) 20 m tall EPCM-TES system integrated to a s-CO_2 powered CSP plant and variations in annual exergetic efficiency with tank radius and capsule radius of (a) 10 m and (b) 20 m tall EPCM-TES system integrated to a Rankine powered CSP plant. Variations in annual exergetic efficiency with longitudinal spacing between the heat pipes and channel width of (a) 25 m and (b) 30 m long HP-TES system integrated to a s-CO_2 powered CSP plant.

longitudinal spacing between the heat pipes and decrease in channel width. The decrease in exergetic efficiency is observed with decrease in channel width due to the high velocity of the HTF in channels of smaller width. The increased velocity reduces the residence time resulting in a slow energy transfer rate between the HTF and PCM, notwithstanding the increase in convective heat transfer coefficient for the higher HTF flow velocity. For a channel length of 25 m (Figure 51e), the highest exergetic efficiency of $\zeta = 98.3\%$ is obtained for a channel width of 1.6 m, corresponding to S_L = 2.5 cm. However, the exergetic efficiency is seen to be relatively invariant between S_L = 2.5 cm and 3.3 cm, that a longitudinal spacing of 3.3 cm is preferred due to the significant cost saving as a result of almost half the number of heat pipes compared to S_L = 2.5 cm. However, with further increase in the longitudinal spacing, the exergetic efficiency falls below the SunShot requirements of $\zeta > 95\%$. The highest exergetic efficiency ($\zeta = 98.9\%$) is obtained for the largest channel width and length and the smallest longitudinal spacing of S_L = 2.5 cm (Figure 51f). For a channel length and width of 30 m and 1.6 m, the exergetic efficiency for longitudinal spacing of 5.0 cm is observed to approach that obtained for the smaller longitudinal spacings due to the excess storage capacity in the HTF.

Based on the variations in Figure 51, design criteria on the EPCM-TES and HP-TES parameters may be established so as achieve a minimum exergetic efficiency of 95% as called for in the SunShot target [1], [50]. An example of this design criterion is illustrated in Figure 51f for the HP-TES with a channel length of 30 m, which shows that the requirement of $\zeta > 95\%$ corresponds to a minimum channel width, W_d^L, denoted by the filled circular markers, for any given longitudinal spacing. It is further evident from Figure 51f that the lower bound on the channel width increases with the longitudinal spacing. Using this approach, the lower bound on the channel width (W_d^L) may be derived as a function of S_L for a channel length of 25 m from Figure

51e. It may further be noted from a comparison of the variations in Figure 51e and f that W_d^L decreases with increasing channel length, for a given longitudinal spacing, S_L. Similarly, the lower bounds on the tank radius, R_t^L, may be derived from Figure 51a–d for the EPCM-TES as a function of the tank height and the capsule radius. The lower bounds on R_t^L and W_d^L derived from Figure 51 are presented later in this section.

Figure 52 presents the storage cost of EPCM-TES (Figure 52a and b) and HP-TES (Figure 52c and d) for the various parametric configurations considered in the present study. The SunShot Initiative goal [1], [50] of a levelized cost of a CSP-generated electricity of less than 6 ¢/kWh calls for achieving a TES cost of < \$15/kWh$_t$ for 14 hours of storage capacity to power a 200 MW$_e$ CSP plant. Since the storage capacity of a LTES encompasses both latent and sensible heat capacity, expressing the storage cost as a fraction of the total storage capacity (\$/kWh) leads to an artificially small cost on a kWh basis. A fair basis of analyzing the total capital cost of the storage system is, therefore, comparison to the SunShot absolute cost goal of \$87.95 million (US\$ MM) (~US\$88 MM). As presented in Figure 52a and b, the total storage capital cost of EPCM-TES system increases with increase in capsule radius and the tank radius. The storage cost increases with increase in tank radius due to corresponding increase in material, foundation and overhead cost (Section 6.4). The increase in capsule radius increases the processing and heat treatment cost of the capsules leading to an increase in the total storage capital cost of the EPCM-TES system. Comparing Figure 52a and b, it is observed that the storage cost is high for a larger tank height because of the increased material and insulation cost. For the HP-TES, it is evident from Figure 52c and d that the storage cost increases with increasing channel width and channel length and decreasing longitudinal spacing between heat pipes.

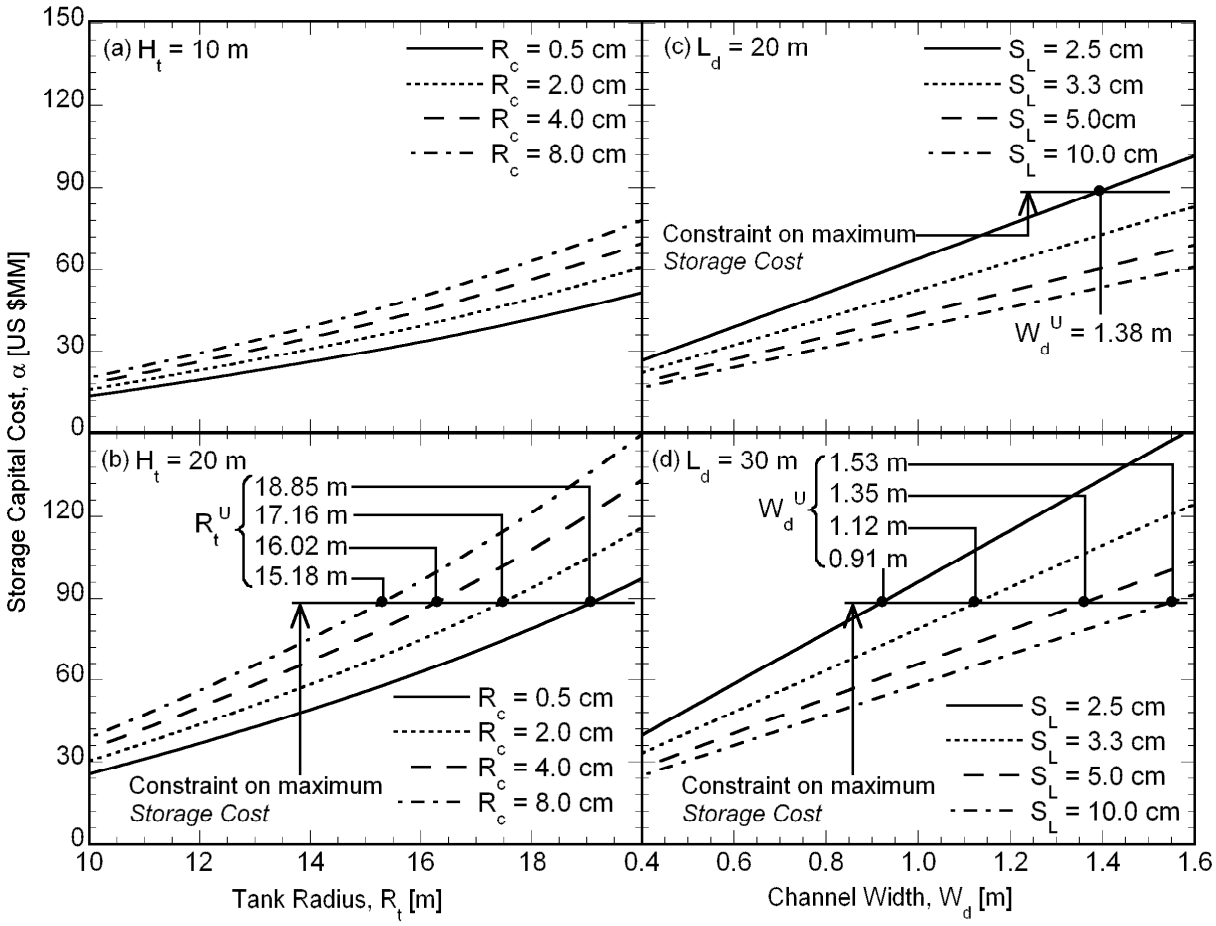

Figure 52: Storage capital cost as functions of capsule radius and channel radius for (a) 10 m and (b) 20 m EPCM-TES system. Storage capital cost as functions of channel width and longitudinal spacing between heat pipes for (a) 20 m and (b) 30 m long HP-TES system.

Based on the variations in Figure 52a and b, design criteria on the EPCM-TES parameters may be established so as to limit the storage cost to be within the SunShot target of US$87.95 MM. Figure 52a shows that for a tank height of 10 m, the storage cost is less than US$87.95 MM over the entire range of tank radius and capsule radius considered. However, for a larger tank height of 20 m, Figure 52b reveals an upper bound on the tank radius, R_t^U, for a given capsule radius, so as to limit the storage cost to within the SunShot target. The upper bound on the tank radius (R_t^U) is seen to decrease with increasing capsule radius, as indicated by the filled markers in Figure 52b.

Likewise, from the variations in total storage capital cost of HP-TES system with channel width and longitudinal spacing, as illustrated in Figure 52c and d, it is observed that there exists an upper limit on the channel width, W_d^U, beyond which the cost exceeds the SunShot target of US$87.95 MM. The upper bound on the channel width, W_d^U, denoted by the filled markers in Figure 52c and d, is observed to increase with increase in longitudinal spacing due to reduction in the number of heat pipes and cost of the HP-TES system. Comparing Figure 52c and d, it is seen that the critical channel width that satisfies the SunShot cost goal decreases with increase in channel length for any given longitudinal spacing between the heat pipes.

Figure 53a and b shows the variation of the levelized cost of electricity, LCE, of an EPCM-TES system with the tank radius and capsule radius for tank heights of 10 m and 20 m, respectively. It is seen that the LCE for an EPCM-TES of smaller height (Figure 53a) is greater than that for a larger height (Figure 53b) due to the decrease in capacity factor of the plant as depicted in Figure 49a and b. Previous studies [57], [87] have shown that for any given solar multiple, there exists an optimum size of a 2-tank molten salt thermal energy storage system at which the LCE is the least. In the same manner, within the range of parametric values considered for the present study, it is observed in Figure 53b that the LCE decreases with increase in tank radius as capacity factor increases (Figure 49b), reaches a minimum and increases again with further increase in tank radius, due to a distinct increase in storage capital cost (Figure 52b) and a negligible improvement in the capacity factor (Figure 49b). As an illustration, for the EPCM-TES system height of 20 m and capsule radius of 2.0 cm (Figure 53b), the LCE decreases from 6.13 ¢/kWh for R_t = 10 m to 5.69 ¢/kWh for R_t = 15 m and then again increases to a LCE of 6.10 ¢/kWh for R_t = 20 m. It is further evident from Figure 53b that the optimum tank radius, R_t^*, shifts toward larger values with increase in the capsule radius. Similar trends also exist for the shorter

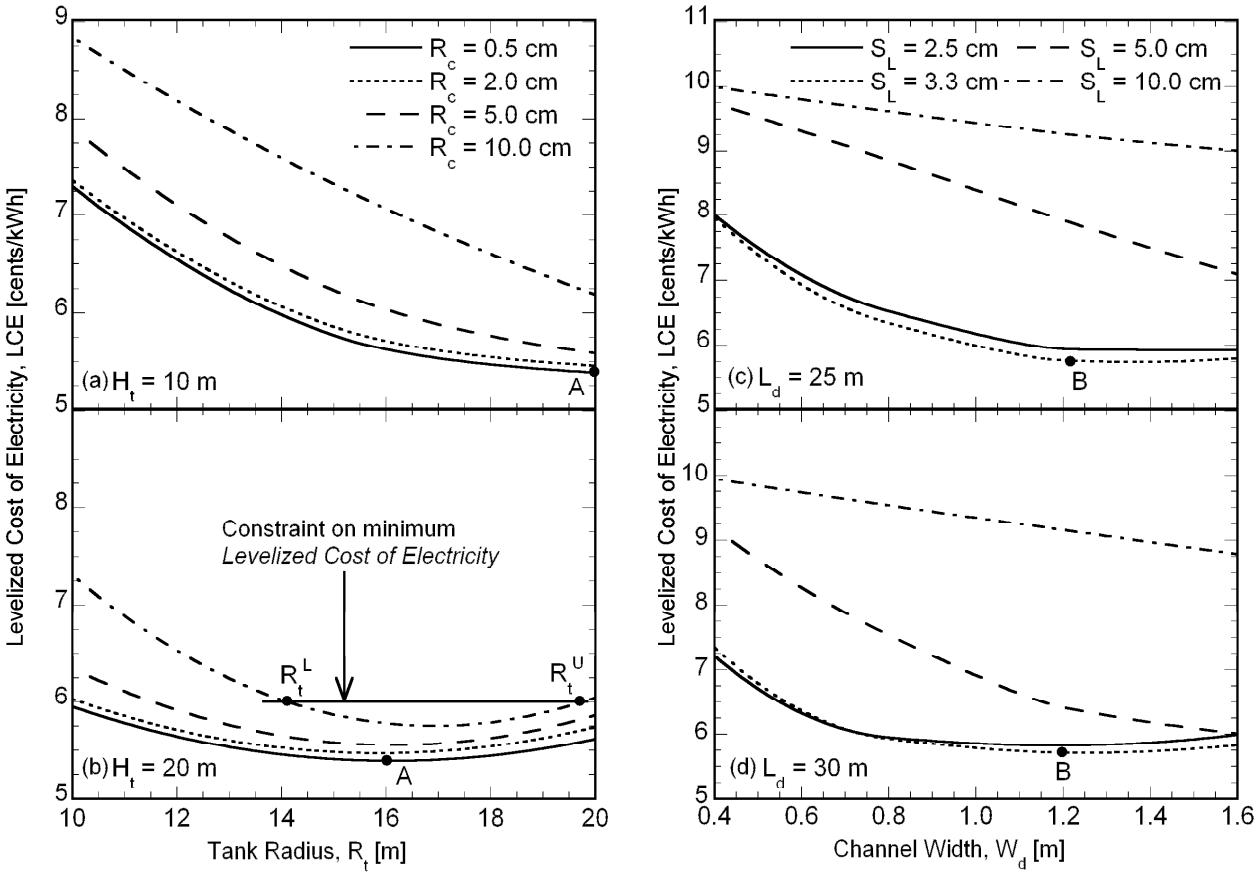

Figure 53: Variations in levelized cost of electricity with tank radius and capsule radius of (a) 10 m and (b) 20 m tall EPCM-TES system integrated to a s-CO_2 powered CSP plant and variations in levelized cost of electricity with longitudinal spacing between the heat pipes and channel width of (a) 25 m and (b) 30 m long HP-TES system integrated to a s-CO_2 powered CSP plant

tank height of 10 m, although the minima in the variations occur for tank radii greater than the range of plot in Figure 53a.

Analogous trends of the LCE with the geometric parameters of the HP-TES system are also evident in Figure 53c and d. For the smaller channel width, the storage cost is small (Figure 52c and d), but the capacity factor is also low (Figure 50a and b), leading to a high LCE. For the large channel widths, the capacity factor is relatively invariant with channel width (Figure 50a and b), whereas the storage cost increases significantly with width (Figure 52c and d), resulting in an

increase in the LCE. It is, therefore, seen that the LCE is minimized for a certain optimum channel width, W_d^*, which is greater for the smaller channel length (Figure 53c) compared to that for the larger channel length (Figure 53d), for any given spacing, S_L. Note that for the HP-TES systems with larger longitudinal spacing and, in turn, fewer heat pipes, the optimum channel width occurs beyond the range of the plots in Figure 53c and d. Furthermore, the LCE does not exhibit a monotonic variation with the longitudinal spacing; the minimum LCE is seen to be for S_L = 3.3 cm for most channel widths considered in Figure 53c and d.

From the LCE plots in Figure 53a–d, it is seen that the lowest LCE is obtained at 5.39 ¢/kWh for the EPCM-TES system consisting of (a) 10 m tall tank and 20 m radius filled with PCM in capsules of radius 0.5 cm and at 5.37 ¢/kWh for (b) 20 m tall tank and 16 m radius filled with PCM in capsules of radius 0.5 cm, as shown by the points A in Figure 53a and b. For the HP-TES system, the lowest LCE of approximately 5.83 ¢/kWh is obtained for (a) a channel length of 25 m, channel width of 1.19 m and longitudinal spacing of 3.3 cm. These design points are denoted by the points B in Figure 53c and d. Figure 53a–d may also be used to derive bounds on the tank radius and the channel width for the respective TES systems, so as to meet the SunShot target of the LCE < 6 cents/kWh. Because of the nonmonotonic variation of the LCE with respect to the tank radius or the channel width in Figure 53a–d, the constraint of LCE < 6 cents/kWh yields a lower bound as well an upper bound between which the constraint is satisfied, as exemplified in Figure 53b for R_c = 10.0 cm and a tank height of 20 m. Similarly, bounds may be developed for the other configurations presented in Figure 53. Note that for those cases where the minima in the LCE and, in turn, the upper bound on the tank radius or the channel width fall outside the range of the plots, the upper bounds are taken to be the upper limits of the range of the respective plots, i.e., $R_t^U = 20$ m and $W_d^U = 1.6$ m.

The lower and upper bounds on the tank radius and the channel width identified from Figure 51–Figure 53 corresponding to the SunShot targets of exergetic efficiency, $\zeta > 95\%$, storage cost, $\alpha <$ US$87.95 MM, and LCE < 6 cents/kWh, are used to construct design windows to derive information on optimum designs of ECPM-TES (Figure 54a and b) and HP-TES systems (Figure 54c and d). The discussion of Figure 51–Figure 53 indicated that the exergetic efficiency constraint yields a lower bound, the storage cost constraint yields an upper bound, whereas the LCE constraint yields both lower and upper bounds on the tank radius as a function of the capsule radius, for each tank height, in the case of EPCM-TES and on the channel width as function of the longitudinal spacing, for each channel length, in the case of HP-TES. In Figure 54, the dotted lines denote the lower bounds from the $\zeta > 95\%$ constraint, the solid lines denote the lower bound based on the LCE constraint, and the chain-dashed lines represent the upper bound based on the storage cost constraint. In most cases, the upper bound based on the LCE constraint falls on the upper limit of the range of the tank radius or the channel width on the plots. The design windows illustrated in Figure 54 for both the EPCM-TES system and the HP-TES system are formed between the upper bounds dictated by the storage capital cost and lower bounds dictated by the maximum LCE.

The shaded portion in Figure 54a presents the design window identifying the feasible design regime of the storage tank radius and capsule radius that satisfies the above constraints for EPCM-TES of height 10 m. It is seen that the feasible range of design parameters is wide for a smaller capsule radius and for larger capsule radius, both the bounds dictated by the storage capital cost (higher encapsulation cost) and the LCE (decrease in capacity factor) approach each other to yield a narrow design window. The feasible design window for capsule radius greater than 4.0 cm is restricted by the storage cost requirement. As the tank height is increased, a feasible design

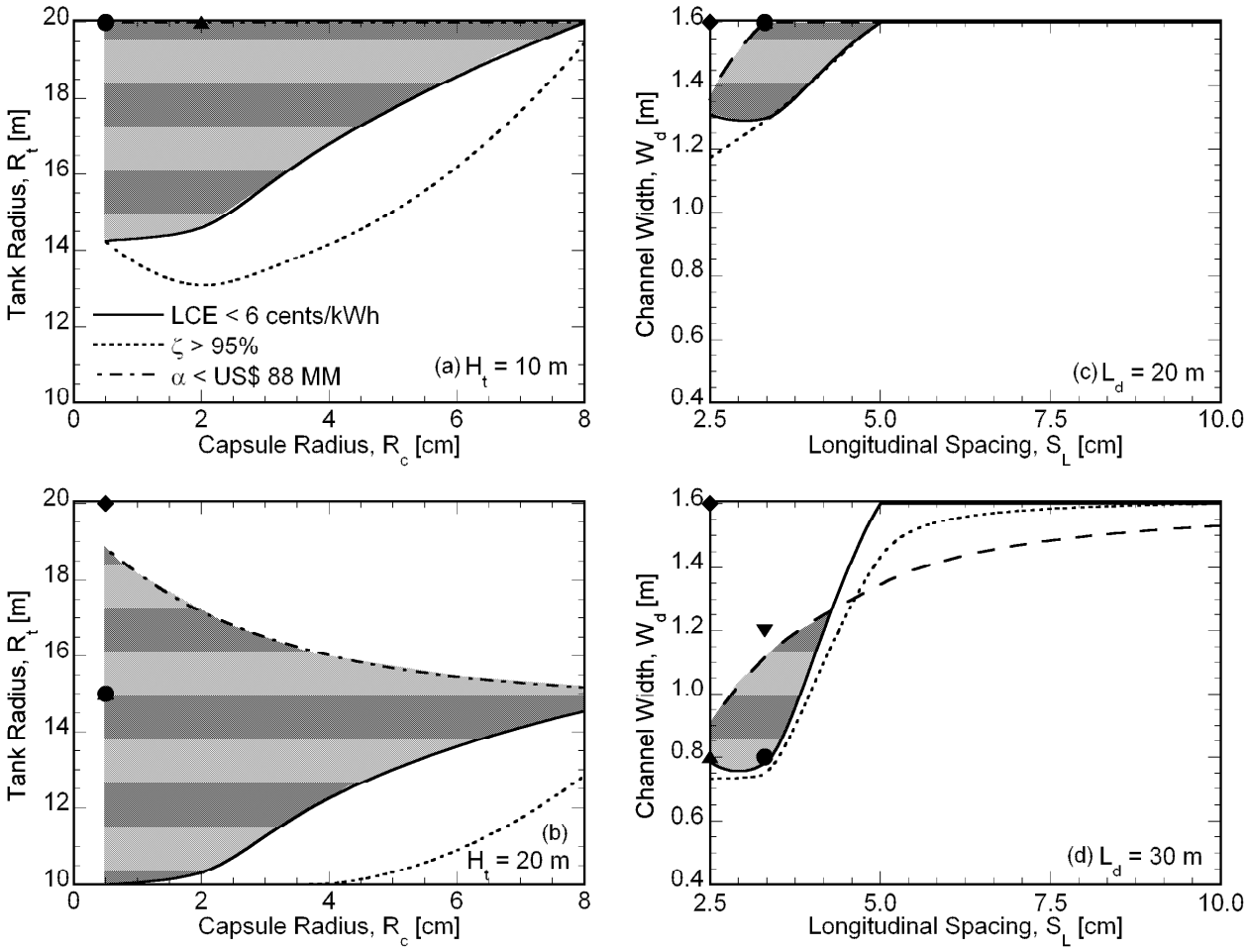

Figure 54: Design envelopes for (a) 10 m and (b) 20 m tall EPCM-TES system and (c) 20 m and (d) 25 m long HP-TES system that satisfy SunShot [50] requirements. The maximum annual exergetic efficiency and the minimum levelized cost of electricity within the design window for each of the storage system are represented by filled triangles and circles, respectively.

window is obtained for small EPCM-TES tank radius due to increase in capacity factor as a result of increased storage capacity. However, for a large tank radius, the storage cost exceeds the SunShot requirements and no feasible design window is obtained. In the case of the HP-TES system, the design window for a channel length of 25 m is not obtained for longitudinal spacing greater than 5.0 cm. As observed from Figure 54c and d, the design window that satisfies SunShot requirements is obtained for small channel widths as channel length increases.

Within the feasible design window in Figure 54a and b, the design parametric values which give the least LCE of 5.51 ¢/kWh and 5.54 ¢/kWh for tank heights of 10 m and 20 m, respectively is indicated as filled circle. To the same extent, the maximum exergetic efficiency of $\zeta = 98.8\%$ (H_t = 10 m) and $\zeta = 99.0\%$ (H_t = 20 m) obtained are indicated by filled triangles in Figure 54a and b, respectively. The filled diamond marker in Figure 54b corresponds to the overall maximum annual exergetic efficiency obtained from the storage system integrated into a CSP plant working on s-CO_2 power conversion cycle. The minimum LCE and the maximum exergetic efficiency obtained for HP-TES system within the design window corresponds to 5.77 ¢/kWh (solid circle in Figure 54c) and 97.1% (solid triangle in Figure 54c). The overall minimum LCE of 5.71 ¢/kWh and maximum exergetic efficiency of 98.9% for HP-TES system is represented by filled inverted triangle and diamond markers, respectively in Figure 54d.

The corresponding combinations of the optimum design parameters and the performance metrics are tabulated in Table 15. Since the heat pipe cost and the encapsulation cost is vital to the calculation of storage capital cost and hence the LCE, Table 15 also shows the sensitivity of the LCE to the heat pipe cost and the encapsulation cost. In addition to that, Table 15 also compares the impact of the storage system on the LCE of 200 MW_e CSP plant working on a Rankine cycle and s-CO_2 cycle integrated with 2-tank molten salt storage system. For the solar multiple of 2.7, minimum LCE of 6.45 ¢/kWh is obtained for a 2-tank sensible energy storage system of radius, 18.5 m (Figure 53c) which is relatively higher than that obtained for EPCM-TES (Figure 53b) of the same tank radius, LCE = 5.50 ¢/kWh due to lower storage capital cost of EPCM-TES and higher storage capacity of EPCM-TES. Since the exit temperature of the HTF discharged from the 2-tank sensible heat storage to the power block is always at the highest operation temperature, the annual exergetic efficiency is close to 100% and hence not tabulated here. Among all the

configurations studied, the minimum LCE of 5.37 ¢/kWh (cf. Table 15b(i)) is obtained for s-CO_2 based CSP plant integrated with EPCM-TES of height 15 m and tank radius 15 m for the smallest capsule radius of 0.5 cm which is two times lesser than that obtained for CSP plant with no storage (cf. Table 15a). It is also seen that even doubling the encapsulation cost satisfies the SunShot requirements. A Rankine cycle based CSP plant offers a minimum LCE of only 9.05 ¢/kWh (cf. Table 15b(ii)) when integrated with a EPCM-TES system and also requires a higher storage capacity (H_t = 20 m) to achieve the minimum LCE compared to s-CO_2 based CSP plant operation. The minimum LCE for HP-TES system is obtained for a longitudinal spacing of 0.33 cm with a total number of 15.62 million heat pipes (cf. Table 15c(i)). The critical or maximum unit cost of heat pipes beyond which LCE less than 6 ¢/kWh is not obtained correspond to $4/unit HP (cf. Table 15c(i)). For a Rankine cycle based CSP plant, as observed in the case of EPCM-TES system a longer channel height and width embedded with a total of 24.9 million heat pipes is required to achieve the lease LCE of 9.69 ¢/kWh (cf. Table 15c(i)). Compared to a the minimum LCE obtained for s-CO_2 based CSP plant operation integrated with 2-tank molten salt storage system (Table 15a) the LCE of the EPCM-TES system is atleast 1 ¢/kWh less (Table 15b(i)).

The findings of the present system analysis study illustrated the cost saving benefits of CSP integrated with LTES system, the LCE of currently existing 2-tank sensible storage system being atleast 1 ¢/kWh and 0.68 ¢/kWh higher compared to EPCM-TES and HP-TES systems, respectively. Overall, this chapter presents a methodology for model based design and optimization of the latent thermocline storage system based on the systematic parametric studies and consideration of SunShot Initiative's 2020 targets.

Table 15: Optimum storage design configurations obtained from CSP plant integrated system analysis

a. Optimum 2-Tank design configuration for least LCE

Power Plant Cycle	Storage Type	Tank Radius, R_t [m]	Tank Height, H_t [m]	Annual Net Energy O/P Q_e, [GWh]	Capacity Factor, β [%]	Storage Capital Cost [US$ MM]	LCE [¢/kWh]
Supercritical SCO_2	No TES	-	-	553.5	31.6	-	11.07
	2-Tank	*18.6*	*20*	*1118.9*	*65.4*	*158.1*	*6.45*
Rankine	No TES	-	-	565.5	32.3	-	17.46
	2-Tank	23.7	20	1160.3	66.2	204.6	9.92

b. Optimum EPCM-TES system design configuration for least LCE

Power Plant Cycle	Encapsulation Cost, [$/kg-PCM]	Tank Radius, R_t [m]	Tank Height, H_t [m]	Capsule Radius, R_c [cm]	Annual Net Energy O/P Q_e, [GWh]	Capacity Factor, β [%]	Storage Capital Cost [US$ MM]	LCE [¢/kWh]	Exergetic Efficiency, ζ [%]
Supercritical SCO_2	**(i) *0.75***	***15***	***15***	***0.5***	***1204.9***	***68.77***	***42.8***	***5.37***	***96.04***
	(ii) 1.50	*15*	*15*	*0.5*	*1204.9*	*68.77*	*58.1*	*5.47*	*96.04*
Rankine	(i) 0.75	20	15	0.5	1157.6	66.07	74.6	9.05	98.42
	(ii) 1.50	20	15	0.5	1157.6	66.07	101.8	9.24	98.42

c. Optimum LTES-HP system design configuration for least LCE

Power Plant Cycle	Heat Pipe Cost [$/unit]	Channel Length, L_d [m]	Channel Width, W_d [m]	Longitudinal Spacing, S_L [cm] (No. of HPs)	Annual Net Energy O/P Q_e, [GWh]	Capacity Factor, β [%]	Storage Capital Cost [US$ MM]	LCE [¢/kWh]	Exergetic Efficiency, ζ [%]
Supercritical SCO_2	(i) *2.0*	*25*	*1.2*	*3.3 (15624164)*	*1158.7*	*66.14*	*78.61*	*5.77*	*97.05*
	(ii) 4.0	*25*	*1.2*	*3.3 (15624164)*	*1158.7*	*66.14*	*110.5*	*6.05*	*97.05*
Rankine	(i) 2.0	30	1.6	3.3 (24898663)	1122.1	64.05	124.7	9.69	97.61
	(ii) 4.0	25	1.2	3.3 (24898663)	1122.1	64.05	175.7	10.05	97.61

7.5 Nomenclature used in Chapter 7

b	capsule wall thickness [m]
c	specific heat [J/kg-K]
C'	cost per unit mass [$/kg]
C''	cost per unit area [$/m^2]
f_l	melt fraction
h	convective heat transfer coefficient [W/m^2-K]
h_l	latent heat of fusion of PCM [J/kg]
H	height [m]
k	thermal conductivity [W/m-K]
L	length [m]
LCE	levelized cost of electricity [¢/kWh]
$\dot{m}$	mass flow rate [kg/s]
N	number
Q_e	net electric output [W-h]
Q	energy [W-h]
R	radius [m]
S_L	longitudinal spacing between heat pipes
t	time [s]
T	temperature [K]
T_m	melting temperature [K]
U	HTF velocity [m/s]
W	channel width [m]

Subscripts and Superscripts

c	capsule
C	charging
d	channel
D	discharging
f	heat transfer fluid
HP	gravity assisted heat pipes
L	latent
p	phase change material
S	sensible
t	tank
T	total
eff	effective

Greek Symbols

α	storage capital cost [$/kWh]
ε	porosity of the packed bed
μ	dynamic viscosity
ρ	density
ξ	exergetic efficiency [%]

Chapter 8: Conclusions and Future Work

The presented studies analyzed two different approaches of improving the low heat transfer rates and low exergetic efficiency of latent thermal energy storage system for deployment in CSP systems. Overall, this dissertation presents a methodology for model based design and optimization of the latent thermal energy storage systems based on the systematic parametric studies to achieve the SunShot goal [50] of a levelized cost of electricity of 6 ¢/kW_h, to make unsubsidized solar energy cost competitive with fossil fuel energy.

8.1 Analysis and Design of LTES with embedded heat pipes

In the first part of this dissertation, an approach to reducing the thermal resistance of PCM through embedded heat pipes which are passive heat transfer devices that efficiently transfer large amount of thermal energy between the phase change material and a heat transfer fluid (HTF) was investigated. A thermal resistance network model was developed to simulate the transient response of an LTES system with four embedded heat pipes. Considering two different modules of the system, the influence of the heat pipes on the performance of the system during charging and discharging cycles were studied in terms of an effectiveness as well as the total energy stored (charged) or discharged. In general, it was found that increase in the HTF mass flow rate, module length and tube radius reduced the effectiveness of the heat pipes; while increase in the length of the condenser section, the length of the evaporator section and the vapor core radius enhanced its effectiveness. Optimum design conditions were presented for the two modules, which showed that the effectiveness of the heat pipes in augmenting the thermal performance of the LTES is significantly higher for Module 1 while the effective charging (discharging) rate of the PCM is

found to be higher for Module 2.

Next, a detailed transient three-dimensional computational analysis of a shell-and-tube LTES embedded with heat pipes is performed for melting (charging) and solidification (discharging) to determine the position of melt front, energy stored and an effectiveness of the heat pipe embedded configurations as a function of time. The influence of the number and orientation of heat pipes and the configuration of the system are analyzed to identify designs that lead to improved effectiveness. The results presented in this chapter illustrate a methodology to determine the performance enhancement in LTES due to the usage of heat pipes. It was found that the effectiveness was higher for the case of 4-HP for both the modules during both charging and discharging. Substantially higher effectiveness is observed for the different heat pipe arrangements in Module 1 as the melt fronts fused with the periodically repeating unit cells at the top and bottom. Module 2 resulted in a higher melt fraction compared to Module 1 while the energy stored in the case of Module 1 was higher. The results also showed that the natural convection currents mainly influenced the performance of LTES embedded with heat pipes over the heat transfer between HTF and heat pipes, while thermal stratification was clearly observed in Module 2.

A comprehensive transient model of a large scale Latent thermal storage system embedded with gravity assisted heat pipes (HP-TES) is presented in Chapter 4, and systematic parametric investigations are conducted over a wide range of the HP-TES operating and design parameters to understand the dynamic behavior of the system. Using the simulation results, maximum discharge time, exergetic efficiency and minimum storage cost is obtained as a function of various operating and design parameters constrained to SunShot targets. The results provide direct usable information for optimum operating and design of HP-TES systems for integration with CSP plant.

8.2 Analysis and Design of Encapsulated PCM Thermal Energy Storage (EPCM-TES) system

The second portion of this dissertation presented an investigation of enhancing the heat transfer rate of latent thermal storage system by storing the PCM is small spherical capsules, thereby enhancing the surface area for heat interaction between the HTF and PCM. A computational model of a latent thermocline energy storage system, accounting for axial variation of temperature in the HTF and radial temperature variation in the PCM at any axial position was presented. Using the model, the effects of various non-dimensional variables on the steady and dynamic performance of the thermocline storage system were analyzed. The important results from the analysis can be summarized as follows: (1) smaller radii capsules yield higher total and latent utilization; (2) larger values of the Reynolds number and, in turn, higher mass flow rate leads to decrease in the utilization of the system due to expansion of the heat exchange zone; (3) an increase in the inverse Stefan number and the capacitance ratio are accompanied by a decrease in the system utilization and an increase in the total storage capacity; (4) the effect of the PCM melt temperature on the system utilization is non-monotonic, with higher latent utilization for PCM's whose melt temperature is either greater than the discharge cut-off temperature or lesser than the charge cut-off temperature. The results of the study were used to illustrate a procedure for designing a latent thermocline energy storage system for practical operating considerations of a CSP plant. By means of practical design illustrations, it was shown that the use of smaller PCM capsules greatly reduces the tank volume requirement, which translates to reduction in material cost. Based on a systematic parametric analysis on the various performance metrics, feasible operating regimes and design conditions are identified which meet the SunShot Initiative requirements: (a) charge time less than

6 hours, (b) discharge time greater than 6 hours, (c) exergetic efficiency greater than 95% and (d) storage cost less than \$15/kWh$_t$.

The last part of the dissertation presents the first effort to construct and analyze latent thermal energy storage (LTES) integrated CSP plant performance that can help decision makers in assessing the impact, cost and performance of LTES systems on power generation from molten salt power tower CSP plant. The influence of design parameters of the storage system on the performance of a 200 MW$_e$ capacity power tower CSP plant is studied to establish design envelopes that satisfy the U.S. Department of Energy SunShot Initiative requirements: (a) LCE less than 6 ¢/kWh, (b) exergetic efficiency greater than 95% and (c) storage cost less than \$US 88MM. The minimum LCE obtained from the parametric study and the design window is less than the SunShot 2020 target of 6 ¢/kWh for EPCM-TES system at 5.37 ¢/kWh. Also, it is found that the maximum cost of heat pipes embedded in LTES which satisfies the SunShot requirements is \$4/unit HP.

8.3 Future Work

In future studies involving the computational modeling of latent thermal storage systems with embedded heat pipes, a more detailed numerical model of heat pipes to analyze the impact of its frozen start-up process on the performance of LTES. The phase change modeling of the PCM may be extended to quantify the effects of volume expansion and shrinkage during melting and solidification, respectively on the heat transfer rate between the HTF and PCM.

In the studies involving large scale encapsulated PCM thermal storage system (EPCM-TES), the potential for the occurrence of thermal ratcheting should be analyzed through a detailed finite

element analysis to evaluate the peak hoop stress on the tank during the cyclic operation of the system. Future work on system analysis may involve a comprehensive analysis of CSP plant working on supercritical CO_2 cycle integrated with other LTES systems, such as metal foam enhanced LTES to obtain design and operating envelopes that satisfy the SunShot 2020 target of 6 ¢/kWh. Further investigation may be undertaken to address the corrosion and material stability issues in latent thermal storage systems subjected to repeated charge and discharge cycles.

Bibliography

[1] J. Stekli, L. Irwin, and R. Pitchumani, "Technical Challenges and Opportunities for Concentrating Solar Power with Energy Storage," *ASME Journal of Thermal Science Engineering and Applications*, vol. 5, no. 2, p. In Press, 2013.

[2] U. Herrmann and D. W. Kearney, "Survey of Thermal Energy Storage for Parabolic Trough Power Plants," *Journal of Solar Energy Engineering*, vol. 124, no. 2, p. 145, 2002.

[3] B. Zalba, J. M. Marín, L. F. Cabeza, and H. Mehling, "Review on thermal energy storage with phase change: materials, heat transfer analysis and applications," *Applied Thermal Engineering*, vol. 23, no. 3, pp. 251–283, Feb. 2003.

[4] H. Michels and R. Pitz-Paal, "Cascaded latent heat storage for parabolic trough solar power plants," *Solar Energy*, vol. 81, no. 6, pp. 829–837, Jun. 2007.

[5] W.-D. Steinmann and R. Tamme, "Latent Heat Storage for Solar Steam Systems," *Journal of Solar Energy Engineering*, vol. 130, no. 1, p. 011004, 2008.

[6] P. Verma and S. Singal, "Review of mathematical modeling on latent heat thermal energy storage systems using phase-change material," *Renewable and Sustainable Energy Reviews*, vol. 12, no. 4, pp. 999–1031, May 2008.

[7] P. Lamberg, R. Lehtiniemi, and A.-M. Henell, "Numerical and experimental investigation of melting and freezing processes in phase change material storage," *International Journal of Thermal Sciences*, vol. 43, no. 3, pp. 277–287, Mar. 2004.

[8] K. W. Ng, Z. X. Gong, A. S. Mujumdar, T. S. Group, and M. Quebec, "Pergamon PII S0735-1933(98)00050-5," vol. 25, no. 5, pp. 631–640, 1998.

[9] E. Assis, L. Katsman, G. Ziskind, and R. Letan, "Numerical and experimental study of melting in a spherical shell," *International Journal of Heat and Mass Transfer*, vol. 50, no. 9–10, pp. 1790–1804, May 2007.

[10] S. Jegadheeswaran and S. D. Pohekar, "Performance enhancement in latent heat thermal storage system: A review," *Renewable and Sustainable Energy Reviews*, vol. 13, no. 9, pp. 2225–2244, Dec. 2009.

[11] V. Shatikian, G. Ziskind, and R. Letan, "Numerical investigation of a PCM-based heat sink with internal fins," *International Journal of Heat and Mass Transfer*, vol. 48, no. 17, pp. 3689–3706, Aug. 2005.

[12] M. Gharebaghi and I. Sezai, "Enhancement of Heat Transfer in Latent Heat Storage Modules with Internal Fins," *Numerical Heat Transfer, Part A: Applications*, vol. 53, no. 7, pp. 749–765, Nov. 2007.

[13] J. Wang, G. Chen, and H. Jiang, “Theoretical study on a novel phase change process,” *International Journal of Energy Research*, vol. 23, no. 4, pp. 287–294, 1999.

[14] S. Shaikh and K. Lafdi, “Effect of multiple phase change materials (PCMs) slab configurations on thermal energy storage,” *Energy Conversion and Management*, vol. 47, no. 15–16, pp. 2103–2117, Sep. 2006.

[15] S. Kim and L. T. Drzal, “High latent heat storage and high thermal conductive phase change materials using exfoliated graphite nanoplatelets,” *Solar Energy Materials and Solar Cells*, vol. 93, no. 1, pp. 136–142, Jan. 2009.

[16] C. Guo and W. Zhang, “Numerical simulation and parametric study on new type of high temperature latent heat thermal energy storage system,” *Energy Conversion and Management*, vol. 49, no. 5, pp. 919–927, May 2008.

[17] J. Fukai, M. Kanou, Y. Kodama, and O. Miyatake, “Thermal conductivity enhancement of energy storage media using carbon fibers,” *Energy Conversion and Management*, vol. 41, no. 14, pp. 1543–1556, 2000.

[18] J. M. Khodadadi and S. F. Hosseinizadeh, “Nanoparticle-enhanced phase change materials (NEPCM) with great potential for improved thermal energy storage,” *International Communications in Heat and Mass Transfer*, vol. 34, no. 5, pp. 534–543, May 2007.

[19] J. L. Zeng, L. X. Sun, F. Xu, Z. C. Tan, Z. H. Zhang, J. Zhang, and T. Zhang, “Study of a PCM based energy storage system containing Ag nanoparticles,” *Journal of Thermal Analysis and Calorimetry*, vol. 87, no. 2, pp. 371–375, Dec. 2006.

[20] B. Horbaniuc, G. Dumitrascu, and A. Popescu, “Mathematical models for the study of solidification within a longitudinally finned heat pipe latent heat thermal storage system,” *Energy Conversion and Management*, vol. 40, pp. 1765–1774, 1999.

[21] Z. Liu, Z. Wang, and C. Ma, “An experimental study on heat transfer characteristics of heat pipe heat exchanger with latent heat storage. Part I: Charging only and discharging only modes,” *Energy Conversion and Management*, vol. 47, no. 7–8, pp. 944–966, May 2006.

[22] W.-S. Lee, B.-R. Chen, and S.-L. Chen, “Latent Heat Storage in a Two-Phase Thermosyphon Solar Water Heater,” *Journal of Solar Energy Engineering*, vol. 128, no. 1, p. 69, 2006.

[23] F. Tardy and S. M. Sami, “Thermal analysis of heat pipes during thermal storage,” *Applied Thermal Engineering*, vol. 29, no. 2–3, pp. 329–333, 2009.

[24] A. Faghri, *Heat Pipe Science and Technology*. New York: Taylor & Francis, 1995.

[25] H. Shabgard, T. L. Bergman, N. Sharifi, and A. Faghri, “High temperature latent heat thermal energy storage using heat pipes,” *International Journal of Heat and Mass Transfer*, vol. 53, no. 15–16, pp. 2979–2988, Jul. 2010.

[26] Z. J. Zuo and A. Faghri, “A network thermodynamic analysis of the heat pipe,” *International Journal of Heat and Mass Transfer*, vol. 41, no. 11, pp. 1473–1484, Jun. 1998.

[27] T. W. Kerslake, “Multi-dimensional modeling of a thermal energy storage canister, NASA Technical Memorandum 103731,” Cleveland, OH, 1991.

[28] Y. Cao and A. Faghri, “Transient two-dimensional compressible analysis for high-temperature heat pipes with pulsed heat input,” *Numerical Heat Transfer , Part A: Applications*, vol. 18, pp. 586–594, 1990.

[29] F. P. Incropera, D. P. DeWitt, T. L. Bergman, and A. S. Lavine, *Fundamentals of Heat and Mass Transfer*, vol. 6th. John Wiley & Sons, 2007, p. 997.

[30] R. A. Seban and R. Bond, “Skin friction and heat transfer characteristics of a laminar boundary layer on a cylinder in axial incompressible flow,” *Journal of the Aeronautical Sciences*, pp. 671–675, 1951.

[31] K. T. Yang, “Natural convection in enclosures,” in *Handbook of Single-Phase COnvective Heat Transfer*, S. Kakac, R. Shah, and W. Aung, Eds. New York: Wiley, 1987, p. 13.7.

[32] L. C. Thomas, *Heat Transfer*. Englewood Cliffs: Prentice-Hall, 1993.

[33] J. C. Butcher, *Numerical methods for ordinary differential equations*. John Wiley & Sons, 2003.

[34] H. Price, E. Lüpfert, D. Kearney, E. Zarza, G. Cohen, R. Gee, and R. Mahoney, “Advances in Parabolic Trough Solar Power Technology,” *Journal of Solar Energy Engineering*, vol. 124, no. 2, p. 109, 2002.

[35] P. E. Gill, W. Murray, and M. H. Wright, *Practical Optimization*. London: Academic Press, 1981.

[36] M. J. D. Powell, “A fast algorithm for nonlinearly constrained optimization,” *Springer Verlag*, vol. 630, 1976.

[37] S. P. Han, “A globally convergent method for nonlinear programming,” *Journal of Optimization Theory and Applications*, vol. 22, no. 3, pp. 297–309, Jul. 1977.

[38] A. Trp, “An experimental and numerical investigation of heat transfer during technical grade paraffin melting and solidification in a shell-and-tube latent thermal energy storage unit,” *Solar Energy*, vol. 79, no. 6, pp. 648–660, Dec. 2005.

[39] M. M. Farid, A. M. Khudhair, S. A. K. Razack, and S. Al-Hallaj, “A review on phase change energy storage: materials and applications,” *Energy Conversion and Management*, vol. 45, no. 9–10, pp. 1597–1615, Jun. 2004.

[40] J. Zuo and A. Faghri, “A network thermodynamic analysis of the heat pipe,” *International Journal of Heat and Mass Transfer*, vol. 41, no. 11, pp. 1473–1484, 1998.

[41] C. B. Sobhan, S. V Garimella, and V. V Unnikrishnan, “A Computational Model for the Transient Analysis of Flat Heat Pipes,” in *ASME International Heat Transfer Conference*, 2000, pp. 106–113.

[42] T. Kaya and J. Goldak, “Three-dimensional numerical analysis of heat and mass transfer in heat pipes,” *Heat and Mass Transfer*, vol. 43, no. 8, pp. 775–785, Jul. 2006.

[43] V. R. Voller and C. Prakash, “A fixed grid numerical modeling methodology for convection-diffusion mushy region phase-change problems,” vol. 30, 1987.

[44] A. D. Brent, V. R. Voller, and K. J. Reid, “Enthalpy-porosity technique for modeling convection-diffusion phase change_ application to the melting of a pure metal,” *Numerical Heat Transfer*, vol. 13, pp. 297–318, 1988.

[45] K. Nithyanandam and R. Pitchumani, “Analysis and optimization of a latent thermal energy storage system with embedded heat pipes,” *International Journal of Heat and Mass Transfer*, vol. 54, no. 21–22, pp. 4596–4610, Oct. 2011.

[46] B. J. Jones, D. Sun, S. Krishnan, and S. V. Garimella, “Experimental and numerical study of melting in a cylinder,” *International Journal of Heat and Mass Transfer*, vol. 49, no. 15–16, pp. 2724–2738, Jul. 2006.

[47] K. Nithyanandam and R. Pitchumani, “Computational studies on a latent thermal energy storage system with integral heat pipes for concentrating solar power,” *Applied Energy*, vol. 103, pp. 400–415, Mar. 2013.

[48] “High Energy Advanced Thermal Storage,” *Department of Energy, U.S. DOE FOA: DE-FOA-0000471.*, 2012.

[49] Z.-X. Gong and S. Mujumdar, “Thermodynamic optimization of the thermal process in energy storage using multiple phase change materials,” vol. 17, no. ll, pp. 1067–1083, 1997.

[50] “SunShot Vision Study: February 2012,” *SunShot, Energy Efficiency and Renewable Energy, U.S. Department of Energy. NREL Report No. BK5200-47927; DOE/GO-102012-3037*, 2012.

[51] H. Shabgard, C. W. Robak, T. L. Bergman, and A. Faghri, “Heat transfer and exergy analysis of cascaded latent heat storage with gravity-assisted heat pipes for concentrating solar power applications,” *Solar Energy*, vol. 86, no. 3, pp. 816–830, Mar. 2012.

[52] M. M. Kenisarin, “High-temperature phase change materials for thermal energy storage,” *Renewable and Sustainable Energy Reviews*, vol. 14, no. 3, pp. 955–970, Apr. 2010.

[53] G. G. Nrel, “Developing a Cost Model and Methodology to Estimate Capital Costs for Thermal Energy Storage Developing a Cost Model and Methodology to Estimate Capital Costs for Thermal Energy Storage,” *NREL Technical Report*, no. NREL/TP-55, 2011.

[54] “Enertron Inc.” [Online]. Available: htttp://www.enertron-inc.com/store.asp.

[55] C. Robak, “Latent Heat Thermal Energy Storage with Embedded Heat Pipes for Concentrating Solar Power Applications,” University of Connecticut, 2012.

[56] “MEPS International Ltd.” [Online]. Available: www.meps.co.uk.

[57] B. Kelly and D. Kearney, “Thermal Storage Commercial Plant Design Study for a 2-Tank Indirect Molten Salt System Final Report Thermal Storage Commercial Plant Design Study for a 2-Tank Indirect Molten Salt System Final Report,” *NREL Report*, no. NREL/SR-550–40166, 2006.

[58] P. Gilman, N. Blair, M. Mehos, and C. Christensen, “Solar Advisor Model User Guide for Version 2.0,” *NREL Technical Report*, no. NREL/TP-670–4370, 2008.

[59] “Using Encapsulated Phase Change Material in Thermal Storage for Baseload Concentrating Solar Power Plants,” *US DOE FOA: DE-EE0003589 Terrafore, Inc.*

[60] D. E. Beasleyt and J. A. Clark, “Transient response of a packed bed for thermal energy storage,” vol. 21, no. 9, pp. 1659–1669, 1984.

[61] T. E. W. Schumann, “Heat Transfer: A liquid flowing through a porous prism,” *J. Franklin Inst.*, vol. 208, pp. 405–416, 1929.

[62] Z. Yang and S. V. Garimella, “Thermal analysis of solar thermal energy storage in a molten-salt thermocline,” *Solar Energy*, vol. 84, no. 6, pp. 974–985, Jun. 2010.

[63] Z. Yang and S. V. Garimella, “Cyclic operation of molten-salt thermal energy storage in thermoclines for solar power plants,” *Applied Energy*, vol. 103, pp. 256–265, Mar. 2013.

[64] J. T. Van Lew, P. Li, C. L. Chan, W. Karaki, and J. Stephens, “Analysis of Heat Storage and Delivery of a Thermocline Tank Having Solid Filler Material,” *Journal of Solar Energy Engineering*, vol. 133, no. 2, p. 021003, 2011.

[65] P. Li, J. Van Lew, W. Karaki, C. Chan, J. Stephens, and Q. Wang, “Generalized charts of energy storage effectiveness for thermocline heat storage tank design and calibration,” *Solar Energy*, vol. 85, no. 9, pp. 2130–2143, Sep. 2011.

[66] M. Hänchen, S. Brückner, and A. Steinfeld, "High-temperature thermal storage using a packed bed of rocks – Heat transfer analysis and experimental validation," *Applied Thermal Engineering*, vol. 31, no. 10, pp. 1798–1806, Jul. 2011.

[67] K. A. R. Ismail and J. R. Henr, "Numerical and experimental study of spherical capsules packed bed latent heat storage system," vol. 22, pp. 1705–1716, 2002.

[68] A. F. Regin, S. C. Solanki, and J. S. Saini, "Heat transfer characteristics of thermal energy storage system using PCM capsules: A review," *Renewable and Sustainable Energy Reviews*, vol. 12, no. 9, pp. 2438–2458, Dec. 2008.

[69] H. Singh, R. P. Saini, and J. S. Saini, "A review on packed bed solar energy storage systems," *Renewable and Sustainable Energy Reviews*, vol. 14, no. 3, pp. 1059–1069, Apr. 2010.

[70] A. Felix Regin, S. C. Solanki, and J. S. Saini, "An analysis of a packed bed latent heat thermal energy storage system using PCM capsules: Numerical investigation," *Renewable Energy*, vol. 34, no. 7, pp. 1765–1773, Jul. 2009.

[71] S. Wu and G. Fang, "Dynamic performances of solar heat storage system with packed bed using myristic acid as phase change material," *Energy and Buildings*, vol. 43, no. 5, pp. 1091–1096, May 2011.

[72] T. R. Galloway and B. H. Sage, "A model of the mechanism of transport in packed, distended, and fluidized beds," *Chemical Engineering Science*, vol. 25, no. 3, pp. 495–516, Mar. 1970.

[73] S. V. Patankar, *Numerical heat transfer and fluid flow*. Taylor & Francis, 1980.

[74] J. E. Pacheco, S. K. Showalter, and W. J. Kolb, "Development of a Molten-Salt Thermocline Thermal Storage System for Parabolic Trough Plants," *Journal of Solar Energy Engineering*, vol. 124, no. 2, p. 153, 2002.

[75] N. Nallusamy, S. Sampath, and R. Velraj, "Experimental investigation on a combined sensible and latent heat storage system integrated with constant/varying (solar) heat sources," *Renewable Energy*, vol. 32, no. 7, pp. 1206–1227, Jun. 2007.

[76] "Solar Thermocline Storage Systems-Preliminary design study," *EPRI Public copy*, 2010.

[77] A. Mathur, "Personal Comunication."

[78] J. A. Nelder and R. Mead, "A Simplex Method for Function Minimization," *The Computer Journal* , vol. 7 , no. 4 , pp. 308–313, Jan. 1965.

[79] A. Mawardi and R. Pitchumani, “Optimal Temperature and Current Cycles for Curing of Composites Using Embedded Resistive Heating Elements,” *Journal of Heat Transfer*, vol. 125, no. 1, p. 126, 2003.

[80] W. H. Press, B. P. Flannery, S. A. Teukolsky, and W. T. Vettering, *Numerical Recipes in FORTRAN*. New York, NY: Cambridge University Press, 1992.

[81] D. P. Bertsekas, *Nonlinear Programming*. Belmont, MA: Athena Scientific, 1999.

[82] V. Dostal, “A Supercrtitical Carbon Dioxide Cycle for Next Generation Nuclear Reactors,” Massachusetts Institute of Technology, 2004.

[83] C. S. Turchi, “Supercritical CO2 for Application in Concentrating Solar Power Systems,” in *Proceeding of SCCO2 Power Cycle Symposium 2009*, 2009, pp. 1–5.

[84] W. Seidel, “Model Development and Annual Simulation of the Supercritical Carbon Dioxide Brayton Cycle for Concentrating Solar Power Applications,” University of Wisconsin, Madison, 2010.

[85] I. Purohit and P. Purohit, “Techno-economic evaluation of concentrating solar power generation in India,” *Energy Policy*, vol. 38, no. 6, pp. 3015–3029, Jun. 2010.

[86] A. Jain, T. Vu, R. Mehta, and S. K. Mittal, “Optimizing the Cost and Performance of Parabolic Trough Solar Plants with Thermal Energy Storage in India,” *Environmental Progress & Sustainable Energy*, pp. 1–6, 2012.

[87] S. Janjai, J. Laksanaboonsong, and T. Seesaard, “Potential application of concentrating solar power systems for the generation of electricity in Thailand,” *Applied Energy*, vol. 88, no. 12, pp. 4960–4967, Dec. 2011.

[88] T. Telsnig, L. Eltrop, and H. Winkler, “Efficiency and costs of different solar power plant configuration for sites in gauteng and Northern Cape: SA,” in *12th Southern African Solar Energy Conference*, 2012, pp. 1–10.

[89] K. Ravi Kumar and K. S. Reddy, “4-E (energy-exergy-environmental-economic) analyses of line-focusing stand-alone concentrating solar power plants,” *International Journal of Low-Carbon Technologies*, vol. 7, no. 2, pp. 82–96, Feb. 2012.

[90] G. Manzolini, A. Giostri, C. Saccilotto, P. Silva, and E. Macchi, “Development of an innovative code for the design of thermodynamic solar power plants part A: Code description and test case,” *Renewable Energy*, vol. 36, no. 7, pp. 1993–2003, Jul. 2011.

[91] S. J. Smith, “Long-Term Modeling of Solar Energy: Analysis of Concentrating Solar Power (CSP) and PV Technologies,” *PNNL Technical Report*, no. PNNL 16727, 2008.

[92] N. Blair, M. Mehos, and C. Christensen, “Sensitivity of concentrating solar power trough performance, cost , and financing with the solar advisor model,” in *2008 14th Biennial CSP SolarPACES (Solar Power and Chemical Energy Systems) Symposium*, 2008, no. March.

[93] G. J. Kolb, “Evaluation of Annual Performance of 2-Tank and Thermocline Thermal Storage Systems for Trough Plants,” *Journal of Solar Energy Engineering*, vol. 133, no. 3, p. 031023, 2011.

[94] J. J. Burkhardt, G. a Heath, and C. S. Turchi, “Life cycle assessment of a parabolic trough concentrating solar power plant and the impacts of key design alternatives.,” *Environmental science & technology*, vol. 45, no. 6, pp. 2457–64, Mar. 2011.

[95] M. Wagner, “Simulation and Predictive Performance Modeling of Utility-Scale Central Receiver System Power Plants by,” University of Wisconsin, Madison, 2008.